Measured Behavior of a Balanced Cantilever Erected Curved Segmental Concrete Bridge

by

Michael Keith Thompson, B.S.

Thesis

Presented to the Faculty of the Graduate School of

The University of Texas at Austin

in Partial Fulfillment

of the Requirements

for the Degree of

Master of Science in Engineering

The University of Texas at Austin

May 1998

Measured Behavior of a Balanced Cantilever Erected Curved Segmental Concrete Bridge

Approved by
Supervising Committee:

John E. Breen

Michael E. Kreger

Measured Behavior of a Balanced Cantilever Erected Curved Segmental Concrete Bridge

by

Michael Keith Thompson, B.S.

Thesis

Presented to the Faculty of the Graduate School of

The University of Texas at Austin

in Partial Fulfillment

of the Requirements

for the Degree of

Master of Science in Engineering

The University of Texas at Austin

May 1998

Measured Behavior of a Balanced Cantilever Erected Curved Segmental Concrete Bridge

Approved by
Supervising Committee:

John E. Breen

Michael E. Kreger

Acknowledgments

The author would like to express his appreciation to Dr. John Breen for his guidance and friendship during the course of this project. His suggestions and tutelage have been invaluable in the writing of this thesis. Thanks is also given to Dr. Michael Kreger who also supervised the creation of this thesis.

The Ferguson Laboratory staff were a great help in fulfilling this study. My deepest thanks go to Sharon Cunningham, Laurie Golding, April Jenkins, Blake Stasney, Wayne Fontenot, Mike Bell, Ray Madonna, Pat Ball, and the late Wayne Little.

There were several individuals with TXDOT, Eby Construction, and Flatiron Structures Company whose cooperation was essential to the completion of this research. Tom Rummel, Dean Vand Landuyt and Jim Evans from TXDOT provided many suggestions for areas of study as well as much information from the design and construction stages of U.S. 183. Ron Fletcher ran the precasting yard for the U.S. 183 project and was always attentive to our needs during the instrumentation phase of the study. Donnie Lamb, the erection supervisor of the balanced cantilever ramp, was always cooperative to our needs. Many nights out on the ramp were often filled with frustration after frustration. Throughout, Donnie never once complained about our presence and, was in fact, always polite to the research group. His cooperation was greatly appreciated.

My appreciation is extended to the other Master's candidates who worked on this study. Valerie Andreas, Bryan Wood, and Wade Bonzon helped to set the standard for which this thesis was written. Wade was also a good friend who helped during the instrumentation of the ramp even though he was quite busy with the writing of his own thesis and had little time to spare.

Rodney Davis was the individual who lead the U.S. 183 study. It was his guidance which made the study succeed. He has also been a good friend. I owe him much gratitude for all of the nights he provided me with free dinner.

I also wish to thank all of the friends I have at Ferguson laboratory who have been there to listen to me gripe and woe about my stories of the bridge.

I owe a debt of gratitude to all of the people at Figg Engineering Inc. who introduced me to the field of segmental bridge design and instilled in me the interest which lead me to work on this study.

Finally, I wish to thank my parents for all of their support and love. Their care has provided me with the ability to fulfill my goals. Without their lifetime of commitment to my growth, I would not be where I am today.

May, 1998

Measured Behavior of a Balanced Cantilever Erected Curved Segmental Concrete Bridge

by

Michael Keith Thompson, M.S.E.

The University of Texas at Austin, 1997

Supervisor: John E. Breen

A five span continuous precast segmental horizontally curved concrete bridge erected in balanced cantilever as part of the U.S. Highway 183 interchange with Interstate Highway 35 in Austin, Texas was instrumented with concrete strain gauge devices and thermocouples. The response of the structure was studied during erection, during a live load test, and under the actions of daily applied thermal gradients that occurred over a period of nine months. Measured data are presented and compared to calculated values. The measured data are also used to evaluate design specifications in current highway bridge codes. Observations of the construction process and comments regarding the efficiency of the construction methods used to build the bridge are presented. Recommendations concerning bridge design specifications and construction practices are also presented.

Table of Contents

List of Tables

List of Figures

CHAPTER 1

INTRODUCTION

1.1 GENERAL

This thesis presents results from the study of a five span continuous precast segmental horizontally curved concrete bridge structure constructed in balanced cantilever. This structure is part of a fly-over ramp between northbound IH-35 and northbound U.S. 183 in Austin, Texas. This research has been conducted as part of a study by the Texas Department of Transportation to investigate the structural performance of the U.S. 183 elevated highway that was recently completed in north central Austin. The results of this research will be applied by TXDOT engineers to improve the design and construction of segmental bridges in Texas and the U.S. This research was carried out by the Phil M. Ferguson Structural Engineering Laboratory of the University of Texas at Austin. Four Master's degree candidates, one Ph.D. candidate, two supervising professors, and several volunteers performed the research. The overall study focused on the performance of four structures within the U.S. 183 project: an innovative Y-shaped cast-in-place pier, a three span semi-continuous precast segmental superstructure unit constructed span-by-span, a tall precast segmental pier, and the five span continuous precast segmental bridge structure constructed in balanced cantilever. The performance of the last structure will be the topic of this thesis. The other three structures have already been reported on in the theses of Valerie Andres, Wade Bonzon, and Bryan Wood respectively [4,6,22]. The Ph.D. dissertation of Rodney Davis will summarize the results of these theses and present information on various U.S. 183 bridge components and advanced topics related to segmental bridges [7].

1.2 U.S. 183 PROJECT OVERVIEW

U.S. Highway 183 runs north-south from southern South Dakota to the south-eastern part of Texas near Corpus Christi. Part of U.S. 183 passes through the northern part of Austin, Texas and serves as an important piece of the arterial viaducts that carry traffic in and around the city. Elevated lanes were constructed on the portion of U.S. 183 which runs through north Austin to

alleviate congestion by separating through traffic from local traffic. The project was designed by TXDOT and contracted by Martin K. Eby Construction in a joint venture with Flatiron Structures Company.

An important design consideration for the TXDOT bridge engineers who worked on U.S. 183 was the aesthetics of the project. Negative public response to the previously built IH-35 elevated freeway on the eastern edge of Austin prompted designers to give heavy consideration to the appearance of the U.S. 183 project. The size of the project (over 10 kilometers of bridge structure) and the need to reduce the amount of substructure for ground level right-of-way limitations made a precast segmental box girder solution optimal. The simple form and lightweight appearance of this type of superstructure was deemed a more aesthetically pleasing structure than the typical pretensioned I girder superstructures used in most Texas bridges. The box girder choice also allowed for longer spans and a reduction of substructure for the project which provided economic benefits and opened up the space beneath the bridge for less intrusion of the structure on local businesses and residential communities. Architectural details of the piers and the superstructure were utilized to further improve the appearance of the bridge.

The solution chosen by the TXDOT designers proved to be very cost effective as well as aesthetic. The average cost of the project which had spans in the 39.6 m (130') range was 420 $\$/m^2$ (39 $\$/ft^2$) as compared with the Texas average of 344 $\$/m^2$ (32 $\$/ft^2$) and the U.S. average of 743 $\$/m^2$ (69 $\$/ft^2$). The latter averages are for a wide range of girder bridges, frequently with much shorter span lengths. The project encompassed 121,000 m^2 (1,300,000 ft^2) of deck space. 198 spans of the elevated highway were constructed span-by-span. Fifteen transition spans were cast-in-place because it was felt that it would be too difficult to modify the precasting forms for these structures. Five spans which had much longer lengths were built in balanced cantilever which helped reduce traffic interruptions in a key intersection. The five spans built in balanced cantilever formed one part of a ramp structure connecting northbound IH-35 with northbound U.S. 183. This ramp was designated as Ramp P in contract drawings. Figure 1.1 shows the location of the U.S. 183 project and the portion known as Ramp P.

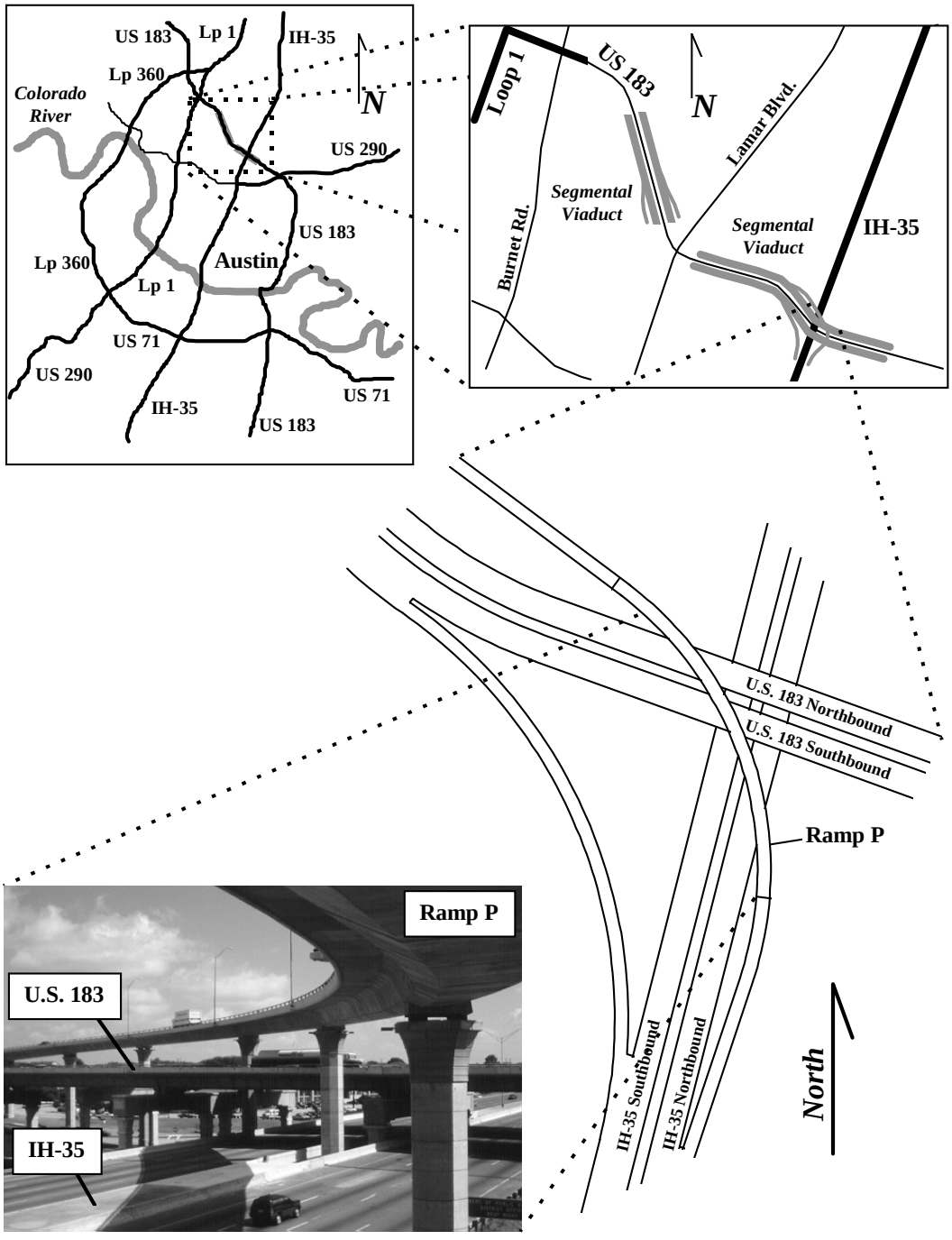

Figure 1.1 - U.S. 183 project location

1.3 DESCRIPTION OF RAMP P

The alignment of the fly-over ramp between northbound IH-35 and northbound U.S. 183 (Ramp P) required the structure to pass over the mainlanes and frontage roads of both of those highways. The congestion in the area beneath the ramp reduced the space available for supporting substructure requiring longer spans in the ramp than were typical of the rest of the project. The alignment of the ramp also followed a fairly tight radius of 221 m (726'). Both of these constrictions made use of the span-by-span construction method, which was used extensively through the rest of the U.S. 183 project, impractical for construction of Ramp P. Therefore, balanced cantilever construction was used to build the ramp.

Figure 1.2 shows the span arrangement of Ramp P. The ramp had heavy anchorage diaphragms for post-tensioning tendons over each pier. The dimensions of the segments which had these diaphragms (four total) are given in Figure 1.3. Typical segments had an increasing bottom flange thickness near the interior piers. The bottom flange modification was necessitated by the heavy negative moment from the free cantilever construction load. Figure 1.4 shows the typical segment dimensions. Figure 1.5 shows the dimensions of the pier cross-section.

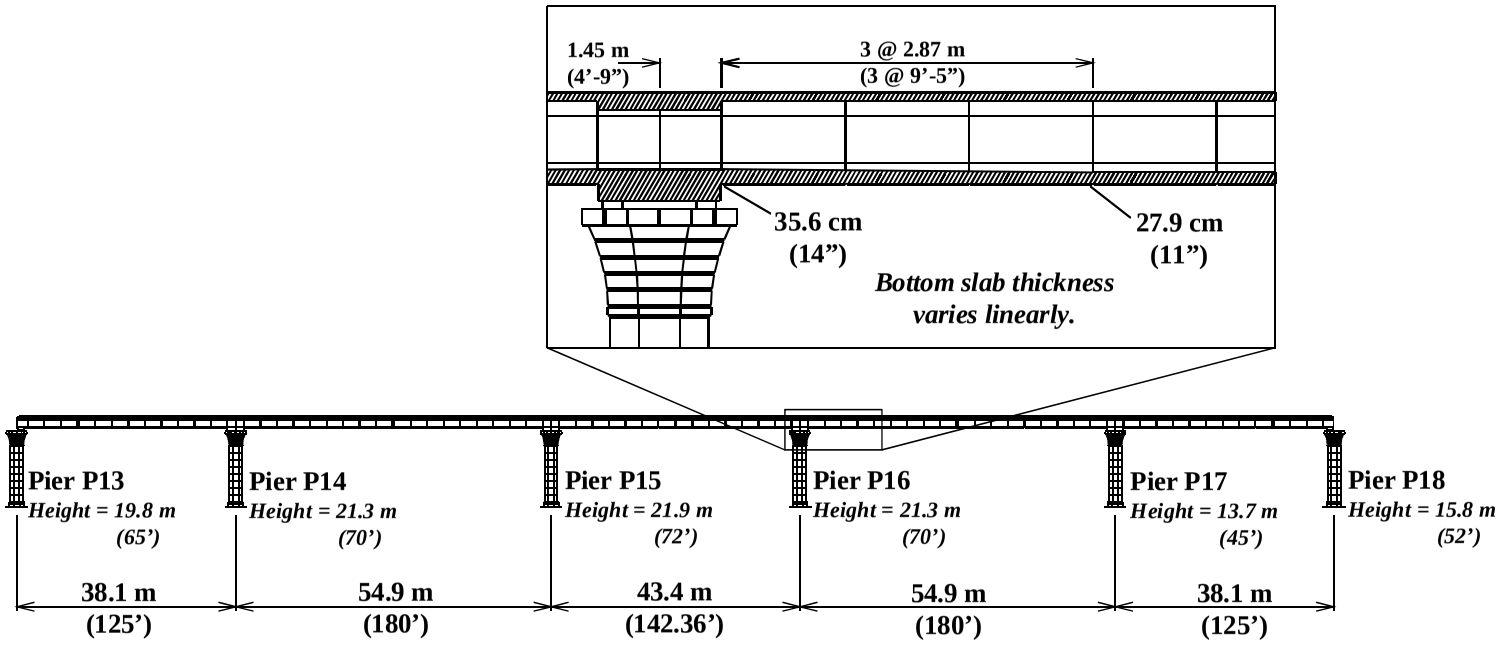

Figure 1.2 - Layout of Ramp P

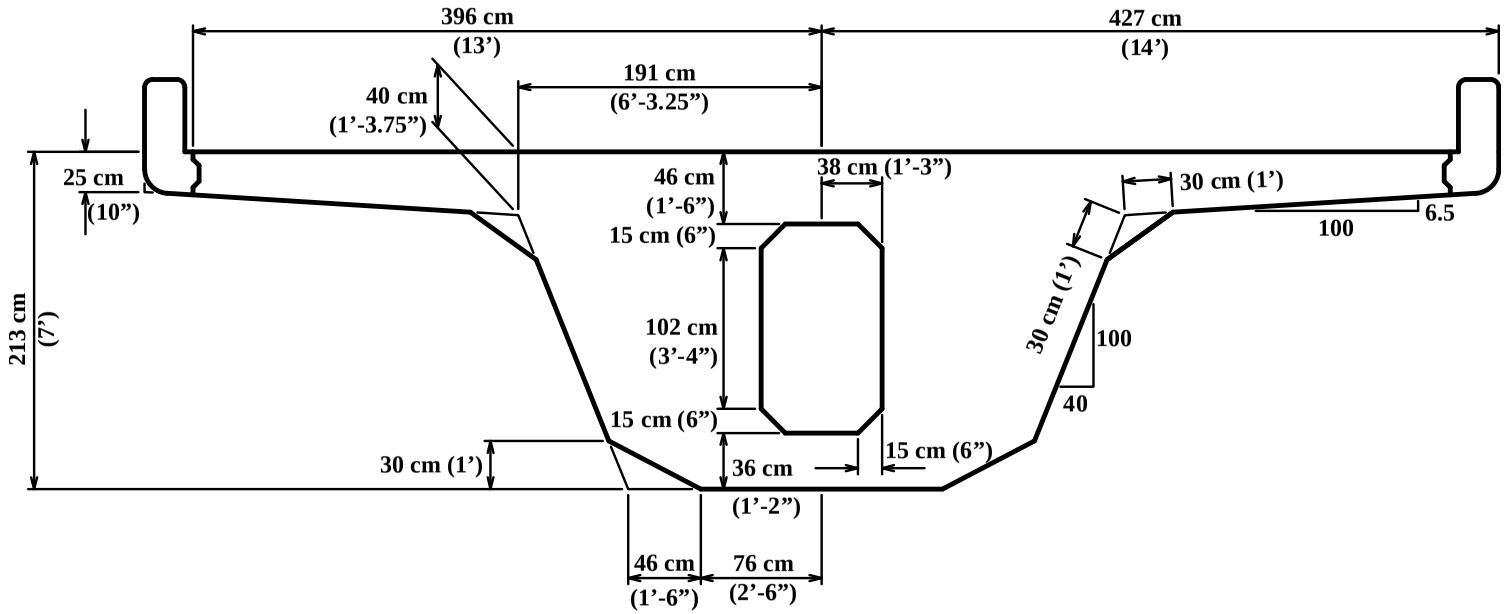

Figure 1.3 - Dimensions for Ramp P interior anchorage segment cross-section

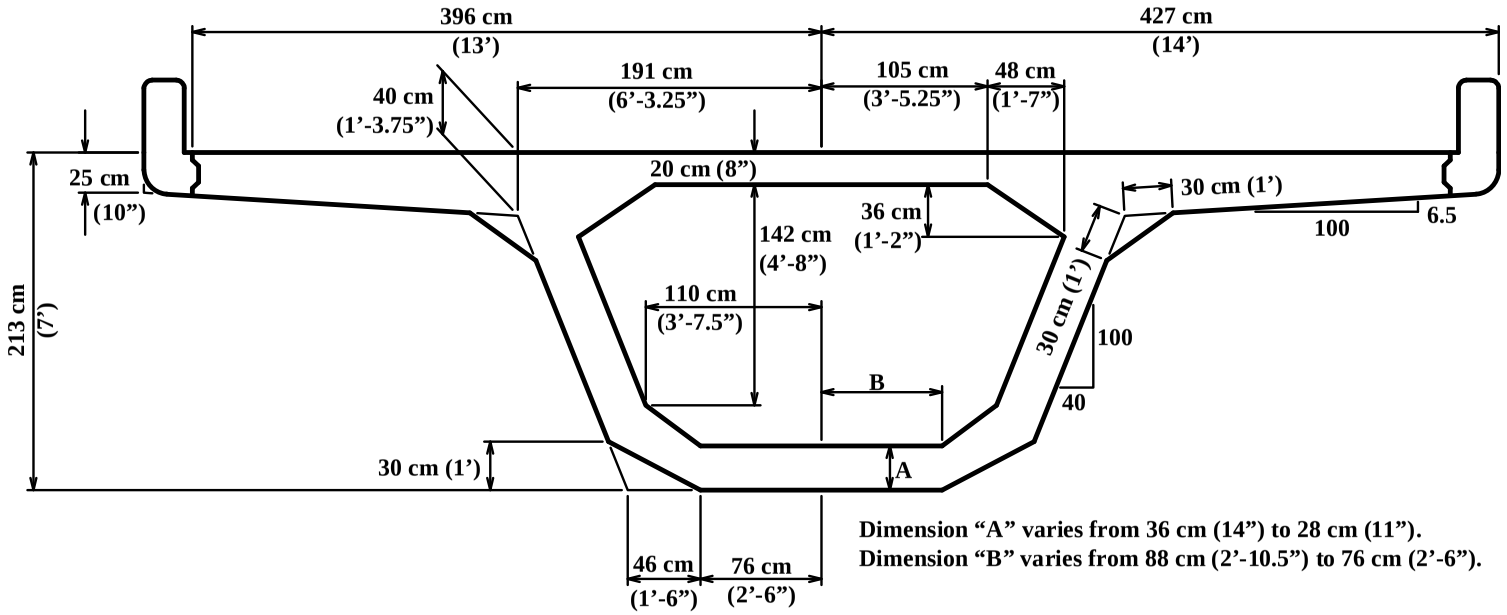

Figure 1.4 - Dimenions for Ramp P typical segment cross-section

Figure 1. 1Figure 1. 2Figure 1. 3Figure 1. 4

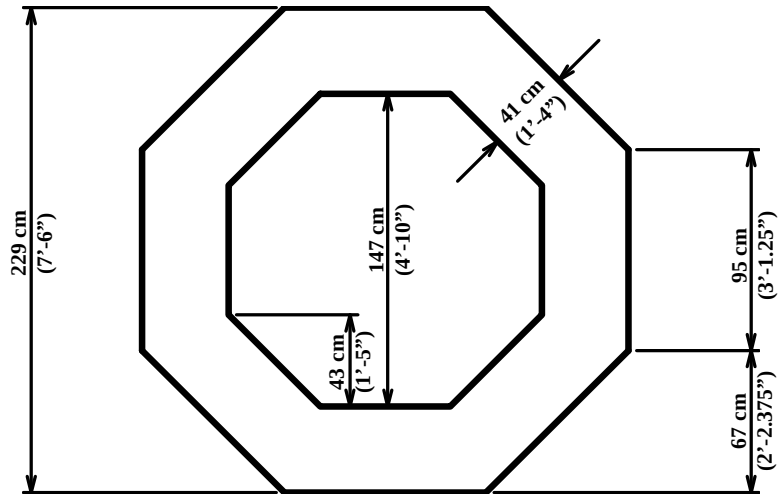

Figure 1.5 - Dimensions for large ramp pier cross-section

1.4 PROBLEM STATEMENT AND OBJECTIVES

Segmental bridge construction is still a relatively new form of technology for many engineers in the U.S. Education of engineering students with respect to design or erection of precast, post-tensioned construction of any form is not common in the curriculum of most U.S. universities. TXDOT has sponsored a broad program of research into segmental bridge topics which began in 1970 with the construction and study of the JFK Memorial Causeway in Corpus Christi. Over the years TXDOT has invested much money into research projects designed to advance the knowledge of the behavior of segmental bridges. Most of the information gained from this research has been implemented in the provisions of the *AASHTO Guide Specifications for Design and Construction of Segmental Bridges* [1]. The *AASHTO Guide Specifications* is one of the only texts available to bridge engineers that provides guidance in the design of segmental bridges. Many of the guidelines in the *AASHTO Guide Specifications* are derived from analytical studies or laboratory research of reduced scale bridge models. Studies from actual bridge structures are not numerous enough to provide confirmation of all of the guidelines nor do they include the full range of bridge structures covered under the *AASHTO Guide Specifications*. The purpose of the study of the U.S. 183 project is to provide data from an actual bridge structure which can be used to verify commonly used analytical methods for bridge design and to point out

problem areas which may have escaped the attention of engineers in the past. Specifically, the study of Ramp P is intended to satisfy the following objectives:

1. To comprehensively instrument the ramp so that its flexural and torsional behavior under various loading conditions can be fully determined.
2. To determine the behavior of the ramp under construction loads.
3. To observe the construction of the ramp and report on constructability problems related to segmental balanced cantilever construction.
4. To determine the behavior of the completed ramp under live load.
5. To measure thermal gradients and creep effects in the ramp over an extended period of time.
6. To determine the response of the ramp to these applied thermal gradients.
7. To make recommendations to TXDOT and AASHTO of any needed changes in design procedures or design specifications based on the indications from the recorded data and the observations of the researchers involved in the study.

1.5 SCOPE OF WORK

The scope of work encompassed by this thesis includes the instrumentation of one span of a five span continuous precast segmental horizontally curved concrete box girder bridge constructed in balanced cantilever. Instruments were monitored at two minute intervals during the construction process and during a live load test performed on the completed structure. Instruments were monitored hourly at all other times (during construction and since completion of the structure) to determine the thermal gradients occurring in the structure and the response to these gradients. Data measured with the instrumentation were then compared to simple analytical calculations of predicted behavior. When applicable, calculations were based on recommended methods from the *Proposed AASHTO LRFD Guide Specifications for Design and Construction of Segmental Bridges* [17] or the *AASHTO LRFD Bridge Design Specifications* [2]. Recommendations for changes in design practices are given when deemed necessary.

1.6 ORGANIZATION OF THESIS

The organization of this report is as follows:

Chapter 1 - Introduction
Chapter 2 - Background
Chapter 3 - Superstructure Instrumentation
Chapter 4 - Superstructure Construction Process
Chapter 5 - Construction Sequence Data
Chapter 6 - Live Load Test
Chapter 7 - Thermal Behavior
Chapter 8 - Conclusions and Recommendations

Chapters 1, 2, and 3 provide background information which will facilitate the reader's comprehension of the chapters that present data and observations (Chapters 4 through 7). Chapters 4 through 7 each contain their own conclusions and recommendations that are relevant to the topics discussed in those chapters. Chapter 8 summarizes the conclusions and recommendations from Chapters 4 through 7.

CHAPTER 2

BACKGROUND

2.1 INTRODUCTION

This chapter is intended to present the reader with background information that is pertinent to the topics that will be discussed in this report. Thus, this chapter contains discussions on:

- the historical background of prestressed segmental construction with emphasis on balanced cantilever construction
- stress distributions in segmental hollow box girders bridges,
- thermal effects on bridges,
- the behavior of curved girders, and
- analysis methods for segmental concrete box girder bridges.

2.2 PRESTRESSED SEGMENTAL CONSTRUCTION

A number of previous reports produced by the Ferguson Structural Engineering Laboratory have included detailed descriptions of the development of segmental bridge construction. Particularly, Arréllaga [5] provides a thorough background summary of prestressed segmental bridge development. In addition, the texts by Podolny and Müller [15] and Menn [11] have served as the traditional resources on segmental bridge design and construction for many years. Both contain very good descriptions of the development of prestressed segmental bridges. However, because both of these texts were published in the 1980's, they are already out of date with regard to the latest accomplishments in this rapidly advancing industry.

2.2.1 Evolution

The modern state of prestressed concrete segmental box girder bridges is the result of developments in materials and techniques used for prestressing and of the technology used in segmental construction.

2.2.1.1 Prestressing

Prestressing was first applied to bridges between 1910 and 1912 by Eugene Freyssinet with the La Veurde Bridge, a three span arch bridge over the Allier River in France. Freyssinet used jacks placed at the apexes of the arches to push the two halves apart and remove creep deflections from the bridge (Figure 2.1). The applied deformations were maintained in the bridge by placing mortar permanently in the apexes of the arches. Freyssinet continued to pursue the idea of using applied forces to enhance the structural performance of bridge structures and eventually patented a steel wire system for prestressing in 1928 [5].

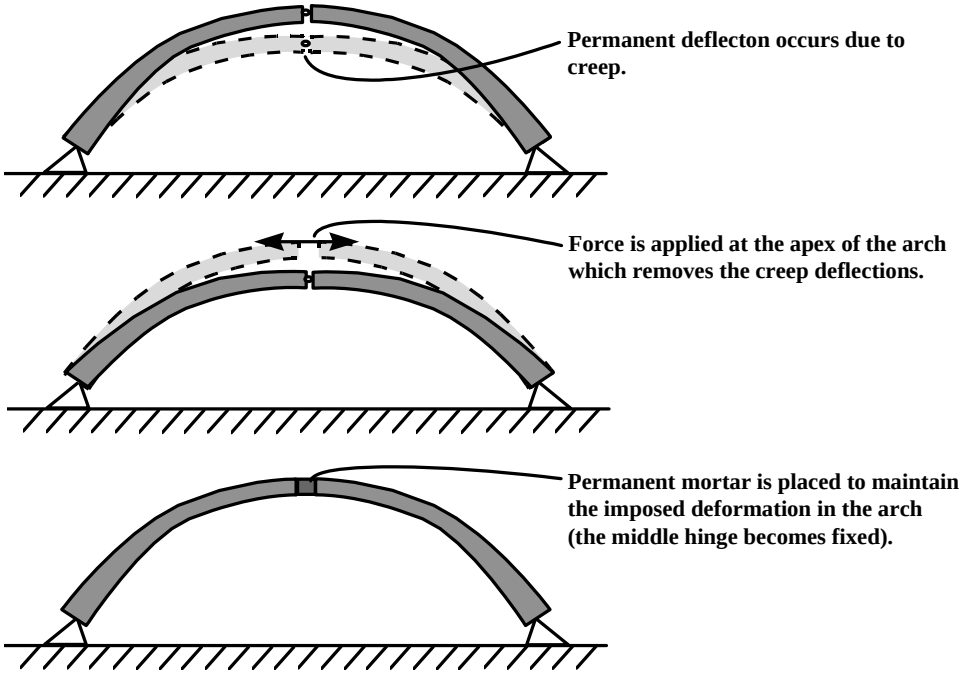

Figure 2.1 - The beginnings of prestressing in bridges

The first modern use of tensioned steel for prestressing of a bridge occurred in 1928. Franz Dischinger used large diameter steel rods to post-tension the 61m (200') long concrete span of the Saale-Brucke bridge in Germany. These rods were of the relatively low strength steel that was available at the time. Eventually, creep and shrinkage of the concrete and relaxation of the steel resulted in losses of 75% of the initial prestress force in the bars. Prestressed concrete was initially hampered by these material phenomena and the difficulties of stressing in the field. However, advances in technology soon produced higher strength steel at economical costs as well as better anchorage and jacking systems for steel bars and wires. By 1939, Freyssinet had developed conical wedges and a double acting jack capable of power seating the wedges. Also at that time, the Magnel-Blaten System was developed in Belgium and the Gifford-Udall System was developed in Britain, both of which allowed for prestressing of multi-strand tendons [5]. Prestressing of concrete rapidly began to appear in bridge designs.

2.2.1.2 Segmental Construction

Segmental construction had been in practice in Europe since the twelfth century. The process evolved from masonry structures to reinforced concrete structures. By 1901, hollow box reinforced concrete sections were being used for arch bridges [11].

Precasting of concrete, which was first applied to short span beam bridges, was combined with segmental construction by Eugene Freyssinet in the early 1940's. The bridge which represented this advance, the Pont de Luzancy, was a precast, prestressed, segmental girder bridge. It was completed in 1946.

2.2.1.3 Cantilever Construction

The first recorded use of the cantilever construction method for bridges was in the fourth century with the Shogun's bridge in the city of Nikko, Japan [15]. Cantilever construction had been used extensively for the construction of steel bridges in the late 1800's. The St. Louis Bridge, a steel truss arch designed by James Eads, was constructed in cantilever so that falsework that would block the flow of river traffic on the Mississippi could be avoided [14]. Elimination of falsework has been the traditional reason for building bridges in cantilever.

The first application of cantilever construction to reinforced concrete was the Rio do Peixe Bridge in Herval, Brazil built in 1930. Cantilever construction was used because the danger

of flash flooding on the river made construction with falsework hazardous [11, 15]. Cantilever construction with cast-in-place prestressed concrete first occurred in 1951 with the Lahn Bridge in Balduistein, Germany [11]. Precast segmental bridges erected in balanced cantilever were built in the 1960's in the former Soviet Union [5].

In 1964 the Choisy-le-Roi Bridge was built over the Seine River in Paris, France. This bridge which was designed by Jean Müller represented the first use of balanced cantilever construction combined with precast segments having epoxied match-cast joints [11, 15]. The use of epoxied match-cast joints was a significant development in segmental construction technology.

Since the construction of the Choisy-le-Roi Bridge, use of segmental balanced cantilever construction has become a common construction method for segmental bridges. The typical span ranges of bridges built in balanced cantilever compared with other segmental construction methods are shown in Figure 2.2. Cantilever construction is generally used for the following reasons:

- Congestion in the area beneath the bridge construction or environmental reasons prevent the use of falsework.
- Span lengths set by the spacing of the substructure elements are too long to build an economical erection truss for span-by-span construction or the size of the project is too small to make an erection truss a cost-effective expenditure.
- The method of construction leaves the bridge with a favorable distribution of dead load forces.

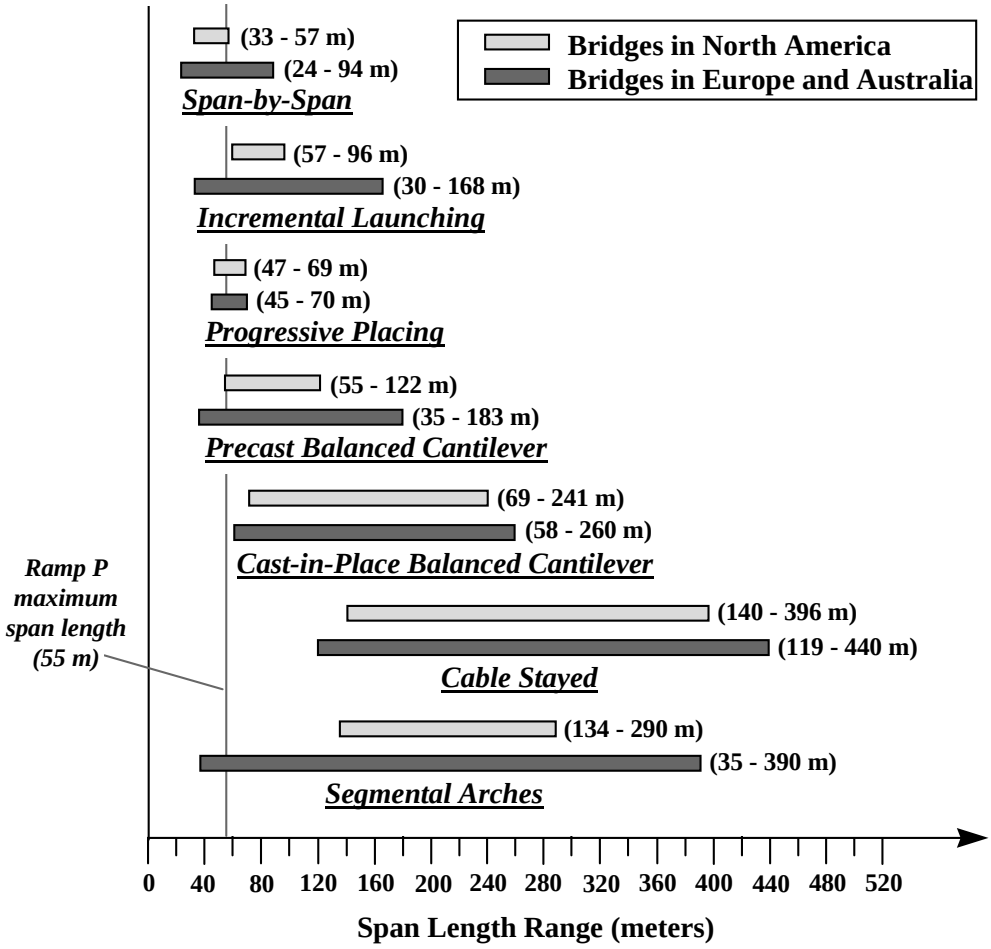

Figure 2.2 - Span ranges for various segmental construction methods (after Arrélaga [5])

2.2.2 Segmental Bridge Codes in the United States

In the U.S., design and construction of segmental bridges is currently controlled by two manuals: The first is the *AASHTO Guide Specifications for Design and Construction of Segmental Bridges* [1], a specific set of code provisions focused on segmental issues only. The second is the *AASHTO Standard Specifications for Highway Bridges* [3], the general set of code provisions intended to govern the design of all bridge types in the U.S. The *AASHTO Guide Specifications* were first published in 1988 as a report for NCHRP (National Cooperative Highway Research Program) Project 20-7/32. This report was approved one year later by the Highway Subcommittee on Bridges and Structures of AASHTO and adopted as guide specifications.

Currently a proposed LRFD (Load and Resistance Factor Design) revision of the *AASHTO Guide Specifications* is under the process of review. The new *AASHTO LRFD Guide Specifications for Design of Segmental Bridges* [17] (as yet unpublished) will rely on the provisions of the new *AASHTO LRFD Bridge Design Specifications (1994 Edition)* [2]. These two manuals will shortly replace the previous *AASHTO Guide Specifications* and the *AASHTO Standard Bridge Design Specifications* as the controlling codes for segmental bridge design. Eventually, the *AASHTO LRFD Guide Specifications* will be completely incorporated into the *AASHTO LRFD Bridge Design Specifications*, and only one code manual will be used. This report will thus reference the two LRFD codes when discussing code provisions for segmental design.

2.3 STRESS DISTRIBUTIONS IN BOX GIRDERS

Three phenomena cause non-linear stress distributions in box girder cross-sections. The first is the diffusion of post-tensioning that occurs near anchorage zones. The second is shear lag. The third is non-linear thermal gradients. The first two of these topics will be covered in this section. The last will be covered in the subsequent section dealing with thermal effects on bridges.

2.3.1 Diffusion of Post-Tensioning Forces

The concentrated force that is applied to the concrete from a post-tensioning anchorage takes a certain distance to distribute into the full cross-section of the girder. Near the anchorages, only a small portion of the cross-section will be active in resistance against the concentrated force. Thus, peaks occur in the stress distribution near those locations. Figure 2.3 taken from Kristek [10] shows an elastic folded plate solution for the cross-section pictured in the figure. Longitudinal normal stress and transverse splitting stress distributions are shown. The effect of the diffusion of the concentrated loads into the section is clearly seen. Away from the concentrated load, beam theory can be used to calculate the linear stress distribution, but near the loads, the peak stresses in the cross-section are much greater than would be calculated with beam theory assumptions. Furthermore, transverse splitting stresses are produced by the post-tensioning forces.

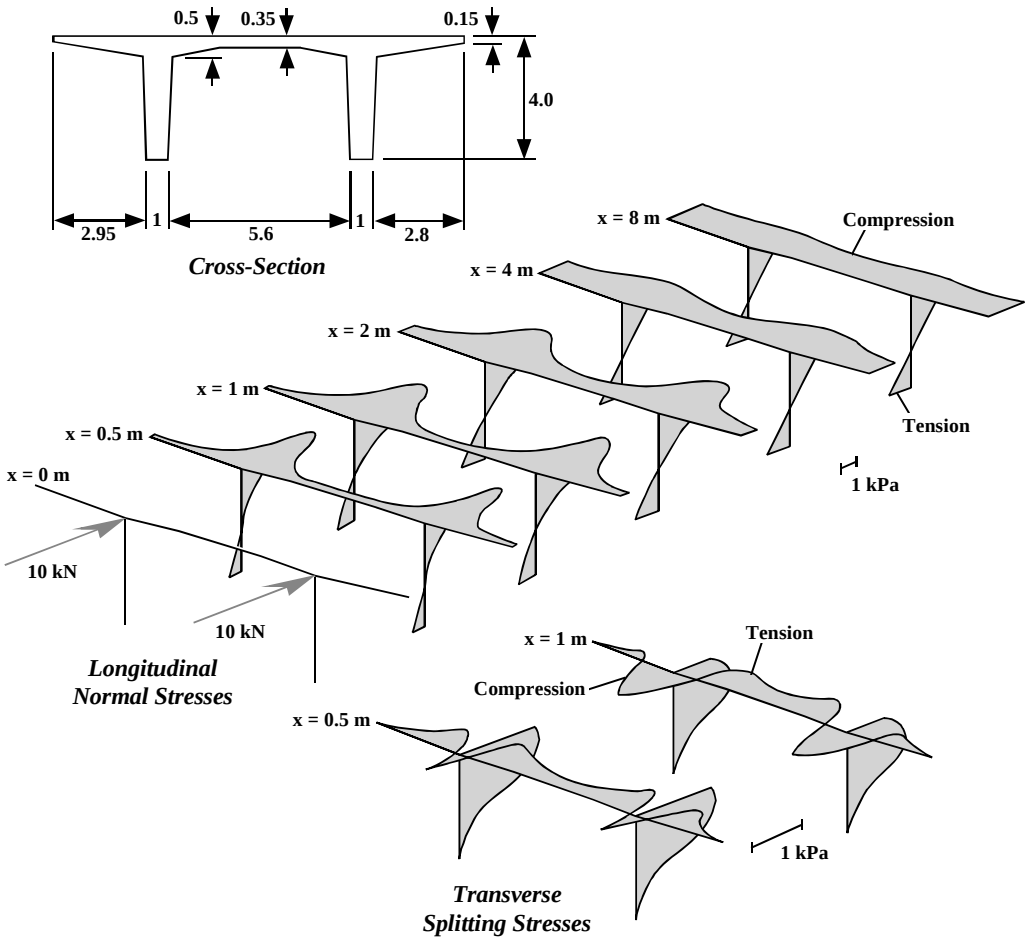

Figure 2.3 - Example of the effects of the diffusion of post-tensioning forces (after Kristek [10])

Elastic solutions such as the one in Figure 2.3 from Kristek are rarely used for design. One approximate solution which is often used is to assume that the force diffuses into the girder in the form of a wedge projected outward from the anchorage zone. A typical angle of diffusion which would be used to define the wedge would be $\pm 30^{o}$ from the line of action of the concentrated force from the post-tensioning. The area inside of the wedge would be taken as the effective cross-section used to calculate the normal and flexural stresses caused by the concentrated load. Such a method is recommended in the *AASHTO LRFD Bridge Design Specifications* [2].

2.3.2 Shear Lag

Shear lag is an effect caused by warping of the box girder section under applied shear loads. A cut taken between the top flange and the top of the webs shows that there must be a large force resultant transferred into the flange from the shear in the web (Figure 2.4). This force resultant causes deformations in the flange that bend it out of the plane of the cross-section. The force creates a distribution of normal stresses that is non-uniform across the transverse width of the web.

Folded plate or finite element analyses will show shear lag effects directly. However, normal beam theory analysis will miss the effects of shear lag because of the plane section remain plane assumption that the theory is based on. Thus, designers generally handle shear lag by using the approximate effective flange width method. This method reduces the areas of the top and bottom flanges which are considered effective for resisting normal and flexural forces. Thus, higher stresses will be calculated for the section in the flanges than if the entire section were considered effective. The effective width is chosen so that the peak stresses calculated using the effective section match those that would be calculated using more exact methods.

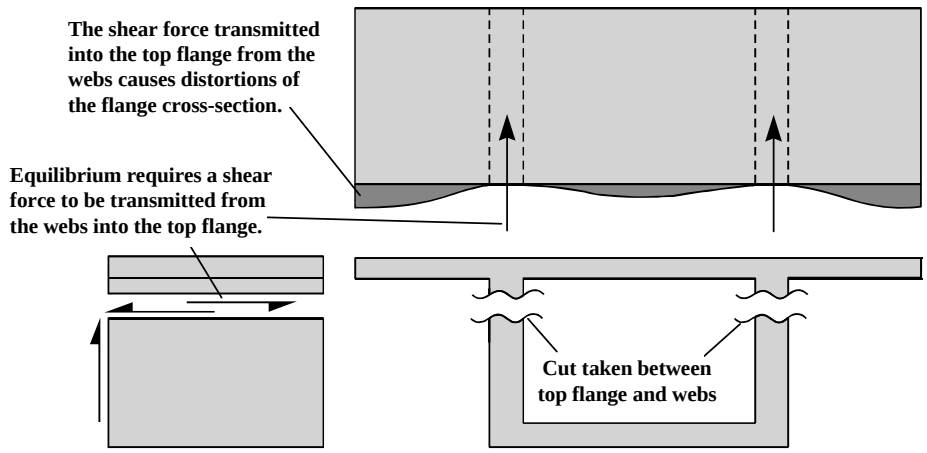

Figure 2.4 - The effects of shear lag

2.3.3 AASHTO Specifications

The *AASHTO LRFD Bridge Design Specifications* [2] deal with non-uniform stress distributions from concentrated axial forces and shear lag using effective flange width methods. These specifications are presented in Section 4.6.2.6.2 of the code. The provisions of Clause 3-10.2 of the *1983 Ontario Highway Bridge Design Code* [13] are also allowed as an alternative.

The effective flange width requirements for box girders are defined by four figures in Section 4.6.2.6.2 which are reproduced in Figures 2.5 through 2.8. The variables used are:

d_o = depth of superstructure (in)
b = flange width on each side of the web (in)
b_m = generalized effective flange width used in conjunction with Figure 2.6 to determine b_{mf} and b_{ms} depending on the position of the section of interest in the span (in)
b_{mf} = effective flange width for interior portions of a span (in)
b_{ms} = effective flange width at interior support or for a cantilever arm (in)
a = portion of span subject to a transition in effective flange width taken as the lesser of the physical flange width on each side of the web shown in Figure 2.7 or one quarter of the span length in inches (in)
l_i = a notional span length specified in Figure 2.5 for the purpose of determining b_f and b_s specified in Figure 2.6
b_s = coefficient for determining effective flange width at supports and for cantilever arms
b_f = coefficient for determining effective flange width for interior portions of spans

The effective flange widths b_{mf} and b_{ms} are determined as the product of the coefficient b_f and b_s, given as b_m/b in Figure 2.6, and the physical distance b, as given in Figure 2.7. The following interpretations apply:

- b shall be taken as the flange width either side of the web; i.e., b_1, b_2, or b_3 in Figure 2.7,

- for $b \leq 0.3d_o$, no reduction in flange width need be considered,
- for $b > 0.3d_o$, the effective width may be determined in accordance with Figures 2.5 and 2.6,
- in any event, neither b_{mf} nor b_{ms} shall be taken as greater than b,
- the effects of unsymmetrical loading on the effective flange width may be disregarded,
- the value of b_{ms} shall be determined using the greater of the effective span lengths adjacent to the support, and
- if b_{mf} is less than b_{ms} in a span, the pattern of the effective width within the span may be determined by the connecting line of the effective widths b_{ms} at the adjoining support points.

For the superposition of local and global force effects, the distribution of stresses due to the global force effects may be assumed to have a straight line pattern in accordance with Figure 2.7 c). The linear stress distribution should be determined from the constant stress distribution using the conditions that the flange force remains unchanged, and that the maximum width of the linear stress distribution on each side of a web is 2.0 times the effective flange width.

The flange properties for normal forces (such a concentrated post-tensioning loads) may either be based on the pattern according to Figure 2.8, or be determined by more rigorous analysis.

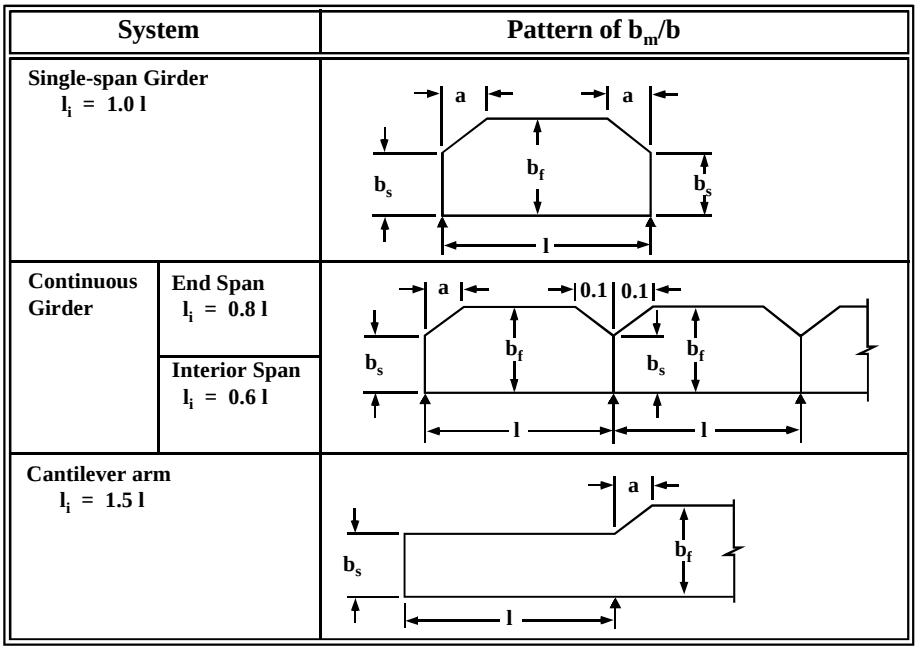

Figure 2.5 - Pattern of effective flange width coefficients, b_f and b_s (Figure 4.6.2.6.2-1 from the AASHTO LRFD Bridge Design Specifications [2])

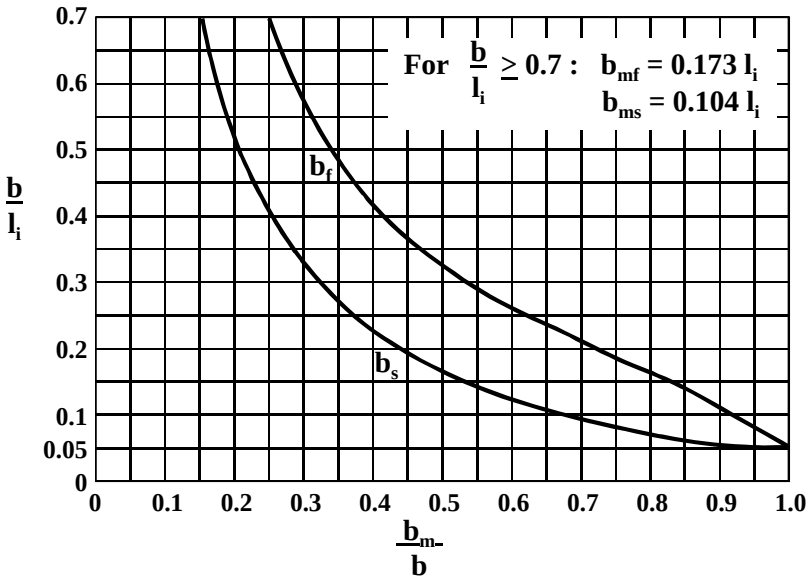

Figure 2.6 - Values of the effective flange width coefficient b_m/b, for the given values of b/l_i (Figure 4.6.2.6.2-2 from the AASHTO LRFD Bridge Design Specifications [2])

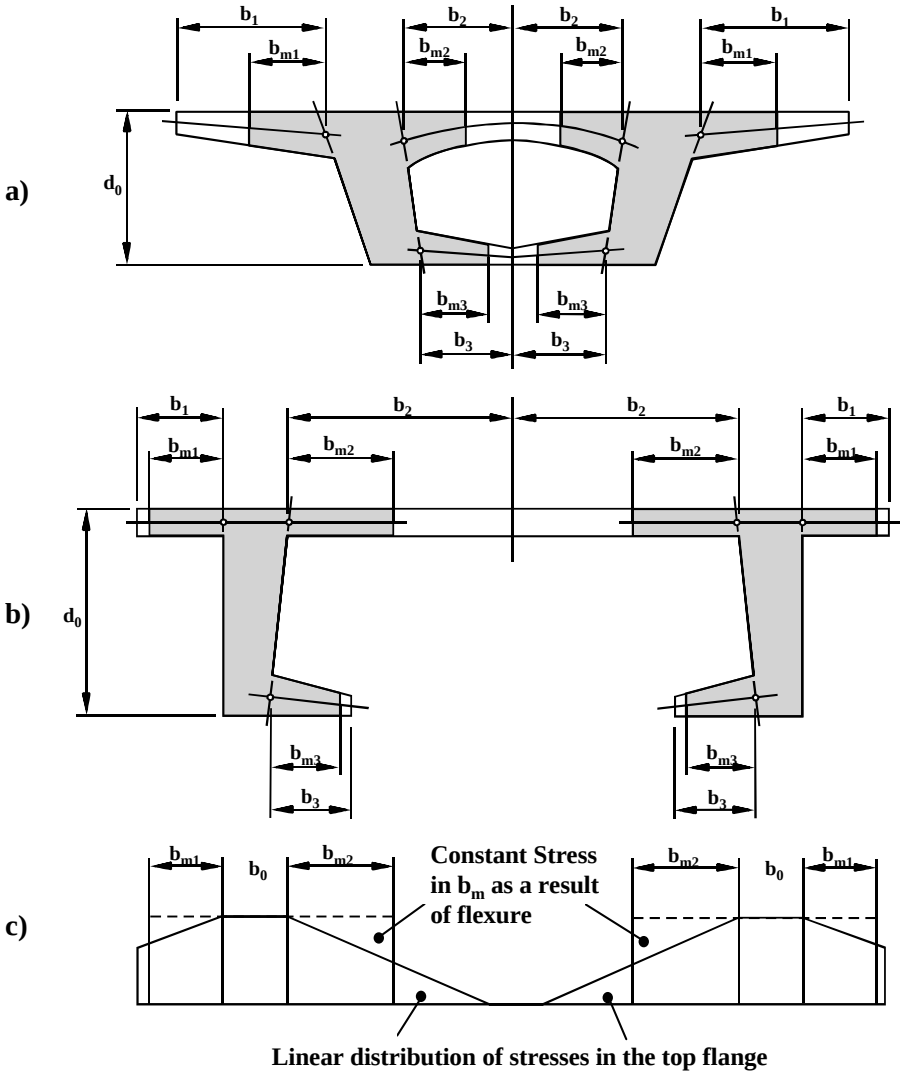

Figure 2.7 - Cross-sections and corresponding effective flange widths, b_m, for flexure and shear (Figure 4.6.2.6.2-3 from the AASHTO LRFD Bridge Design Specifications [2])

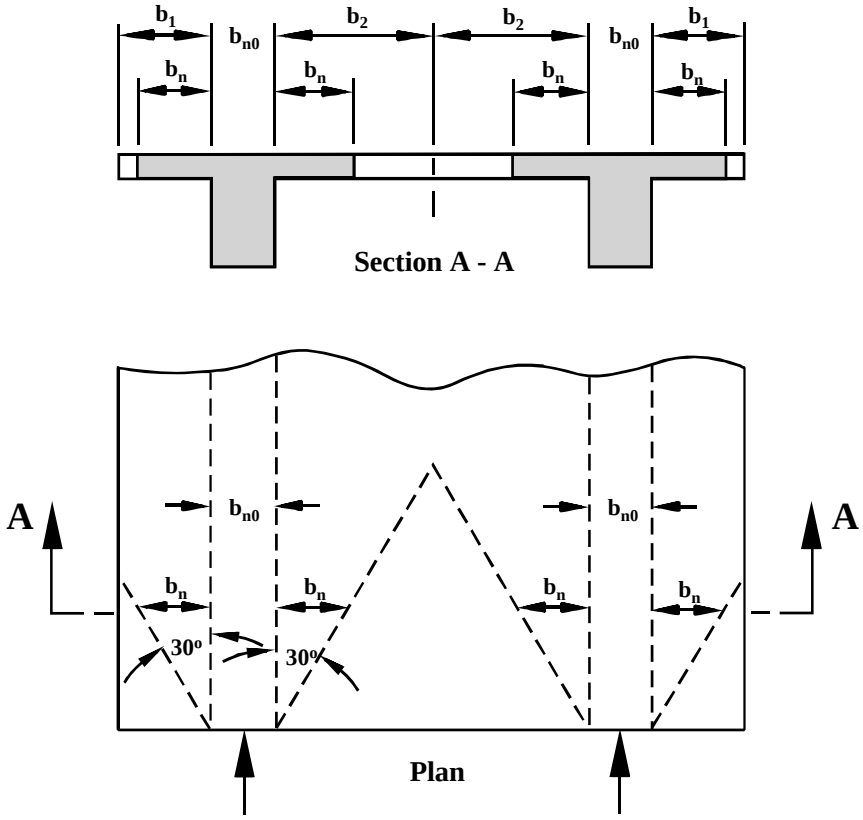

Figure 2.8 - Effective flange widths, b_n, for normal forces (Figure 2.6.2.6.2-4 from the AASHTO LRFD Bridge Design Specifications [2])

2.4 THERMAL EFFECTS ON BRIDGE STRUCTURES

There are two types of thermal activity that occur in bridges which are of interest for design. The first is the annual variation of the average temperature of the bridge. This variation causes expansion and contraction of the bridge's length over the course of the year. This effect is well understood, and designers know how to accommodate it.

The second effect is the daily variation of the thermal gradient in the bridge. The daily setting and rising of the sun as well as other climatic factors tend to heat and cool a bridge's superstructure unevenly through its depth. During the day, the solar radiation causes the exposed

deck of the bridge to heat up. However, concrete is a relatively poor heat conductor. Thus, heat tends to accumulate in the top of the cross-section and causes the temperature there to be greater than in the lower parts of the cross-section. At night, most of the heat is dissipated through the external perimeter of the cross-section causing the interior of the cross-section to be much warmer than the exterior. These phenomena are known as non-linear thermal gradients. Little is known about the magnitudes of these gradients and what effects they have on bridges. This section will discuss thermal effects on bridges in two parts: the shape of the thermal distribution in the cross-section, then the structural effects from the application of the temperature distribution to the superstructure cross-section.

2.4.1 Shapes of Thermal Gradients

2.4.1.1 Factors Affecting Thermal Gradients

Typically, designers are interested in two types of non-linear thermal gradients: a positive gradient, defined where the temperature of the top deck is warmer than the temperature of the webs, and a negative gradient, defined where the webs have higher temperatures than the deck and usually the bottom flange. Two types of factors affect the shape and magnitude of these thermal gradients:

1. Climatic factors that affect the amounts of thermal energy that are applied to the bridge.
2. Material and shape properties of the cross-section that affect how the section conducts the applied thermal energy.

The major climatic factors that affect thermal gradients are solar radiation, ambient temperature, wind speed, and precipitation. Figure 2.9 shows how climatic factors affect the shape and magnitude of the thermal gradient. Solar radiation strikes the top deck and warms it up over the course of the day. Solar radiation is the primary contributor to the magnitude of the top spike in a positive gradient. Precipitation can suddenly cool the top deck and decrease the magnitude of the top spike, potentially adding to the severity of a negative gradient. Over the day, the ambient temperature rises and becomes warmer than the average temperature of the bridge. The ambient temperature will then begin to heat up the exterior of the bridge cross-section while the inside of

the cross-section generally stays at a relatively stable temperature. At night, the ambient temperature drops below the average temperature of the bridge and starts to cool the exterior of the cross-section. Wind blowing over the exterior surface of the cross-section helps the concrete to re-radiate energy into the surrounding atmosphere.

A maximum positive gradient is expected when clear warm weather, with very light winds, follows a period of cool overcast weather. A maximum negative gradient is expected when a harsh cold front, accompanied by precipitation, follows several days of warm weather.

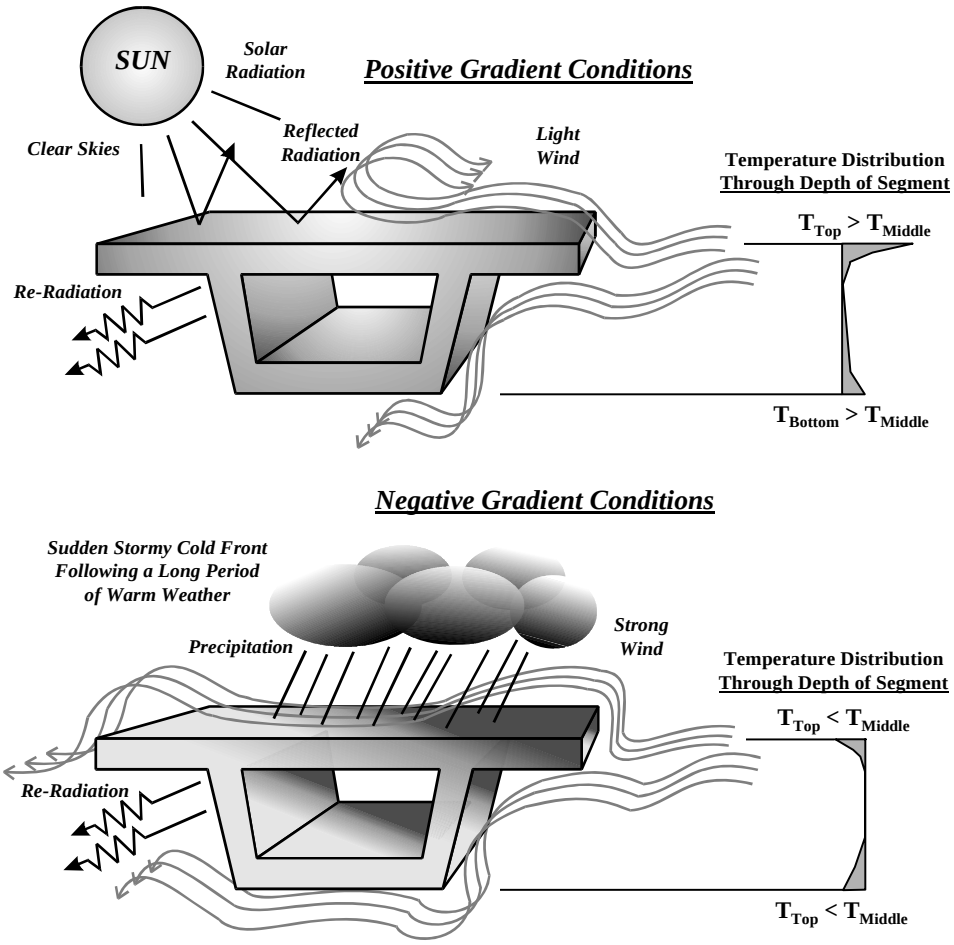

Figure 2.9 - Climatic effects on thermal gradients

The material properties that affect the gradient are the conductivity, density, absorptivity, and specific heat. Concrete has a low conductivity which allows large non-linear gradients to occur. The external portions of the structure can be heated or cooled quickly by the external environment, but the concrete cannot transfer thermal energy to or from the interior quickly enough to even out the temperature distribution through the cross-section. Asphalt on the deck tends to insulate the concrete underneath thus reducing the magnitudes of the thermal gradients.

The shape of the cross-section also has complex effects on the shape of the thermal gradient. In a box girder section, the wide top flange provides a large surface for absorption of thermal energy from solar radiation, but this thermal energy can only be transferred into the depth of the cross-section at the webs. The webs act as heat sinks for the top flange. The spacing, thickness, and number of webs plus the thickness of the top flange at the junction to the webs affect the efficiency of the webs to conduct heat out of the top flange. More webs or thicker webs obviously allow more heat to be conducted out of the top flange. A greater spacing between webs requires the thermal energy to travel further across the top flange before it can be conducted into the webs. As the junctions of the top flange with the webs become thicker, more thermal energy can be passed into the webs at the junction points. Across the width of the top flange, the temperature will drop off over the webs during a positive gradient. As the webs become more efficient at conducting thermal energy out of the top flange, the top peak of the positive gradient will be reduced and distributed further into the depth of the cross-section. Figure 2.10 illustrates these points. Thick web and flange walls also result in large transverse gradients through the thickness of the web walls. As a result, the interior of the box girder tends to remain at a fairly constant temperature through the course of the day while the exterior fibers of the section change temperature significantly. A low concrete conductivity mitigates the effects of cross-section proportioning on the shape of thermal gradients.

The result of the material and cross-sectional affects on thermal gradient shape is that two box-girder sections of the same depth and with the same amount of asphalt blacktop placed on their decks can experience very different thermal gradients under the same climatic conditions if they have very different cross-sectional proportions or concrete properties.

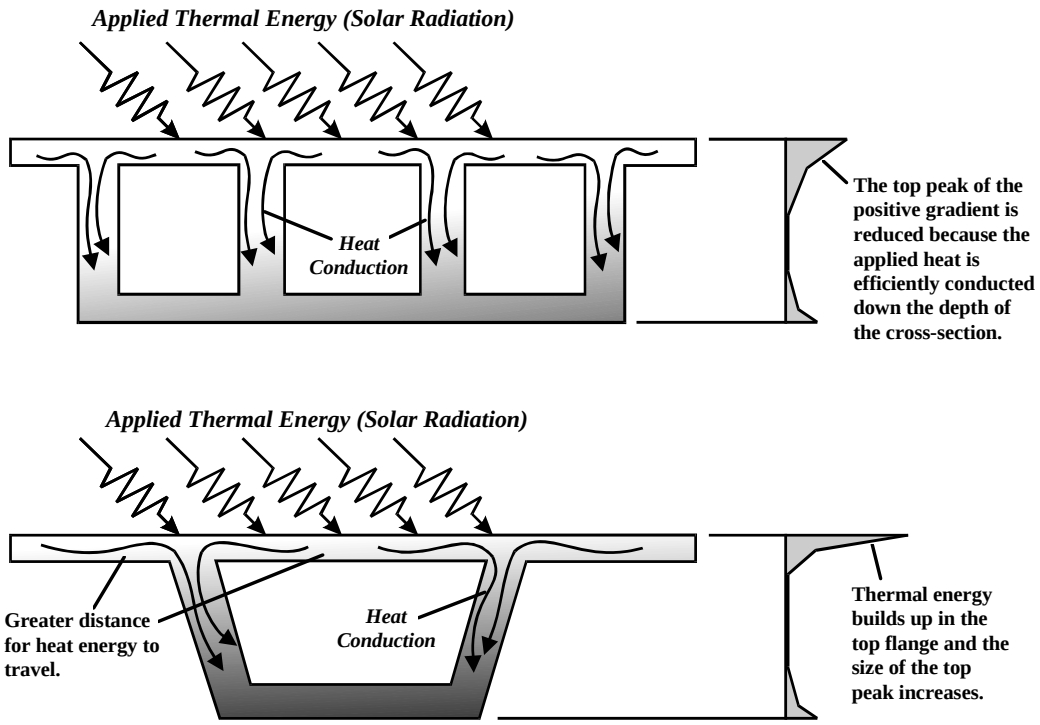

Figure 2.10 - The effects of cross-section on thermal gradient shape

2.4.1.2 AASHTO Recommended Gradient Shapes

A thorough review of literature on thermal gradients will reveal several recommended shapes for design gradients. This section will not deal with all of the design gradients that have been recommended, nor will it summarize all of the research which has been conducted. Such literature studies have already been conducted in the works of Roberts [19], Bonzon [6], and Wood [22]. This section will instead focus on the current recommended gradients in the *AASHTO LRFD Bridge Design Specifications* [2], how they were developed, and some questionable aspects of these gradients.

The *AASHTO LRFD Bridge Design Specifications* provides recommended design gradients in Section 3.12.3. In this section, a map of solar radiation zones for the United States and a diagram of the proposed gradient shape with a table are given. These figures are reproduced in Figures 2.11 and 2.12. Values for positive gradient T_1 and T_2 come from the table. Negative

gradient values are calculated by multiplying the positive gradient values by -0.5. T_3 is specified to be 0.0 ^{o}C (0.0 ^{o}F) unless a site specific study is performed to determine an appropriate value, but shall not exceed 2.8 ^{o}C (5 ^{o}F) for the positive gradient and -1.4 ^{o}C (-2.5 ^{o}F) for the negative gradient. The dimension "A" is specified to be:

- 300 mm (12") for concrete superstructures which are 400 mm (16") in depth or greater,
- Depth - 100 mm (4") for concrete superstructures which are less than 400 mm (16") in depth, or
- 300 mm (12") for steel superstructures, where the value "t" is equal to the thickness of the concrete deck.

Thus, for the U.S. 183 elevated highway in Austin, Texas, the design positive gradient would have values for T_1, T_2, and A of 20.0 ^{o}C (36 ^{o}F), 6.7 ^{o}C (12 ^{o}F), and 300 mm (12") respectively, and the design negative gradient would have values of -10.0 ^{o}C (-18 ^{o}F), -3.35 ^{0}C (-6 ^{o}F), and 300 mm (12") respectively. The value of T_3 will most likely be chosen as 0.0 ^{o}C (0.0 ^{o}F) for any bridge design gradient because it is unlikely that the design engineers will have access to site specific data that would justify otherwise.

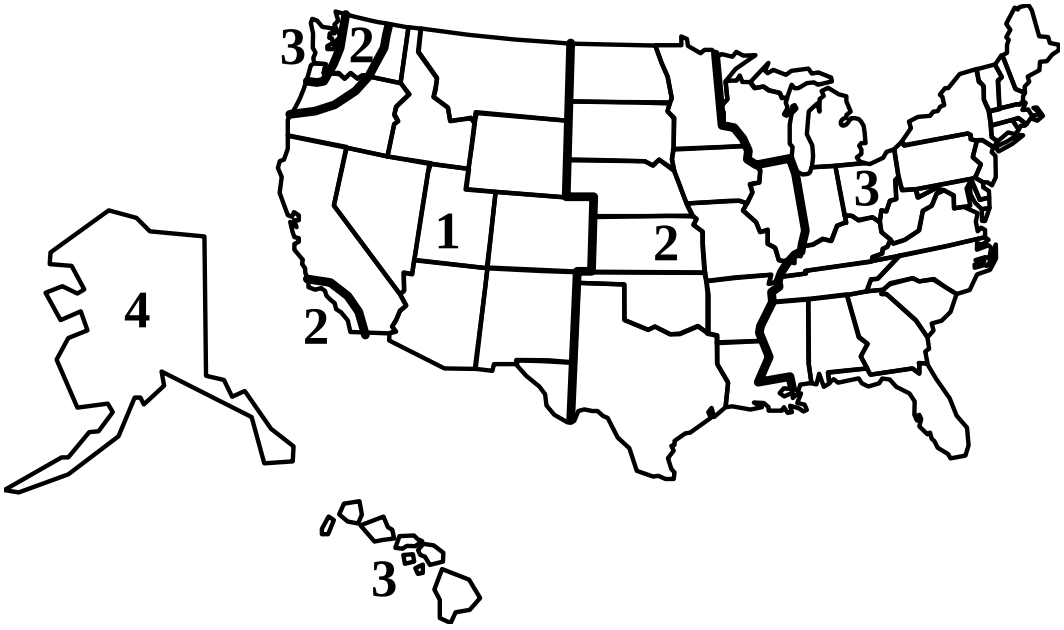

Figure 2.11 - Solar radiation zones for the United States (Figure 3.12.3-1 from the AASHTO LRFD Bridge Design Specifications [2])

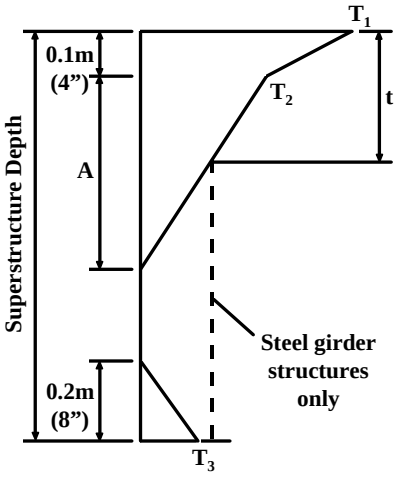

Plain Concrete Surface			50 mm Asphalt (2" Asphalt)		10 mm Asphalt (4" Asphalt)	
Zone	T_1 °C (°F)	T_2 °C (°F)	T_1 °C (°F)	T_2 °C (°F)	T_1 °C (°F)	T_2 °C (°F)
1	30 (54)	7.8 (14)	23.9 (43)	7.8 (14)	17.2 (31)	5 (9)
2	25.6 (46)	6.7 (12)	20 (36)	6.7 (12)	13.9 (25)	5.6 (10)
3	22.8 (41)	6.1 (11)	18.3 (33)	6.1 (11)	12.8 (23)	6.1 (11)
4	21.1 (38)	5 (9)	16.1 (29)	5 (9)	12.2 (22)	6.1 (11)

Figure 2.12 - Positive vertical temperature gradient in concrete and steel superstructures (Figure 3.12.3-2 and Table 3.12.3-1 from the AASHTO LRFD Bridge Design Specifications [2])

The recommended design gradients from the *AASHTO LRFD Bridge Design Specifications* were developed based on research from Potgieter and Gamble [16] and the British Standard BS 5400 [21]. Potgieter and Gamble performed analytical studies based on weather station data from around the United States in conjunction with a finite difference one-dimensional heat flow program. From these studies they determined what conditions would produce maximum positive non-linear temperature gradients and what the shapes and magnitudes of these gradients would be. The results of their theoretical work were verified against four measured positive thermal gradients from the Kishwaukee River Bridge. The negative gradient was developed from the recommendations in the British Standard BS 5400 code which have no analytical or recorded field data to substantiate them [19]. The recommended design gradients were first published in the *1989 AASHTO Bridge Guide Specifications for Design and Construction of Segmental Highway Bridges* [1]. Since then, field studies have been performed which have not always measured maximum thermal gradients with magnitudes as high as the recommended gradients. The majority

of these studies have not agreed with each other on a definitive set of maximum magnitudes nor shapes for the gradients. When the *AASHTO LRFD Bridge Design Specifications* [2] were published in 1994, the magnitudes of the original design gradients were kept, though the shapes were simplified slightly to make design calculations easier to perform.

The philosophy which has previously been applied to the choice of recommended gradient shapes has been to instrument a bridge structure with thermocouple gauges and then to choose as design gradients the maximum positive and negative gradients measured in the bridge over a period of observations. This philosophy is questionable for several reasons. The first question is whether the gradient should be chosen from the absolutely worst measured case or whether the design gradients should instead be chosen based on a reasonable rate of occurrence from a database of thermal gradients measured over a sufficient period of time with a sufficient frequency of measurements. Most design loads are specified based on probabilistic rates of occurrence such that the actions well represent the 95^{th} fractile or only five percent of actions that might occur would be greater. The choice of design thermal gradients should follow the same philosophy. Absolute maximum measured thermal gradients are unnecessarily severe for design purposes because they occur infrequently over the service life of a bridge. Secondly, in the past, no consideration has been given for the effects of cross-sectional shape except for the depth of the member. As discussed earlier, the shape and proportioning of a box girder cross-section effects the way heat is conducted through the section. Thus, they affect the shape of the thermal gradient that occurs. This behavior raises three questions:

- If design gradients are to be verified by comparison with field measured data, how can a gradient measured in one bridge superstructure be applied to the design of another bridge superstructure which has substantially different cross-sectional proportions?
- How can the effects of cross-section variations be incorporated in the determination a single pair of positive and negative design gradients for the AASHTO code?
- Is the influence of cross-sectional shape and proportion significant enough that different design gradients should be specified for significant variations in box girder proportions?

Lastly, measurement of thermal gradients in the field has previously focused only on the collection of temperature data. Measurement of the stresses caused by these thermal gradients has largely been ignored. Thus, there is little confirmation that the gradients which have been assumed as the most severe are actually the thermal gradients which cause the highest stresses. Possibly, different shapes of the applied gradient will cause different behavior of the structure such that one applied positive gradient may produce critical stresses for one part or one type of a bridge structure while another (with a different shape) may cause critical stresses at a different part or in a different type of bridge structure. The problem is analogous to placing live load on a structure in different patterns to produce an envelope of critical stresses. Furthermore, thermal stresses only need to be considered under service limit state conditions. Due to the relief of restraint induced actions when elastic material behavior is exceeded, the effects of temperature stresses will be negligible at factored loads [11]. Are the current provisions for thermal design appropriate for the stresses which really occur in bridge structures?

2.4.2 Structural Response to Thermal Gradients

2.4.2.1 Factors That Affect Structural Response

For analysis purposes, non-linear thermal gradients are typically divided into three components. First, a uniform temperature component is removed from the initial gradient. Second, a linear thermal gradient is removed. The remainder after removing these first two components is a self-equilibrating temperature distribution. Figure 2.13 shows the three components of the non-linear thermal gradient. The effects of these components on the bridge structure depends on three factors: the statical determinacy of the structure, the susceptibility of the cross-section to warping, and the stress range of the concrete under which the loading occurs which determines whether the behavior will be elastic or inelastic.

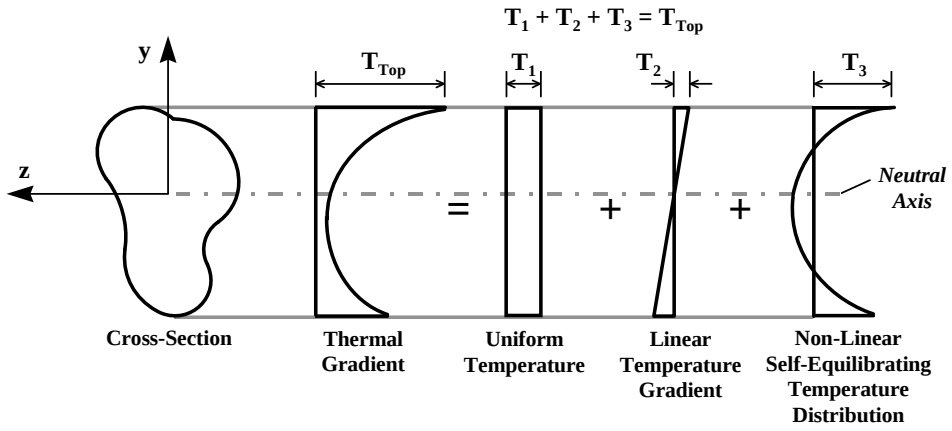

Figure 2.13 - Components of a non-linear thermal gradient

The effects of the first two components of the thermal gradient depend primarily on the statical determinacy of the structure. The first component, the uniform temperature, causes a uniform expansion or contraction of the unrestrained superstructure. Generally, this phenomenon is accommodated by expansion joints or rolling bearings. If the structure is continuous and two or more of the interior supporting piers are rigidly fixed to the superstructure, they will provide restraint against such movement. This restraint will produce moments and axial forces in the structure. The second component, the linear thermal gradient, will produce a uniform curvature in the unrestrained superstructure. Only if the superstructure is a simply supported single span can the bridge deform freely (Figure 2.14). Otherwise, if the structure is continuous over two or more spans, the internal piers will restrain the superstructure from deforming in such a manner. Thus, secondary moments are introduced into the structure. This effect is shown in Figure 2.15.

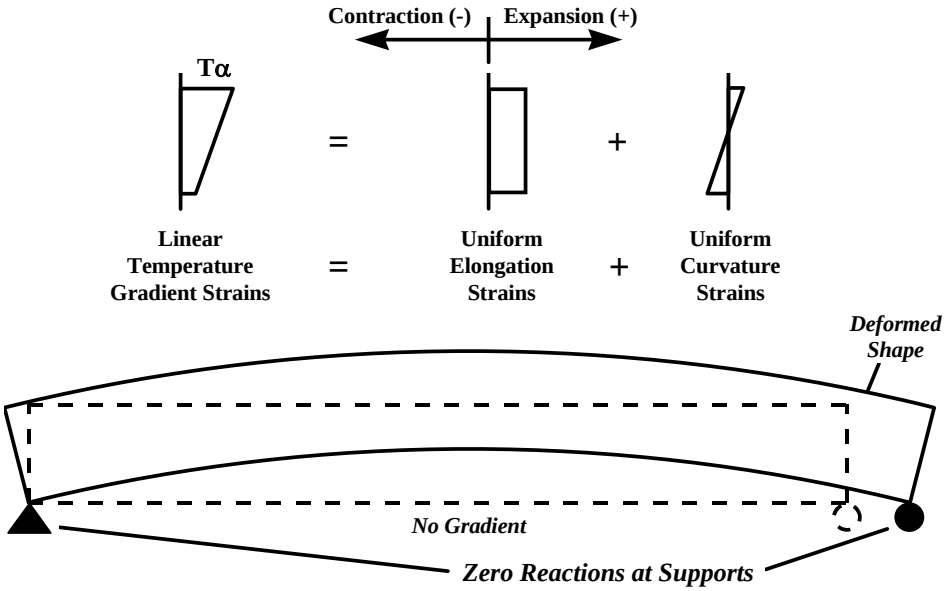

Figure 2.14 - Effect of linear thermal gradient components on a statically determinate span

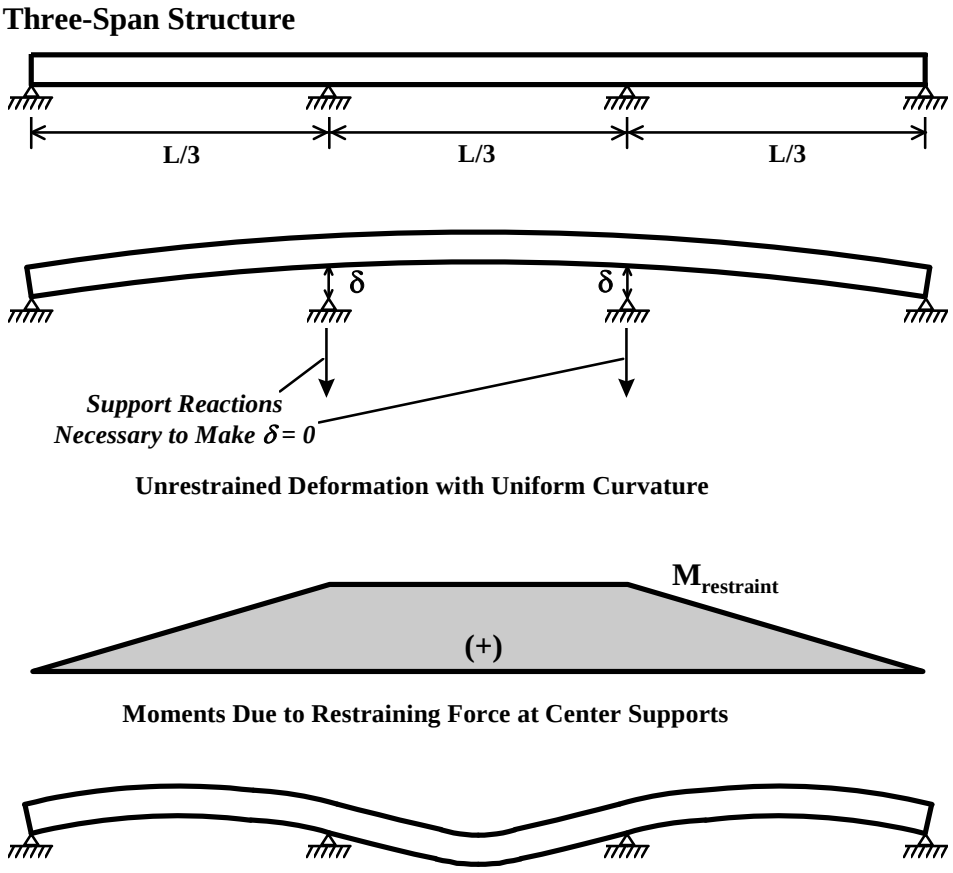

Figure 2.15 - Effects of linear thermal gradient components on a statically indeterminate bridge structure

The third component, the self-equilibrating temperature distribution, will cause self-equilibrating internal stresses in the bridge cross-section. The effect of this component depends on the susceptibility of the cross-section to warping. If plane sections remain plane, the stresses produced by the remaining component of the thermal gradient can be solved for fairly easily. Under this assumption, the self-equilibrating stresses can be calculated by assuming that the member is fully restrained against any thermal deformation as in Figure 2.16. The following variables are used in the calculation:

y = distance measured perpendicular to the longitudinal axis at the center of gravity

of the cross-section

$T(y)$ = temperature at a depth y

$b(y)$ = net section width at a depth y

E = modulus of elasticity

α = coefficient of thermal expansion

$\sigma_{SE}(y)$ = self-equilibrating stress at a depth y

A = cross-sectional area

I = moment of inertia

In all calculations, the z and y axes are assumed to be principal axes of the cross-section. The force necessary to restrain the member axially at the fixed ends is calculated by:

$$\text{Restrained Axial Load, } P = \int_{depth} E\alpha T(y)b(y)dy \qquad (2\text{-}1)$$

The moment necessary to restrain the member rotationally at the fixed ends is calculated by:

$$\text{Restrained Moment, } M = \int_{depth} E\alpha T(y)b(y)ydy \qquad (2\text{-}2)$$

In the unrestrained case, however, these loads will not be acting on the member. Thus they must be removed. The stresses obtained after removing the fully restrained moment and axial force are then the self-equilibrating stresses acting to keep cross-sections plane through the member:

$$\sigma_{SE}(y) = E\alpha T(y) - P/A - My/I \qquad (2\text{-}3)$$

This calculation method is applicable for calculating internal stresses in continuous or simple span structures so long as warping does not occur.

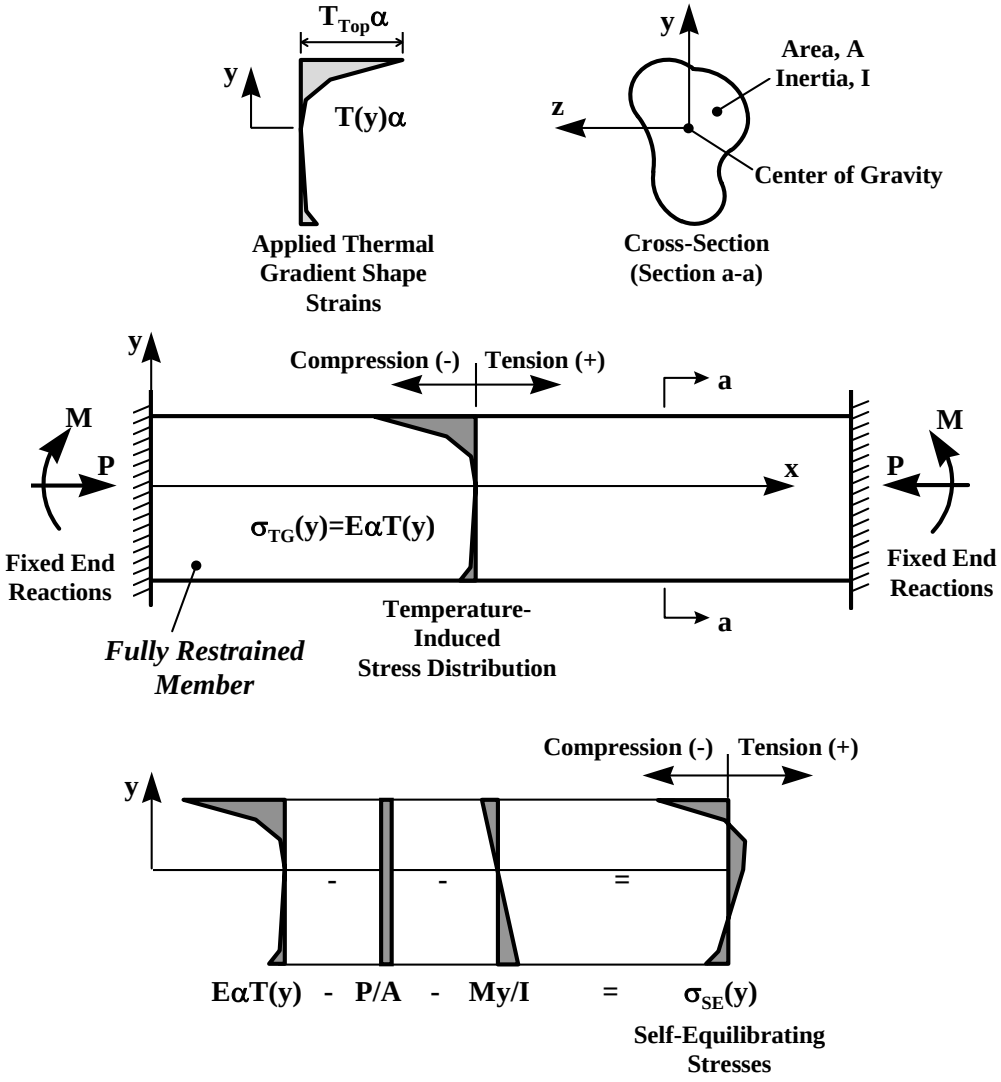

Figure 2.16 - Calculation of self-equilibrating stresses from a non-linear thermal gradient when plane section remain plane

In a continuous bridge, the problem of determining the secondary moments caused by constraint from the piers is solved by applying a deformed shape to the superstructure consistent with the axial elongation (or contraction) and the constant curvature that would be caused by the uniform temperature and linear thermal gradient components of the applied thermal gradient. The forces in the interior piers would then be the forces necessary to bring the structure back to a zero

deflection at the pier locations (already shown in Figure 2.15). The unrestrained axial strain and curvature of the superstructure are calculated as:

$$\text{Axial Strain, } \varepsilon_{axial} = P/EA \tag{2-4}$$

$$\text{Curvature, } \phi = M/EI \tag{2-5}$$

The above discussion has focused on the equations used to solve the one-dimensional gradient problem. If the gradient varies across the width of the cross-section as well as the depth (Figure 2.17), then the equations are simply modified as:

y = vertical distance measured to the center of gravity of the cross-section

z = transverse distance measured to the center of gravity of the cross-section

$T(z,y)$ = temperature at transverse distance z and depth y

$\sigma_{SE}(z,y)$ = self-equilibrating stress at transverse distance z and depth y

I_z = moment of inertia about z axis

I_y = moment of inertia about y axis

$$\text{Restrained Axial Load, } P = \int_{depth}\int_{width} E\alpha T(z,y)\,dz\,dy \tag{2-6}$$

$$\text{Restrained Moment about z axis, } M_z = \int_{depth}\int_{width} E\alpha T(z,y)\,y\,dz\,dy \tag{2-7}$$

$$\text{Restrained Moment about y axis, } M_y = \int_{depth}\int_{width} E\alpha T(z,y)\,z\,dz\,dy \tag{2-8}$$

$$\sigma_{SE}(z,y) = E\alpha T(z,y) - P/A - M_z y/I_z - M_y z/I_y \tag{2-9}$$

Generally, most engineers would ignore the moment about the y axis because the linear gradient component across the width of the cross-section is likely to be small, and the moment of inertia about the y axis is likely to be large. However, the variation in the self-equilibrating internal stresses across the width of a cross-section may not be negligible for some bridges structures.

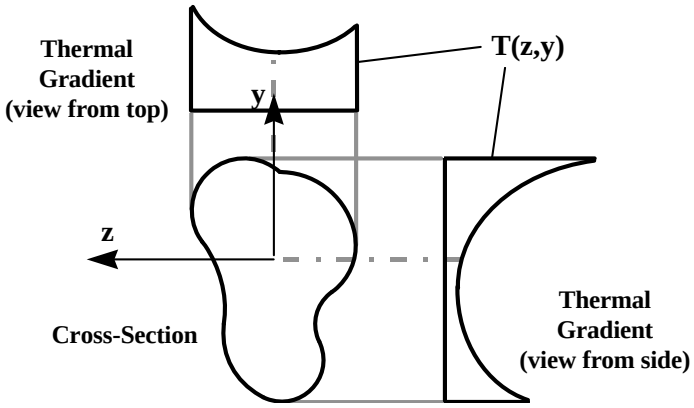

Figure 2.17 - Thermal gradient that varies across the width and depth of a cross-section

Thermal gradients may also act across the section transversely. In a hollow box girder section, the temperature distribution varies not only through the depth of the section, but from the inside perimeter to the outside perimeter as well. Thus, thermal gradients will be present through the thickness of the flanges and webs (Figure 2.18). These gradients cause transverse stresses through the girder cross-section. A simplified method to solve for these stresses is to take a transverse slice of unit width out of the girder and analyze it as a two dimensional frame. The slice is broken into individual members as in Figure 2.18 and appropriate thermal gradients are applied to each member. Each member can be treated in the same manner that was described for the longitudinal behavior and the stresses caused by the transverse gradients can be solved for.

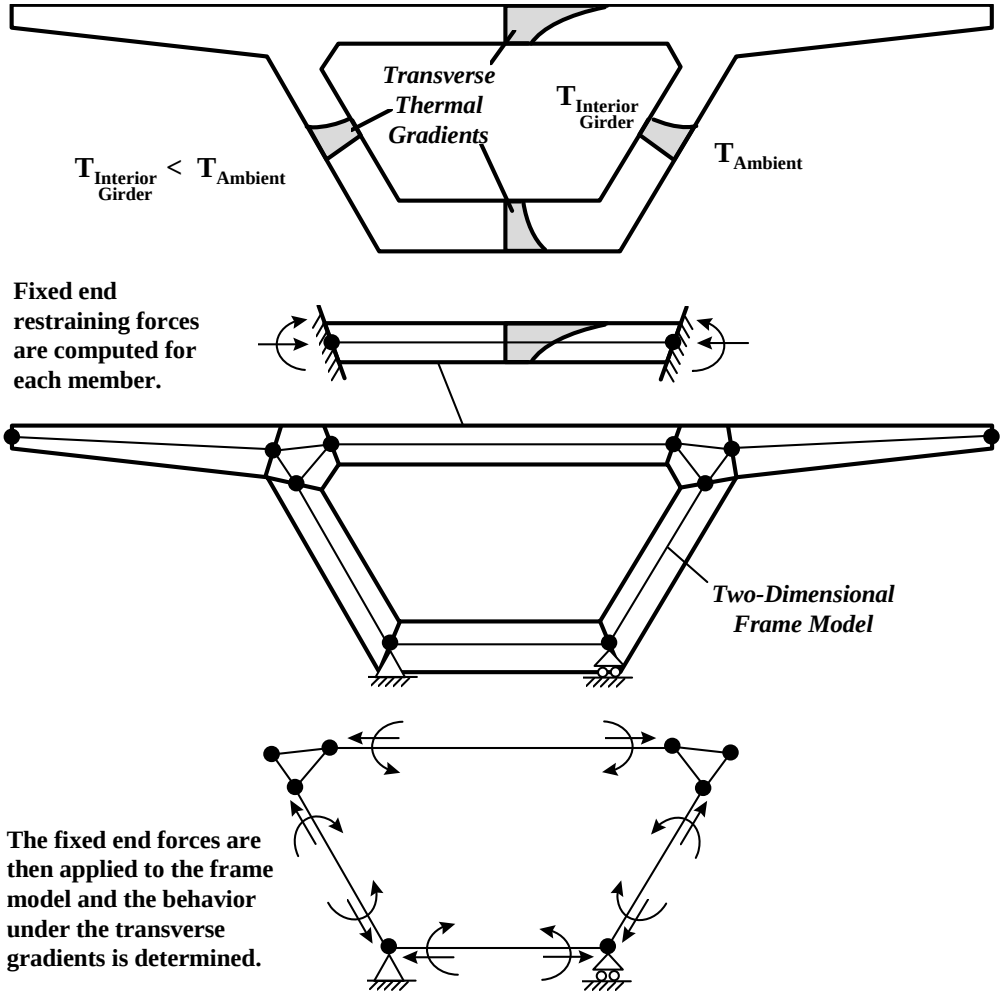

Figure 2. 18 - Analysis of transverse thermal gradients

The structural response to thermal gradients has been discussed for simple span and continuous box girders for sections that do not warp. The next step is to consider what happens to the stress distribution in the box girder if warping does occur. In Figure 2.19a, a cut is made between the top flange and the rest of the section shown in the figure. When a positive gradient is applied to the span, the upper portion of the gradient causes the top flange to bow and elongate much more than the lower portion of the gradient causes the bottom part of the span to bow and elongate. In order to bring the two halves of the span into a consistent shape, stresses like the ones

shown in Figure 2.19a must be produced. Thus, local bending and axial load occur in the top flange just over the webs. Furthermore, the lower portion of the span is much stiffer than the top flange by itself, so one can expect that the top flange will undergo most of the deformation necessary when the two halves of the span are brought together into a consistent shape. Figure 2.19b shows the resulting distribution of normal stresses in the top flange of the span. Transverse stresses across the top flange are produced as well because the top flange must bend across its width to achieve the final shape shown in Figure 2.19b. The peak normal stresses produced by the warping are then greater than would be expected if the cross-section remained plane. The difference occurs because the induced stresses concentrate in the top flange over the webs. The phenomenon has results similar to shear lag though the mechanism of the distortion is different.

Finally, all of the above discussion has been for elastic response in the lower ranges of the service limit state. For concrete near the ultimate limit state, the behavior becomes very different. Because the structure is trying to satisfy strain compatibility and not external load equilibrium, the stresses will be greatly reduced by cracking or even micro-cracking of the concrete. Under such conditions, the concrete is free to expand and contract much more than under perfectly homogeneous conditions. For this reason, analysis of thermal gradients is generally only performed for service load cases. The effects of thermal gradients are greatly relieved by cracking and hence are usually ignored for ultimate loading conditions.

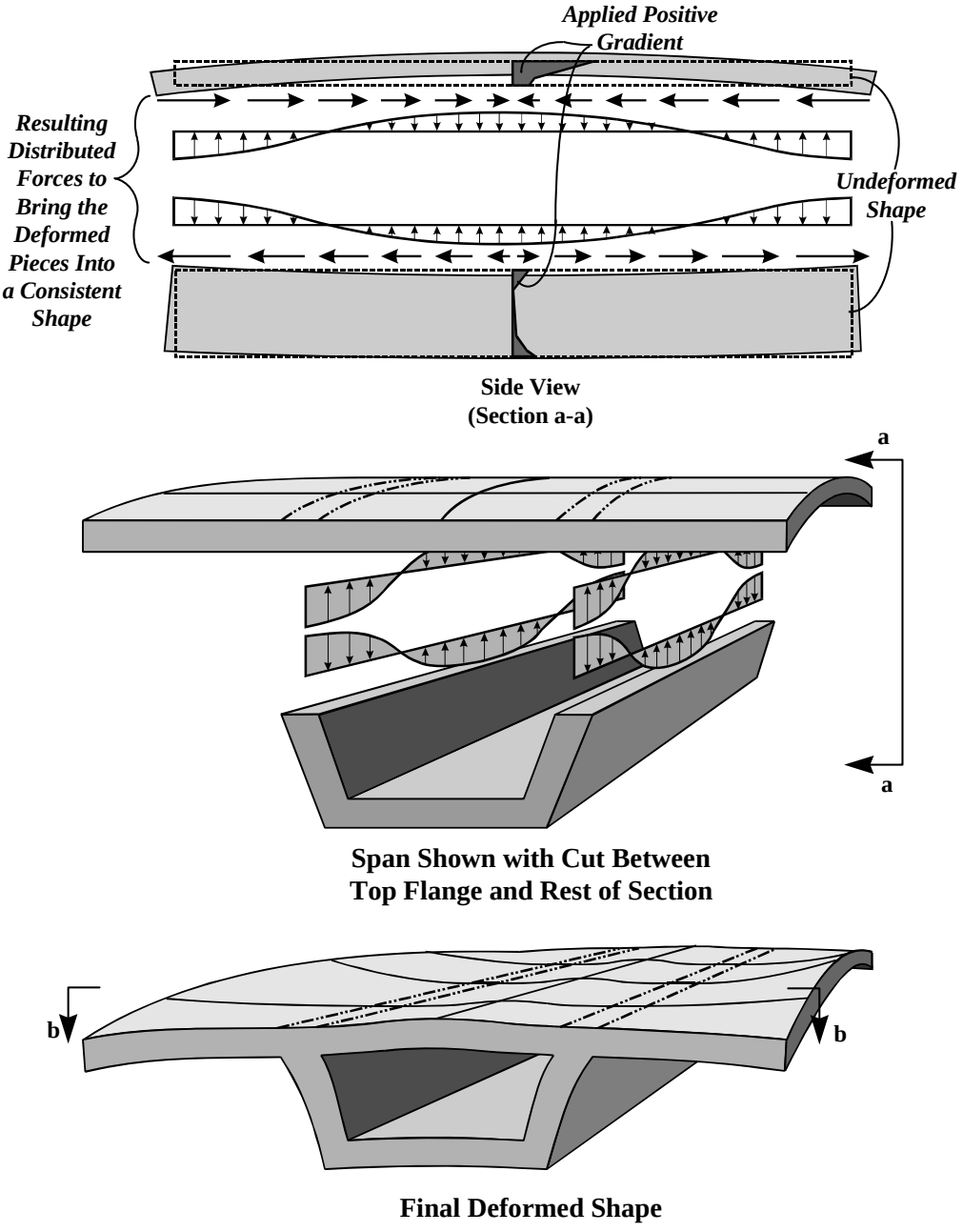

Figure 2.19a - Effect of an applied positive gradient when warping occurs

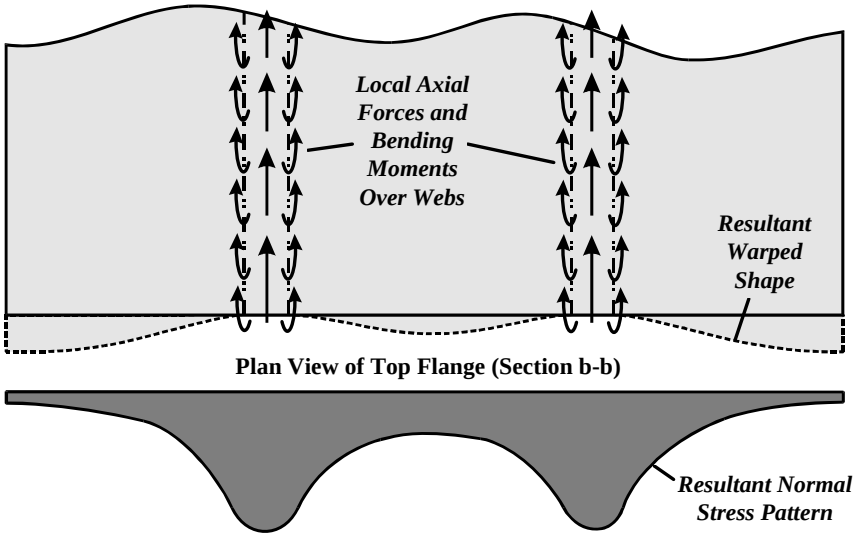

Figure 2.19b - Effect of an applied positive gradient when warping occurs (continued)

2.4.2.2 AASHTO Recommended Method of Analysis

The *AASHTO LRFD Bridge Design Specifications* [2] recommend a method for analysis of structures with applied thermal gradients in Section 4.6.6. Analysis of all three components of the thermal gradient is required. A recommended method is provided in the commentary and follows the procedure which was outlined in the previous section for elastic behavior without warping. Design for thermal effects is only required under load combinations Service I through V in Section 3.4.1 of the *AASHTO LRFD Bridge Design Specifications*.

2.5 CURVED GIRDERS

The problem of solving for the internal forces in a curved girder is difficult. The mechanics of a curved member requires an interdependency between the moments and torques in the member. This results in analysis problems that many engineers do not know how to solve. In bridge design, curved horizontal alignments are quite common. However, in general, the radius of curvature of most bridges is large compared with the span lengths. Thus, the horizontal curvature along any single span is often negligible. This allows design engineers to neglect the moment and torsion interdependency in most designs. The exceptions to this approach usually occur with

freeway interchanges in urban or environmentally sensitive areas where tight radii are required in the alignment of the interchange ramps and little ground space is available for supporting substructure. The U.S. 183 Ramp P is such a bridge. The problem of the moment and torsion interdependency was of some concern for the designers of Ramp P.

2.5.1 General Curved Girder Theory

The proceeding derivation will follow the form given in Nakai and Yoo [12]. A similar derivation can be found in Kristek [10].

Consider the curved differential segment shown in Figure 2.20. The right hand rule should be used for interpretation of all moment and torque vectors shown in the figure. The variables in the figure are defined as:

ds = the arc length of the curved differential segment
$d\theta$ = the angle subtended by the arc of the curved differential segment
R = the radius of curvature of the curved differential segment
w = the distributed load over the length of the curved differential segment (only the resultant is shown in the figure)
t = the distributed torque over the length of the differential curved segment (only the resultant is shown in the figure)
V_0 = the shear at the downstation face of the curved differential segment
M_0 = the moment at the downstation face of the curved differential segment
T_0 = the torque at the downstation face of the curved differential segment
V_1 = the shear at the upstation face of the curved differential segment
M_1 = the moment at the upstation face of the curved differential segment
T_1 = the torque at the upstation face of the curved differential segment
a, b, c, and d are dimensions defined in the figure

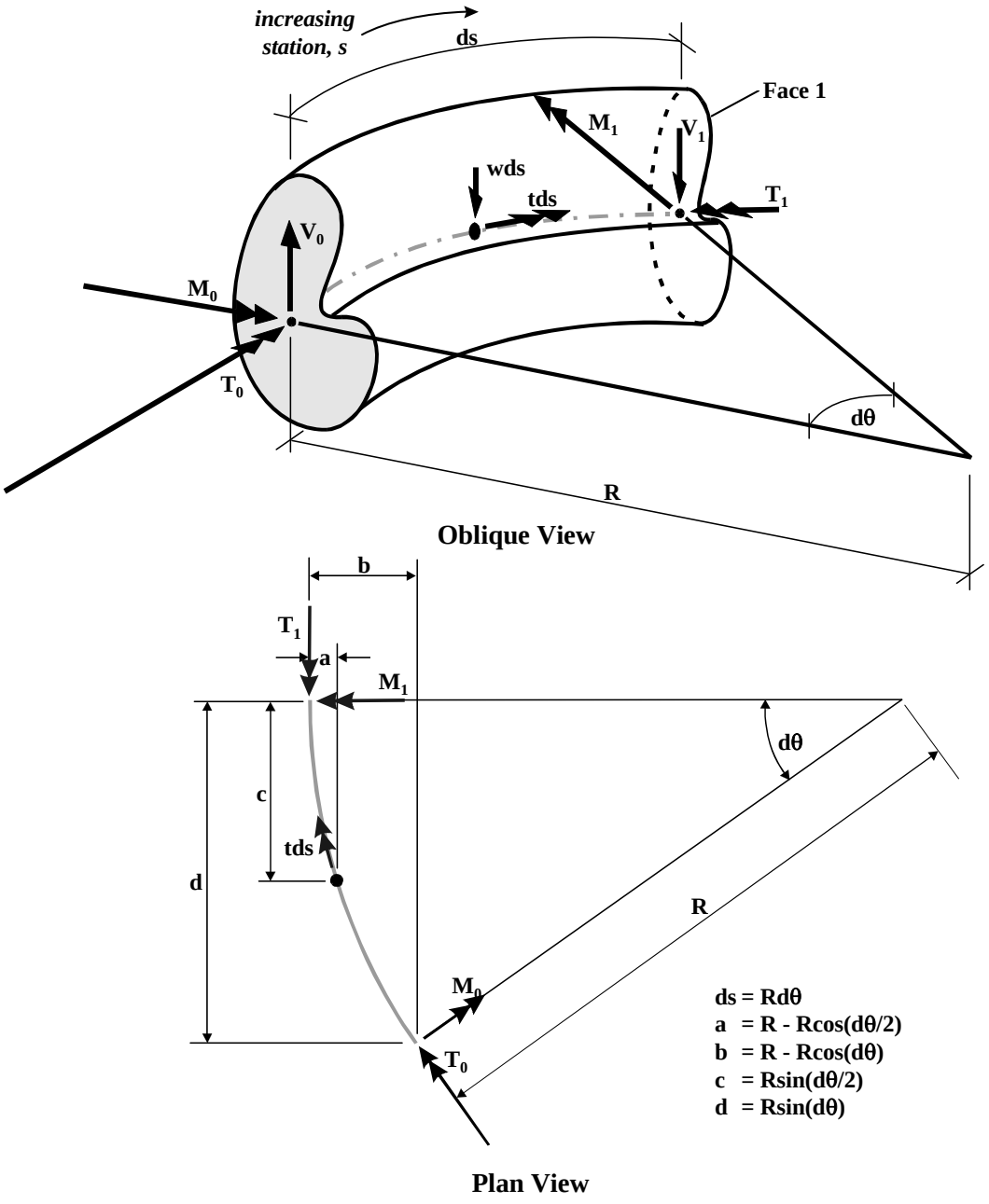

Figure 2.20 - Curved differential segment with applied loads

External equilibrium at face 1 of the segment requires the following relationships:

$$V_1 = V_0 - wds \tag{2-10}$$

$$M_1 = - T_0\sin(d\theta) + M_0\cos(d\theta) - V_0R\sin(d\theta) - tds*\sin(d\theta/2) + wds*R\sin(d\theta/2) \tag{2-11}$$

$$T_1 = T_0\cos(d\theta) + M_0\sin(d\theta) - V_0(R-R\cos d\theta) + tds*\cos(d\theta/2) + wds*(R-R\cos(d\theta/2)) \tag{2-12}$$

Small angle theory is then used to make the following simplifications:

$$\cos(d\theta) \cong 1$$

$$\sin(d\theta) \cong d\theta$$

$$\cos(d\theta/2) \cong 1$$

$$\sin(d\theta/2) \cong 0$$

When these approximations are applied to equations (2-11), and (2-12), the equations reduce to:

$$M_1 = -T_0d\theta + M_0 - V_0Rd\theta \tag{2-13}$$

$$T_1 = T_0 + M_0d\theta + tds \tag{2-14}$$

Equations (2-10), (2-13), and (2-14) are rearranged so that like terms are moved to the left hand sides of the equations, and a substitution of ds/R is made for dθ:

$$dV = V_1 - V_0 = -wds \tag{2-15}$$

$$dM = M_1 - M_0 = -T_0ds/R - V_0ds \tag{2-16}$$

$$dT = T_1 - T_0 = M_0ds/R + tds \tag{2-17}$$

Equations (2-15), (2-16), and (2-17) are then put in their final form by a division of ds:

$$\frac{dV}{ds} = -w \tag{2-18}$$

$$\frac{dM}{ds} = -\frac{T}{R} - V \tag{2-19}$$

$$\frac{dT}{ds} = \frac{M}{R} + t \tag{2-20}$$

Differentiation of equation (2-19) and substitution with equation (2-20) yields the following differential equation and solution:

$$\frac{d^2M}{ds^2} + \frac{M}{R^2} = \frac{t}{R} - w \tag{2-21}$$

$$M = A\sin\theta + B\cos\theta - wR^2 + tR \tag{2-22}$$

where A and B are constants determined from boundary conditions.

The forces in equations (2-18) through (2-22) are related to deformations in a curved girder by the relations:

$$-\frac{M}{EI} = \frac{d^2y}{ds^2} - \frac{\beta}{R} \tag{2-23}$$

$$\frac{T}{GK} = \frac{d\varphi}{ds} \tag{2-24}$$

$$\varphi = \beta + y/R \tag{2-25}$$

The variables in the above equations are defined as:

E = the modulus of elasticity of the girder
I = the moment of inertia about the horizontal axis of the girder cross-section
G = the shear modulus of the girder
K = the torsional constant of the girder cross-section
y = the deflection of the girder at a station, s, along its length
β = the tilt of the girder at a station, s, along its length
φ = the torsional angle of the girder at a station, s, along its length

The torsional constant, K, is generally defined for a concrete box girder according to Bredt's formula [9]:

$$K = \frac{4A^2 t_{avg}}{P} \qquad (2\text{-}26)$$

A = the area enclosed by the centerline of the box girder walls

t_{avg} = the average thickness of the box girder walls

P = the perimeter measured along the centerlines of the box girder walls

Figure 2.21 shows the geometric relations between β, y, and φ.

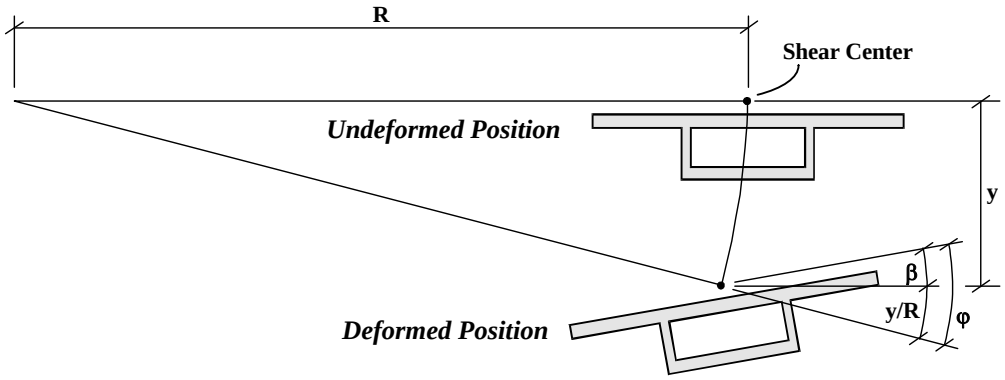

Figure 2.21 - Variables used to define the deformation of a curved girder

One of the important results which can be determined from curved girder theory regards the torsional effect of internal post-tensioning on a curved girder. Figure 2.22 shows the forces transmitted into a curved girder from an internal post-tensioned tendon. The following variables are used in the figure and in this discussion:

P = the axial load from the post-tensioning

u = the uniformly distributed transverse load caused by redirection of the post-tensioning tendon around the horizontal curve of the girder

e = the eccentricity of the post-tensioning tendon measured from the cross-sectional center of gravity

$e_{S.C.}$ = the eccentricity of the cross-sectional shear center measured from the cross-sectional center of gravity

M_{PT} = the total moment from post-tensioning = M_{sec} + Pe

M_{sec} = the secondary moments from post-tensioning

R_u = the radially oriented resultant concentrated force from the sum of the distributed load, u, over a differential length of girder, ds

R_P = the radially oriented resultant concentrated load from the axial stresses on both faces of a differential length of girder, ds

From Figure 2.22, the following relationships are determined:

$$u = \frac{P}{R} \tag{2-27}$$

$$R_u = uds = \frac{P}{R} ds \tag{2-28}$$

$$R_P = 2(P\sin(\frac{d\theta}{2})) \cong Pd\theta = \frac{P}{R} ds \tag{2-29}$$

Thus, the distributed torque resultant from a differential curved segment is:

$$tds = (\frac{P}{R} ds)e_{S.C.} - (\frac{P}{R} ds)(e + e_{S.C.}) = -\frac{Pe}{R} ds$$

or

$$t = -\frac{Pe}{R} \tag{2-30}$$

Substituting this result into equation (2-20) leads to:

$$\frac{dT}{ds} = \frac{M_{PT}}{R} + t = \frac{M_{sec}}{R} + \frac{Pe}{R} - \frac{Pe}{R}$$

$$\frac{dT}{ds} = \frac{M_{sec}}{R} \tag{2-31}$$

Thus, no torsion should be produced by internal prestressing except by the secondary moments from the prestressing. The preceding result does not apply to external tendons which transmit forces into the girder at discrete locations.

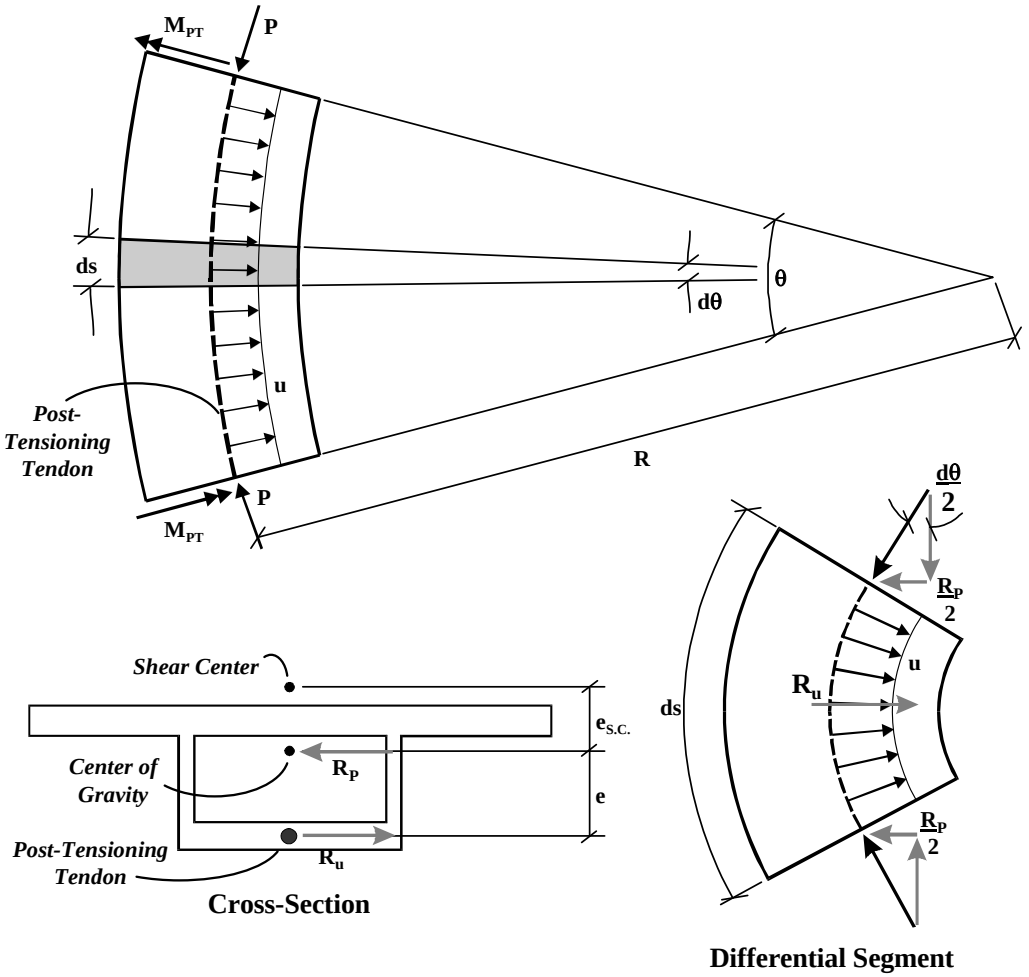

Figure 2.22 - Internal post-tensioning in a curved girder

2.5.2 AASHTO Specifications and Analysis Approaches

The requirements for torsional analysis of curved girders are governed by Section 4.6.1.2 of the *AASHTO LRFD Bridge Design Specifications* [2]. No methods for analysis are recommended in that section. The section gives criteria defining when consideration of horizontal

curvature in a girder must be considered in design analysis and how permanent loads must be treated on such a girder. Curved girders must be analyzed as curved if the central angle subtended by a span is greater than 12.0^{o}. The section also requires that analysis of such girders shall consider the transverse eccentricity of dead and live loads in the curved configuration. No requirements are given for the precision of techniques to be used for the analysis of curved girders.

Software which is capable of three-dimensional analysis of segmental prestressed concrete bridges is not common in the design industry. Many segmental bridge design firms and state transportation agencies usually treat curved box girders as straight for flexural design and perform a separate torsion analysis using any convenient three-dimensional frame solver. Thus, the flexural design will reflect the effects of creep, shrinkage, and prestressing, but the torsional analysis may not include such effects or will treat such effects in approximate ways.

In general, neglect of the torsional contribution to moment is conservative, but neglect of the moment contribution to torsion is not. Thus, designers sometimes perform flexural analysis on an equivalent straightened bridge rather than the curved bridge. The torsional analysis can then be performed by inserting the analogous straight bridge moment diagram into equation (2-20) for M. This approximation uncouples the relationship between the moment and torque distributions and allows moment analysis to be performed independently of the torsional analysis (Note: All distributed torsion loads are still determined from the curved geometry).

CHAPTER 3

SUPERSTRUCTURE INSTRUMENTATION

3.1 INSTRUMENTATION OBJECTIVES

The objective of the study of the northbound IH-35/northbound U.S. 183 fly-over ramp, henceforth referred to as Ramp P, was to determine the moments, torques, and thermal gradient-induced actions that occur during construction and long-term service of a curved, precast, prestressed concrete segmental box girder bridge erected in balanced cantilever. In order to determine those moments, torques, and actions it was necessary to satisfy the following instrumentation objectives:

1. Determine the longitudinal strain distribution across the box at several sections along the ramp.
2. Determine the torsional shear strains at several sections along the ramp.
3. Determine the strains in the external post-tensioning strands.
4. Determine the temperature distribution across the box so that the thermally-induced strains could be determined.

In addition to these instrumentation objectives, the behavior of an anchor diaphragm, anchor blister, and deviator block in the ramp were also to be studied. These bridge components were instrumented, but the results of their instrumentation and the objectives relating to their instrumentation will be reported by Davis [7]. Furthermore, figures and discussion relating to instrument location in this thesis will not refer to the diaphragm, blister, or deviator instrumentation.

3.2 SPAN SELECTION

The portion of Ramp P constructed by the balanced-cantilever method consisted of a five span continuous unit with span lengths of 38.1m-54.9m-43.4m-54.9m-38.1m (125'-180'-142.36'-180'-125'). Instrumentation of the entire structure would have been expensive and time

consuming. In addition, the resulting data would be too overwhelming to reduce. Thus, only one span of the structure was studied. It was decided that one of the 54.9m (180') spans should be chosen for instrumentation. Because pier P16 had been instrumented previously as an earlier part of the U.S 183 study (see Bonzon [6]), the upstation 54.9m (180') span between piers P16 and P17 was chosen.

3.3 SEGMENT SELECTION

Three segments in the span between piers P16 and P17 were instrumented: P16-2, P16-10, and P16-17. Figure 3.1 shows a plan drawing of Ramp P and the locations of the instrumented segments. All three of these segments were located on the pier P16 upstation cantilever. Segment P16-2 was at the base of the cantilever where the maximum negative moment (tension in the top fiber of the section) and torque occurred during construction. Segment P16-10 is near the quarter point of the completed span where an inflection point in the live load moment diagram of the span would occur. Segment P16-17 is near the midpoint of the completed span where the maximum positive moment from load will occur. It was decided that instrumentation of these locations within the span would provide an adequate picture of the most crucial points on the torque and moment diagrams of the span.

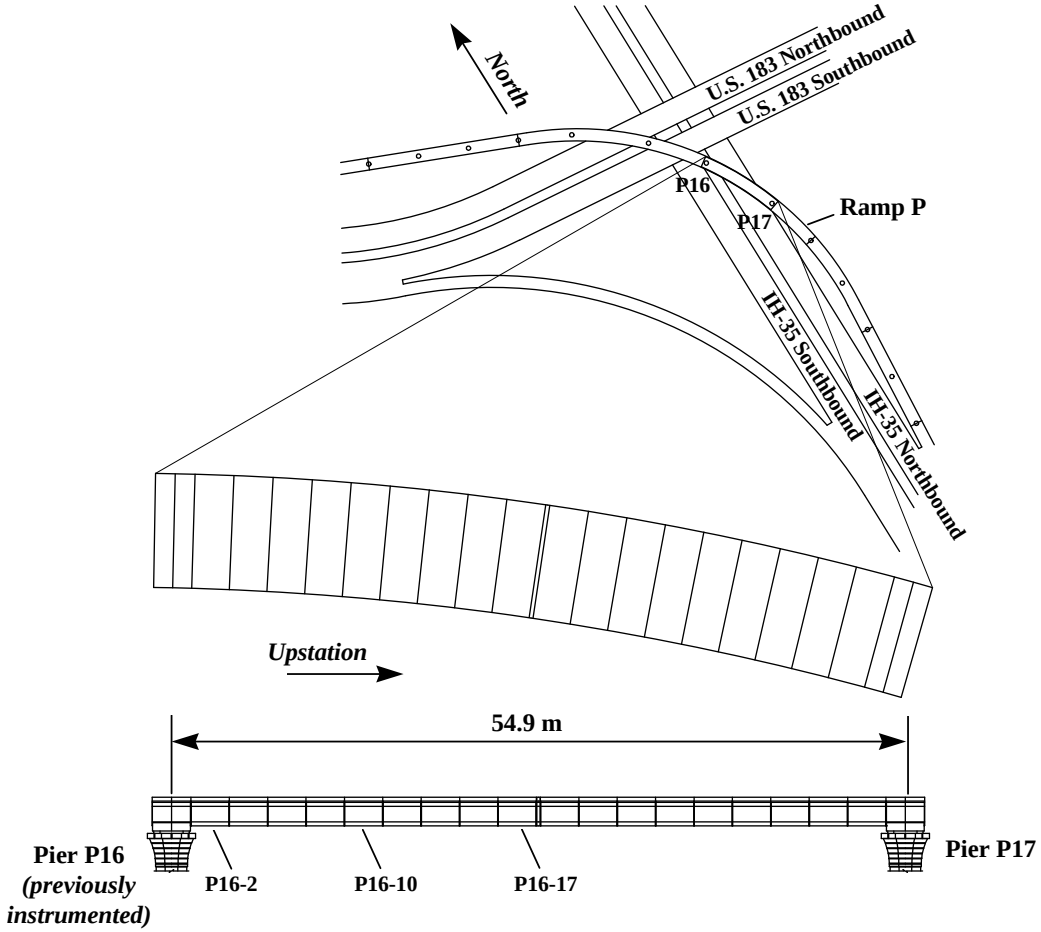

Figure 3.1 - Instrumented sections in Ramp P

3.4 GAUGE TYPES

Four different types of instruments were installed in the Ramp P superstructure: concrete strain gauges, steel strain gauges, Demec points, and thermocouples. In addition, a companion program conducted by the Applied Research Laboratories, a division of the University of Texas at Austin, provided a Model 800P Portable Tiltmeter manufactured by Applied Geometrics to monitor the slope and twist of the pier P16 cantilevers during construction. This section describes these instruments.

3.4.1 Concrete Strain Gauges

Concrete strain gauges are capable of measuring the strain in the concrete in regions where cracking does not occur. The concrete strain gauges used on the U.S. 183 study consisted of an electronic strain gauge mounted on a short length of small diameter steel round. These units were attached to the rebar cages of the segments just before casting. A detailed description of the development and workings of this gauge is provided by Arréllaga [5].

All of the concrete strain gauges used for the U.S. 183 instrumentation were manufactured by the U.S. 183 researchers at the Ferguson Structural Engineering Laboratory. A 4.76mm ($^3/_{16}$") diameter steel round was cut to a length of about 235mm (9 $^1/_4$") and 20mm ($^3/_4$") of each end was threaded. The middle of the round was carefully sanded and cleaned and a 350 Ω electronic strain gauge was glued to the steel. The gauge was coated with acrylic paint then covered with a protective shrink tubing to protect it from the harsh concrete environment. Nuts and washers were then screwed onto the threaded ends of the steel round to provide a positive anchorage with the concrete and ensure strain compatibility between the concrete and the steel. These gauges were installed in the segments by tying them to the rebar cages at the precasting yard just before placement of the concrete. In the early stages of the U.S. 183 instrumentation, a series of tests was performed to determine the most reliable gauge possible. These tests and the results are described by Andres [4]. Figure 3.2 illustrates the concrete strain gauge. Figure 3.3 shows researchers installing gauges to the rebar cage of segment P16-2, and Figure 3.4 shows a completed concrete strain gauge in place on a rebar cage, just before placement of the concrete.

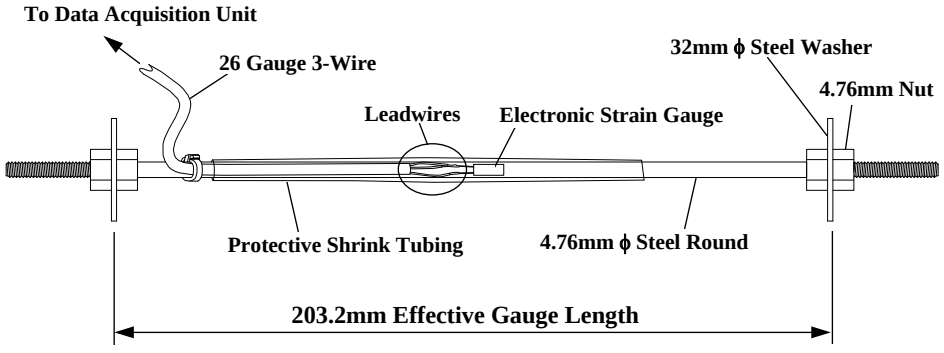

Figure 3.2 - Diagram of concrete strain gauge

Figure 3.3 - Installation of concrete strain gauges

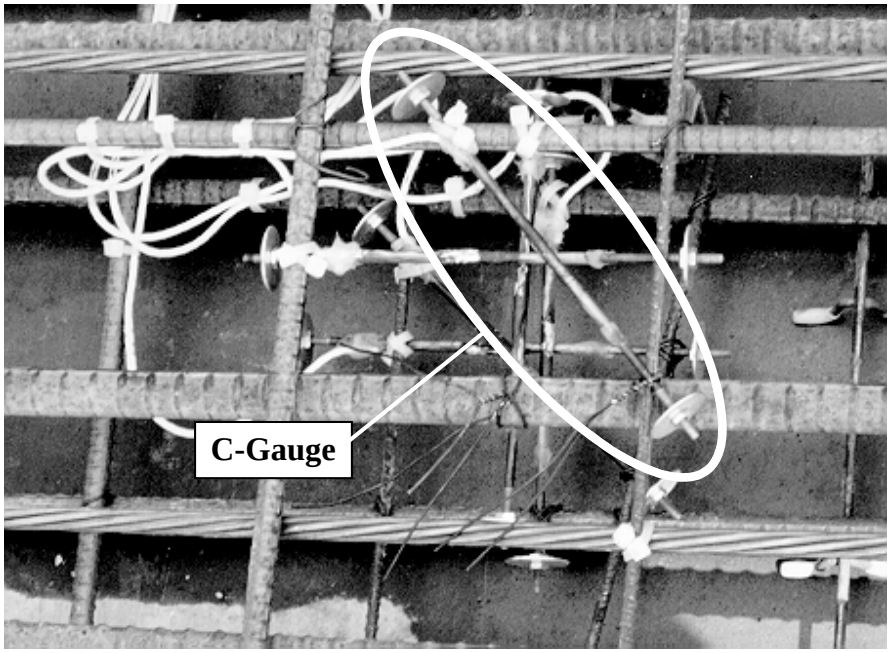

Figure 3.4 - Concrete strain gauge tied in place on a rebar cage

The electronic strain gauges used on the U.S. 183 project were temperature compensated. The output of the gauge is calibrated not to shift with unrestrained thermal changes in steel for the temperature range of about 50 ^{o}F to 100 ^{o}F. Since the coefficient of steel is approximately the same as concrete, the output of the gauge should not vary for unrestrained thermal expansion or contraction of concrete. Thus, unrestrained expansion of the bridge from a linear thermal change (a situation which would not produce any stress in the bridge) would not cause a change in the output of the gauge despite the fact that strain does occur over the gauge. On the other hand, restrained thermal changes in the bridge which do cause stress would register in the output of the gauge. Thus, the output from the gauge is a true measure of the stress in the concrete and no calibration for thermal volumetric changes needs to be done to interpret the gauge output. A series of tests to determine the output behavior of the concrete strain gauges from thermal changes in concrete specimens and in the data logging equipment was performed. The results of these tests are described by Davis [7].

3.4.2 Steel Strain Gauges

In areas where the concrete was expected to crack or where forces in the steel reinforcement were desired, a steel strain gauge was bonded directly to the steel reinforcement. The steel strain gauges discussed in this section were bonded onto external post-tensioning strands.

Before the external tendons were stressed electronic strain gauges were attached to the strands. The tendons were threaded into place inside protective polyethylene tubing. Small holes were cut into the tubing at desired locations, exposing the strands. A wire from a strand was lightly sanded and cleaned and a gauge was glued to the wire's surface. Then acrylic paint and a fast drying epoxy were placed on the gauge to protect it from rubbing against the polyethylene tubing during stressing and also against corrosion from the grout which was pumped inside the tubing afterward. The hole in the polyethylene tubing was patched just before grouting. Only one wire per 15.24mm (0.6") strand was gauged. Each external tendon contained 19 strands. Three strands in each tendon were gauged at locations where information was desired. Arréllaga discusses the use of electronic strain gauges on prestressing strand in more detail [5].

3.4.3 Demec Points

Despite the reliability of the concrete strain gauges, very often a gauge will be damaged during casting. Sometimes the gauge wires will be broken and the electronic signal to the gauge is lost. The steel round that the electronic gauge is attached to can also become bent and the output from the gauge will be unreliable. The gauge might even de-bond from the steel round after a certain amount of time. If one of the two latter problems occurs, it will not be known until analysis of the data begins. It is sometimes difficult to make the judgment that a gauge has gone bad with only one's intuition about what the data should look like as a guide. A simple and reliable backup to the concrete strain gauge is to use a Demec extensometer.

A Demec extensometer is a mechanical device that measures strain on the surface of the concrete. The device is simple. Two steel points are installed into the concrete after it has hardened. These points can be glued to the concrete surface, however, for the U.S. 183 project, HILTI® brand hit anchors were used to anchor the points into the concrete to a depth of about 32mm (1 $^{1}/_{4}$"). A small 0.8mm ($^{1}/_{32}$") diameter hole was drilled into the head of the hit anchor. The hit anchor was installed into the concrete at the precasting yard storage area. A 10mm ($^{3}/_{8}$") hole was drilled into the concrete. A small amount of epoxy was injected into the hole. The hit anchor was placed in the hole and hammered firm. Another hit anchor was placed a distance of 400mm (15 $^{3}/_{4}$") away from the first point and in the direction that the strain was to be measured. The Demec extensometer has points on each of its ends that fit into the holes in the hit anchors. One of the points can pivot to accommodate movement between the hit anchors, and a dial gauge on the reader registers the amount of movement. The Demec extensometer mechanically measures changes in the distance between the two 0.8mm ($^{1}/_{32}$") holes in the hit anchors and gives readings in terms of strain. The Demec extensometer used in the U.S. 183 study had an accuracy of $4x10^{-6}$ m/m. Demec points installed in Ramp P gave alternative strain data to compare the electronic data with. Figure 3.5 gives an illustration of the Demec extensometer and its parts. Figure 3.6 shows a picture of the Demec extensometer used in the U.S. 183 study.

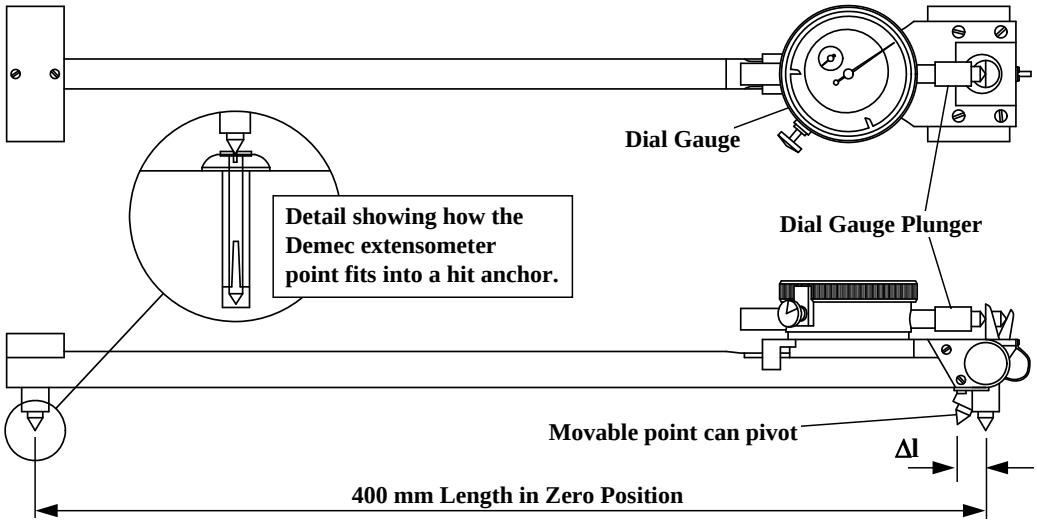

Figure 3.5 - Diagram of the Demec extensometer

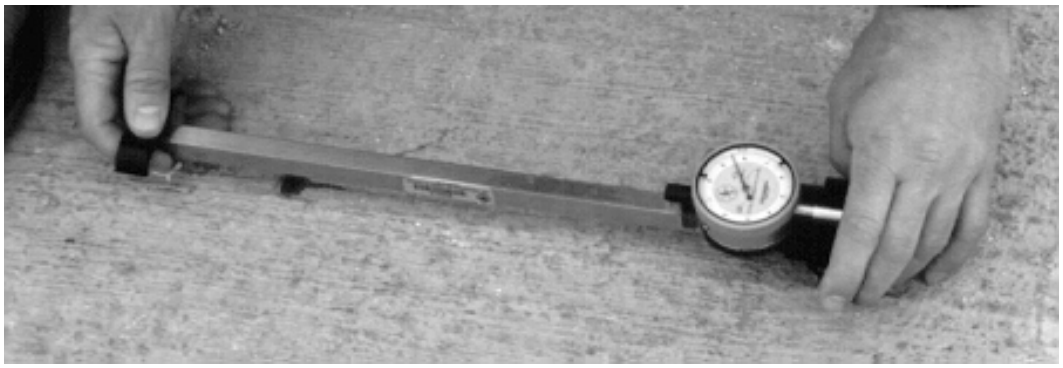

Figure 3.6 - Picture of the Demec extensometer used in the U.S. 183 study

Demec points have the disadvantages that they are less accurate and slower to read data from than the electronic strain gauges. Because Demec readings are taken manually, they can suffer from human error. Demec points give values of strains at the surface level of the concrete, whereas the concrete gauges are embedded a certain depth and provide strain readouts for concrete beneath the surface level, therefore there is not a direct comparison between strain values from the two instruments. Demec points are also not temperature compensated. Thermal strains that have no stress associated with them will appear in the data from the Demec points. Therefore,

Demec points are most useful for reading short-term changes in concrete strain under controlled loading conditions where the temperature of the concrete does not vary significantly. Still, if read properly by a person who has experience with the Demec gauge, they can provide a useful comparison to the electronic concrete strain gauge data for some loading conditions. A detailed study of the use and accuracy of Demec points was performed by Arréllaga [5].

3.4.4 Thermocouples

Thermocouples were used to measure the concrete temperatures. The thermocouple is a simple electrical connection between two wires of dissimilar metals. The resistance of the connection between the two wires varies as the temperature of the connection. Thus, the temperature can be determined electronically. The thermocouples used in the U.S. 183 study were fabricated from type T wire, which uses copper and constantan for the two dissimilar metals. Copper and constantan both perform well in the corrosive concrete environment. Figure 3.7 provides a schematic of the electrical circuit that made up the thermocouples.

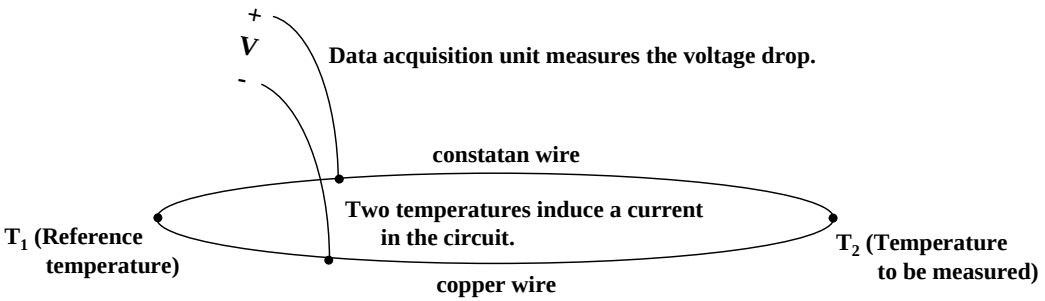

Figure 3.7 - Thermocouple electrical circuit

3.4.5 Tiltmeter

The tiltmeter used to measure slope and twist of the pier P16 cantilevers during construction was a Model 800P Portable Tiltmeter manufactured by Applied Geometrics. Use of the tiltmeter came through the cooperation of the Applied Research Laboratories of The University of Texas in Austin. The 800P Tiltmeter uses electrolytic resistance cells to measure angles from the baseline gravity vector (a straight line towards the center of the Earth, or in other words, a very precise plumb line). The precision of the 800P is smaller than 1 microradian (1 mm

vertical change over a 1 km distance). Ceramic tiltplates (also manufactured by Applied Geometrics) were cemented to the deck of the bridge. The tiltplates are mounts for the tiltmeter that allow precise placement and orientation of the tiltmeter for every measurement. The 800P tiltmeter device has indexing bars attached to its bottom surface so that it can be precisely fitted to the tiltmeter plates every time measurements are taken. Four measurements are made with the tiltmeter at each tiltplate and these measurements are used to calculate a magnitude and direction of tilt. The data is read using a voltmeter. A Model 800 Tiltmeter is shown in figure 3.8. Further study of the use of tiltmeters for bridge instrumentation has been conducted by Hyzak [8].

Figure 3.8 - Picture of a Applied Geometrics Model 800 Tiltmeter

3.5 DATA LOGGING EQUIPMENT

All of the electrical instrumentation systems used in the U.S. 183 study required some form of automated data logging device. The data logging device used was a 21X Micrologger produced by Campbell Scientific, Inc. The electronic strain gauges were connected to the 21X Microloggers in Wheatstone bridge circuits. The 21X Microloggers are capable of recording 8 channels connected in full Wheatstone bridge circuits. The capacity of these devices was increased by using AM416 Relay Multiplexers (also produced by Campbell Scientific, Inc.) for channel switchers. A 21X Micrologger coupled with four AM416 Multiplexers is capable of receiving 128 channels of data. Three 21X Microloggers were required to record the data in the

superstructure of Ramp P. Data was usually recorded every one or two minutes for important events in the life of the bridge and hourly the rest of the time to track the long term behavior of the bridge. The 21X Microloggers have a limited memory capacity which required data to be downloaded from the data logging units every five days. To download the data, a portable notebook computer was carried into the bridge and connected directly to the 21X Micrologger devices through a parallel port connection. Then software supplied by Campbell Scientific, Inc. (named PC208) was used to retrieve the data and store it in text files. More information on the 21X Micrologger and AM416 Multiplexor units can be found in Arréllaga [5]. Figure 3.9 shows a Wheatstone bridge circuit diagram. Figure 3.10 shows a picture of the data logging equipment used in Ramp P, and Figure 3.11 shows the author retrieving data from segment P16-2 using a notebook computer.

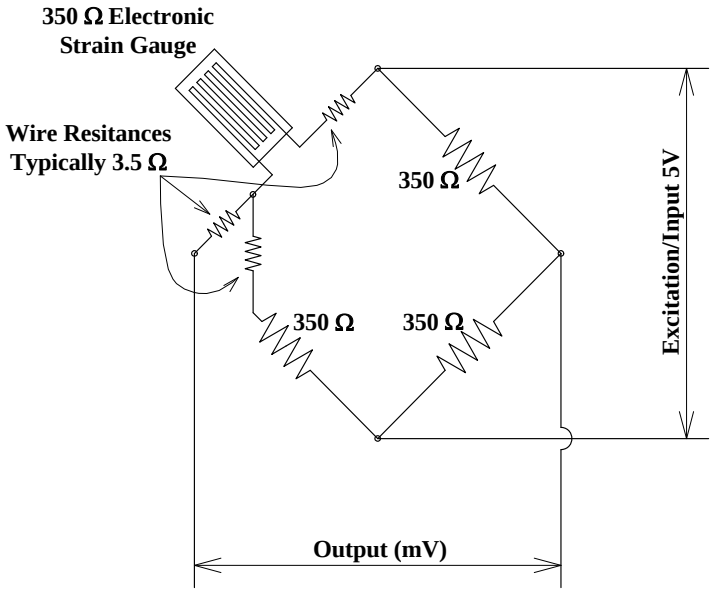

Figure 3.9 - Wheatstone bridge circuit

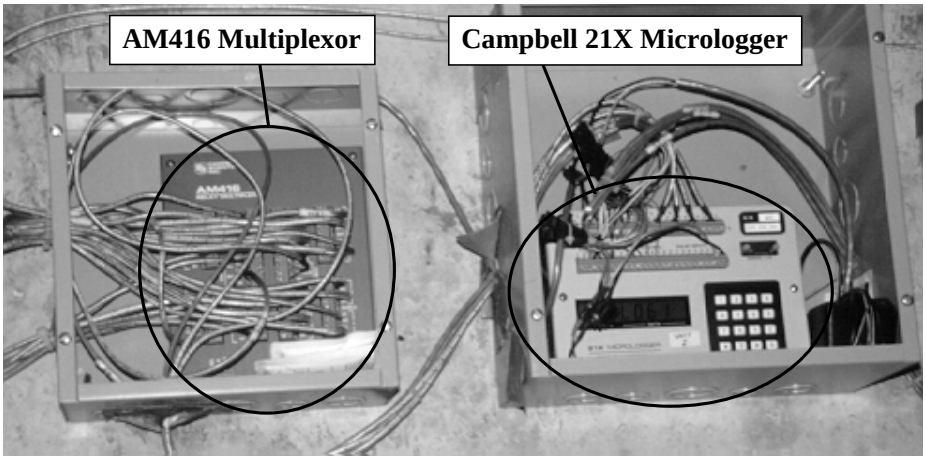

Figure 3.10 - Picture of the data logging equipment used in the U.S. 183 study

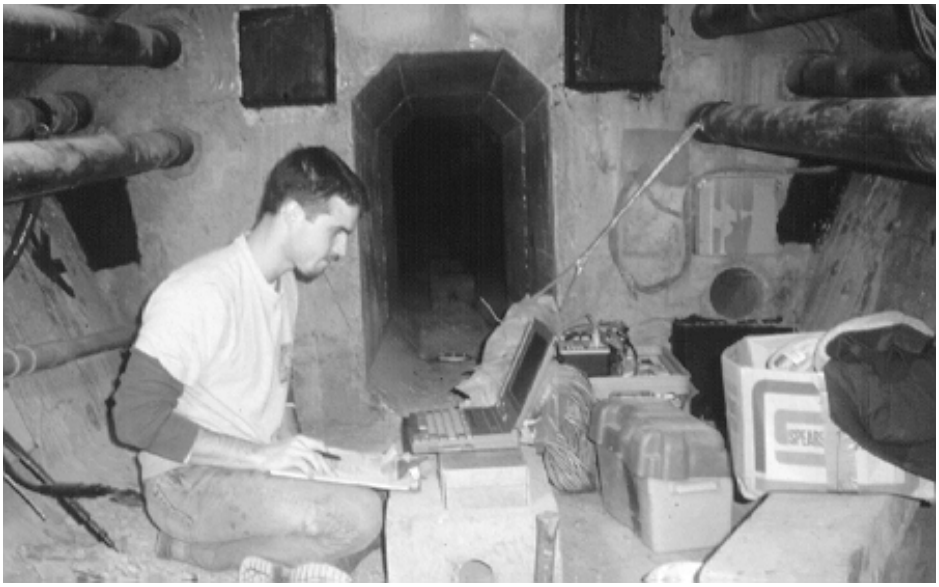

Figure 3.11 - Retrieval of data from Ramp P using a portable notebook computer

3.6 OVERALL INSTRUMENTATION SCHEME

This section will describe in detail the locations of the various gauges used to instrument the Ramp P superstructure and the reasons for selecting those locations. The organization of this

section is divided into sections by instrumentation objective: longitudinal strains, torsional shear strains, post-tensioning strains, and thermal behavior.

3.6.1 Longitudinal Strains

Concrete strain gauges and Demec points were placed across three cross-sections in the P16/P17 span in Ramp P: A, next to pier P16, B, at the quarter point of the span, and C and D, near the midpoint. Figure 3.12 shows the locations of the instrumented cross-sections and their dimensions from the centerline of pier P16. All of these gauges were oriented to measure longitudinal strains and they were distributed across the cross-section such that a complete picture of the longitudinal strain distribution could be determined.

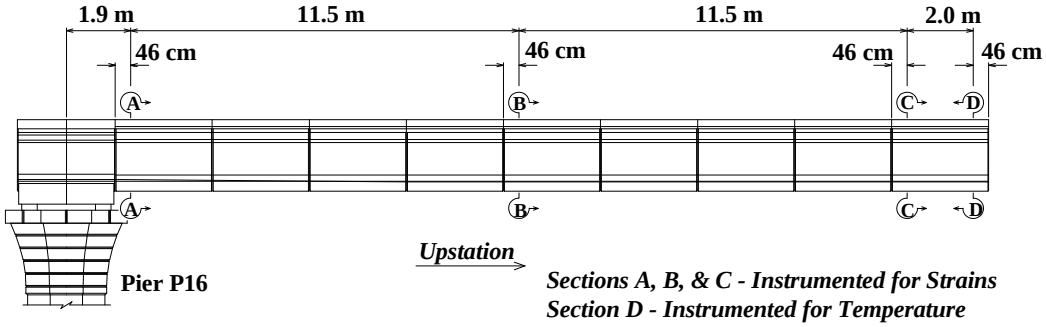

Figure 3.12 - Locations of the instrumented sections in Ramp P

3.6.1.1 Longitudinally Oriented Concrete Strain Gauges

All concrete strain gauge designations used in the U.S. 183 study begin with the letter "C" for "Concrete strain gauge." Figure 3.13 shows the locations of the longitudinally oriented concrete strain gauges in segment P16-2. A total of 48 concrete strain gauges were placed in segment P16-2; 32 of those gauges were oriented longitudinally. Gauges were placed throughout the entire cross-section. More gauges were placed at the intersection of the webs and the top flange because peaks in the strain due to shear lag and diffusion of the cantilever post-tensioning forces were expected in these regions. The instrumented cross-section was located at a distance of 460mm (18") from the segment face to avoid edge effects from the joint. The same distribution of concrete strain gages was used in segments P16-10 and P16-17 as shown in Figures 3.14 and 3.15.

Concrete strain gauges in segment P16-2 were numbered in the 600's. Similarly, gauges in segments P16-10 and P16-17 were numbered in the 700's and 800's respectively.

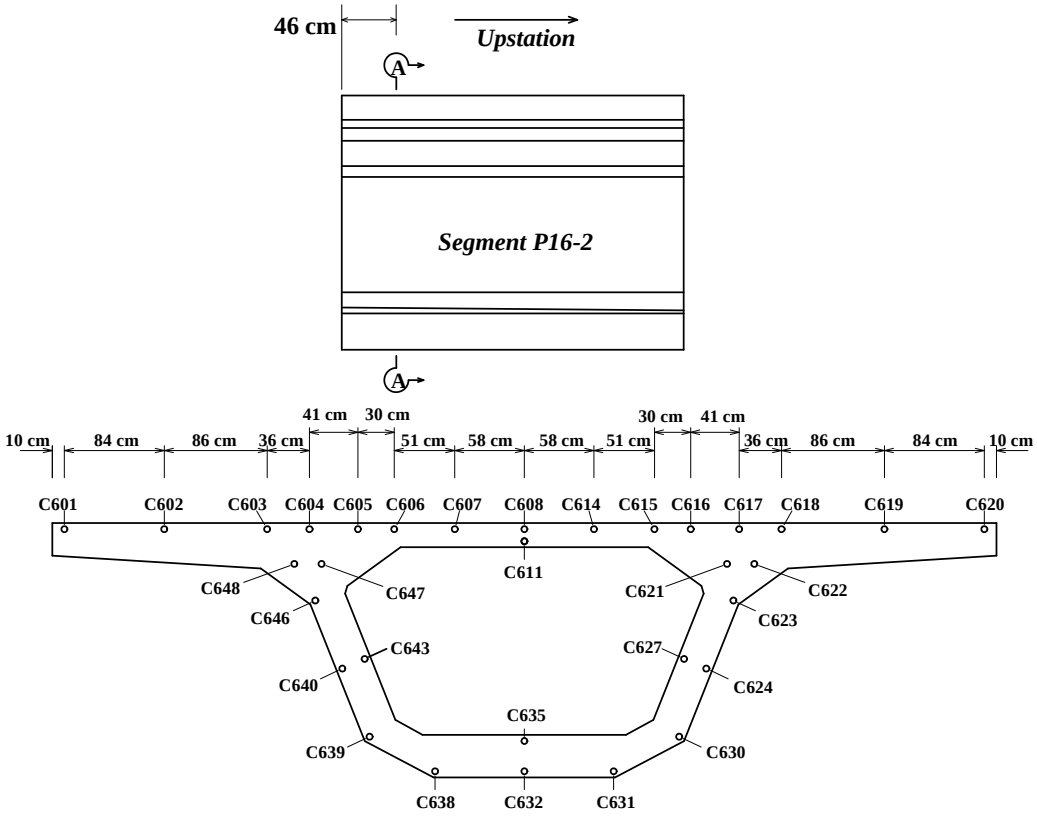

Figure 3.13 - Longitudinal concrete strain gauges in segment P16-2

Section B-B same as designated in figure 3.11.

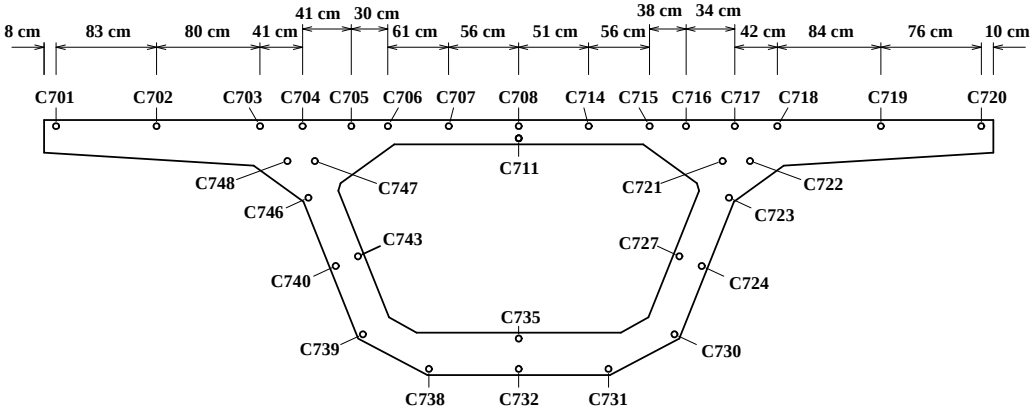

Section B-B

Figure 3.14 - Longitudinal concrete strain gauges in segment P16-10

Section C-C same as designated in figure 3.11.

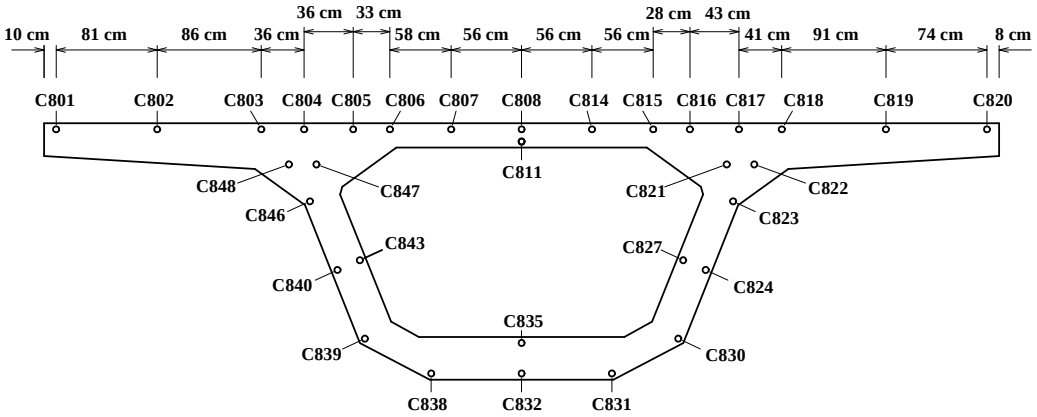

Section C-C

Figure 3.15 - Longitudinal concrete strain gauges in P16-17

3.6.1.2 Longitudinally Oriented Demec Points

All Demec point designations used in the U.S. 183 study begin with the letter "D" for "Demec point." Figure 3.16 shows the locations of the longitudinally oriented Demec points on segment P16-2. Demec points are only useful if they are located where they are accessible for manual measurement. Therefore, the Demec points were only placed inside the box and on the deck of the bridge. A total of 33 sets of Demec points was placed on segment P16-2; 21 of these sets were oriented longitudinally. The same distribution of Demec points was used in segments P16-10 and P16-17 as shown in Figures 3.17 and 3.18. Demec points on segment P16-2 were numbered in the 600's as were the concrete strain gauges in that segment. Similarly, Demec points on segments P16-10 and P16-17 were numbered in the 700's and 800's. Figure 3.19 shows some Demecs in place on the deck of Ramp P being read by a University of Texas researcher. Use of the Demec points on the deck of the bridge was forfeited when the asphalt wearing surface was applied. Fortunately, a live load test of Ramp P was performed before that time.

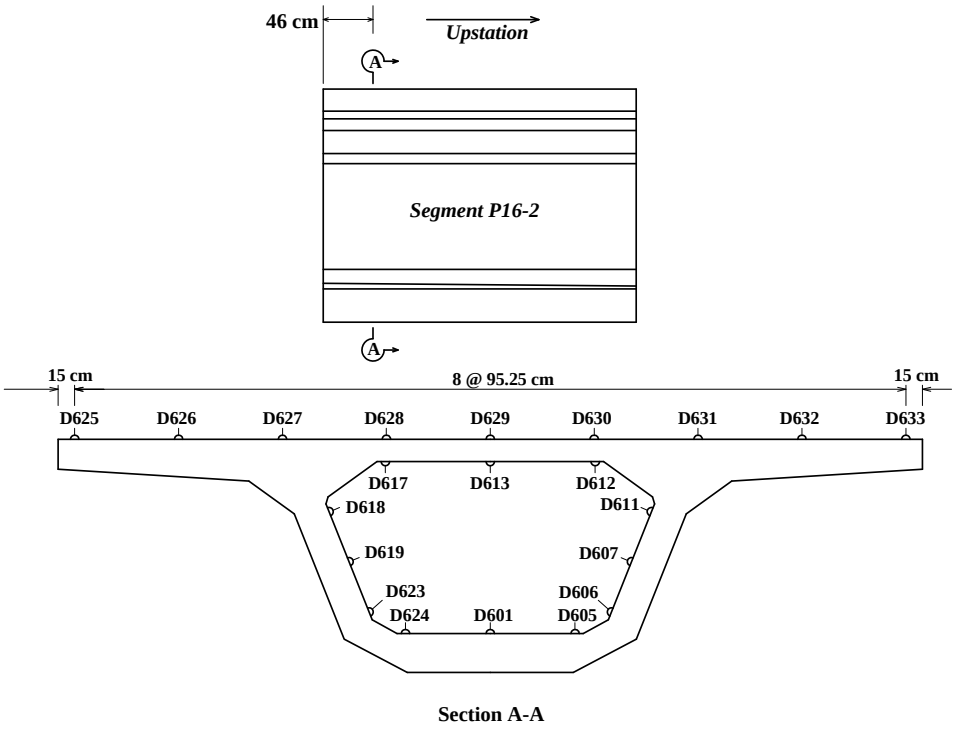

Figure 3.16 - Longitudinal sets of Demec points in segment P16-2

Section B-B same as designated in figure 3.11.

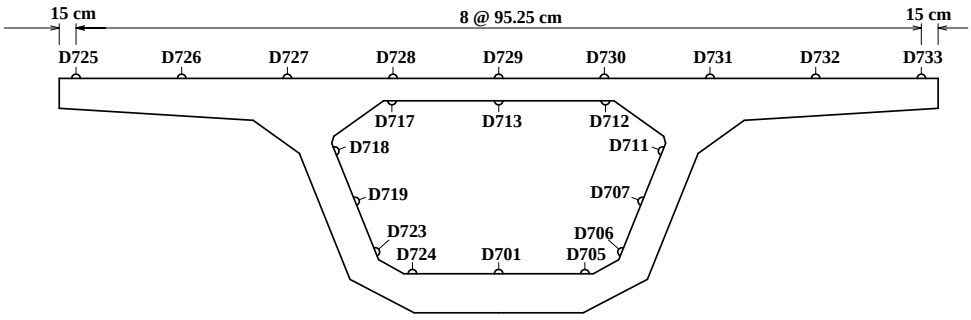

Section B-B

Figure 3.17 - Longitudinal sets of Demec points in segment P16-10

Section C-C same as designated in figure 3.11.

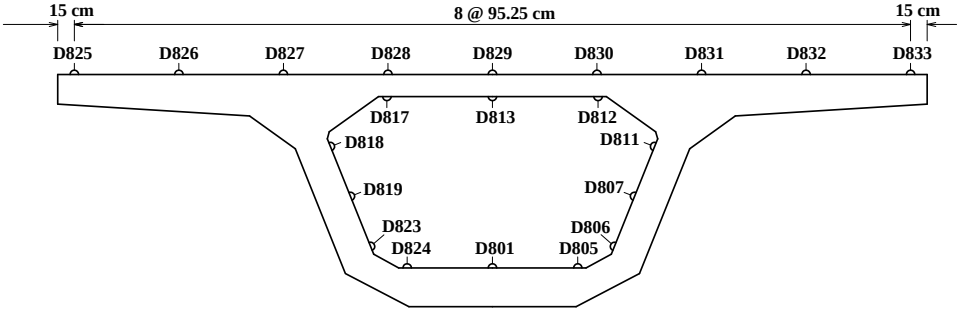

Section C-C

Figure 3.18 - Longitudinal sets of Demec points in segment P16-17

Figure 3.19 - A researcher takes measurements from Demec points installed on the deck of RampP

3.6.2 Principal Strains from Shear and Torsion

At the same locations which were instrumented for longitudinal strains (see Figure 3.12), concrete strain gauges and Demec points were placed in the webs and on the top and bottom slabs of the segments in rosette arrangements so that principal strains in those areas could be determined.

3.6.2.1 Concrete Strain Gauge Rosettes

Figure 20 shows a rosette arrangement of concrete gauges. The locations and designations of the concrete strain gauges which were arranged into rosette patterns are shown in Figures 3.21, 3.22, and 3.23.

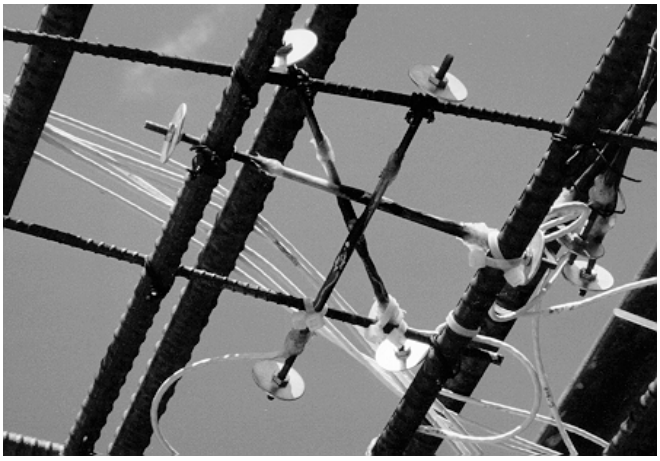

Figure 3.20 - Concrete strain gauges arranged in a rosette pattern

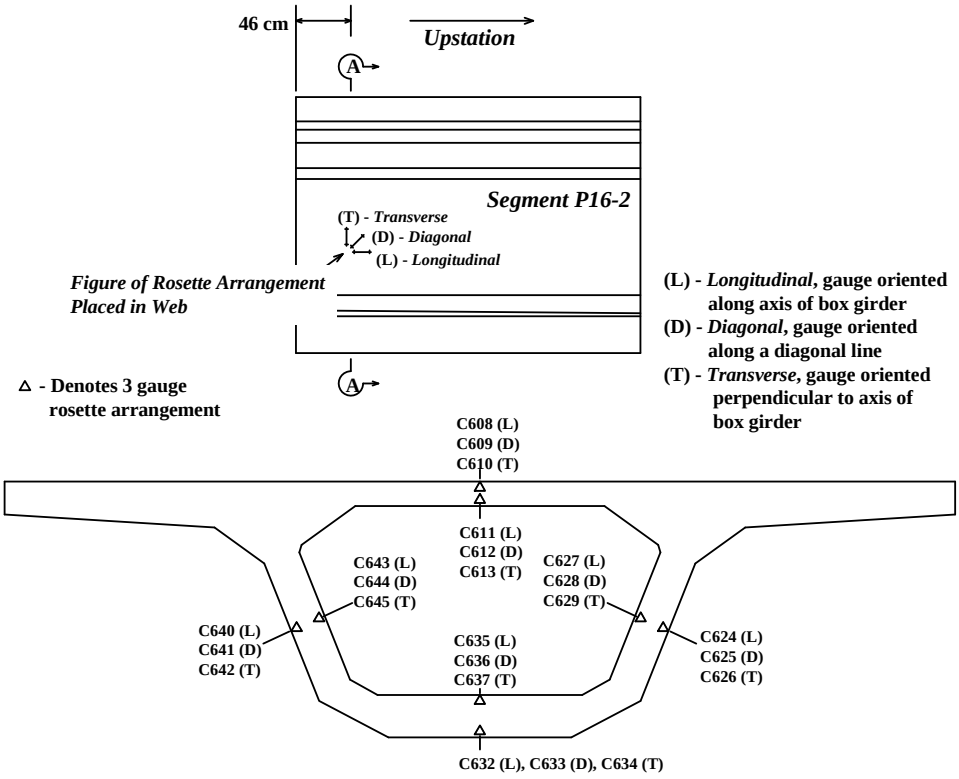

Figure 3.21 - Concrete strain gauge rosettes in segment P16-2

Section B-B same as designated in figure 3.11.

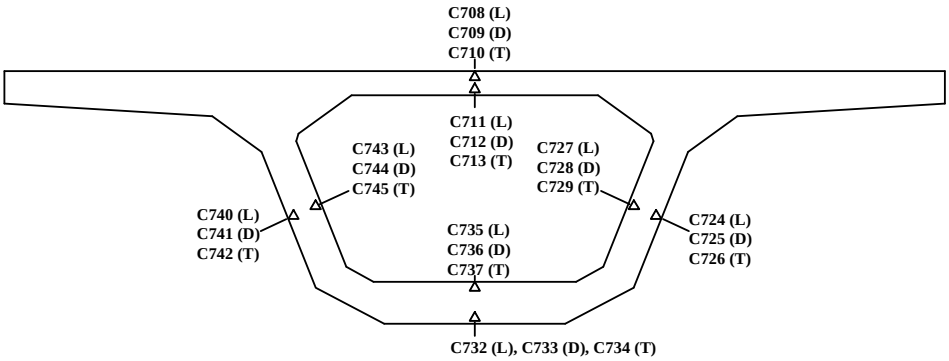

Section B-B

Figure 3.22 - Concrete strain gauge rosettes in segment P16-10

Section C-C same as designated in figure 3.11.

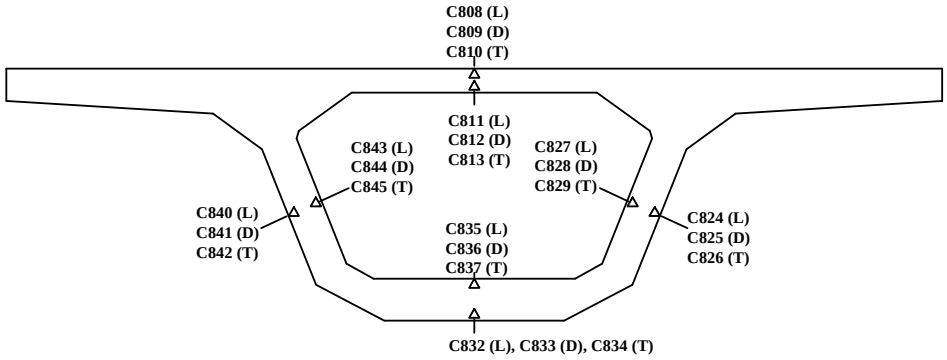

Section C-C

Figure 3.23 - Concrete strain gauge rosettes in segment P16-17

3.6.2.2 Demec Point Rosettes

Demec points were also installed into the concrete surface on the interior of the segments in order to back up the electronic strain gauge data. The Demec point rosettes were made by installing four sets of points in a circular arrangement with each set of points at a 45^{o} angle from the next set. A typical Demec rosette wheel is shown in Figure 3.24. The locations of the Demec rosette wheels are shown in Figures 3.25, 3.26, and 3.27.

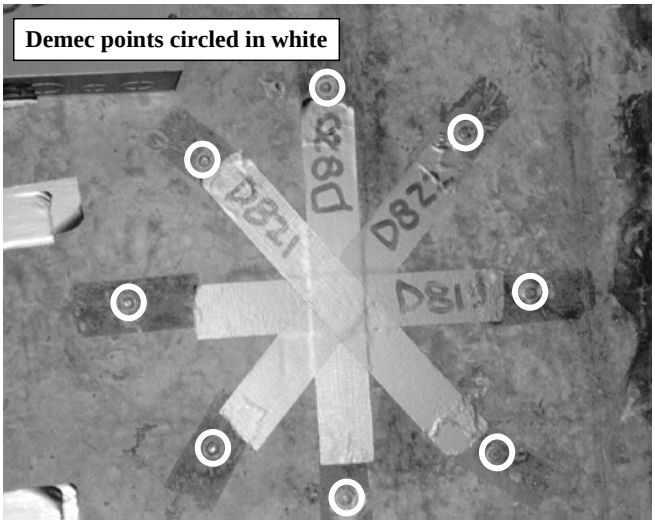

Figure 3.24 - Picture of a Demec rosette wheel from segment P16-17

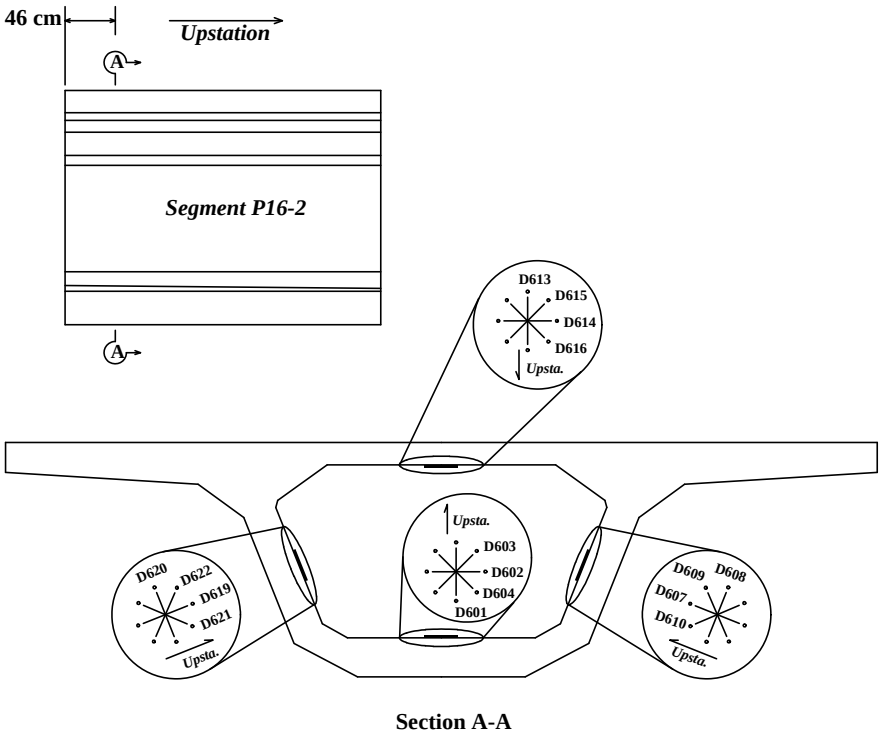

Figure 3.25 - Demec rosette wheels in segment P16-2

Section B-B same as designated in figure 3.11.

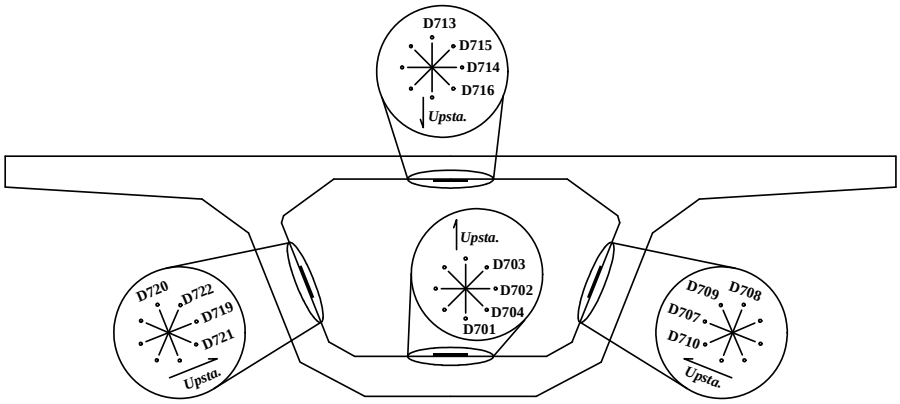

Section B-B

Figure 3.26 - Demec rosette wheels in segment P16-10

Section C-C same as designated in figure 3.11.

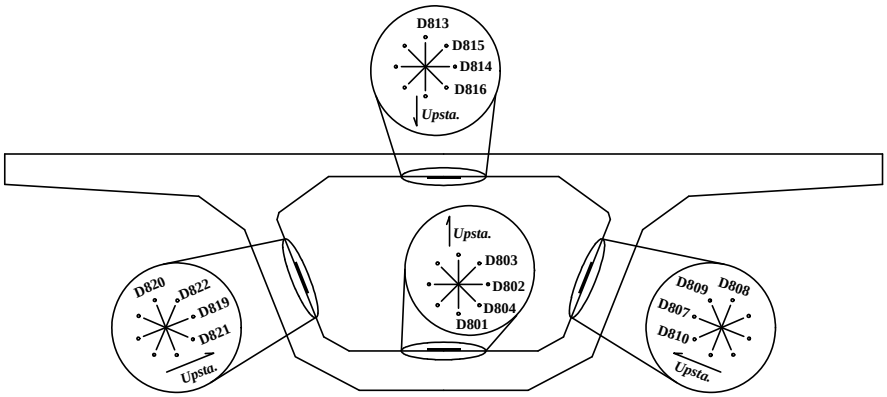

Section C-C

Figure 3.27 - Demec rosette wheels in segment P16-17

3.6.3 Strains in the External Post-Tensioning Strands

The external post-tensioning strands are debonded from the bridge structure except for a few points at the deviators and anchorages. Therefore, their interaction with the structure is difficult to predict. Furthermore, friction losses across the deviators need to be known for an

accurate construction analysis of the structure. Strain gauges were placed on the external tendons at two locations for each tendon in the instrumented span of Ramp P. These gauges were designated after the tendons they were placed on ("T1," "T2," or "T3") and which side of the girder the tendon was located ("L" for "Left looking upstation" or "R" for "Right looking upstation"). Designations of "a," "b," or "c" were also added to distinguish between individual gauges on each tendon. Thus, a typical external tendon gauge might be designated as T1La to indicate that it was the first gauge placed on the right T1 tendon. Friction losses were measured across the vertical deviator in segment P16-10. Figure 3.28 shows the external tendon layout in the instrumented span and the locations where gauges were placed on the tendons.

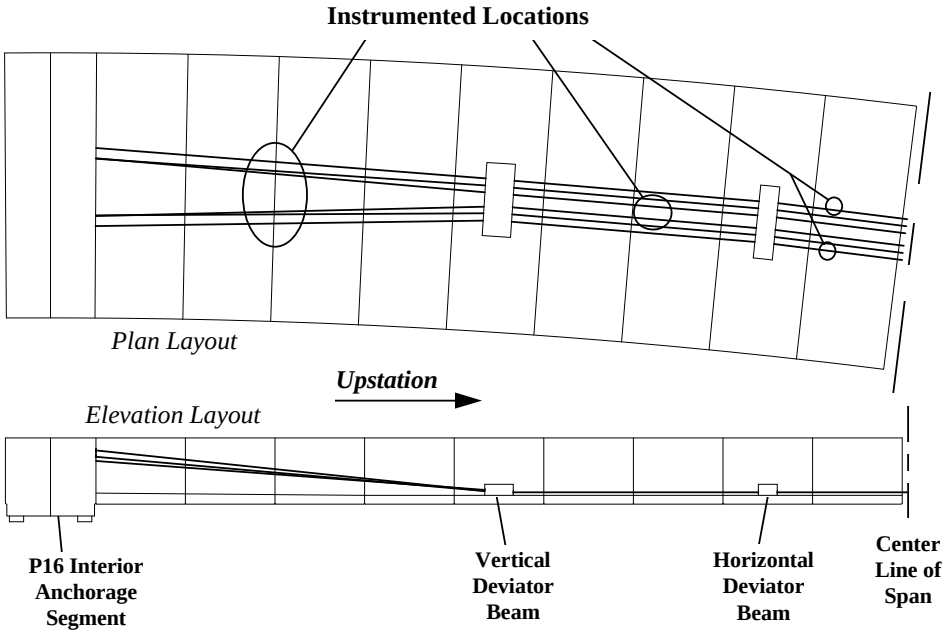

Figure 3.28 - Instrumented locations on the external tendons in span 16

3.6.4 Temperatures in the Ramp

All thermocouple designations used in the U.S. 183 study begin with the letter "T" for "Thermocouple." It was decided for economy that one section instrumented for temperatures would suffice to determine the temperature distribution thoughout the superstructure since the sunlight hits all parts of the deck evenly. Thermocouples were placed on the upstation side of

segment P16-17 near the midspan. These thermocouples were given number designations in the 800's to match the numbers of the other gauges in segment P16-17. Figure 3.29 shows the instrumented cross-section.

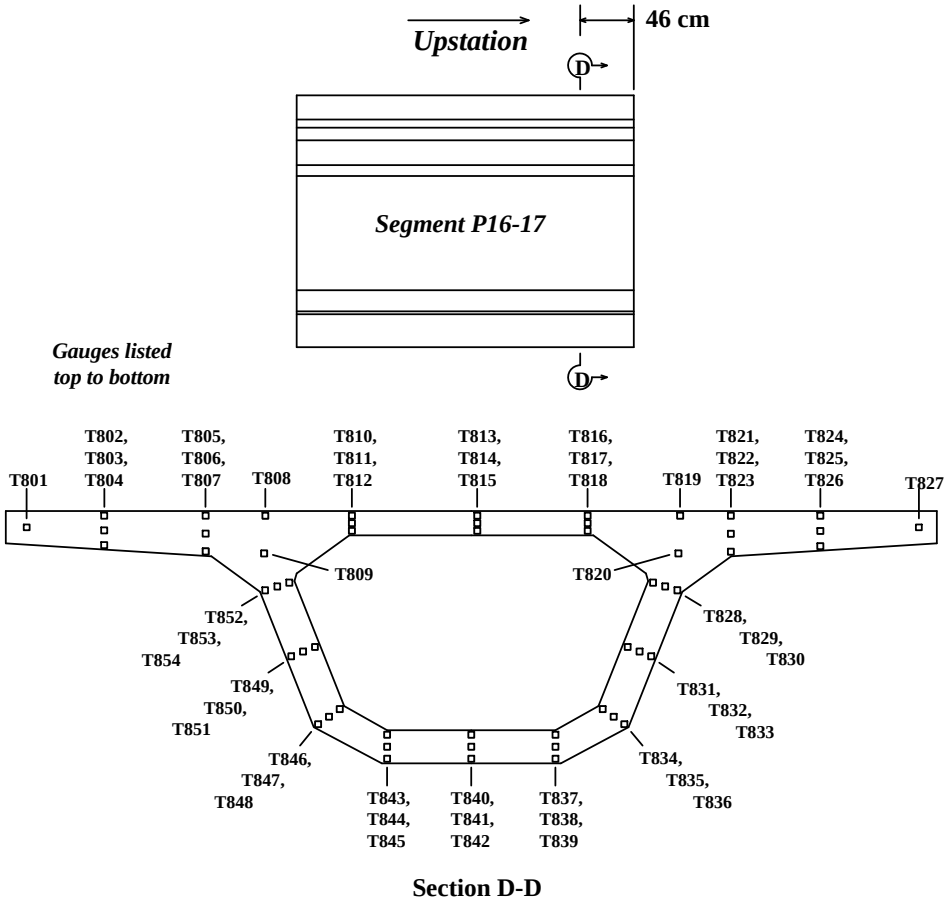

Figure 3.29 - Thermocouple gauges in segment P16-17

3.6.5 Slope and Twist of the Ramp

Tiltmeter plates were cemented at intervals along the centerline of the bridge deck on each of the expanding cantilever arms off of pier P16 as construction occurred. After completion of the bridge structure, the tiltplates were removed and reinstalled inside the bridge for a live load test of the structure. Figures 3.30 and 3.31 show the locations of the tiltmeter plates for each of

these phases of measurement. Figure 3.32 shows a picture of a typical ceramic tiltplate cemented to the inside floor of the bridge.

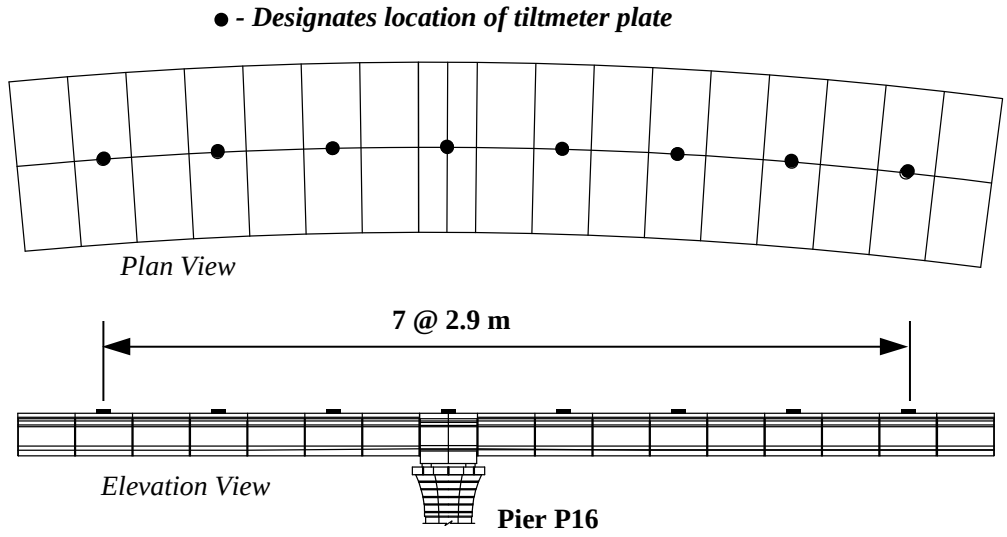

Figure 3.30 - Locations of tiltmeter plates during the Ramp P cantilever construction

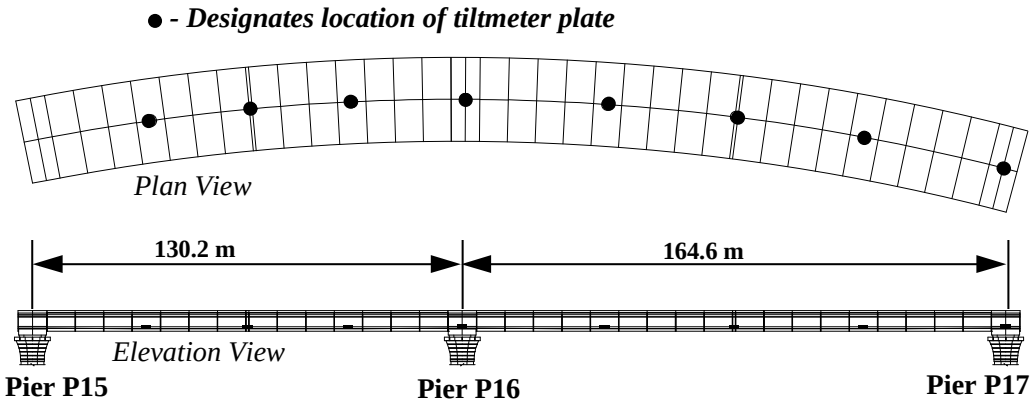

Figure 3.31 - Locations of tiltmeter plates during the Ramp P live load test

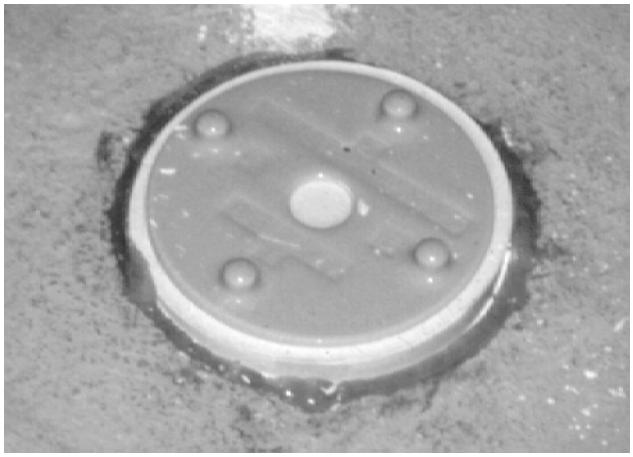

Figure 3.32 - Picture of a tiltmeter plate installed on the concrete surface

3.7 MATERIAL TESTS AND PROPERTIES

Material properties for the concrete were determined from specimens taken at the time of precasting. Precasting of a segment required three truck loads of concrete (Section 4.2.1 of Chapter 4 discusses the precasting procedure). Three specimens of concrete from the second truck load were taken when each instrumented segment was cast. These specimens consisted of 15.2 cm x 15.2 cm x 53.3 cm (6” x 6” x 21”) plain concrete prisms. After the prisms had hardened, pairs of Demec points were installed on each of the four long-axis faces of the prism. Figure 3.33 shows the details of a typical prism. These specimens were used to determine modulus of elasticity and coefficient of thermal expansion values for the concrete.

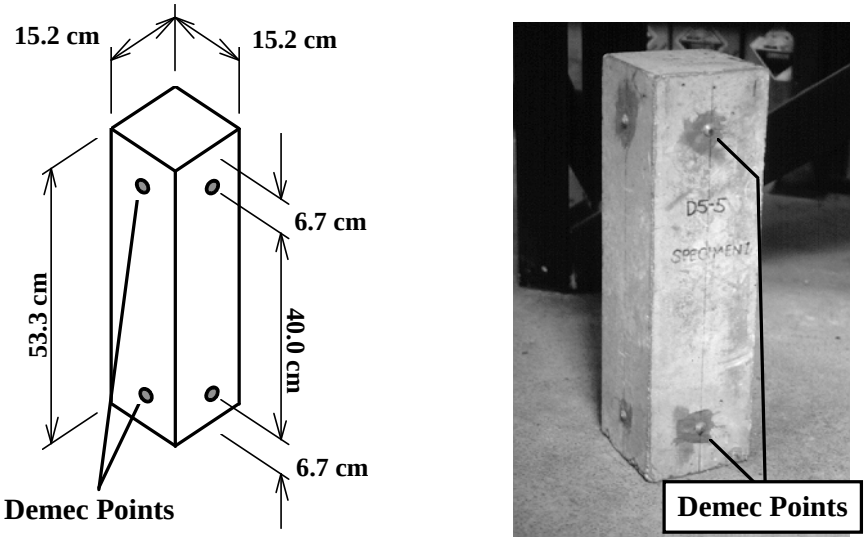

Figure 3.33 - Typical concrete prism used for material tests

3.7.1 Modulus of Elasticity

The modulus of elasticity was determined twice for the specimens: once during September of 1996 and a second time during June of 1997. The specimens were placed in a hydraulic load frame and axially loaded to 22,240 kN (5000 kips) in 4,448 kN (1000 kip) intervals. At each load interval, Demec readings were taken on each face of the specimen. The modulus of elasticity was then determined from the average strain across the four faces of the prism. Table 3.1 gives the results from both modulus of elasticity tests for the three instrumented segments in Ramp P. The average values that are given represent the averages from the three specimens for each segment.

Test Date	P16-2 (Cast 5/24/96)	P16-10 (Cast 6/4/96)	P16-17 (Cast 6/10/96)
9/24/96	43800 MPa (6350 ksi)	40900 MPa (5940 ksi)	41000 MPa (5950 ksi)
6/17/97	41900 MPa (6080 ksi)	37700 MPa (5470 ksi)	38400 MPa (5570 ksi)

Table 3.1 - Modulus of elasticity values for selected Ramp P segments

Table 3.1 shows that the modulus of elasticity decreased with time for all of the segments. This is most likely due to hydration losses within the specimens. This behavior may not be typical of the concrete in the actual Ramp P structure. Curing conditions for the specimens and the concrete in the segments were not the same. The webs and the flanges of the segments were thicker than the width of the specimens. Thus, the concrete in the segments was more confined and better protected from hydration losses than the concrete in the specimens. Also, because more mass of concrete was present in the segments, the curing temperatures that occurred in the segments were probably higher than those in the specimens. For these reasons, it was felt that the measured moduli were probably lower than the actual moduli of the segments. The first set of measured moduli were chosen for conversion of the measured strains into stresses and for material properties in calculation models.

3.7.2 Coefficient of Thermal Expansion

Coefficient of thermal expansion tests were performed on single specimens for segments P16-2, P16-10, and P16-17. These testes were performed in July of 1997. The specimens were placed in a refrigerated climate at 5 ^{o}C (41 ^{o}F) for two nights until they reached a uniform temperature throughout their volume. Demec readings were taken immediately after removal of the specimens from the cold. The specimens were then placed in a warm environment at 33 ^{o}C (92 ^{o}F) for two nights until they again reached a uniform temperature throughout their volume. Demec readings were taken at the end of this period. The coefficient of thermal expansion was calculated as the change in the strain of the specimens divided by the change in temperature. Table 3.2 summarizes the results for the three specimens.

	P16-2	**P16-10**	**P16-17**	**Average**
Coefficient of Thermal Expansion, α	$9.0(10^{-6})$ /^{o}C	$9.7(10^{-6})$ /^{o}C	$9.4(10^{-6})$ /^{o}C	**$9.4(10^{-6})$ /^{o}C**

Table 3.2 - Coefficient of thermal expansion values for selected Ramp P segments

3.8 INTERPRETATION OF THE ELECTRONIC OUTPUT

After the instrumentation was in place inside the finished Ramp P structure, the first task of the data analysis from the electronic gauges was to examine the output for broken or debonded gauges. Broken gauges typically have a bad connection somewhere along their circuit and provide no output. Debonded gauges typically give erratic output which is apparent when output from all of the gauges is plotted over time. Figure 3.34 shows the output from the concrete gauges in segment P16-10 plotted over a period of three days.

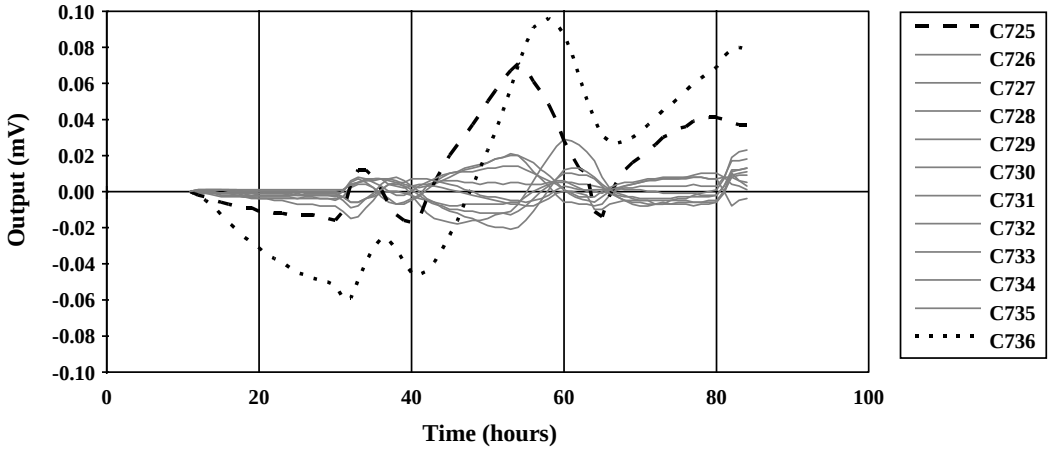

Figure 3.34 - Sample of output from some concrete strain gauges in P16-10

The plot in Figure 3.34 makes it apparent that gauges C725 and C736 exhibit odd behavior. Thus, those gauges were excluded from the data base. Table 3.3 lists the gauges that were excluded from the data base and the diagnosed problems for them. Eighteen concrete gauges were excluded out of a total of 144 giving a success rate of 88%. The success rate for the external tendon steel gauges was much lower. Fourteen out of 36 gauges were excluded from the measured results (a success rate of only 61%). Installation of the external tendon gauges took place under less than ideal conditions within the box girder, and the stressing process was very hard on the gauges, so it is not surprising that so many of these gauges had to be discarded.

Gauge	Problem
C605	Debonded or Bent
C608	Debonded or Bent
C618	Broken Leads
C619	Broken Leads
C621	Broken Leads
C641	Debonded or Bent
C648	Broken Leads
C706	Broken Leads
C718	Debonded or Bent
C725	Debonded or Bent
C736	Debonded or Bent
C737	Broken Leads
C747	Broken Leads
C802	Debonded or Bent
C824	Broken Leads
C828	Debonded or Bent
C831	Loose Leadwire
C832	Debonded or Bent
T1La (Downstation)	Debonded
T2La (Downstation)	Debonded
T2Lc (Downstation)	Debonded
T2Rb (Downstation)	Debonded
T1La (Upstation)	Debonded
T1Lb (Upstation)	Debonded
T1Lc (Upstation)	Debonded
T1Rb (Upstation)	Debonded
T2La (Upstation)	Broken Leads
T2Lb (Upstation)	Debonded
T2Lc (Upstation)	Debonded
T3Lc (Upstation)	Debonded
T3Ra (Upstation)	Debonded
T3Rb (Upstation)	Debonded

Table 3.3 - Summary of bad electronic strain gauges

Data from the gauges were recorded in units of millivolts (mV). These values were converted to strains by multiplication of a gauge factor number (1902 με/mV). Longitudinal stresses were then determined using measured values of the modulus of elasticity from the concrete prism specimens. Shear stresses involved more work. The shear stress could only be determined from a complete knowledge of the strain Mohr's circle at a given point on the concrete. For this reason, shear stresses could only be determined if all three concrete gauges were

undamaged within a strain gauge rosette. First, the center of the circle was determined from the strains given by the longitudinal and transverse gauges. Then the shear strain could be determined from the transverse strain gauge. The shear stress was then calculated by multiplication of the shear modulus. Figure 3.35 shows the orientation of the gauges within a concrete strain gauge rosette, the corresponding Mohr's circle and the equations used to calculate the shear stress.

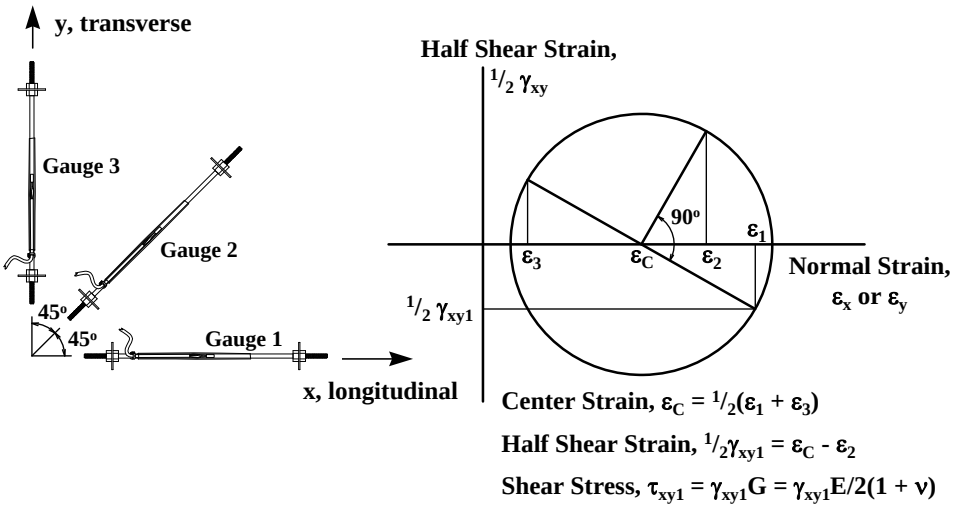

Figure 3.35 - Mohr's circle for concrete strain gauge rosette

3.9 COMMENTS ON THE DEMEC POINT DATA

While the general stress trends recorded by the Demec point data matched the trends of the electronic concrete gauges, the final stress plots through the section from the Demec points did not match the stresses from the electronic concrete gauges very well. Because most of the concrete gauges survived the casting process, the data from the Demec points were not necessary for the most part and are not presented in this report. Data from the Demec rosette wheels were particularly bad for determining the principal stresses. The area circumscribed by the Demec rosette wheels was simply too large to act as a suitable stress block in the concrete. The size of the concrete member would have to be much larger in relation to the Demec rosette wheel for the data to be of much use.

CHAPTER 4

SUPERSTRUCTURE CONSTRUCTION PROCESS

4.1 INTRODUCTION

Typically for segmental bridges, the largest stresses that the bridge must withstand occur during the construction process. The sequence of construction greatly affects the final distribution of dead load and prestressing moments and torques. Furthermore, the events of the construction process greatly effect the economy and durability of the final structure. This chapter will describe the construction sequence for the northbound I-35 to northbound U.S. 183 flyover ramp, called Ramp P for short. The precasting and erection processes for the superstructure will be outlined in detail, and the various problems that were encountered during these processes will be discussed.

4.2 PRECASTING OPERATIONS

The precasting yard for the U.S. 183 elevated bridge was located in south Austin about 40 kilometers (24 miles) from the construction site. All of the precast components of the project, except for precast straddle bents, were precast at the yard and stored there until the time of erection. At the peak of precasting, eleven beds were used in the production of superstructure segments. Typical production rate for the beds was one segment per day. In addition to the beds used to precast superstructure segments, one bed precast segments for thirteen segmental piers. Twelve of these piers constituted the substructure for the Ramp P flyover. One of these segmental piers was instrumented and studied by the U.S. 183 research team. The precasting and construction procedures for the segmental piers are discussed in detail by Bonzon [6].

The Ramp P superstructure segments were precast in three beds. One bed precast all of the typical segments for the ramp, another precast the two end anchorage segments of the five-span continuous unit, and a special bed was constructed to precast the interior anchorage segments so that they could be match-cast on both faces. Figure 4.1 shows the completed superstructure of the bridge with the different components of the structure labeled. Precasting of the interior

anchorage segments did not occur until late in the precasting yard's life. Precasting of these segments was delayed until erection of the Ramp P substructure was completed so that the final alignment of the ramp piers could be determined and accounted for in the geometry of these segments.

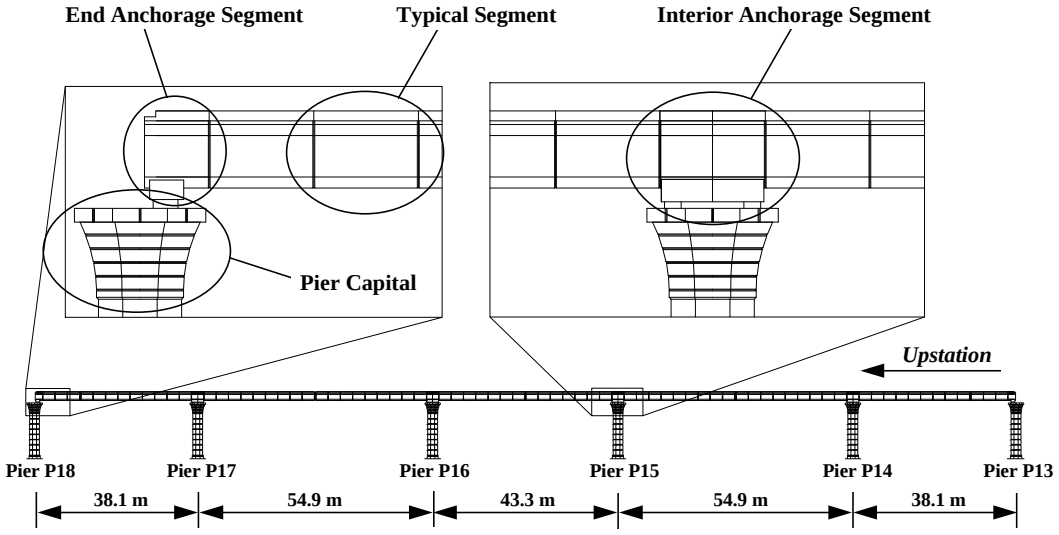

Figure 4.1 - Various components of the ramp

4.2.1 Precasting of the Typical Segments

The segments of the Ramp P superstructure were cast in a short line precasting bed. Figure 4.2 shows the set-up for the bed and the basic precasting steps. The fabrication of a segment occurred in two stages: the assembly of the rebar cage and the placement of the concrete. Each morning at the start of the work day, about 5:00 am, the iron workers who tied together the rebar cages would begin to assemble a new rebar cage (Figure 4.3). They would spend most of the day fabricating a cage which would be used on the following day in the casting of a new segment. Meanwhile, the precasting inspectors broke cylinders for all of the previous day's segments. If the concrete had reached the necessary strength of 27.6 MPa (4000 psi), then the forms would be pulled off and transverse pretensioning in the top flange of the segment was released. A final survey was performed to determine the as-cast alignment of the fresh segment. The previous segment that had been used for the match-cast face (segment A in Figure 4.2) was pulled away

and moved to a finishing rack where surface flaws such as broken shear keys were repaired. Thereafter, this segment would be moved to the storage area. The forms were pulled away from the newest segment (segment B in Figure 4.2), and it was moved forward to become the match-cast face for the next segment that would be cast in the bed (segment C in Figure 4.2). A bond breaker was then applied to the face of the new match-cast segment.

The forms were quickly cleaned and sprayed with form oil, and then the new cage was lifted and placed inside the forms (Figure 4.4). The forms came in two parts: an outer shell and an inner core (Figure 4.5). After dropping the cage in the form, post-tensioning ducts and anchorages were tied into the top flange (Figure 4.6) and then additional steel was added to the webs. The inner core form was then inserted. Next, transverse pretensioning tendons in the top flange were placed and stressed (Figure 4.7). The cage was finished by placing the last layer of steel in the top flange, a simple rectangular grid of bars that was tied on the ground and then lifted into place by crane. Before casting the concrete, a surveyor checked the alignment of the match-cast segment (Figure 4.8), and the rebar was checked by an inspector who would oversee the casting of the segment. Placement of the concrete usually began by 5:00 PM.

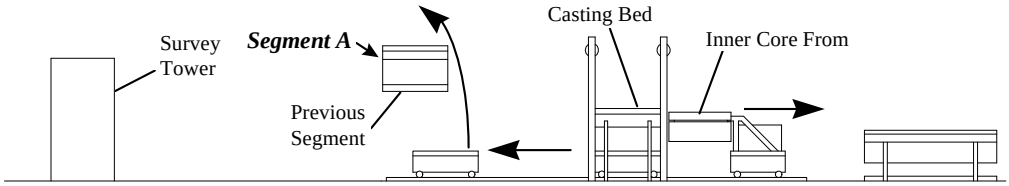

1. The previous match-cast segment is pulled away and moved to a finishing rack. The core form is removed.

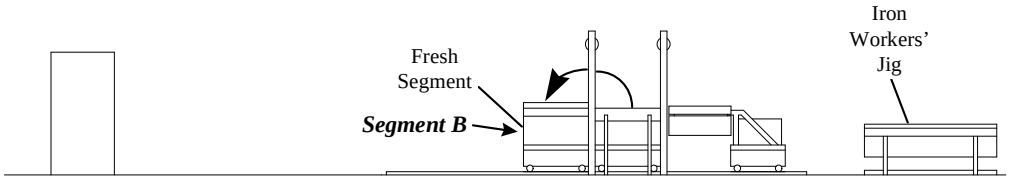

2. The fresh segment is moved forward to be utilized as a match-cast face.

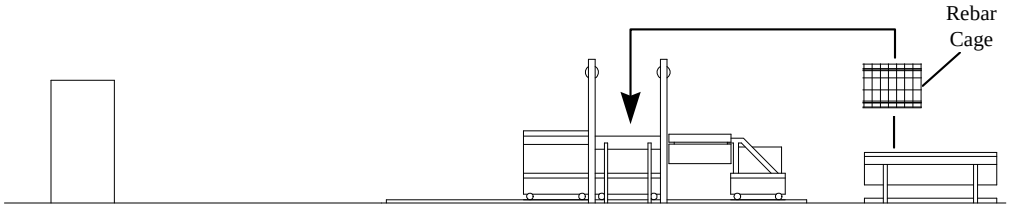

3. A new rebar cage is moved from the iron workers' jig and placed inside the casting bed forms.

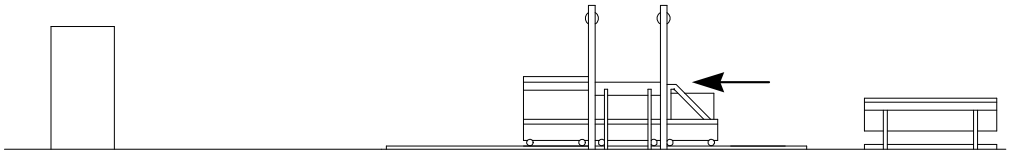

4. Additional work is done on the cage. The core form is inserted. Prestressing in the top flange is stressed.

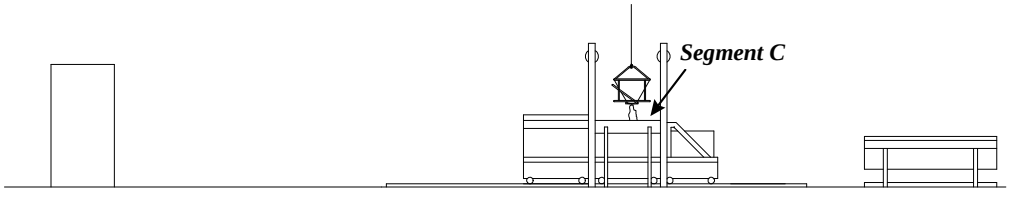

5. A final survey of the alignment is performed. Concrete is placed.

Figure 4.2 - Steps in the precasting process

Figure 4.3 - Iron workers tie together a rebar cage

Figure 4.4 - Rebar cage is placed in the forms

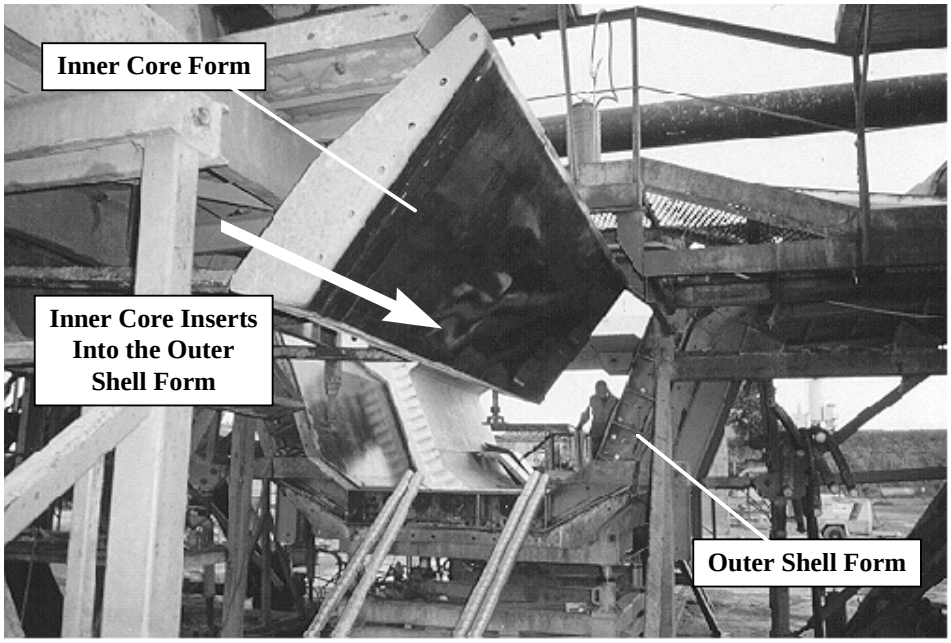

Figure 4.5 - Components of the precasting forms

Figure 4.6 - Workers install post-tensioning tendon ducts

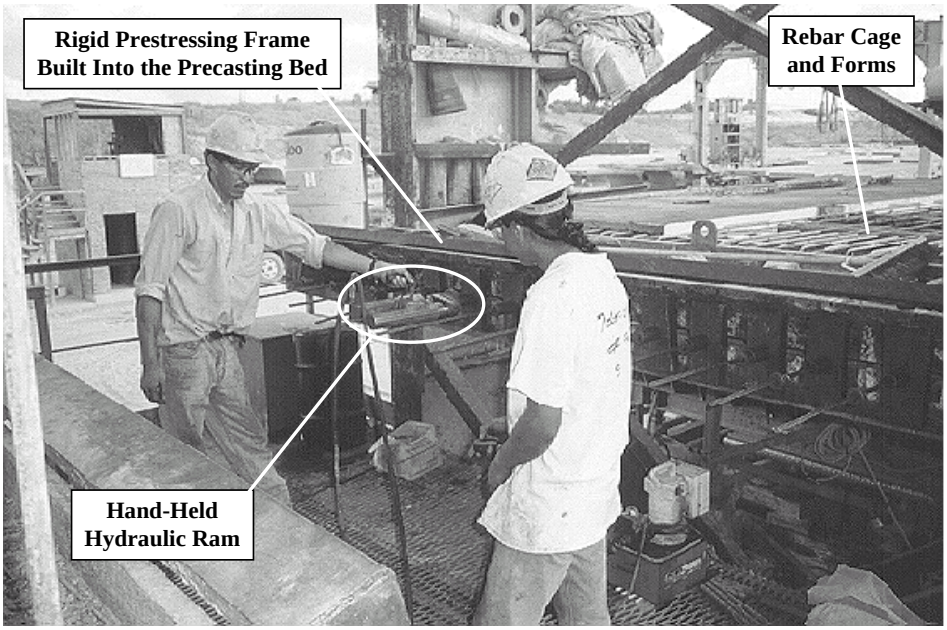

Figure 4.7 - Transverse top flange tendons are stressed

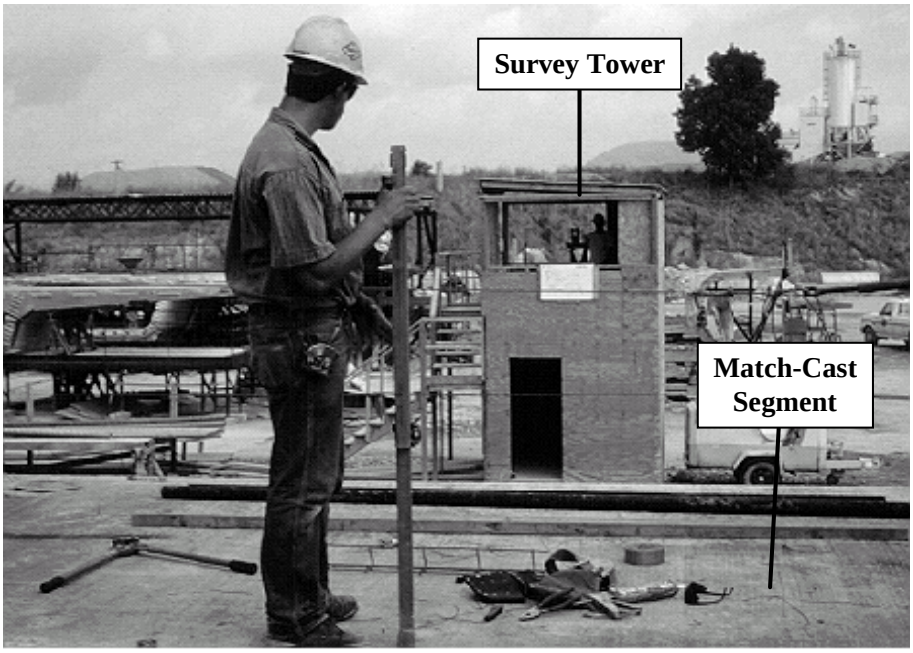

Figure 4.8 - The geometry of the match-cast segment is surveyed

The concrete batch plant was located at the precasting yard. Three truck loads of concrete were necessary for the casting of one Ramp P superstructure segment (about 12 cubic meters of concrete or 16 cubic yards in customary units). Concrete was first placed in the webs of the segment where congestion of steel usually made proper placement difficult. In addition to the congestion of steel, the first load of concrete was usually mixed with less slump than the next two loads. This was to keep the concrete placed in the webs from running out into the bottom flange. Proper vibration of the concrete was essential to eliminate voids. Concrete was vibrated through the webs until it just began to flow into the lower flange of the segment. Additional concrete was then dropped through a hole in the top of the core form directly to the lower flange until it was filled. The remaining concrete was placed in the top flange. The casting of the concrete generally took about an hour to complete. Figure 4.9 shows the basic steps in the placement of the concrete. Figures 4.10 and 4.11 show some pictures of concrete placement for a typical segment. Afterwards, the deck surface was finished and brushed, a curing compound was sprayed on the concrete, and the exposed surfaces were covered to keep the concrete moist. The concrete would usually reach the necessary strength for prestress transfer within 12 hours. This allowed the new segment to be released from the bed and the casting cycle could begin again the next day.

Precasting operations for end anchorage segments followed the same procedures as the typical segments, except that different formwork was used.

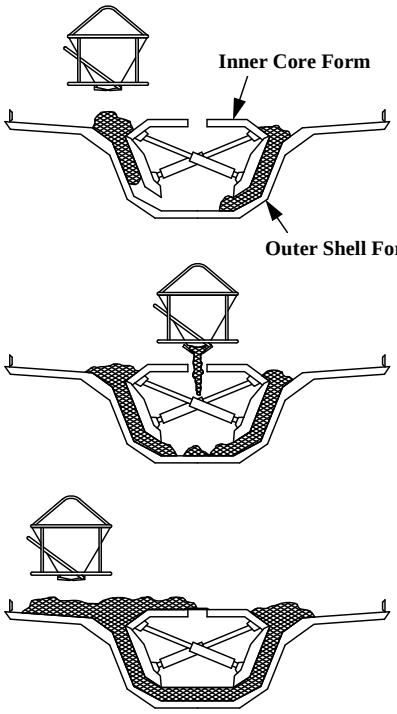

1. First concrete is placed in the webs.

2. Concrete is then dropped through a hole in the core form to fill in the bottom flange.

3. A lid is placed over the hole in the core form, and then concrete is placed in the top flange.

Figure 4.9 - Procedure for placement of the concrete

Figure 4.10 - A crane lifts a concrete bucket over the precasting bed

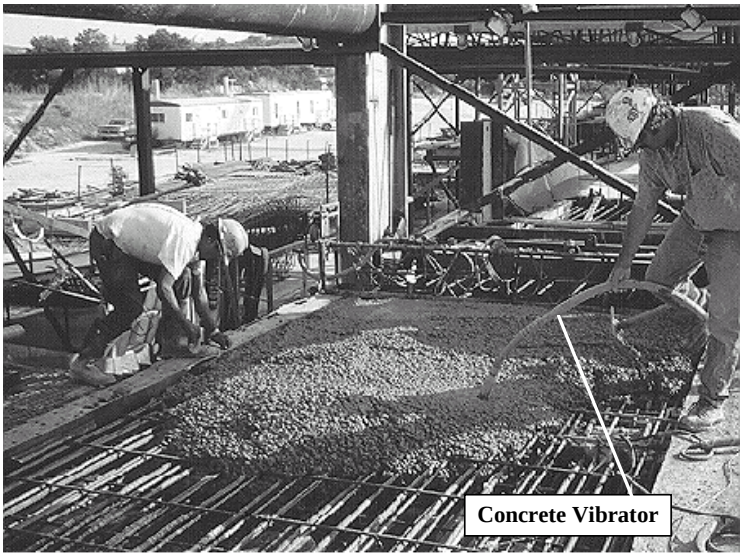

Figure 4.11 - Concrete is vibrated into the webs

4.2.2 Precasting of the Interior Anchorage Segments

Precasting of the interior anchorage segments involved a special bed because of the necessity to match-cast against both faces at the same time. Precasting of an interior anchorage segment began by placing the two typical match-cast segments on either end of the bed. Figure 4.12 shows the layout of the bed. The anchorage segment was cast in two half-segment pieces because of weight lifting restraints imposed by the available cranes on the project. An intermediate form was placed in the center of the bed where the joint would be between the two halves of the segment. The rebar cage was tied together inside the form for one of the two halves, a process which required several days (Figure 4.13 shows the cage at a nearly completed stage). Next, the core form was placed. Final geometry was checked and inspection was performed on the cage before the concrete was placed for the first half segment. After curing, the intermediate form was removed, and a bond breaker was placed on the face of the new half segment. The cage was assembled for the second half. The geometry was surveyed and the cage inspected before casting of the second half began. After curing, the segments were separated from each other and moved to storage. The forms were cleaned and the process began all over again.

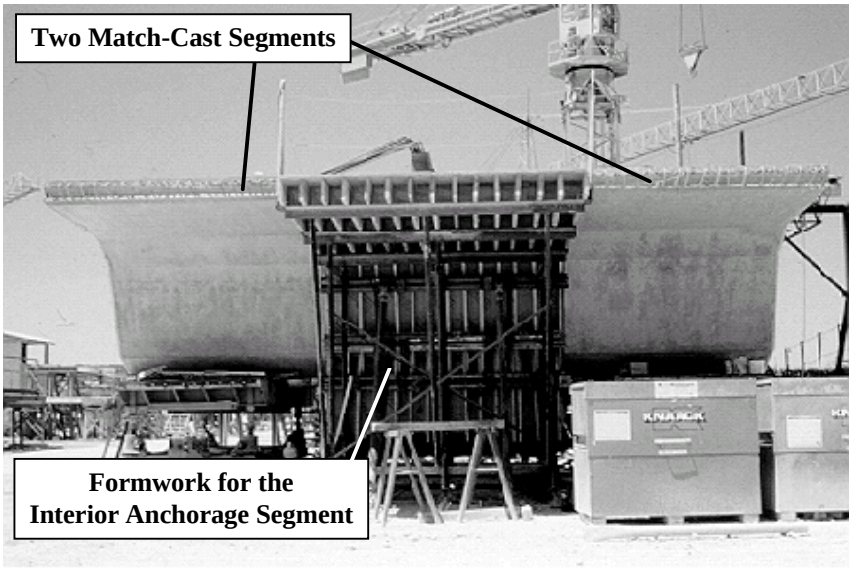

Figure 4.12 - The layout of the interior anchorage segment bed

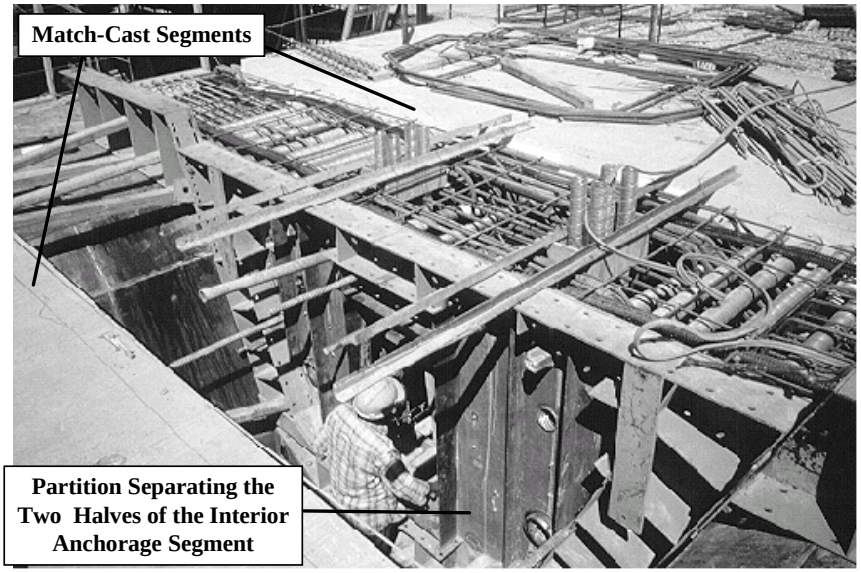

Figure 4.13 - Prior to casting one segment half

Precasting of the four interior anchorage segments did not begin until after all of the typical Ramp P segments had been precast. These four segments had, by far, the slowest production rate for any of the segments produced at the precasting yard. The reasons for the slow

production rate of these segments are simple. The segments were cast in two halves so that they could be erected one half at a time, reducing the weight, and allowing for a smaller crane at the construction site. The bed had to allow for match-cast segments on both ends which made the layout of the bed complicated and unlike the other casting operations that had occurred at the yard. The steel layout for these segments was complex because of the high number of anchorage zones present in these segments. The rebar cages for these segments were assembled directly in the forms because of the complex steel layouts. All of these factors prevented a smooth operational cycle such as had been established with the other beds. These precasting operations also occurred in the final stages of the precasting yard's life as the yard was being shut down and dismantled. The experienced workers had already moved on to other construction projects. Only a skeletal, inexperienced crew remained to work the interior anchorage segment bed. Because only four of these segments were produced the crew assigned to the bed never had time to develop a good experience base for their production. Also, the steel layout was not the same for every interior anchorage segment; unique reinforcing details were required in each anchorage segment to meet the number and placement of the saddles and anchorages necessitated by geometry of the external tendons. The bed which was set up for the production of these segments was rather makeshift because it only had to be used four times, and it was not set up with the emphasis on rapid turn-around that had gone into the design of the other beds in the yard.

In the contractor's favor, the precasting yard had consistently maintained a heavy lead in their production of segments over the ability of the crews at the construction site to erect the segments. Therefore, there had been no time pressure on the production of the interior anchorage segments for Ramp P. Their fabrication was slow, but in no way impaired the pace of the entire construction project. The complications that occurred were most likely anticipated by the contractor and did not raise a great amount of concern because they did not interfere with the critical paths in the construction plan.

4.2.3 Storage of the Segments

Segments were stored at the precasting yard until the night they were to be erected. They were given no protection from the external climate during the storage time and no special curing provisions were provided for the concrete after the forms were removed. Additional finishing work was often performed in the storage area. Just before the segments were to be transported to

the erection site, they were power sprayed to remove dust and other dirt which accumulated on the surfaces of the segments. Figure 4.14 shows the storage area.

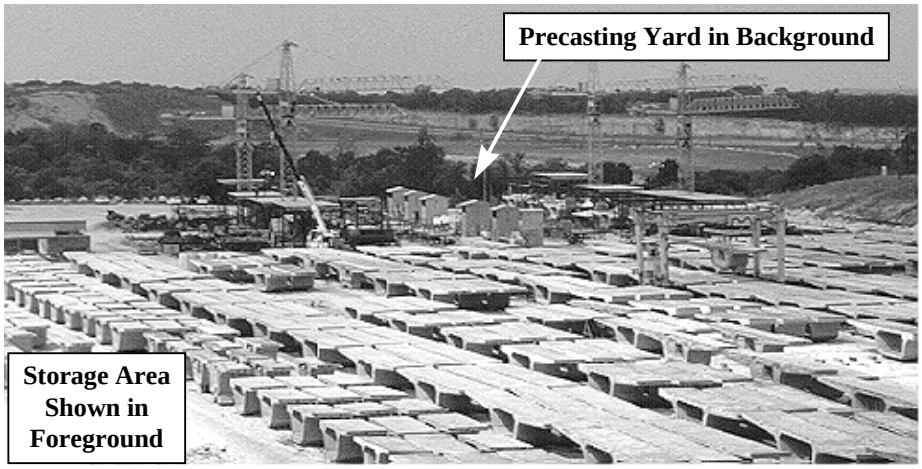

Figure 4.14 - View of the storage area

Precasting of the Ramp P substructure occurred in the summer of 1995 and erection was in the spring of 1996. Precasting of the superstructure occurred in the summer of 1996 and erection was in the fall of 1996. Ramp P opened to traffic in March of 1997.

4.3 SUPERSTRUCTURE ERECTION

The central five spans of the superstructure of Ramp P were erected in balanced cantilever and then made continuous. Additional spans upstation and downstation from this five span unit were constructed span-by-span with a pair of traveling erection trusses. Most of the erection occurred at night. This section deals only with the construction of the five span continuous unit which was constructed in balanced cantilever. The construction process has been broken into seven phases for discussion in this section. These phases are depicted in Figure 4.15. Problems that occurred during the construction will be discussed in Section 4.4.

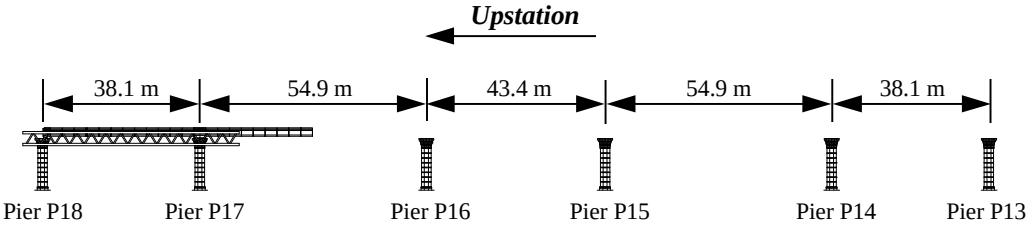

Phase I: Construction of the P17 cantilever unit and the completion of the upstation endspan.

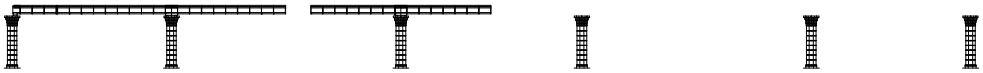

Phase II: Construction of the P16 cantilever unit.

Phase III: Construction of the P14 cantilever unit. Construction begins on the P15 unit.

Phase IV: Completion of the downstation endspan and the P15 cantilever unit.

Phase V: The central span is completed. The free cantilever wings of the P15 and P16 units are extended by one segment.

Phase VI: Final bearing adjustaments are made on P17. The upstation 54.9 m span is completed. The same process is repeated on the downstation half of the bridge.

Phase VII: The last external tendons are placed and stressed. The barriers are cast and a wearing surface is applied to the deck.

Figure 4.15 - Construction Phases for Ramp P

4.3.1 Phase I

On the upstation side of the five span unit at pier P17, the trusses used to construct the span-by-span portion of the bridge were moved forward and used to help construct the first 38.1 m (125') span of the balanced cantilever unit. The two halves of the interior anchorage segment for pier P17 (segments P17-1a and P17-1b) were lifted onto the erection trusses by crane, and then brought together to make a whole segment. The interior anchorage segment was aligned and then dropped onto temporary bearings and tied down to the pier capital with Dywidag post-tensioning bars. Figure 4.16 shows the interior anchorage segment for P17 after this sequence of events.

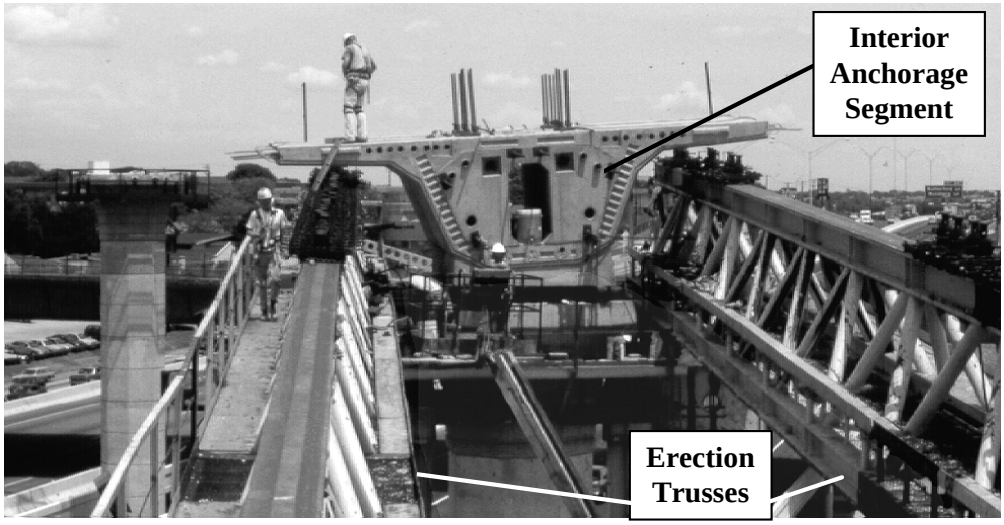

Figure 4.16 - Interior anchorage segment for P17 after erection

With the interior anchorage segment in place, construction of the cantilever began. The steps involved for erecting the segments are described in detail in the section dealing with Phase II of the construction. Figure 4.17 shows the P17 cantilever during construction. After the cantilever was finished, the 38.1 m (125') span was completed by adding the end anchorage segment and three typical segments onto the erection trusses. These segments were temporarily stressed together with Dywidag post-tensioning bars. Then a cast-in-place joint was placed to connect these segments to the cantilever, thus completing the span. After the joint had hardened, post-tensioned tendons were stress through the bottom flange of the girder to provide full continuity of

the span. Figure 4.18 shows the completed span. Figure 4.19 shows the locations of post-tensioning tendons for the construction of the first span.

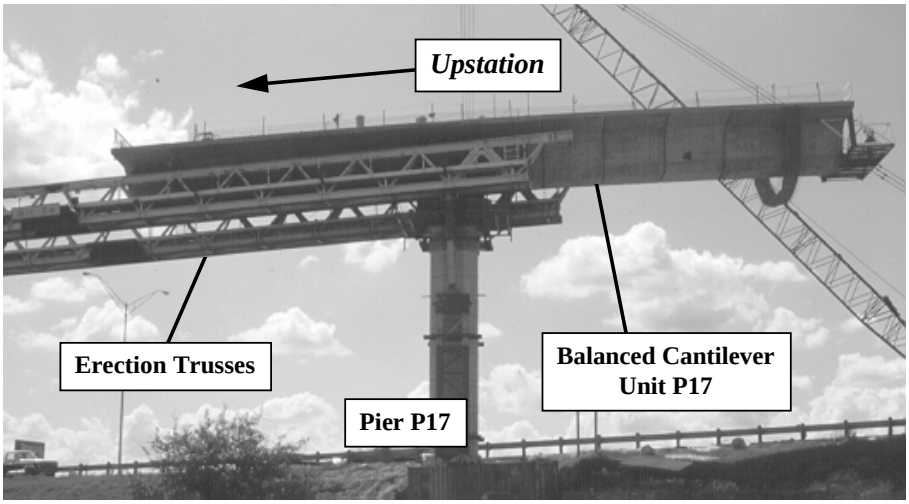

Figure 4.17 - P17 cantilever unit during construction

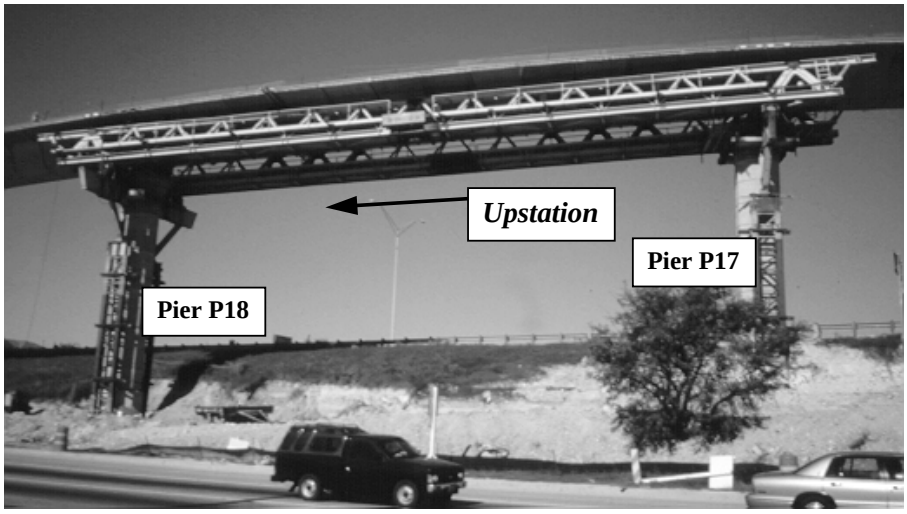

Figure 4.18 - Completed endspan between piers P17 and P18

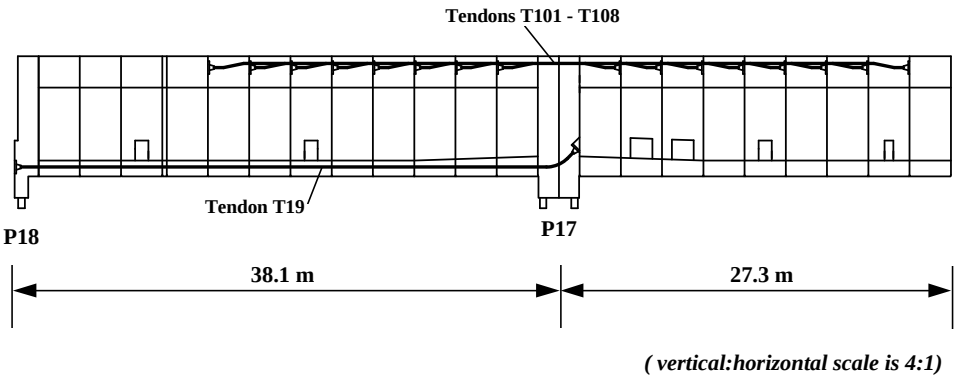

Figure 4.19 - Post-tensioning layout at the end of Phase I

4.3.2 Phase II

Because no erection trusses were available at pier P16, the erection procedure for the interior anchorage segment was complex. Figures 4.20a and 4.20b show the steps involved in the erection of the interior anchorage segment. In step one, one half of the interior anchorage segment was lifted by crane and placed onto shims on one side of the pier capital. In step two, steel roller bearings were positioned on the free half of the capital, and the second half of the interior anchorage segment was placed on them. The second half of the anchorage segment was pushed up to the first half for a complete dry fitting of the joint. This was necessary so that the alignment of the two halves could be checked. If the two halves of the segment were pulled together with epoxy on the joint faces and it was then discovered that the two halves could not be brought together because they were slightly out of line with one another, then the epoxy would harden before the two halves could be pulled apart, re-aligned and brought back together. The hardened epoxy would compromise the match-cast fit of the joint.

After a successful dry fit of the joint (step three), the two halves were pulled apart. Permanent post-tensioning bars were placed through ducts in the diaphragm and epoxy was applied to both faces of the joint (step four). The two halves were then stressed together (step five). After the two halves of the interior anchorage segment had been joined, the whole segment was lifted with hydraulic rams so that reinforced grout bearings could be cast (step six). At this time permanent tie down bars were dropped through vertical ducts in the anchorage segment and coupled to threaded stubs projecting out of the top of the capital. These tie down bars consisted of

16 Dywidag 36 mm (1 $^{3}/_{8}$") diameter threaded bars. The alignment of the segment was surveyed and checked. When the grout bearings reached a strength of 37.9 MPa (5500 psi), the segment was dropped into place and stressed to the pier capital (step seven).

For the erection of the segments in cantilever, blisters for temporary post-tensioning bars (Dywidag 36 mm (1 $^{3}/_{8}$") diameter threaded bars) were located in the top and bottom of the typical segments. Anchorages for negative moment post-tensioning tendons or cantilever tendons were located in the top flange just over the webs. Figure 4.21 shows the cross-section of a typical segment and the locations of the blisters and anchorages required for the cantilevering process. Temporary post-tensioning bars were used to hold the segment in place and provide compression for the joint epoxy until the cantilever tendons could be placed and stressed through the top flange. For most of the cantilevering process the temporary post-tensioning bars were anchored in the blisters except for the first two segments erected on either side of the interior anchorage segment. The interior anchorage segment did not have blisters or ducts for the temporary post-tensioning bars because the saddles for the external tendons occupied the space where the bars would need to pass. Therefore, instead of stressing bars through the blisters, bars were inserted and stressed through some of the ducts for the as-yet-unused cantilever tendons. After these first segments were temporarily stressed to the interior anchorage segment, cantilever tendons were threaded and stressed across the top flange. With the first set of cantilever tendons stressed, the temporary post-tensioning bars were then removed from the cantilever ducts. A single bar stressed across the bottom flange was left to provide compression until the epoxy had time to cure (one night). Figure 4.22 shows the erection steps for the first two segments erected in cantilever. Figure 4.23 shows the interior anchorage segment for P16 before those steps. Figure 4.24 shows the P16 cantilever unit after those steps.

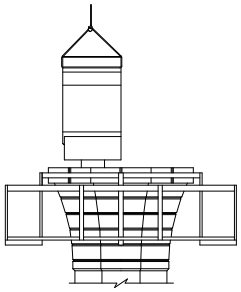

1. The first half of the interior anchorage segment is placed by crane on shims.

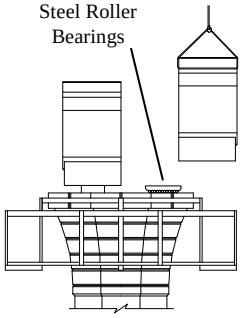

2. The second half of the anchorage segment is placed on steel roller bearings.

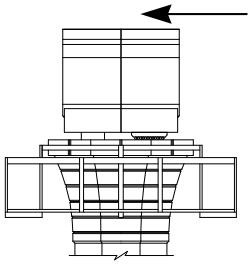

3. The second half of the interior anchorage segment is pushed up against the other half to dry fit the joint. If the two halves do not line up properly, they are adjusted.

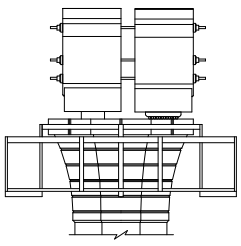

4. After a successful dry fit of the joint, the two halves are pulled apart. Permanent post-tensioning bars are threaded through ducts in the diaphragm and epoxy is applied to both faces of the joint.

Figure 4.20a - Steps in the erection of an interior anchorage segment

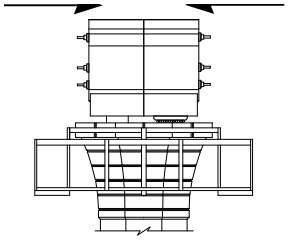

5. The two halves are stressed together.

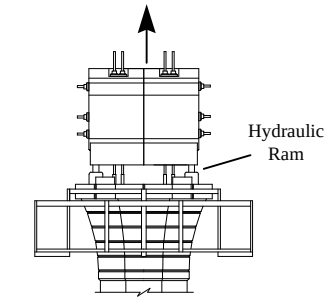

6. The whole segment is lifted with hydraulic rams. Post-tensioning bars are dropped through vertical ducts and coupled to stubs left sticking out of the top of the capital. Reinforced grout bearings are cast underneath the anchorage segment.

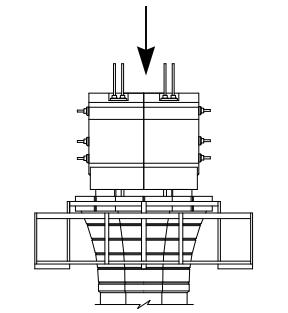

7. After the new grout bearings have reached strength, the vertical post-tensioning bars (tie-down bars) are stressed.

Figure 4.20b - Steps in the erection of an interior anchorage segment (continued)

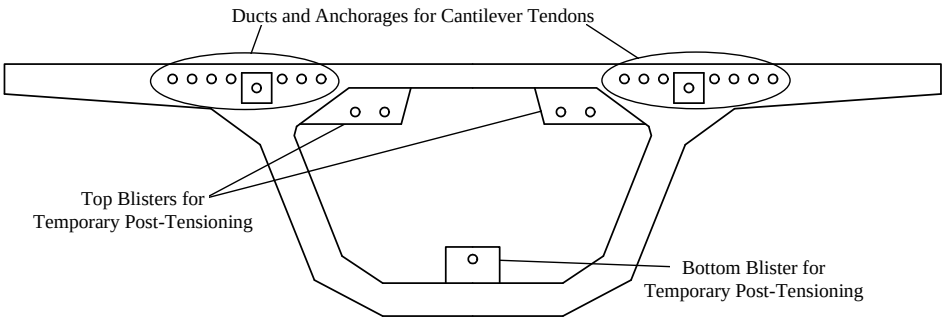

Figure 4.21 - Cross-section of segment showing locations of blisters

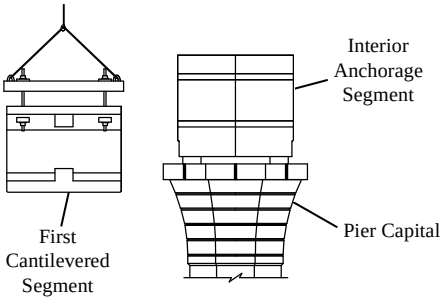

1. A new segment is brought into position by crane. The temporary post-tensioing bars are placed, but not stressed. Epoxy is applied to both faces of the joint only after all of the equipment for stressing is in place.

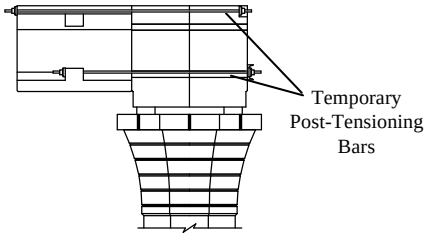

2. The segment is temporarily stressed to the interior anchorage segment with Dywidag post-tensioning bars. When stressing is complete, the segment is released from the crane.

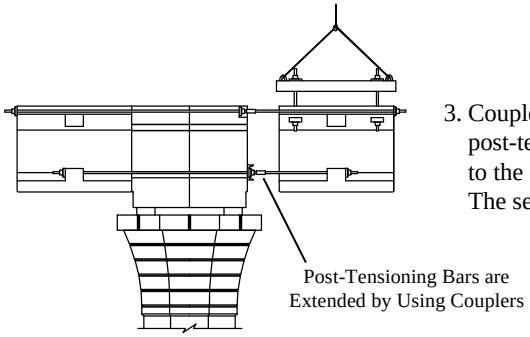

3. Couplers are added to the stub ends of the temporary post-tensioning bars, and the next segment is added to the other side of the interior anchorage segment. The segment is then released from the crane.

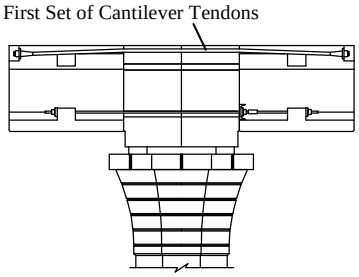

4. Two 9-strand tendons are threaded through the top flange ducts and stressed. Afterwards, the top post-tensioning bars are removed.

Figure 4.22 - Steps in the erection of the first two cantilevered segments

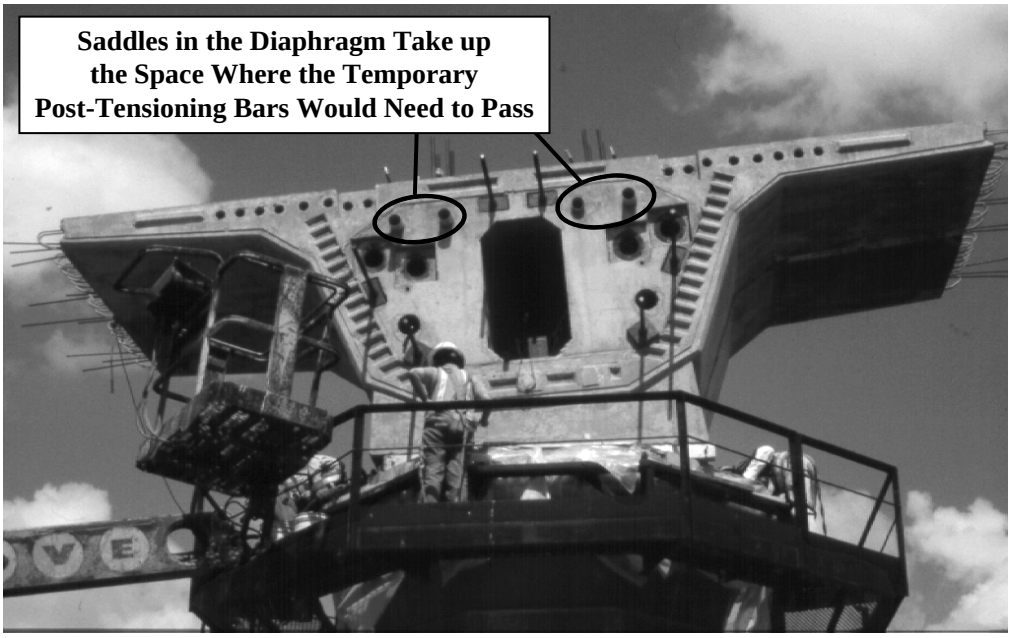

Figure 4.23 - The P16 interior anchorage segment after erection

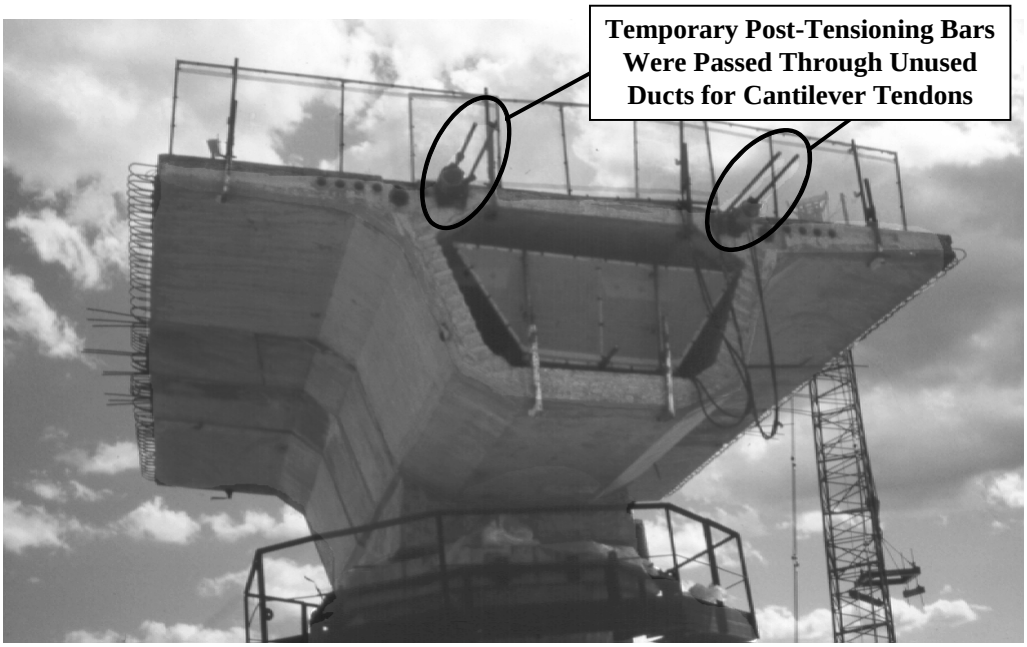

Figure 4.24 - P16 with two cantilevered segments

For all other segments that were erected in cantilever, blisters were used to anchor the temporary post-tensioning. The typical construction sequence for the addition of a new segment to the cantilever is illustrated in Figure 4.25. A segment was brought up to the end of the cantilever by crane. The temporary post-tensioning bars were put in place. After epoxy was applied, the bars were stressed and the segment was released from the crane. This process was repeated for a segment on the other cantilever wing, and then cantilever tendons were threaded through the top flange ducts and stressed. Afterwards, the top post-tensioning bars were detensioned. A new segment was brought into place by crane and the process was repeated. The bottom bars were left tensioned overnight until the joint epoxy had cured.

Seven segments were erected on each wing of the P16 cantilever unit. Six pairs of cantilever tendons were stressed (one pair for each of the first six cantilevered segments). The seventh segment in each cantilever wing was supported by the temporary post-tensioning bars until Phase V. Figure 4.26 shows the P16 cantilever unit during construction. Figure 4.27 shows the layout of the cantilever tendons for the P16 unit.

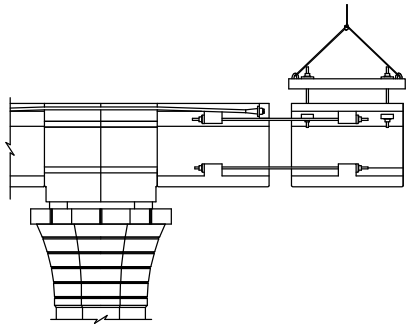

1. A new segment is brought into position by the crane. Temporary post-tensioning bars are threaded through the blisters. Epoxy is placed on both joint faces before stressing of the bars begins.

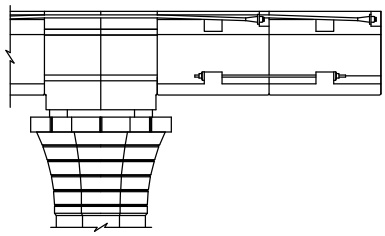

2. After the segment is secured with the post-tensioning bars, the cantilever tendons are pulled through the top flange ducts and stressed. The post-tensioning bars in the top blisters are detensioned, but the bottom bar is left to provide the minimum required compression for curing of the joint epoxy across the bottom flange.

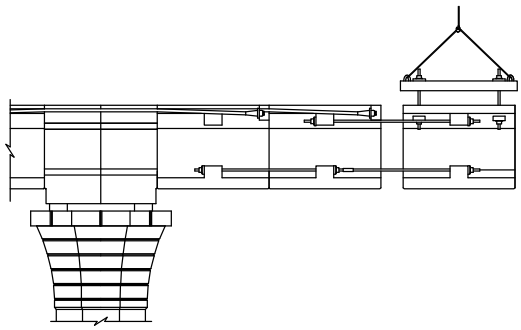

3. The next segment is brought into position. A coupler is added to the bottom bar so that it may be extended to the hanging segment. Otherwise, erection continues as described in steps 1. and 2.

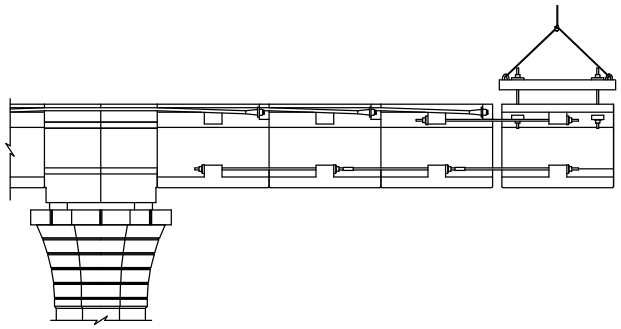

4. Temporary bars were left stressed across the bottom overnight to provide uniform compression while the joint epoxy cured.

Figure 4.25 - Steps in the erection of the cantilever

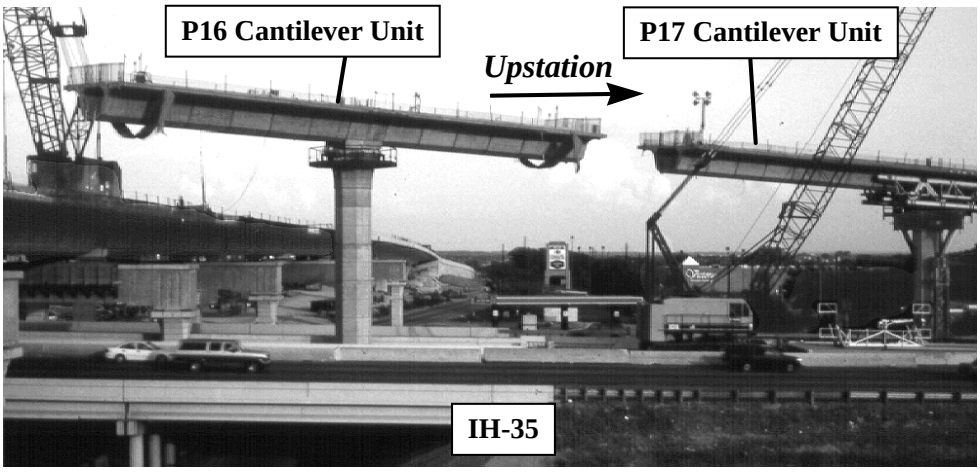

Figure 4.26 - The P16 cantilever unit during construction

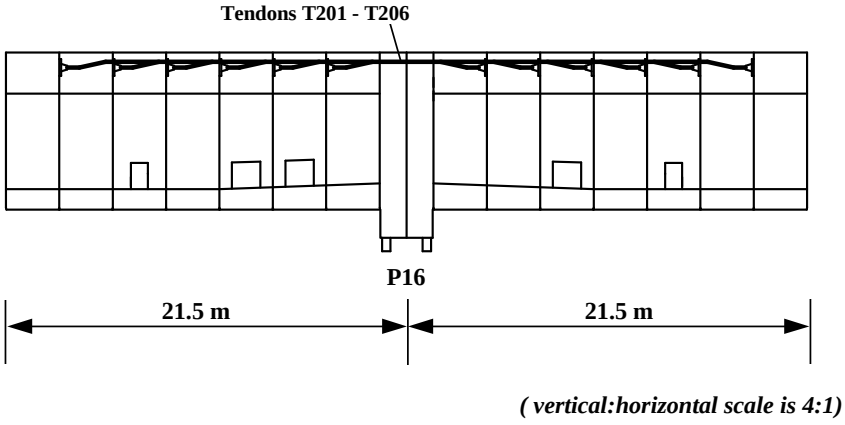

Figure 4.27 - Layout of cantilever tendons for the P16 cantilever

4.3.3 Phase III

At the same time as the construction of the Ramp P superstructure, construction of the U.S. 183 Northbound mainlane was underway. This necessitated that a certain amount of clearance be available underneath the Ramp P construction. For this reason, the contractor decided to place the interior anchorage segment and the first two cantilevered segments on pier P15 and then to move on to erection of the P14 cantilever unit before finishing the P15 unit. Thus, in Phase III, only a small part of the P15 cantilever unit was completed and all of the P14 cantilever unit

was constructed. Figure 4.28 shows the P15 and P14 cantilever unit under construction during this phase as well as the work which was proceeding on the northbound mainlane below. The steps for erection of the interior anchorage segments as well the cantilevering process for the typical segments followed the steps outlined in the discussion for Phase II. The post-tensioning layout for the P14 cantilever unit was identical to the layout for the P17 cantilever unit. The ramp's entire post-tensioning layout was symmetrical about the midspan between P16 and P15

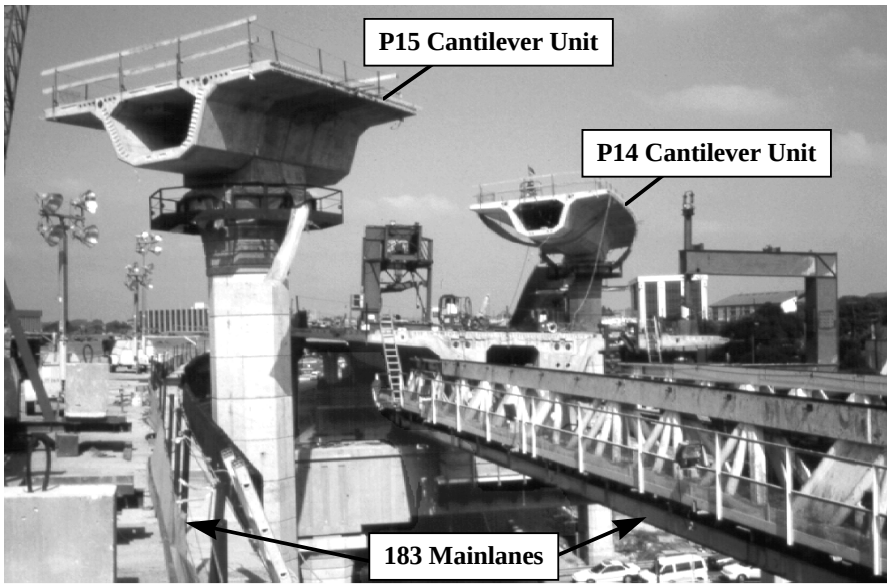

Figure 4.28 - P14 and P15 cantilever units during Phase III of construction

4.3.4 Phase IV

Falsework was erected next to pier P13 for the erection of the last four segments on the downstation 38.1 m (125') span. The segments were lifted into place on the falsework, a closure joint was cast between the end of the P14 cantilever and the end segments, and continuity tendons were stressed. The process was the same as for the upstation endspan in Phase I. The P15 cantilever unit was finished in this phase as well.

4.3.5 Phase V

With the two central cantilevers completed, a closure joint was cast-in-place between the P15 and P16 cantilever units. Figures 4.29 and 4.30 show the joint just before placement of the concrete.

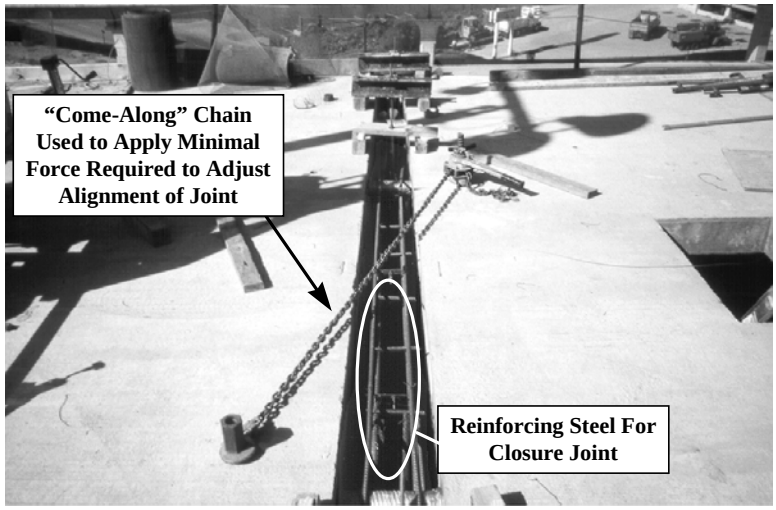

Figure 4.29 - View of the closure joint before casting

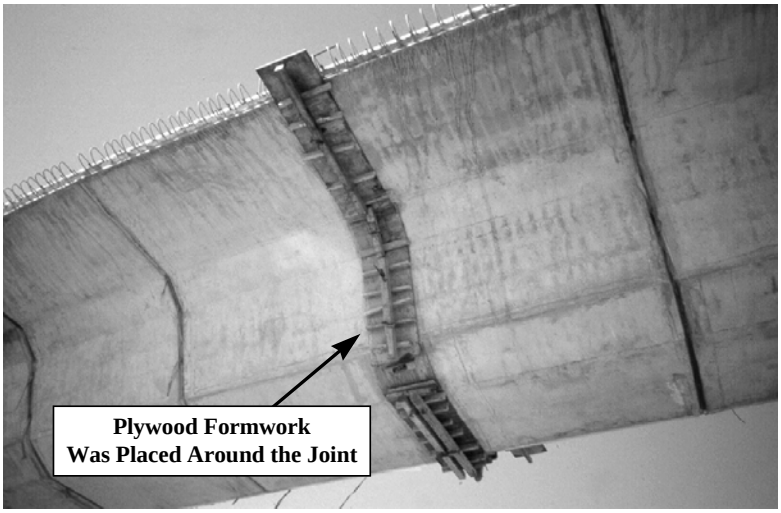

Figure 4.30 - View of the formwork used for the closure joint

After the closure joint had hardened, bottom flange continuity tendons were placed and stressed across the central 43.3 m (142') span (tendon T20) and cantilever tendons were stressed across both of the newly joined cantilever units (tendon T301). Next, segments were erected on each of the free cantilevers and another pair of cantilever tendons was stressed across the entire unit (tendon 302). Figure 4.31 shows the stressing of a continuity tendon. Figure 4.32 shows the arrangement of the tendons that were placed and stressed in Phase V.

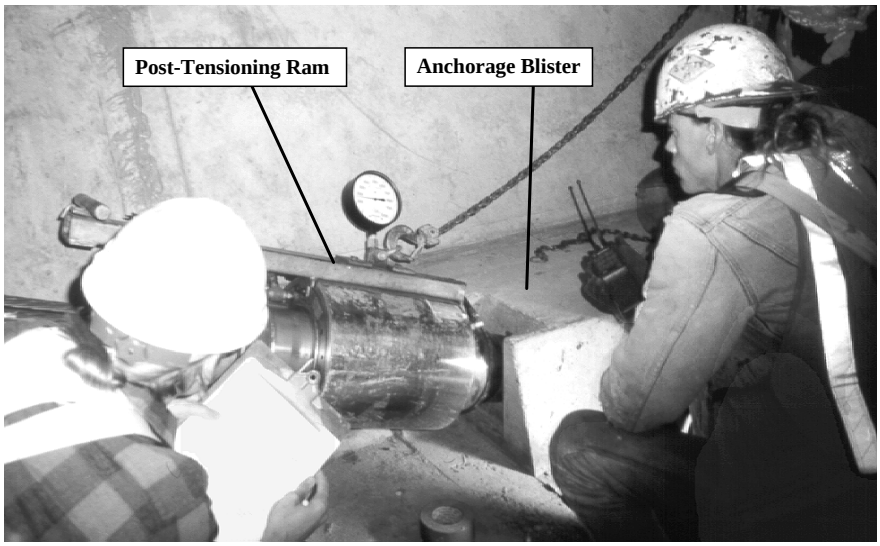

Figure 4.31 - Stressing of a continuity tendon

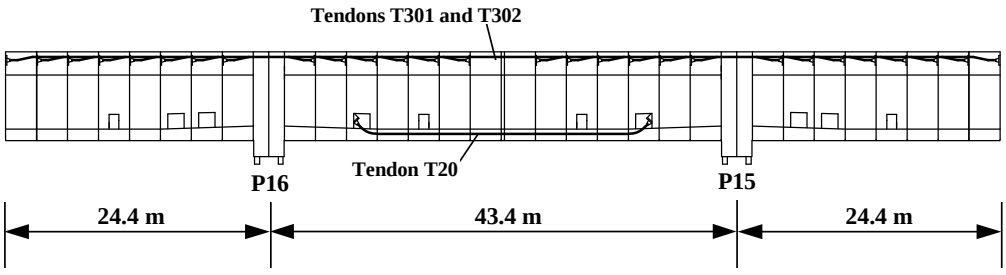

(vertical:horizontal scale is 4:1)

Figure 4.32 - Layout of post-tensioning tendons for the end of Phase V

4.3.6 Phase VI

Segment P16-17 was added to the end of the free cantilever remaining on the P16 unit. Permanent bearings were placed at P17. At the same time, the alignment of the ramp was adjusted so the cantilevers from P17 and P16 lined up well. A closure joint was cast between the P16 and P17 cantilever units. Continuity tendons were placed in the bottom flange of the span and stressed (tendons T21 and T22). External tendons running from the end anchorage segment at pier P18 to the interior anchorage segment at pier P16 were also placed and stressed (tendons T1 and T2). The same process was repeated for the downstation 54.9 m (180') span between piers P14 and P15. Figure 4.33 shows the layout of the post-tensioning tendons that were stressed in the upstation spans between P16 and P18. The downstation spans had the same geometry but were symmetric about the midline of the five span structure.

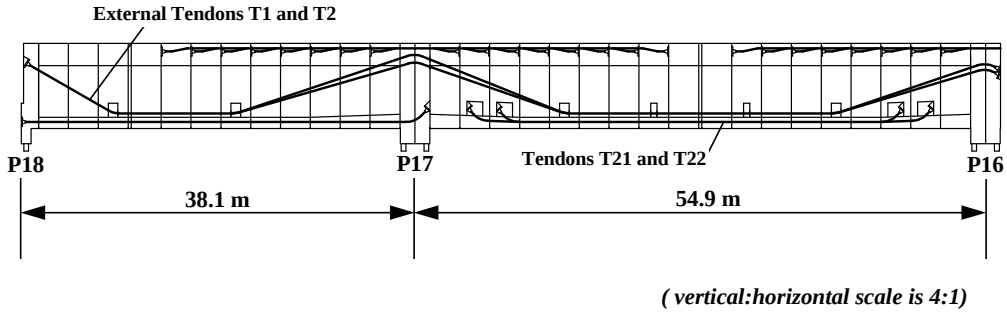

Figure 4.33 - Layout of the post-tensioning tendons stressed in Phase VI

4.3.7 Phase VII

With the erection of the superstructure segments complete, the final stage of the construction process was the placement and stressing of the remaining external tendons in the structure (tendons T3 and T4). Figure 4.34 shows the layout of these tendons. Tendon T3 runs through all three of the spans shown. Tendon T4 runs only through the central span.

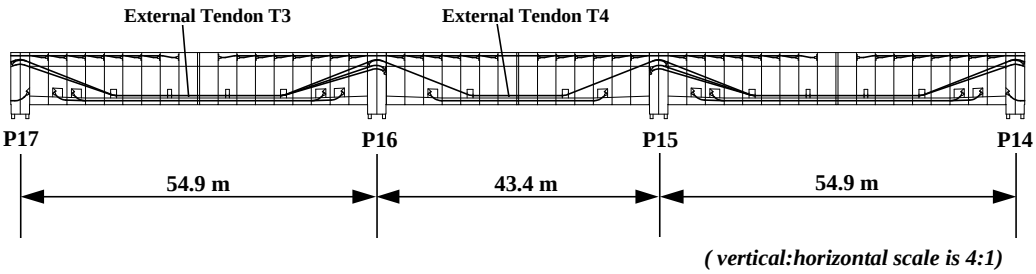

Figure 4.34 - Layout of the last external tendons placed and stressed in Ramp P

After the external tendons were stressed, they were grouted. Barriers were cast on the top deck, and an asphalt overlay was applied. The bridge opened to traffic shortly thereafter. Table 4.1 summarizes the events in the construction of Ramp P and the dates of occurrence.

Date	Event
4/96 - 7/96	Ramp P superstructure segments are precast
8/15/96 - 9/5/96	P17 cantilever erected
9/6/96 - 9/9/96	Remaining segments and CIP closure for span P17 placed
9/9/96 - 9/22/96	P16 cantilever erected, continuity tendon T19 stressed in span P17
9/23/96 - 9/24/96	Segments P15-1a, 1b, 2 and 3 erected for P15 cantilever
9/27/96 - 10/9/96	P14 cantilever erected
10/10/96 - 10/14/96	Remaining segments and CIP closure for span P13 placed
10/15/96 - 10/16/96	Remaining segments for P15 cantilever erected
10/17/96	Continuity tendon T19 stressed in span P13
10/21/96 - 10/24/96	CIP closure and continuity tendon T20 stressed for span P15
10/24/96 - 10/29/96	Tendons T301 and T302 stressed, P15-16, P16-16, and P16-17 erected
11/5/96 - 11/7/96	Alignment at P17 adjusted, CIP closure for span P16
11/11/96 - 11/12/96	Continuity tendons T21 and T22 stressed for span P16, permanent bearings set at P17
11/13/96	P15-17 erected
11/15/96 - 11/19/96	External tendons T1 and T2 stressed in upstation spans
11/19/96 - 11/22/96	CIP closure for span P14, continuity tendons T21 and T22 stressed, permanent bearings set at P14
11/23/96 - 12/7/96	Remaining external tendons T1, T2, T3, and T4 stressed
2/13/97	Live load test performed on Ramp P
2/97 - 3/97	Barriers cast on Ramp P, wearing surface applied
4/97	Ramp P opens to traffic

Table 4.1 - Events and dates for the construction of Ramp P

4.4 CONSTRUCTION PROBLEMS

Several problems were encountered during the construction process for Ramp P. This section lists the problems that occurred and how they effected the construction process.

4.4.1 Erection of the Interior Anchorage Segments

Two major problems occurred during the erection of the interior anchorage segments. First, the contractor had difficulty placing and joining the two separate halves of each segment on top of the pier capitals. Second, difficulty was encountered in stressing the tie down bars on pier P16.

4.4.1.1 Joining the Two Halves of the Segment

The scheme devised for bringing together the two halves of the interior anchorage segment was poorly devised (see Figures 4.20a and 4.20b). Rather than devising a scheme to lower the two halves into proper alignment with each other using the crane, the contractor relied on his ability to push one of the segment halves from the side if the two halves did not line up laterally with one another. This was done using a small hydraulic ram that was fixed to the top of the pier capital with anchor bolts. This ram barely supplied enough force to shove one of the segment halves sideways, and the resulting effort damaged the top of the capital. Figure 4.35 shows the scheme and what occurred. The top of the capital was not detailed for the type of load the ram placed on it, and the concrete at the top edge of the capital was severely cracked.

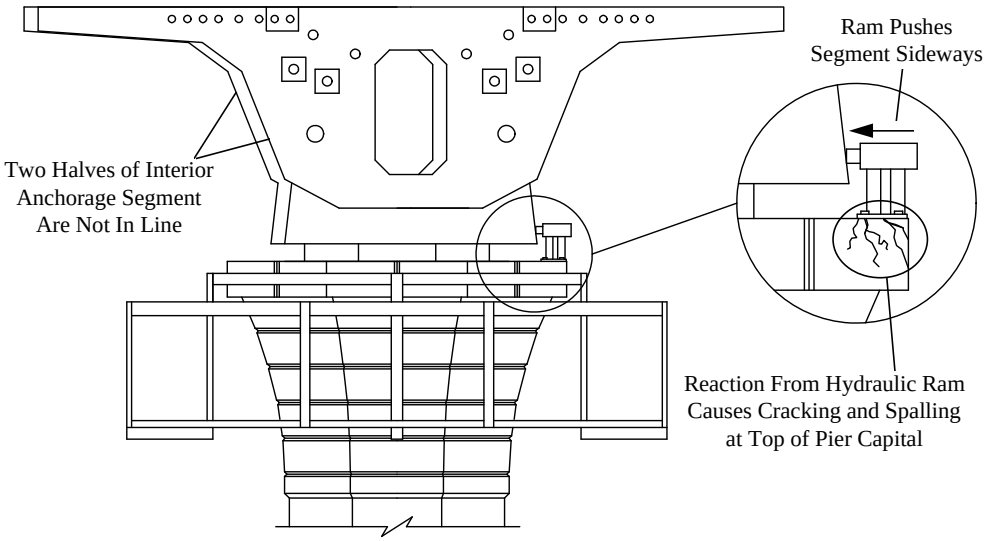

Figure 4.35 - Scheme for moving the two halves of the interior anchorage segment into line

Furthermore, the steel roller bearings which were intended to allow the second half of the anchorage segment to be easily pushed up against the first half had a coefficient of friction that was too high. The contractor found it extremely difficult to move the segment half after it was placed on the capital. Three nights were required to erect the interior anchorage segment for Pier P16 because of these difficulties.

The interior anchorage segment had been split into halves so that a smaller crane could be used on the job site. Had the segment been lifted onto the pier capital as one whole, the weight would have necessitated a much larger crane than the one used. The extra volume of the anchorage diaphragms in the interior anchorage segments made its weight much greater than the other superstructure segments. No problems occurred with the erection of the P17 interior anchorage segment because the erection trusses made manipulation of the two segment halves easy.

4.4.1.2 Stressing the Tie-Down Bars

After the interior segment was in place on Pier P16, problems were encountered with the stressing of the tie-down bars. The tie-down bars on Piers P15 and P16 were permanent. Therefore, the anchorage plates in the deck for these bars were recessed into blockouts that could be filled with grout after completion of the structure. Unfortunately, these blockouts were too constrictive for the original hydraulic ram that the contractor intended to use for stressing the bars. A special long-necked ram was required that would fit down into the blockout. As a result, only a few of the tie-down bars could be stressed before construction of the P16 cantilever unit began. The contractor had to wait for the special ram to be delivered to the job site. Thus, the contractor could not rely on the pier to carry an unbalanced moment from the cantilever. When segments were erected on that unit, two cranes had to be used simultaneously to support segments at both wing tips. Only when both segments were properly attached to the ends of the cantilevers and the unit was in balance could the cranes be released. Fortunately, the contractor already had two cranes at the job site for the erection of Ramp P. Figure 4.36 shows the special long-necked ram required to stress the tie-down bars on Piers P15 and P16. This ram was acquired before erection of the P15 anchorage segment, so the problem was avoided at that unit.

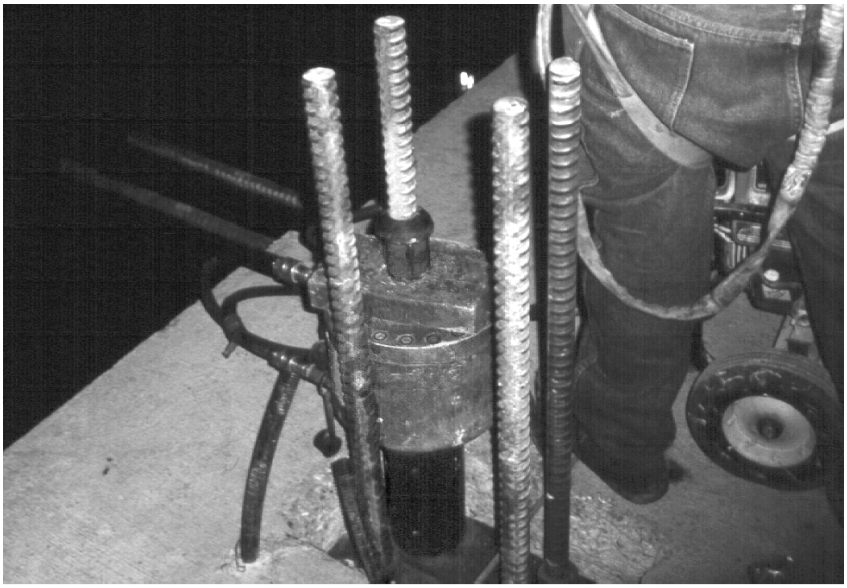

Figure 4.36 - Ram necessary for stressing the tie-down bars on P15 and P16

4.4.2 Erection of the First Two Cantilevered Segments

Problems occurred during the erection of the first two cantilevered segments because the scheme to pass the temporary post-tensioning bars through the ducts for the cantilever tendons was poor (reference Figure 4.23 for the steps involved in this sequence). The ducts for the cantilever tendons had too small of a diameter to properly accommodate the coupler used for the bars. The Dywidag couplers had a diameter of 67 mm ($2\ ^{5}/_{8}$") and the cantilever tendon ducts had a diameter of 76 mm (3") which left almost no spare room for the coupler to fit through the duct. Furthermore, the cantilever tendon ducts had angle breaks at the joint lines because of the horizontal curvature of the bridge. The small angle breaks in the duct forced a small bend in the temporary post-tensioning bars and wedged the coupler up against the side of the duct. When it was time to remove the bars from the tendon ducts, the workers found that the bars were almost impossible to get loose. In at least one instance (for the P16 cantilever unit), the bars had to be extruded from the ducts by using a hydraulic ram. The erection of the first two cantilevered segments on Pier P16 took two complete nights to finish. In contrast, the other segments on that cantilever unit were erected at a rate of six per night. Figure 4.37 shows a detail of how the temporary post-tensioning bars and couplers needed to fit through the top flange tendon ducts. The figure is to scale. It is obvious from the drawing that removing the coupler would be difficult.

Furthermore, if the duct was indented even slightly at the time the segment was cast, removal of the coupler would have become impossible without damaging the concrete.

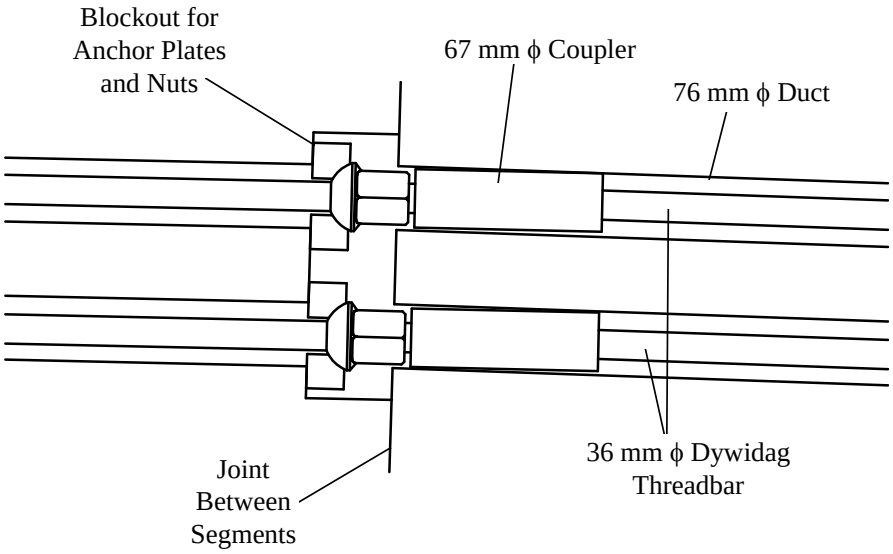

Figure 4.37 - Detail for passing the temporary post-tensioning bars through the cantilever tendon ducts

In contrast to the problems that occurred with the erection of the first two cantilevered segments, the erection of the other segments on the cantilever went quite well. One of the key reasons for this success was the external blisters used for the temporary post-tensioning bars. These blisters allowed a loose fit for the bars and plenty of room to access the anchorage and coupling hardware. The ducts in the blisters were large enough to accommodate the 36 mm diameter (1 $^{3}/_{8}$") threaded bars, and the length of the blisters was so short that the bars had a large amount of play. The couplers were not required to pass through any ducts. Figure 4.38 illustrates how the loose fit of the temporary post-tensioning bars in the blisters helped in the erection of a segment. The worker on the right has to pass the bars between the blister on the foreground segment and the blister on the background segment which is hanging by a crane. It is not necessary for the crane operator to position the hanging segment very precisely because the worker has enough play in the post-tensioning bars to run them through the two blisters when the segments are not completely in line. Once the bars and the rest of the stressing hardware were in place, the segment was easily drawn up to the end of the cantilever by stressing the temporary

bars. When the bars needed to be removed, the workers had adequate access to the nuts and couplers to loosen them.

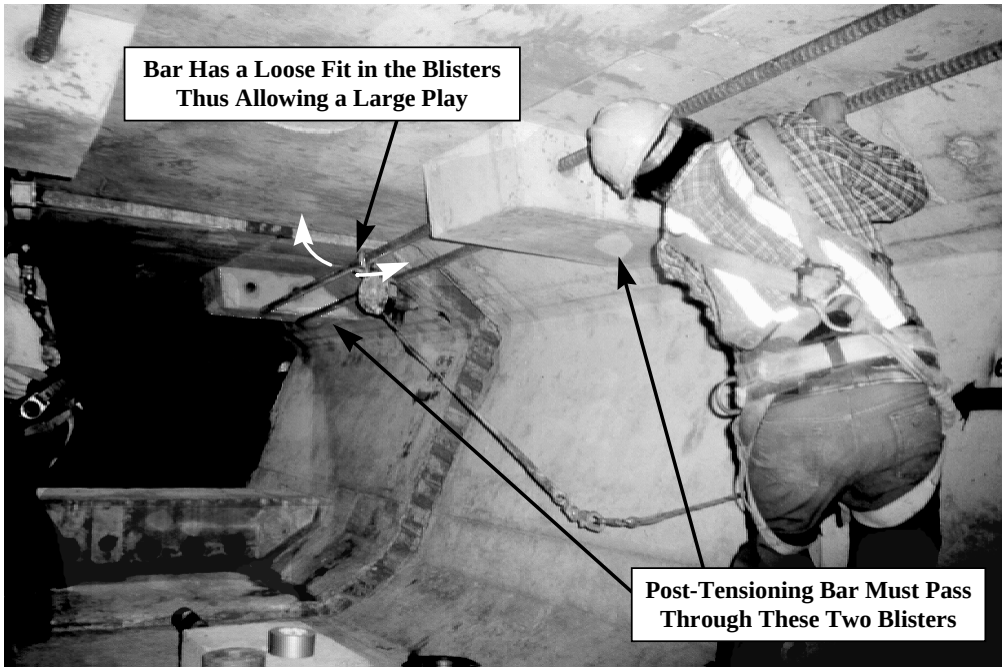

Figure 4.38 - Demonstration of the typical temporary post-tensioning process

4.4.3 Transverse Post-Tensioning Duct

During the grouting of one of the transverse post-tensioning ducts in the top flange of the interior anchorage segment for P16, grout leaked out of the duct within the concrete and into one of the ducts for a top flange cantilever tendon. The transverse duct passed directly over the longitudinal cantilever duct and they were probably in contact with each other. Holes must have also been present in each of these ducts where they crossed. The grout had to be removed from the longitudinal duct because the tendon for that duct had not been placed yet, and the grout was creating an obstruction that would prevent any tendon from being threaded through the duct. The contractor was forced to chisel through the concrete deck to get to this duct and clean it out. Figure 4.39 shows the resulting damage. Many of the transverse prestressing strands in segments P16-1a and P16-2 were damaged during this process.

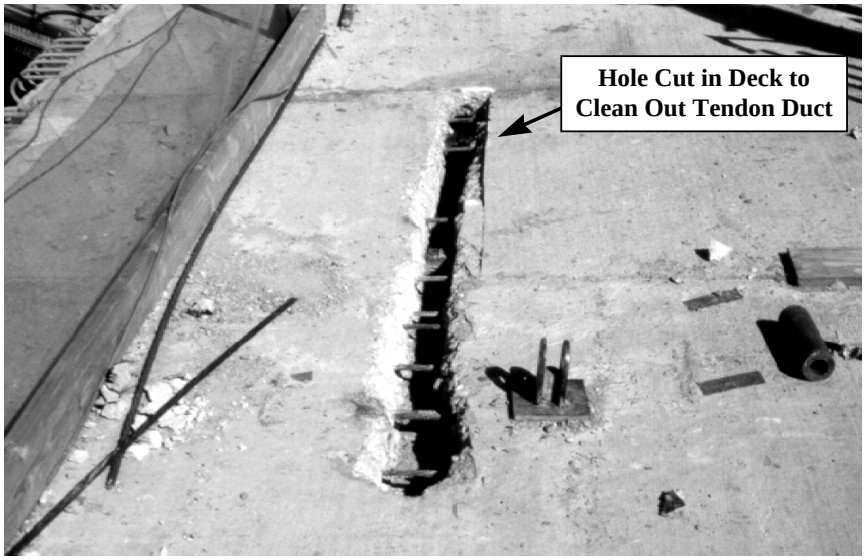

Figure 4.39 - Damage done to the top deck because the cantilever tendon duct became obstructed

4.4.4 Squeeze Out of Joint Epoxy

When segment P17-3 was erected (the downstation segment adjacent to the interior anchorage segment on Pier P17), proper squeeze out of the joint epoxy was not achieved in the bottom flange. When two segments are stressed together, the epoxy applied to the faces of the joints should ooze out everywhere around the perimeter of the joint. This is known as squeeze out. Proper placement of the epoxy and a good seal of the joint faces should result in a uniform squeeze out. Squeeze out is looked for by inspectors at the site. Epoxy had to be injected into the joint between P17-3 and P17-1 (the interior anchorage segment) to fill the voids between the segments. This error was most likely due to a poor match-casting of these segments during the time of precasting. The match-casting of these segments occurred in the special precasting bed discussed in Section 4.2.2 which had several problems with production.

A proper seal is required for segmental joints for durability of the structure. Voids in the joints could allow the intrusion of water around the internal tendons. Furthermore, voids in the joints could also result in stress concentrations. If a void exists at a joint, the stress will divert to the material around the void. Hardened joint epoxy is stronger than concrete. If a void occurs at a

joint and causes overstress, the concrete will fail, not the joint epoxy. This phenomenon was seen in one of the spans of the mainlane construction. Voids present in the bottom flange of one of the joints have been attributed to spalling of concrete in span C47 of the U.S. 183 mainlane.

4.4.5 Mislabeled Segment

During the erection of the P16 cantilever unit, two of the segments were incorrectly labeled. This error was not discovered until the segments were on the crane and epoxy had already been applied to their faces. The error was discovered because the duct holes in the faces of the two segments did not match up with the duct holes at the ends of the cantilevers. The two segments had simply been switched with each other. Because the epoxy began to harden before the segments could be exchanged, work on the bridge had to cease until the epoxy could be ground off. The delay set back the construction schedule one night.

4.4.6 Alignment of the Cantilevers

When the two cantilevers for the upstation 54.9 m (180') span were finally completed, it was discovered that they did not line up vertically by about 15 cm (6"). This flaw was easily corrected by jacking up the girder at Pier P17. Figure 4.40 shows the girder being jacked off of its temporary bearings with hydraulic rams. The girder was lifted until the alignment was corrected. In general, vertical and horizontal alignment problems are easily fixed in segmental bridges by jacking the girder at some pier. Problems with twist can be particularly difficult for the closed cell girders because they are very torsionally stiff, but no problems of that nature occurred in this project.

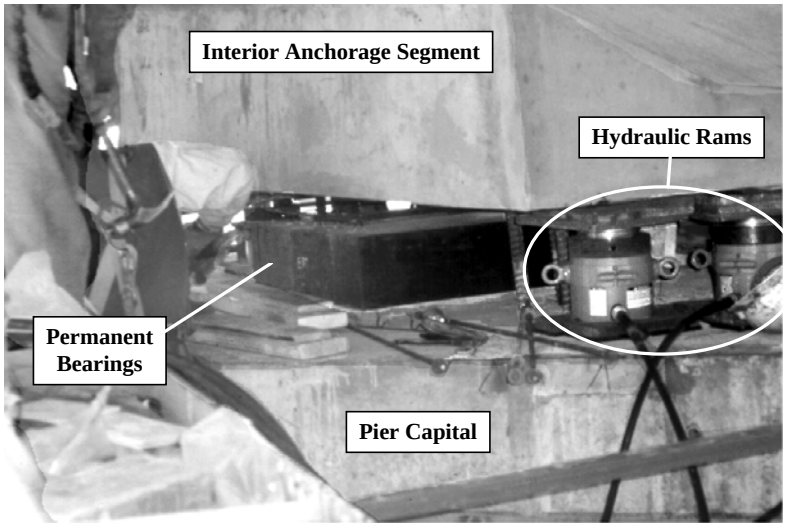

Figure 4.40 - Picture of the hydraulic rams used to jack the girders at the bearings

4.4.7 Work Inside of the Girder

Access to the interior of the girder was a continuous problem during the cantilever erection of Ramp P. Access openings were located at midspan for each of the spans in the continuous unit. Therefore, the access opening for a span did not become available until erection of the last segment on the cantilever. As a result, the only way to get from the top of the deck to inside the girder as the cantilevers were being erected was by riding in a manlift from the deck to the open end of the box girder. This presented a frustration to the workers during the cantilever stages of the construction because they could not easily move about the bridge to perform the erection tasks.

The poor choice of location for the access openings was also a hindrance during the stressing of the continuity tendons. All of the anchorages for continuity or external tendons were located towards the ends of the spans in the interior of the box girder. The hydraulic ram necessary for stressing had to be dropped in at a midspan opening and moved to either end of the span. Movement of the rams within the girders was difficult because of the size and weight of the rams and because there were many obstacles that they had to be moved over such as the deviator beams and the bottom blisters.

Once the ram had been moved through the girder, it was often difficult to get the ram into position against the anchor head. This task generally involved quite a bit of ingenuity on the contractor's part. The contractor was able to get the ram into position by a complicated series of maneuvers involving "come-along" chains (a heavy chain with an attached hand crank for pulling or lifting). Figure 4.41 shows a "come-along" chain being used to maneuver a ram into position against an anchorage blister for a continuity tendon.

Lighting was also a problem inside the girder. Much of the time, workers relied on flashlights for their lighting needs when they had to work inside the girder. A permanent lighting system inside of the girder would have made much of the interior work easier. After closure of the cantilevers, quite a bit of work was done inside the girders including post-tensioning, grouting, and installation of utilities. Furthermore, over the long term life of the bridge, inspection and maintenance must be performed inside the girder. A permanent lighting system would facilitate the performance of all of these tasks.

Finally, the locations of the drain pipes inside of the girders for both the mainline units and the ramps has proven to be an irritation during the performance of any task done inside of the box girder since their installation. The drain pipes were centered across the interior space of the girder cross-section. Thus, they occupy much of the space which is available for workers and inspectors to walk through inside the girder. In the ramps, the space available to pass through the anchorage diaphragms is quite small, and the drain pipes make passage through the ramp girders a significant trial to even small individuals. Furthermore, access holes in the bottom flanges of all of the girders are also located along the midline of the cross-section and the drain pipes prevent complete opening of the hatches of these access holes. A strong cooperative effort should have been made between the structural designers and the designers of the drainage details to prevent this problem. The drain pipes could have easily been located in the corners of the interior cross-section thus placing them out of the way of individuals who must do work inside the completed bridge.

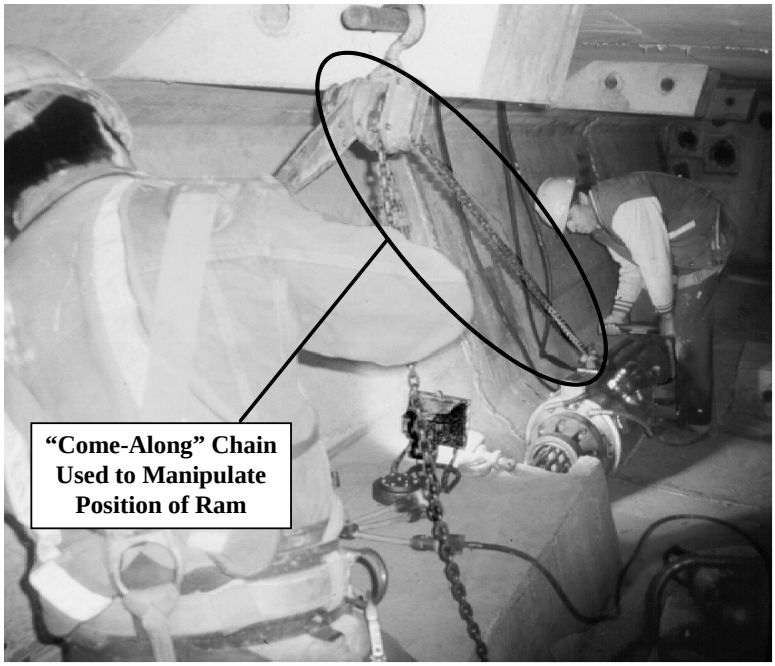

Figure 4.41 - Workers manipulate the hydraulic ram inside of the box girder

4.4.8 External Tendons

4.4.8.1 Failures During Stressing

Three of the twelve external tendons in Ramp P broke during stressing. The reasons for the failures have not been positively identified as of the time of this writing, but the most likely reason for the problem stems from the unusually long length of these tendons and their complicated geometry. The longest of these tendons passed through three spans of the ramp and was over 153.1 m (502') in length. This tendon also passed through four saddles and six vertical deviators. When stressing these tendons (the T3 tendons in Figure 4.34), about 60 cm (2') of slack had to be pulled out of the tendon plus an additional 60 cm (2') of elongation before the final force was reached. Originally, the contractor was not power seating the wedges into the wedge plate each time the ram was stroked. If the wedges are not power seated, the strands will slip back into the duct a small amount before the wedges catch and hold the strand. It is likely that the wedges in the anchor head were not seating equally during this process. The tendons were made up of 19 Dywidag 15.2 mm (0.6") diameter Grade 270 strands with multiplane anchorages (also

from Dywidag). The wedge plate for these tendons is pictured in Figure 4.42. It is likely that the strands passing though the holes on the outside of the plate were slipping further than the strands in the center of the plate before the wedges would seat. This would allow for greater losses on some of the strands. As a result, the total force in the tendon would not be distributed evenly among the strands. The strands experiencing less slip before the wedges caught would have a greater stress in them. The ram was stroked about 8 times before the stressing was completed on these tendons. The cumulative effect of the wedges seating unequally after 8 strokes of the ram may have been substantial enough to cause problems. Post-tensioning of tendons is monitored in two ways: the force in the ram and the elongation of the tendon. The force in the ram is an indicator of the total force in the tendon, but does not tell if that force is distributed evenly among the strands. While the total force in the tendon may have been small, the majority of the force may have been distributed to only a few of the strands in the tendon because of the uneven losses. These strands would be overstressed as the final force for the tendon was approached causing them to break. If this phenomenon occurred, the elongations would not be equal among all the strands. If the inspector measures the elongation of the tendon by just one strand, this effect would be missed. Figure 4.42 shows the slip process that may have occurred during the stressing of these tendons. Problems of getting the ram into proper position against the wedge plate (mentioned in Section 4.4.7) probably contributed to this problem as well.

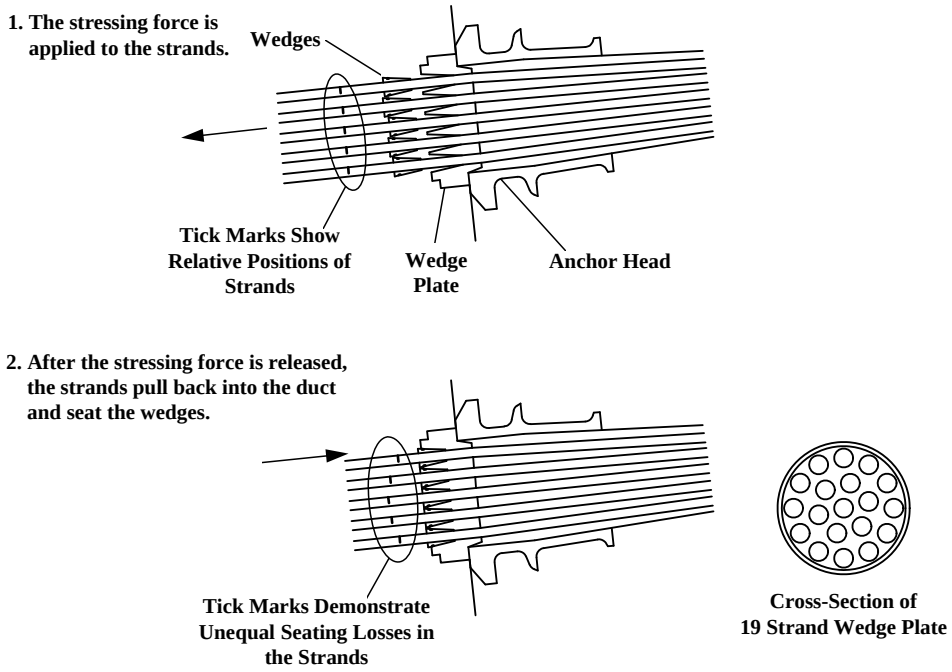

Figure 4.42 - Potential unequal seating of the wedges into the wedge plate

After two tendons had been broken, the contractor began power seating the wedges every time the ram was stroked, but problems still occurred in the longer external tendons. Again, the length of the tendons may have been the problem. When the tendons were placed, the strands within the tendon were not laid out in an orderly manner. The strands crossed over and around each other along the length of the tendon. They had a small amount of tangle. When stressing began, this tangle could have been pulled into a knot near the anchorage. The strands were also being cinched up against the bottom of the duct because the tendon had to pass through a saddle immediately after coming out of the anchor sleeve. This factor could have contributed to the formation of a knot. Such a knot could have resulted in an uneven distribution of force among the strands of the tendon. The same result from uneven seating of the wedges would occur. As the final force in the tendon was being applied, some of the strands would become overstressed and break. Figure 4.43 shows where a knot may have occurred.

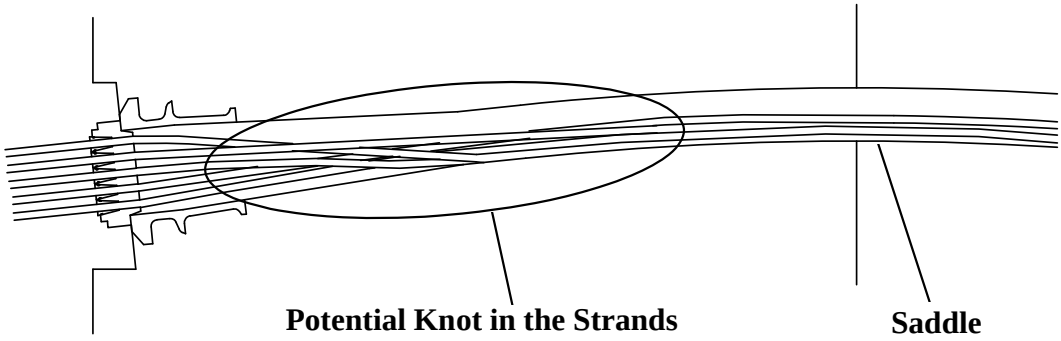

Figure 4. 43 - Knots may have occurred in the external tendons

A further problem that may have occurred which would have contributed to the failures could have been rubbing of the strands against the edges of the saddle and deviation pipes. These pipes had no trumpets (diabolos) at their ends. Because of this, precise alignment of the pipes is necessary to avoid problems with the tendon rubbing against the edges at the ends of the pipes. High friction losses can occur if the tendon does so. Proper control of the alignment of these pipes is difficult in a short line casting bed. The horizontal curvature of the bridge probably contributed further to alignment problems. High friction losses caused by the rubbing of the strands against the deviation pipes would have concentrated most of the tendon force near the stressing end. Wear of the strands would also occur where they rubbed against pipe edges.

Tendons were rejected after two wires had broken. The three failures that occurred were more severe than three broken wires. Typically several wires ruptured or even the entire strand. The breaks occurred just past the wedge plates which might point to knotting of the tendons as the main cause. The problems that occurred would not have been isolated to the three tendons that failed. The tendons currently in the bridge most likely have some problems with knotting and uneven force distribution across their strands though there have been no indications of broken wires in any of these in-place tendons.

4.4.8.2 Horizontal Geometry

The horizontal geometry of external tendons in horizontally curved box girders can be difficult to deal with because the tendon follows chords between deviators. Proper visualization of

the three-dimensional geometry is important to avoid having the tendon scrape up against the sides of the webs or other components within the box. In Ramp P, the horizontal geometry of the external tendons made the stressing of the outside T3 tendon difficult ("outside" meaning the outside of the bridge's horizontal curve). The ram could barely be fit against the anchor head because it was bumping into an adjacent external tendon which was angled towards the center of the box because of the horizontal curve of the bridge. Proper allowance for the size of the ram had not been met because the horizontal geometry of the external tendons and the size of the ram with dial gauge and hose attachments was not properly visualized. Further evidence that the horizontal geometry of the external tendons was not fully visualized came from the temporary post-tensioning blisters in the bottom of the girder. The innermost external tendon on the outside of the bridge curve routinely bumped up against the bottom blisters in Ramp P. This is shown in Figure 4.44. Possible problems with misalignment of the deviation and saddle pipes were already discussed in the previous section but would also be relevant to this topic.

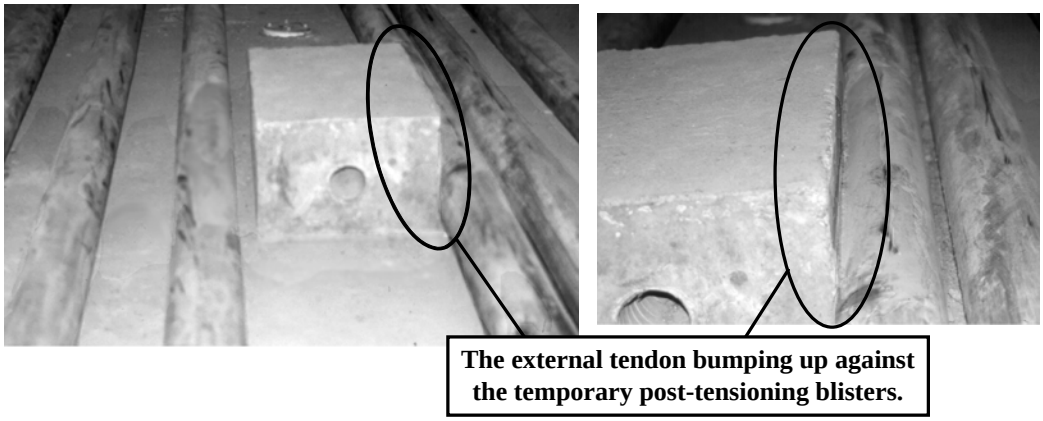

Figure 4.44 - Horizontal alignment problems with the external tendons

4.4.8.3 Grouting

Grouting of the external tendons proved to be difficult because of the long lengths of the ducts. The crew in charge of grouting found it difficult to eliminate voids in the duct. Very often, the workers had to punch holes in the duct to create vents to remove air pockets. External tendons have a great advantage over internal tendons in terms of grouting because voids can easily be detected by tapping against the side of the duct. The worker simply listens for a hollow sound to

indicate an air pocket. The problem with the external tendons in Ramp P was their length. Over such long lengths, it becomes more difficult to maintain a uniform grout pressure which will push air bubbles out the vents. Often the grout in the ducts had to be compressed several times which inevitably lead to leaks occurring at the connections between the polyethylene pipe and the steel saddle pipes.

4.4.9 Temporary Grout Bearings

The original construction plan for Ramp P called for temporary bearings made of reinforced grout to be cast underneath the interior anchorage segments of the ramp. The contractor found these bearings difficult to remove (they had to be chipped out) when it was time to install the permanent bearings. Shortly into construction of the ramp, plastic bearings were allowed instead so that this problem could be eliminated.

4.4.10 Uplift of Superstructure Off of Bearings

As of this writing, the Ramp P superstructure has partially lifted off of one neoprene bearing at Pier P18. There is about a 2 mm ($^1/_{16}$") gap over one third of the area between the top of the neoprene and the mortar plinth on the bearing located on the outside of the superstructure's horizontal curve. Similar problems have also occurred on the curved spans constructed by the span-by-span method. The problem has not been diagnosed as of this time, but could be attributable to torsion created in the structure by the external tendons. Before the external tendons were stressed, the problem had not occurred. It was first noticed after the stressing of the external tendons. Figure 4.45 shows several views of the problematic bearing.

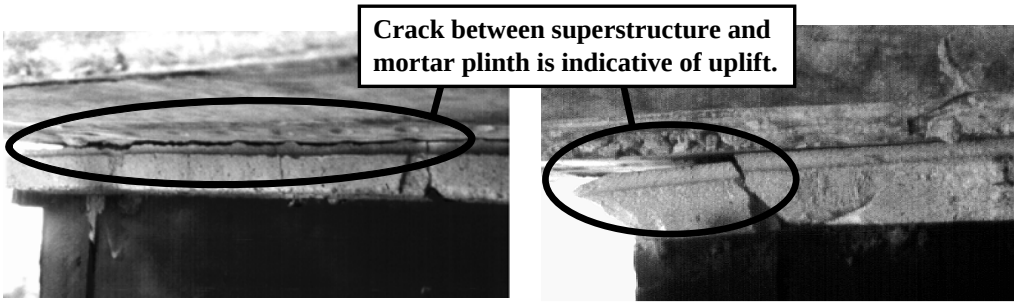

Frontal View (looking upstation)

Side View (looking towards the ouside of the horizontal curve)

Figure 4.45 - Uplift off of one of the P18 bearing pads

4.5 CONCLUSIONS AND RECOMMENDATIONS

The problems described in Section 4.4 can be divided into three categories: design related, construction related, and inspection related.

4.5.1 Design Issues

The problems which were considered pertinent to design topics included the unusually long lengths of the external tendons and the resulting stressing problems, specifications on temporary components such as the grout bearings, the working space inside the girder, access to the inside of the girder, space for placement of rams at anchorage areas, and the uplift of the superstructure from bearing pads. Also mentioned is the correction to the alignment between the P16 and P17 cantilevers.

4.5.1.1 Conclusions

The poor positioning of the access holes at midspan, the inadequate space left for the stressing rams, and the overall difficulties presented by the working area inside the girder reflect a lack of sensitivity in the design and working drawing stages to the details of the construction process. Consideration of these details is important because they affect the workers' abilities to perform the required tasks of the construction process. Poor details will result in a slower construction pace and a decline in quality of the final product. The economy of the structure is affected on a short term basis because of the slowed construction rate, and there is a danger of long-term durability or aesthetic problems because the quality of the structure may be impaired by a lower caliber of workmanship.

Special consideration was necessary for the external tendons because of their long length. Failures probably occurred because of a combination of several factors. The wedges were not power seated every time the ram was stroked leading to unequal seating of the wedges and a non-uniform distribution of stress among the strands of the tendons. The long lengths of the tendons necessitated that over a meter of length needed to be stroked before the final force in a tendon was reached. This led to the formation of a knot in the strands between the anchorage and the nearby saddle. The strands of the tendon were most likely rubbing against the edges of the deviation and

saddle pipes leading to excessive stresses in the strands. Difficulty in placing the ram against the wedge plate inside the girder probably contributed as well. Difficulty was also encountered in grouting the tendons because of the long length of duct and the multiple vertical rises the tendons passed through.

There are problems with uplift of the superstructure off of the bearing pads. This could be a torsional effect related to the horizontal curve of the superstructure and the prestress forces from the external tendons through this curve. However, this is only a hypothesis, no cause has yet been determined.

The ability of the contractor to correct vertical and horizontal alignment problems between cantilevers by adjusting the bearing plinths at the piers demonstrates an adaptability of the balanced cantilever system which is useful for construction. The more adaptable the system is to quick changes, the less bound the designer and constructor are to uncertain variables during the planning stages. Adaptability of the details to change can greatly facilitate construction.

4.5.1.2 Recommendations

Though the contractor and construction engineer will ultimately make the decisions on the details of the construction scheme, the designer's investigation of a potential construction scheme should encompass all of the details of the process. Crucial to this thought process should be a sensitivity for what workers need to do for a specific task, where they have to be, what tools and materials they will have to manipulate, and under what environmental pressures. It was suggested by on-site inspectors that an interior lighting system would have facilitated construction tasks inside the girder and would be useful for long term inspection and maintenance. Interior lighting has been a specified detail for many box girder bridges. The location of drainage details or utility pipes should not be ignored by the structural designer. Space should be allocated for these details so that their final placement does not impede long term inspection and maintenance tasks which have to be performed inside the box girder. Generous space should be allowed for hydraulic rams used for post-tensioning near the anchorages and in areas where the rams will have to be moved. Allowances should be made for dial pressure gauges and hydraulic hoses attached to the ram. Consideration of the three dimensional geometry of the girder is important. The manipulation of these rams is often quite difficult because of their size and weight. The ram does

not just have to fit next to the anchorage, it has to be transported to that location and supported in place. Ideally, detailed records of the methods used by contractors to perform post-tensioning and erection tasks on projects should be kept and made available to subsequent projects. Thus, a database of experience could be established and referred to for design decisions as well as to make recommendations when problems are perceived by inspectors at job sites. Inspector diaries and video tapes of construction details would be the principal means to this end.

The length of tendon next to the live end anchorage of long post-tensioning tendons should be left straight and free of deviation saddles. This will help to allow twist in the strands next to the anchorage to distribute over a greater length of tendon so that the twist will not concentrate into a knot. Deviation pipes for external tendons should have trumpeted ends (diabolos ends) to prevent rubbing of the strands against the edges of the pipe. On-site inspectors should measure tendon elongation across several strands protruding from the back end of the ram to verify that all strands elongate the same amount. Inspectors should also require power seating of the wedges every time the ram is stroked especially for long tendons which require many strokes of the ram to reach the design force.

Currently nothing can be recommended concerning the uplift of the superstructure off of the bearing pad until the problem is further observed and analyzed. Most likely, the solution lies in a better understanding of the effects of external tendons on horizontally curved bridges.

Designers should consider the uncertainties of the design process and evaluate design concepts based on the adaptability of details to possible change. Pre-consideration of potential adaptations in structural components could result in economic and time savings during construction.

4.5.2 Construction Issues

Construction problems that have been classified as issues for the construction engineer include the difficulties in the erection of the two halves of the interior anchorage segment and the first two cantilevered segments. Details of the temporary post-tensioning blisters which were designed by the contractor are also discussed under this heading.

4.5.2.1 Conclusions

The problems that occurred in the erection of the interior anchorage segment and the first two cantilevered segments are the result of lax construction engineering. Similarly, the placement of the bottom flange temporary post-tensioning blisters so that they conflicted with the alignment of the external tendons demonstrates that there was insufficient visualization of the three dimensional geometry of the bridge by the contractor.

4.5.2.2 Recommendations

The contractor had the space and time at the precasting yard to perform a trial, dry fit erection of some of the Ramp P segments and should have done so. This would have immediately made apparent any potential problems in the proposed scheme for the balanced cantilever erection. Opportunities to test proposed erection schemes in controlled situations should not be passed by. The misfortune of discovering flaws in the system when a segment is hanging from a crane at the site can be costly. This type of a test would have demonstrated the problems involved in placing the two halves of the interior anchorage segment and bringing them together in proper alignment on top of the pier capital. A dry fit erection test also presents an opportunity to test the match cast of selected segments.

Erection schemes for segments should include consideration of measures to easily adjust the alignment of the segments while they are being manipulated into position. The erection scheme for the two halves of the interior anchorage segment did not properly meet such a goal.

Temporary post-tensioning details using threaded bars for prestress should permit as much free movement of the bar as possible. They should also allow easy access to coupler and anchorage components. Two alternatives to the method used to erect the first two cantilever segments are suggested here. Additional ducts could have been placed in the segments just for the temporary prestress. Thus, the bars would not have had to be removed after their use in the temporary stressing. Possibly a better suggestion would be to use components that are temporarily attached to the top of the segments and act as blisters for post-tensioning bars. Such a detail was used in the mainlane erection and is pictured in Figure 4.46. Steel blisters were temporarily fitted onto the deck surface of the mainlane segments and post-tensioning bars were threaded through them. It is unknown why such a detail was not used on Ramp P, but the system would have removed much of the erection work from the cramped inside of the girder and put it up onto the deck where plenty of room existed for the workers to perform their tasks.

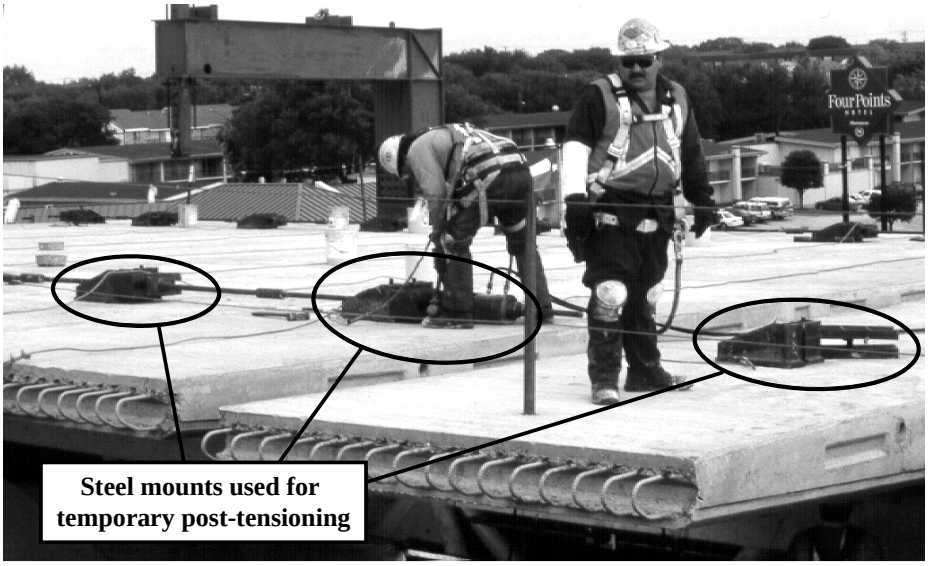

Figure 4.46 - Alternative detail for temporary post-tensioning

Contractor proposals for structural details should include structural drawings that fully demonstrate that no conflicts exist with the other components of the bridge structure. Particular attention should be given to the three-dimensional geometry of the bridge. For example, plan sheets for the temporary post-tensioning blisters should have been drawn showing the horizontal curvature of the bridge and the locations of the external tendons in relation to the bottom flange blisters. This would have prevented the conflict that occurred between these two bridge components. Sheets which demonstrated the specific details of a proposed erection procedure would also help to delineate flaws in its idealization.

4.5.3 Inspection Issues

The on-site inspector should thwart construction problems as they occur at the precasting yard. The mislabeling of the two segments and the grouting problem that occurred with the transverse post-tensioning duct are examples of such problems. Comprehensive quality assurance procedures coupled with thorough inspection at the time of erection can prevent long-term problems with structural performance.

4.5.3.1 Conclusions

Labeling of bridge segments at the U.S. 183 precasting yard was performed by the contractor. It is unknown if an independent check procedure was used by the contractor's staff. Inspectors periodically walked through the storage area and looked over the segments for voids or other surface flaws. It is uncertain if the labeling of the segments was checked at such time.

The grouting problem that occurred with the transverse post-tensioning duct must have been the result of direct contact between the transverse duct and the longitudinal cantilever tendon duct and the presence of holes in these ducts at that junction. The quality assurance personnel could have noticed breaches in the surfaces of the ducts and directed them to be patched with caulk. Post-tensioning ducts should have sound surfaces free of dents or holes so that tendons can pass through them unimpeded once the concrete is cast and set. Pipes were placed through the ducts at the time of casting to help to strengthen the duct against damage at the time the concrete was placed for the precasting of the segments. These pipes prevent the ducts from becoming bent or from collapsing, but small damage can still be done to the surface of the duct especially by the concrete vibrator.

The poor squeeze-out from the joint between P17-3 and P17-1b originated from actions at the precast site. Fortunately the inspector present at the time of the erection of P17-3 paid careful attention to the squeeze out and recommended injection of epoxy into the joint.

4.5.3.2 Recommendations

Quality assurance personnel can easily verify segment labels prior to transport to the site by checking the details of post-tensioning duct locations or special features such as anchorage blisters or deviator beams. Construction and inspection records should be logged verifying the quality and identity of the segment prior to transport to the construction site.

Verification of the integrity of post-tensioning ducts should be a priority task before casting of the segment because correction of flaws after placement of the concrete can be difficult. Primarily, the presence of stiffening pipes in the ducts should be confirmed.

Full attention should be given to epoxy squeeze out between joints during erection. The cross-section of the box girder should be as homogeneous as possible for complete and uniform transfer of stress as well as integrity against environmental forces.

CHAPTER 5

CONSTRUCTION SEQUENCE DATA

5.1 DIFFUSION OF POST-TENSIONING

5.1.1 Temporary Post-Tensioning

Data demonstrating the diffusion of post-tensioning forces directly behind the anchorage zones was collected from the concrete gauges in segment P16-10 at the time the segment was erected. Figure 5.1 shows the stresses from the temporary post-tensioning bars and the dead load of the segment. These stresses are plotted next to the 0.28 MPa (0.040 ksi) compressive stress required by the *Proposed AASHTO LRFD Segmental Guide Specifications* [17] during curing of joint epoxy. The plot of the measured stresses shows a very non-uniform distribution both horizontally and vertically. Horizontally, the stresses were particularly low near the wing tips of the top flange where the minimum compressive stress was not attained. This may be due to poor diffusion of the temporary post-tensioning force out to those portions of the cross-section. Vertically, all sections along the webs had at least the required contact pressure. Additional fluctuations in the stress plot could be due to debris on the joint faces or problems with the match cast fit. Differential shrinkage in the segment or thermal effects during the curing process could have warped the segment face. It should be recalled that the gauges were placed 46 cm (18”) from the joint face. No problems were observed with the squeeze out of the joint epoxy between P16-10 and P16-8.

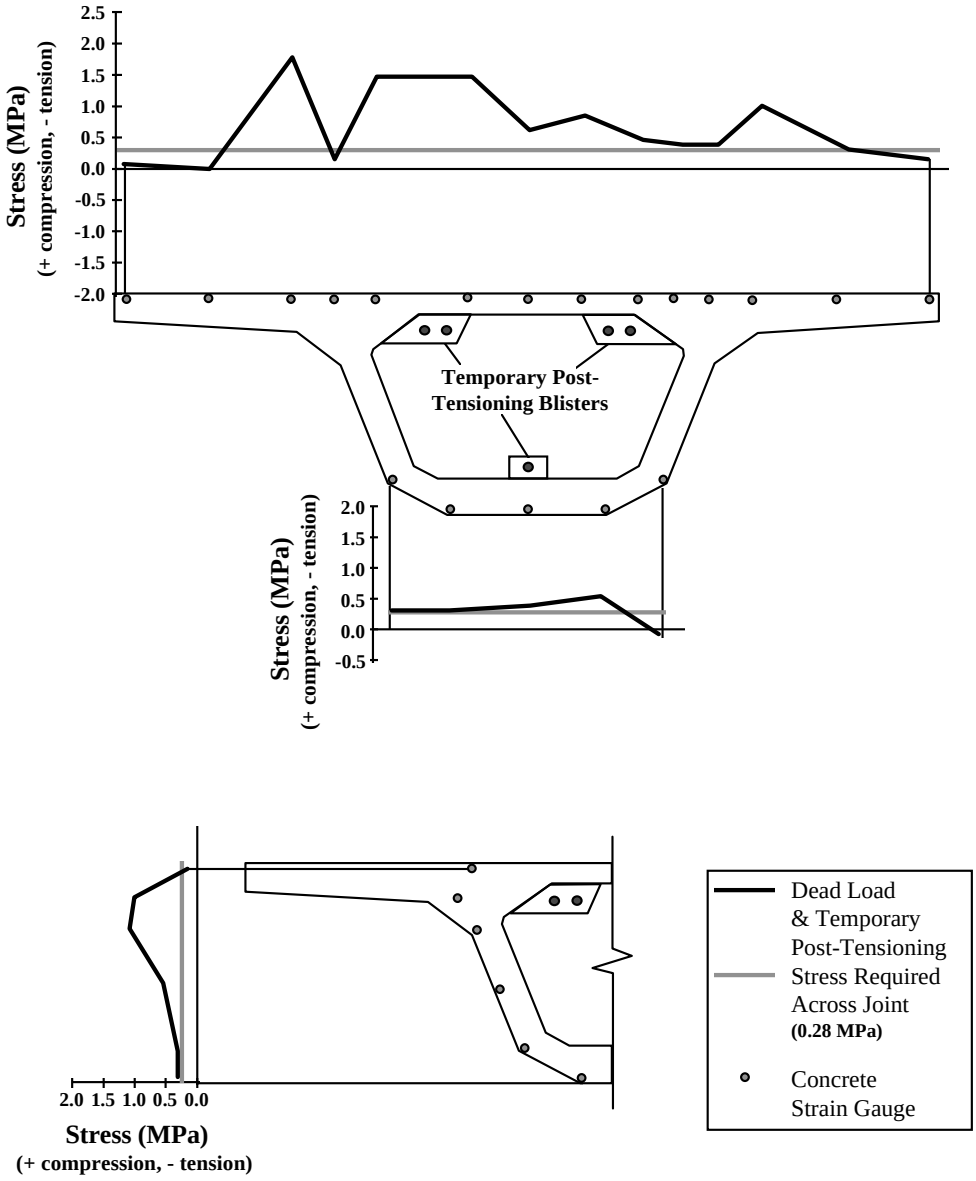

Figure 5.1 - Diffusion of force from temporary post-tensioning in P16-10

5.1.2 Cantilever Post-Tensioning

The distribution of stress from the post-tensioning of the T205 cantilever tendons in P16-10 was calculated in two ways: using the effective flange width method from Section 4.6.4.6.2 of the *AASHTO LRFD Bridge Design Specifications* [2] and using the full section properties under simple beam theory assumptions. These calculations are given in Appendix B. Directions in the commentary of the AASHTO code for the application of the specified effective flange method for normal forces are rather vague (see Section 2.3.3 of Chapter 2). Lines at 30^o angles from the line of action of the concentrated forces are used to distinguish the limits of the effective flange width. However, Figure 4.6.4.6.2-4 in the AASHTO code does not clearly indicate that these lines should originate from the location of the concentrated normal load. In fact, the figure can easily be interpreted to show that the 30^o lines originate from the edges of the webs. Also the AASHTO specifications do not clearly indicate how the horizontal prestressing loads distribute vertically through the webs and into the flanges. There are two considerations in this distribution. Application of strut-and-tie modeling shows the compressive force to spread into the webs and lower flanges following the 30^o inclination from the tendon axis. However, this neglects the compatibility induced zone of tension along the back face and bottom of the flange that is adjacent to the inclined compressive force distribution (indicated by the lightly shaded area in Figure 5.2). Furthermore, if the loads are applied at the level of the top flange, how should the bottom flange be affected? Figures 5.2 and 5.3 show how the AASHTO specifications were applied to the effective flange method calculation for this problem. The 30^o lines were drawn so that they originated at the center of the applied concentrated loads. Figure 5.2 shows the dimensions of the effective flange widths. Because the compatibility requirements near the vertical edge and at the adjacent portion of the bottom flange cannot be ignored in reality (even though they are ignored in strut-and-tie modeling), the area shown lightly shaded in the side view of Figure 5.2 was included in the calculation of stresses from post-tensioning. This is necessary as shown in the recommendations for post-tensioned anchorage zones discussed in Section 5.10.9.4 of the *AASHTO LRFD Bridge Design Specifications* [2] when treating edge tensile forces and spalling forces. This is accomplished by using normal and flexural actions (i.e. $P/A \pm Mc/I$) for these regions. Thus, no reduction of the bottom flange was made as is shown by the shaded area of the cross-section in Figure 5.3. The distribution of measured stresses across the bottom of the cross-section indicates full action of the bottom flange.

Measured stresses are presented for each of the two tendons (the right and left sides) as well as the sum of the two tendons. The right side tendon was stressed first. There is a noticeable difference between the individual stress distributions caused by the left and right tendons. The difference could not be caused by the curvature of the cantilever because no actual horizontal curvature occurs over the length of one segment. The segments themselves have a trapezoidal shape, and the horizontal curvature of the bridge is accomplished by angle breaks at the segmental joints. The cause of the difference is unknown.

Along the vertical stress distribution shown in the lower part of Figure 5.3, it can be seen that the AASHTO method which assumes plane sections will remain plane failed to predict the actual shape of the stress distribution, though it did predict the top and bottom stresses fairly well. The effective flange width method specified by AASHTO may have been developed for correct prediction of stress at extreme fibers where most service level design is concerned. Horizontally, it appears that the beam theory calculation predicted the maximum stress better than the AASHTO method. However, the measured stresses might be too low because of potential error in the measured modulus of elasticity that was used to transform the strain gauge data to stress values as was discussed in Section 3.7.1 of Chapter 3. It should also be obvious that the AASHTO method is predicting the shape of the stress distribution better than beam theory. The AASHTO method correctly predicted the drop in stress in the center of the top flange as well as the drops near the wing tips. Overall, the AASHTO method seems to work reasonably well. Table 5.1 compares predicted stresses from the AASHTO and beam theory methods with the measured values. Ratios of the measured stress to the calculated stress presented in the table which are greater than 1 indicate unconservative results.

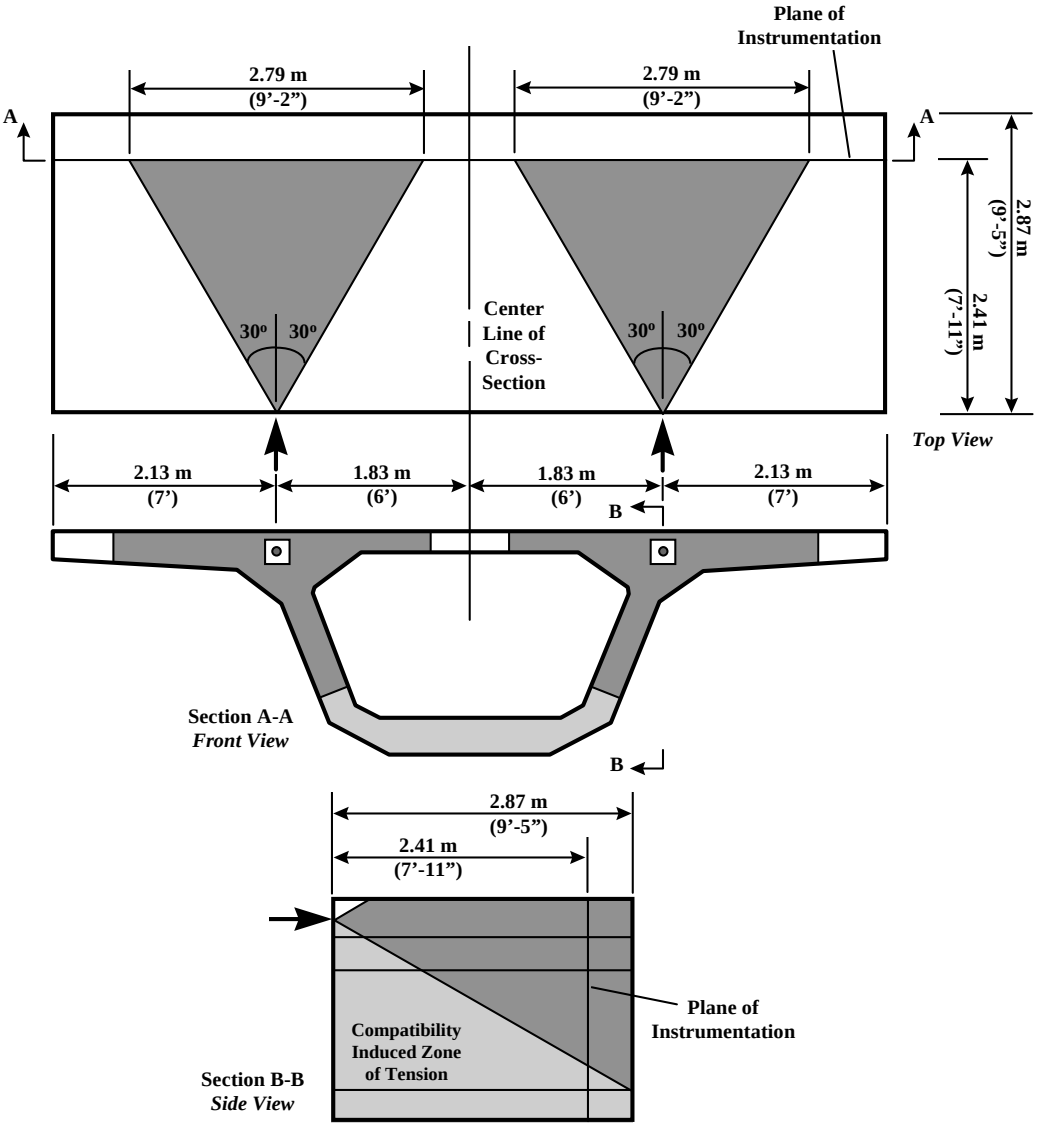

Figure 5.2 - Effective area for calculation of stresses from cantilever post-tensioning

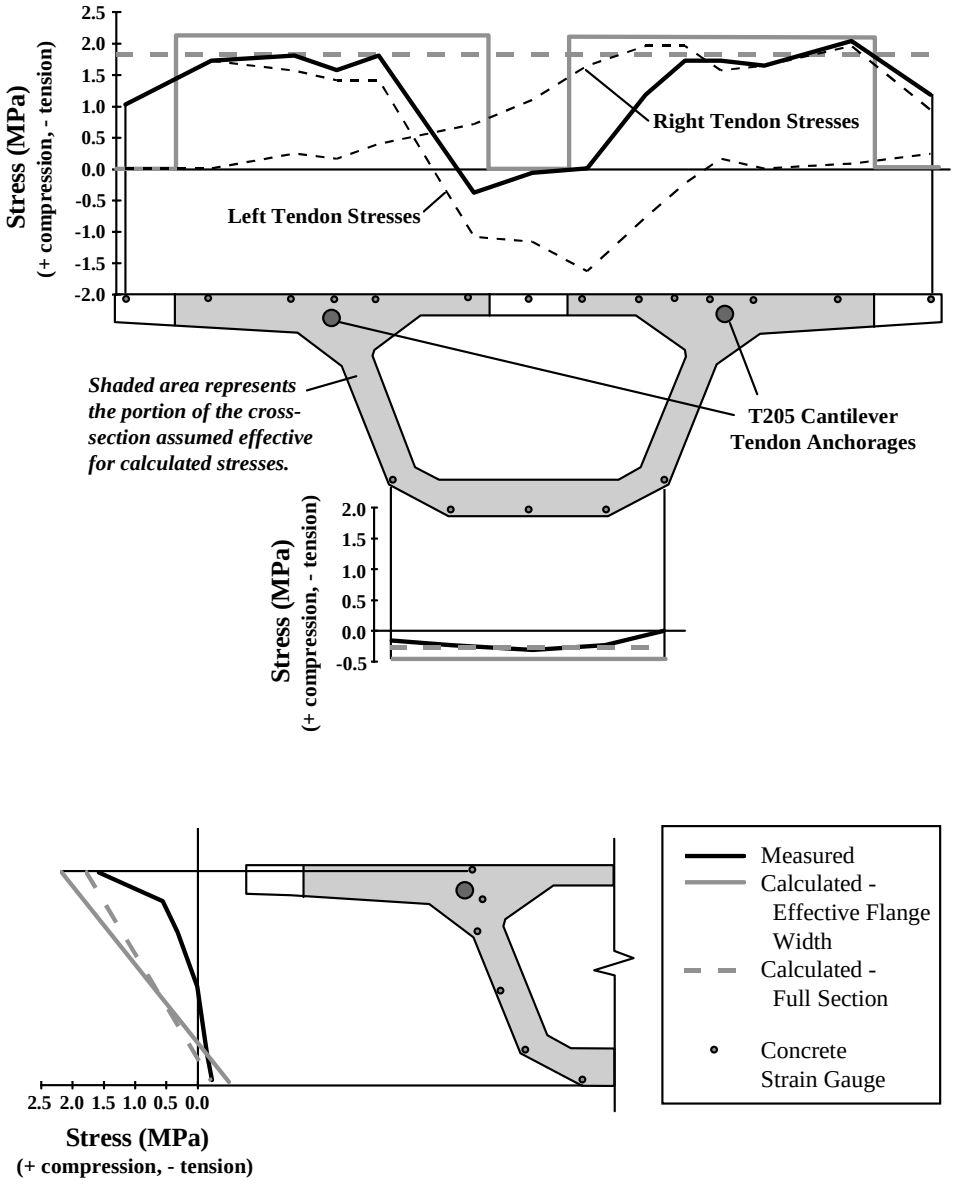

Figure 5.3 - Diffusion of post-tensioning force from the cantilever tendons in P16-10

	Maximum Top Flange Compression (MPa)	Maximum Bottom Flange Tension (MPa)
Measured	2.01	0.31
AASHTO Effective Flange Width	2.21	0.45
Measured/Calculated	*0.910*	*0.689*
Full Section Properties	1.84	0.35
Measured/Calculated	*1.092*	*0.886*

Table 5.1 - Comparison of measured and calculated stresses from diffusion of post-tensioning

Transverse stresses were also measured during the stressing of the cantilever tendons anchored in P16-10. These stresses are presented in Figure 5.4. When only the right side tendon was stressed, some moment was present in the top flange which could be the result of warping. These stresses are very small however, and are only present in the structure for a small period of time. They pose no need for concern. After both sides were stressed, the transverse stresses were reduced to insignificant magnitudes.

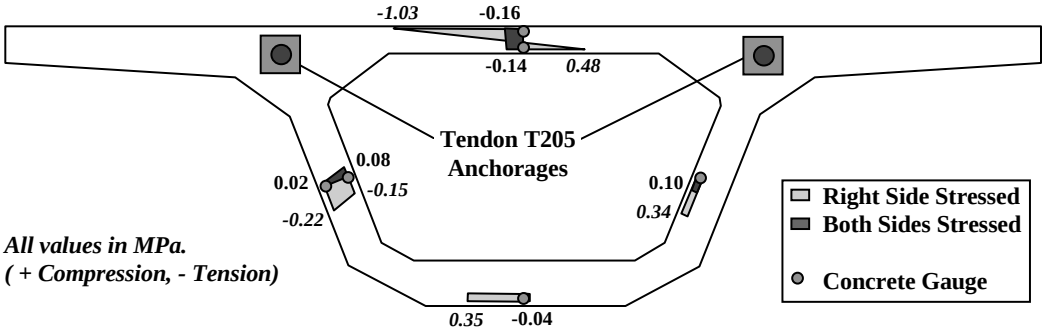

Figure 5.4 - Transverse stresses from the stressing of the cantilever tendons in P16-10

5.2 STRESSES DURING CANTILEVER CONSTRUCTION

The cantilever construction events for which data is presented in this section occurred during Phases II, V, and VI of the Ramp P construction process. Figure 5.5 shows the layout of the segments and cantilever tendons for the P16 upstation cantilever. Recording of the data from the Ramp P superstructure began just after P16-2 was temporarily post-tensioned to the P16

interior anchorage segment. The locations of the instrumentation and the construction process are discussed in greater detail in Chapters 3 and 4 respectively.

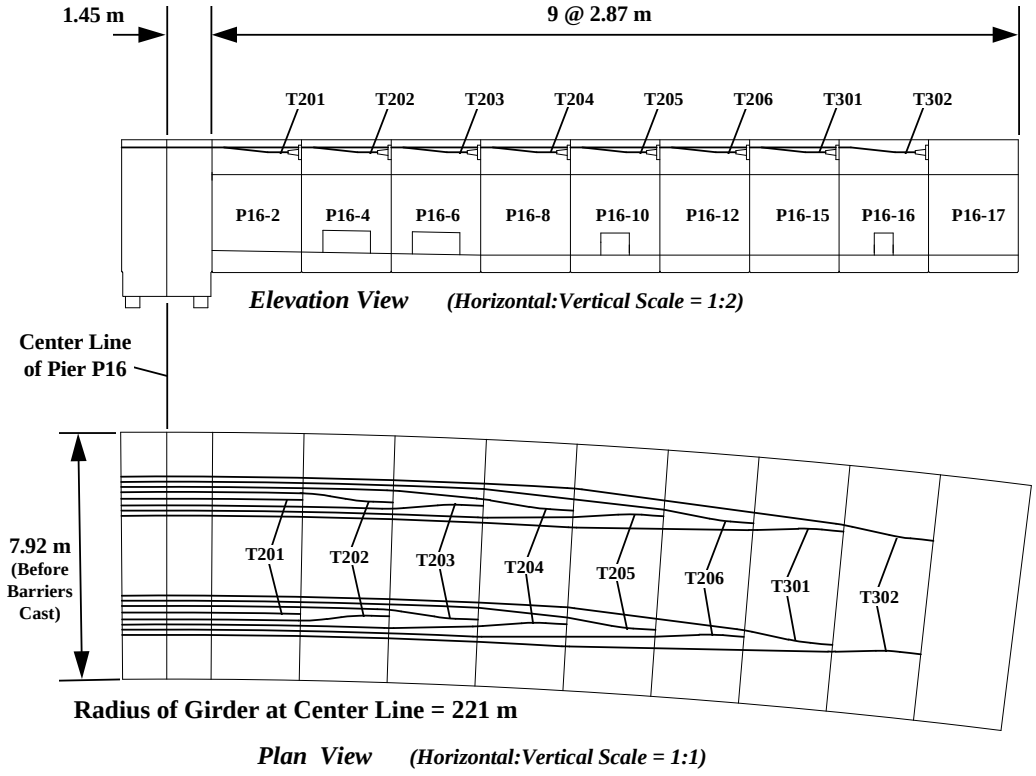

Figure 5.5 - Layout of segments and cantilever tendons in the P16 upstation cantilever

5.2.1 Longitudinal Stresses

Measured and calculated longitudinal stresses for P16-2 after completion of the P16 cantilever are presented in Figure 5.6. The calculations were performed with the aid of a computer spreadsheet. Moments, torques, and shears were calculated at each joint face using the curved girder relations given in equations (2-10) through (2-12) of Chapter 2 and assuming all forces are zero at the free end of the cantilever. These calculations are given in Appendix B.

The measured plots indicate fairly smooth distributions of stress from dead load. According to Section 4.6.2.6.2 of the *AASHTO LRFD Bridge Design Specifications* [2], no shear lag was expected in the Ramp P cross-section under the actions of loads applied on the full

cantilever length. Furthermore, the P16 anchorage diaphragm that is in close proximity to the plane of gauges in P16-2 should provide restraint against shear lag deformations. The calculated post-tensioning stresses agree well with most of the measured data except at the top of the cross-section. The calculated dead load stresses agree very well with the measured stresses at the top of the cross-section but deviate increasingly from the measured values as one looks down the vertical height of the web. The agreement between calculated and measured dead load stresses at the bottom of the cross-section was very poor. It appears as if the neutral axis from the measured stresses is slightly lower than that calculated for the section. The properties of the concrete probably vary somewhat through the section because of the multiple batches of concrete required to cast a segment (see Section 4.2.1 of Chapter 4). Changes in the modulus of the concrete through the depth of the section could affect the location of the neutral axis. It is possible that the assumed weight of the concrete used in the calculations was higher than the actual weight. The difference in the slopes of the calculated and measured dead load stress distributions along the webs indicates that the actual moment was lower than the calculated one. Possibly, a combination of a downward shift in the neutral axis and a lower applied dead load moment account for the good agreement between the calculated and measured dead load stresses at the top of the cross-section and the bad agreement at the bottom of the cross-section. Average measured stresses through the top and bottom lines of concrete gauges in P16-2 are compared to calculated stresses in Table 5.2.

	Cantilever Dead Load			**Cantilever Post-Tensioning**		
P16-2	**Average of Measured (MPa)**	**Calculated (MPa)**	**Measured / Calculated**	**Average of Measured (MPa)**	**Calculated (MPa)**	**Measured / Calculated**
Top	-7.84	-7.86	0.997	11.03	15.30	0.721
Bottom	17.64	20.97	0.841	-4.54	-3.92	1.158

Table 5.2 - Comparison of measured and calculated longitudinal stresses in P16-2 after completion of the P16 cantilever

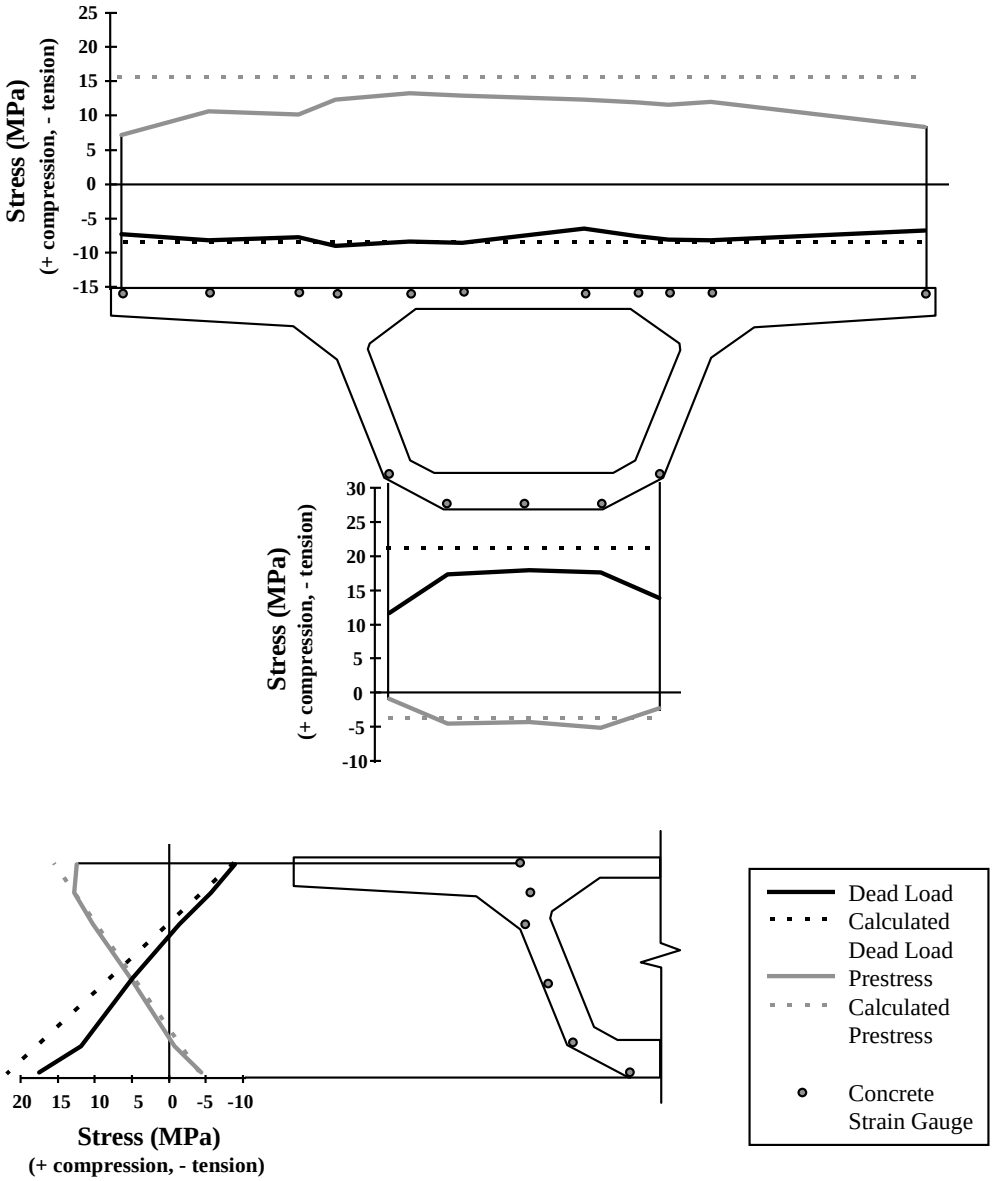

Figure 5.6 - Measured and calculated longitudinal stresses in P16-2 after completion of the P16 cantilever

Three concrete gauges were chosen out of the P16-2 cross-section which were deemed to represent the behavior of the section fairly well: C604 (at the top of the left web), C607 (near the middle of the top flange), and C638 (at the bottom of the left web). Cumulative stresses in these gauges are plotted for the different stages of the cantilever construction process in Figure 5.7. The trends of these gauges show that the dead load moment at P16-2 did not begin to exceed the post-tensioning moment until segment P16-15 was erected. This is indicated when the compressive stress in the bottom flange (gauge C638) becomes larger than the compressive stress in the top flange (gauges C604 and C607).

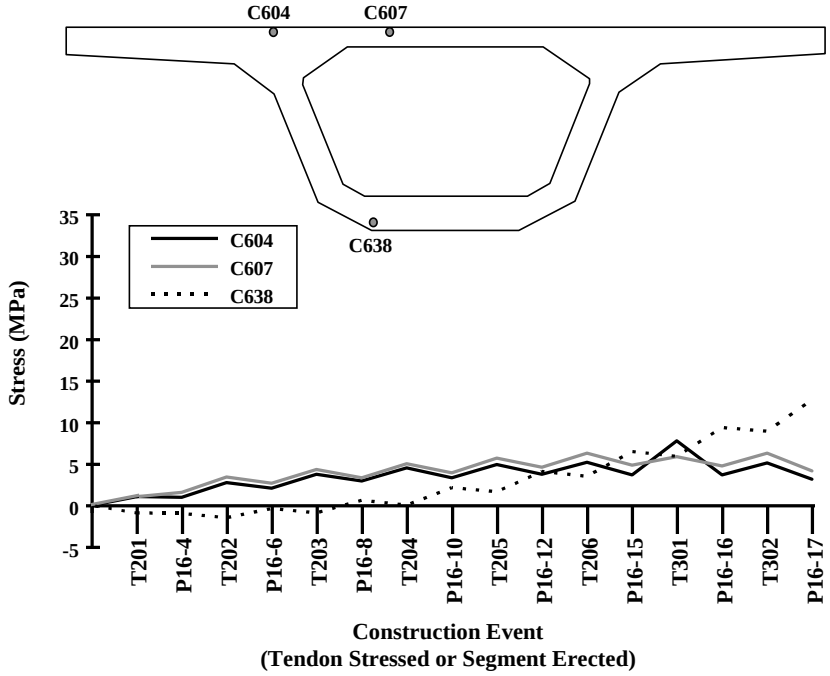

Figure 5.7 - Stresses in selected concrete gauges from P16-2 over the course of the cantilever construction sequence

5.2.2 Shear Stresses

The calculations performed to determine longitudinal stresses in the P16 upstation cantilever also accounted for the torsion from the horizontal curvature of the ramp. Theoretical shear stresses in the webs and top and bottom flanges of the cross-section were calculated and are

plotted next to measured stresses in Figure 5.8. The calculated vertical shear stress did not compare very well to the measured stresses. The proximity of this section of gauges to the support bearings and anchorage diaphragm may have affected the shear stress distribution at that location. Theoretically, no torsional or vertical shear stresses should have been produced by the internal post-tensioning in the cantilever. Only very low stresses were measured from the cantilever post-tensioning.

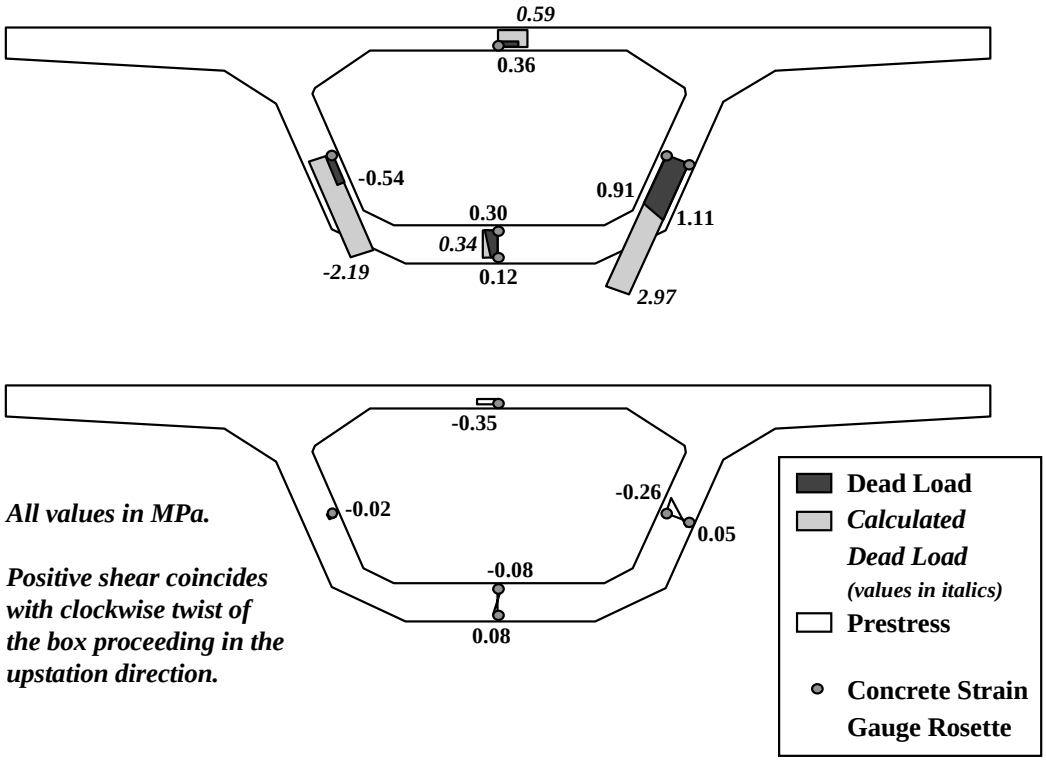

Figure 5.8 - Measured and calculated shear stresses in P16-2 after completion of the cantilever

5.3 STRESSES DURING CONTINUITY POST-TENSIONING

The stressing of the tendons for which data is presented in this section occurred during Phases VI and VII of the Ramp P construction process. Figure 5.9 shows the layout of the segments and continuity tendons for the downstation half of span P16.

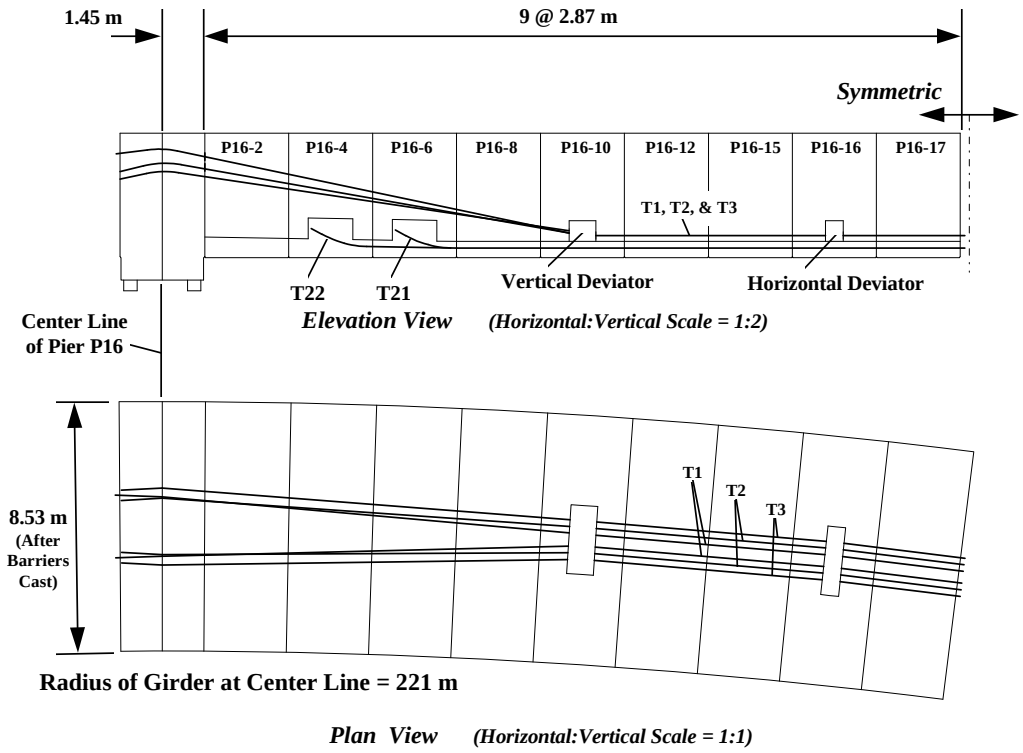

Figure 5.9 - Layout of internal and external continuity tendons in span P16

5.3.1 Longitudinal Stresses

Longitudinal Stresses from the post-tensioning of the internal and external continuity tendons (T21, T22, T1, T2, and T3) are presented in Figures 5.10 through 5.12. Theoretical stresses were calculated using a two-dimensional frame solver, RISA2D (Rapid Interactive Structural Analysis 2-Dimensional) [18]. Details of the calculation model are given in Appendix A. Equivalent loads were placed on the structure to simulate the post-tensioning. Friction losses across deviators were estimated for the external tendons based on equation 5.9.5.2.2b-1 of Section 5.9.5.2.2 of the *AASHTO LRFD Bridge Design Specifications* [2]:

$$f_{p2} / f_{p1} = e^{-\mu\alpha} \qquad (5\text{-}1)$$

Where f_{p2}/f_{p1} is the ratio of tendon force from the dead end to the live end of the deviator, μ is the coefficient of friction (0.25 radians^{-1}), and α is the angle break in radians across the deviator (0.04 radians or 0.08 radians were added to the angle breaks across the deviators and saddles respectively as an allowance for misalignment of the metal ducts). All other losses such as elastic shortening were ignored to simplify the analysis. These calculations are given in Appendix B.

The total stress presented in Figures 5.10 through 5.12 comes from all of the measured events in the construction sequence (erection of segments P16-4 through P16-17, the stressing of cantilever tendons T201 through T302, and the stressing of the continuity tendons T21, T22, T1, T2, and T3 in span P16). The total stresses do not include any creep redistribution of dead load or thermal effects. The figures indicate that there was less moment at all of the sections than anticipated by the calculations. This is demonstrated by comparing the slope of the measured stresses through the web with the slope of the calculated stresses. The stress in P16-2 tends to drop off near the wing tips of the section. A slight reduction in the top flange width was required by Section 4.6.2.6.2 of the *AASHTO LRFD Bridge Design Specifications* [2] for P16-2 under the fully continuous structural configuration. Approximately 30cm (1') was removed on each wing tip of the cross-section at P16-2. The reduction in the flange width made very little difference in the calculated location of the neutral axis or the moment of inertia for that section. Thus, the magnitudes of the calculated stresses were affected very little compared to a full section calculation, but the shape of the calculated top flange stress distribution was changed in such a way that it fit the shape of the measured top flange stress distribution better than a full section calculation would have. Thus, the effective flange specifications seem to have worked reasonably well. The large peak which occurs in the measured stresses over the right web of P16-10 is probably due to a local compressive strut in the concrete emanating from the vertical deviator beam.

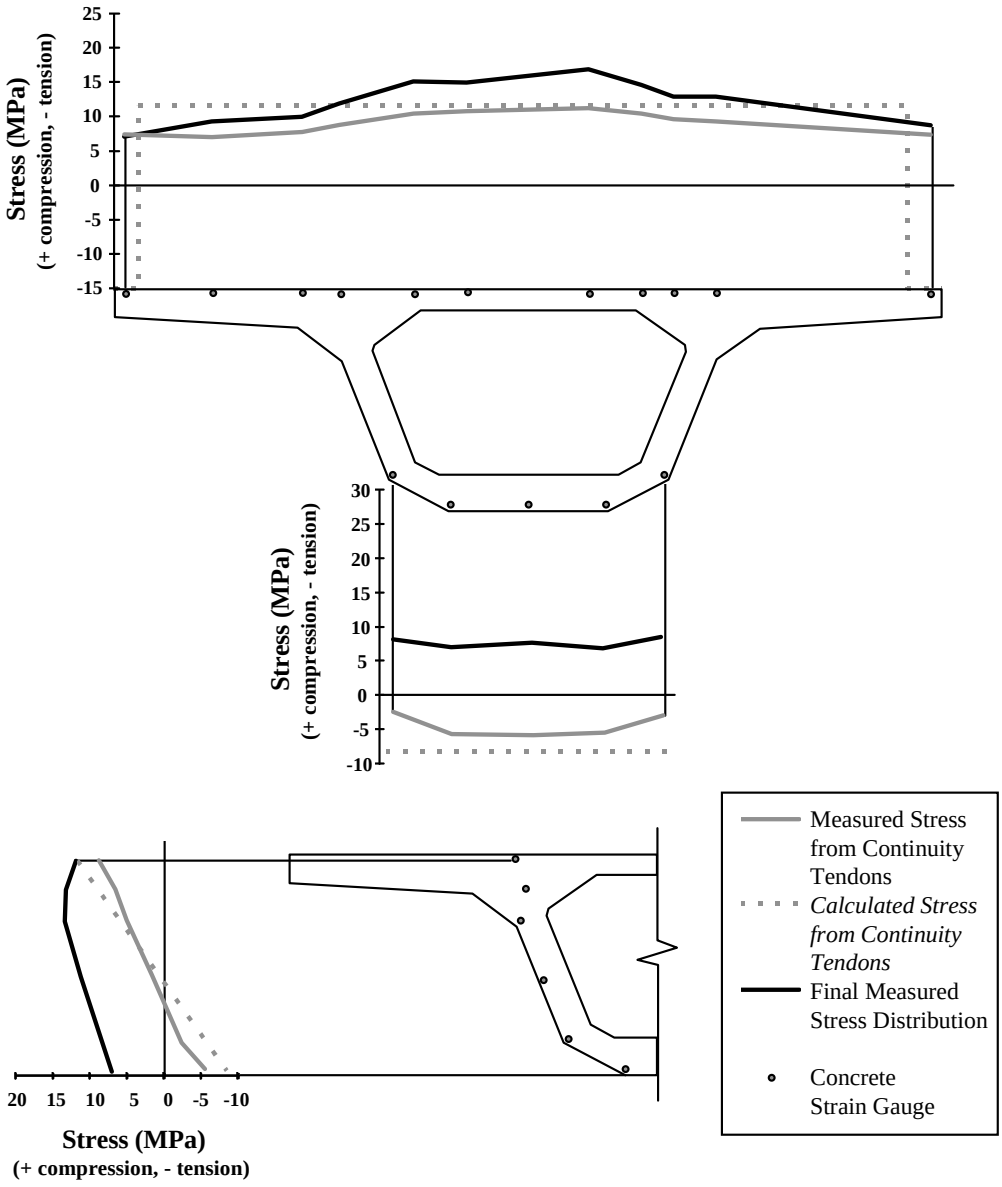

Figure 5.10 - Measured and calculated stresses in P16-2 after stressing of the continuity tendons in Span P16

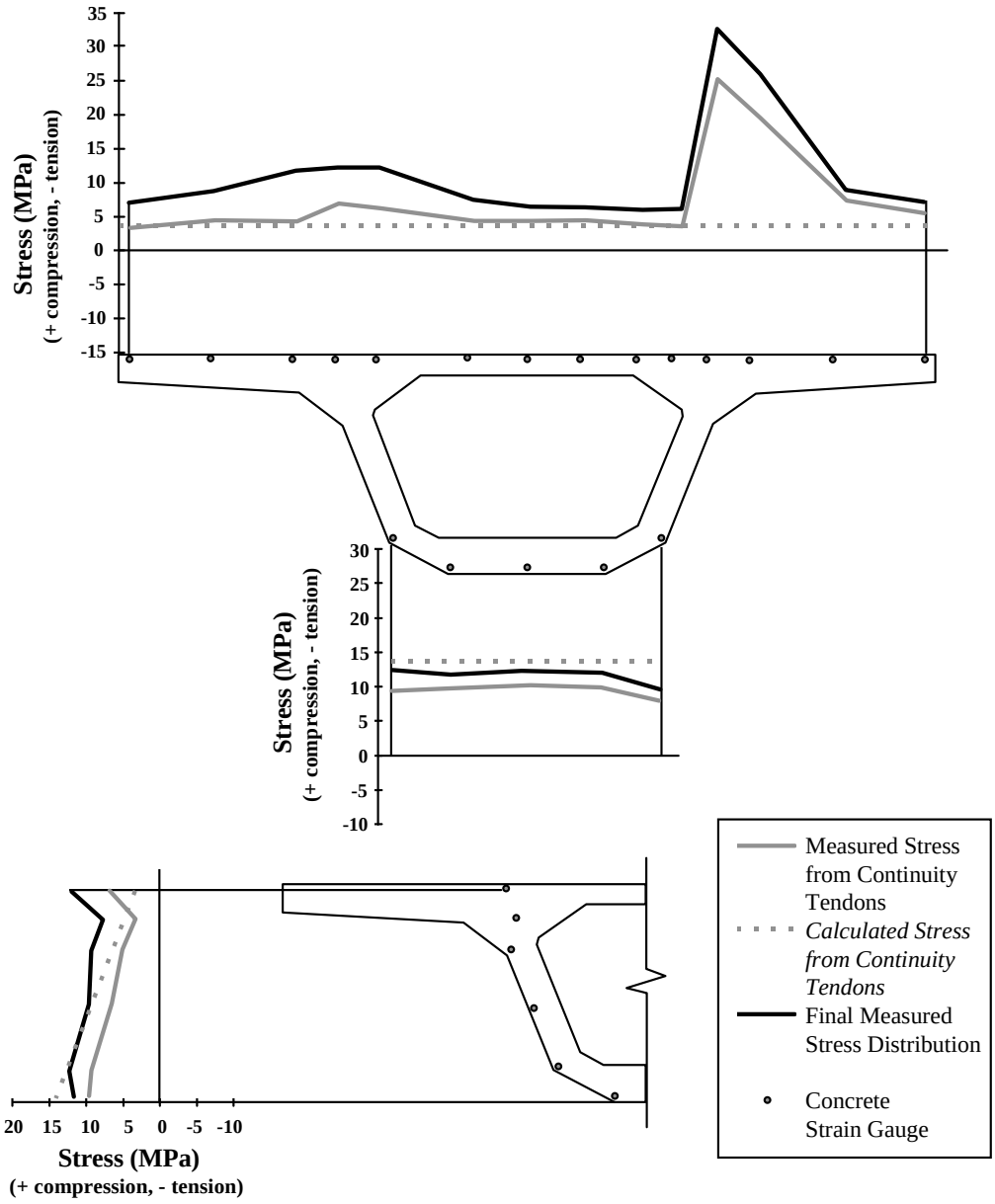

Figure 5.11 - Measured and calculated stresses in P16-10 after stressing of the continuity tendons in Span P16

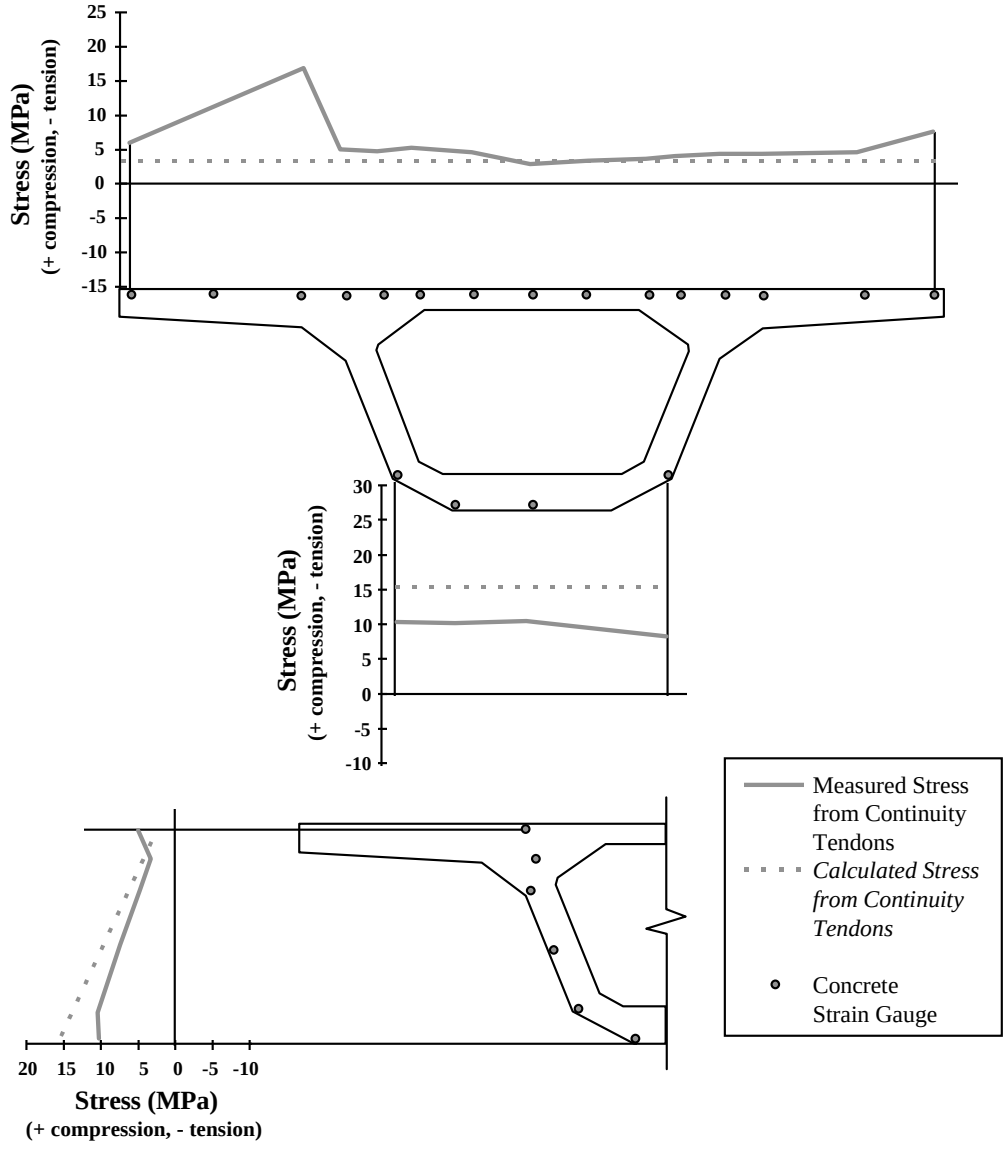

Figure 5.12 - Measured and calculated stresses in P16-17 after stressing of the continuity tendons in P16-17

The averages of the measured stresses from the continuity stressing are compared to calculated values in Table 5.3. The most likely reason for the large differences between the

measured and calculated stresses is that the true bearing and fixity conditions present between the piers and the superstructure were not represented in the calculation model which assumed idealized fixed or pinned connections at those locations.

	Stressing of Continuity Tendons		
	Average of Measured (MPa)	**Calculated (MPa)**	**Measured / Calculated**
P16-2			
Top	8.97	11.65	0.770
Bottom	-5.75	-8.25	0.697
P16-10			
Top	7.09	3.61	1.964
Bottom	9.94	13.92	0.714
P16-17			
Top	6.22	2.93	2.123
Bottom	10.45	15.25	0.685

Table 5.3 - Comparison of measured and calculated stresses from the stressing of the continuity tendons in Span P16

Cumulative stresses from selected gauges in each of the three instrumented segments during the continuity stressing operations are plotted in Figures 5.13 through 5.15. These plots demonstrate the changes that occur in the moment diagram during the continuity stressing process. Reversal of moment occurs in P16-2 as is indicated when the bottom flange stresses become less than the top flange stresses (a switch from negative to positive moment). The opposite switch begins to occur in P16-10 but is not quite as great. This section of gauges must be close to the inflection point of the moment diagram. No reversal of moment occurs in P16-17. The stresses start out at zero and a negative moment is applied to the section from the continuity tendons. The sharp but steady rise in stress measured by gauge C717 in P16-10 indicates that almost all of the continuity tendons are contributing to the sharp peak that occurs in the stress diagram over the right web of that segment.

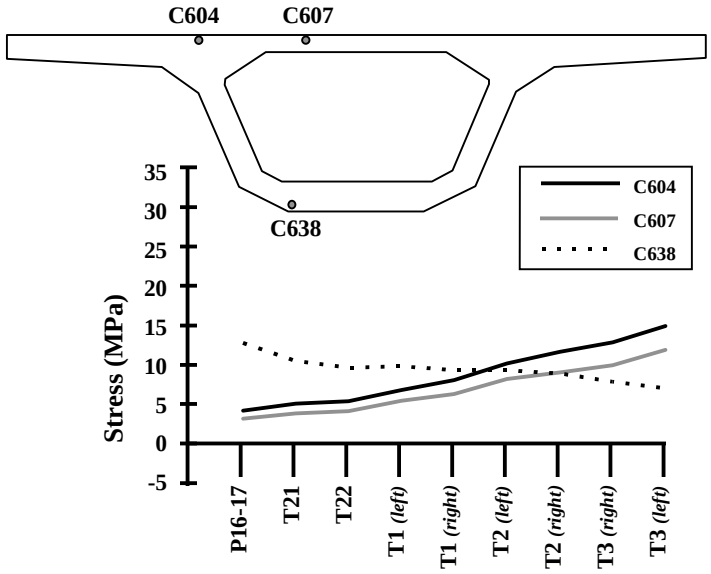

Figure 5.13 - Stresses in selected concrete gauges from P16-2 over the course of the continuity stressing sequence

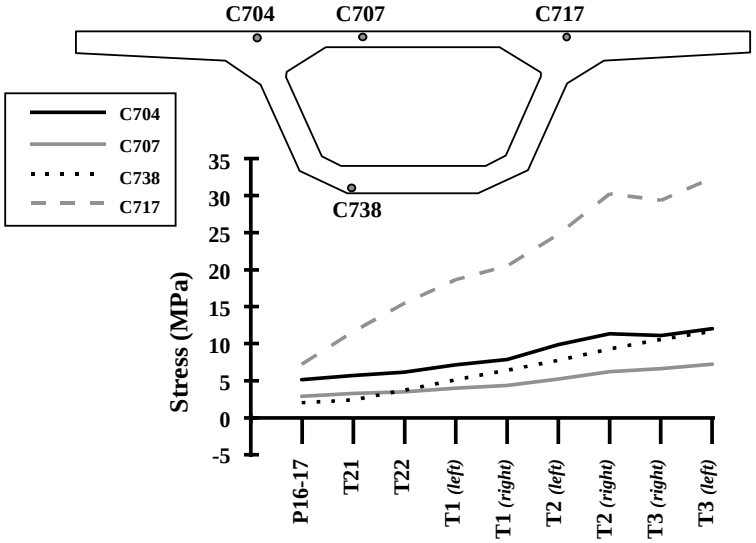

Figure 5.14 - Stresses in selected concrete gauges from P16-10 over the course of the continuity stressing sequence

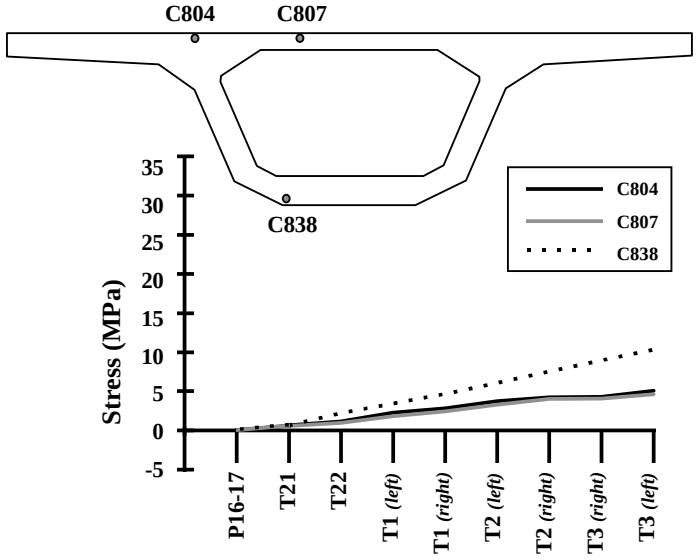

Figure 5.15 - Stresses in selected concrete gauges from P16-17 over the course of the continuity stressing sequence

5.3.2 Shear Stresses

Shear stresses caused by the stressing of the external continuity tendons were determined from the concrete strain gauge rosettes. These results are presented in Figure 5.16. No calculations of theoretical stresses were attempted. The maximum final shear stress was 0.95 Mpa (0.14 ksi) which is $0.14\sqrt{f'_c}$ (with f'_c in units of MPa). No problems due to shear should occur in the ramp.

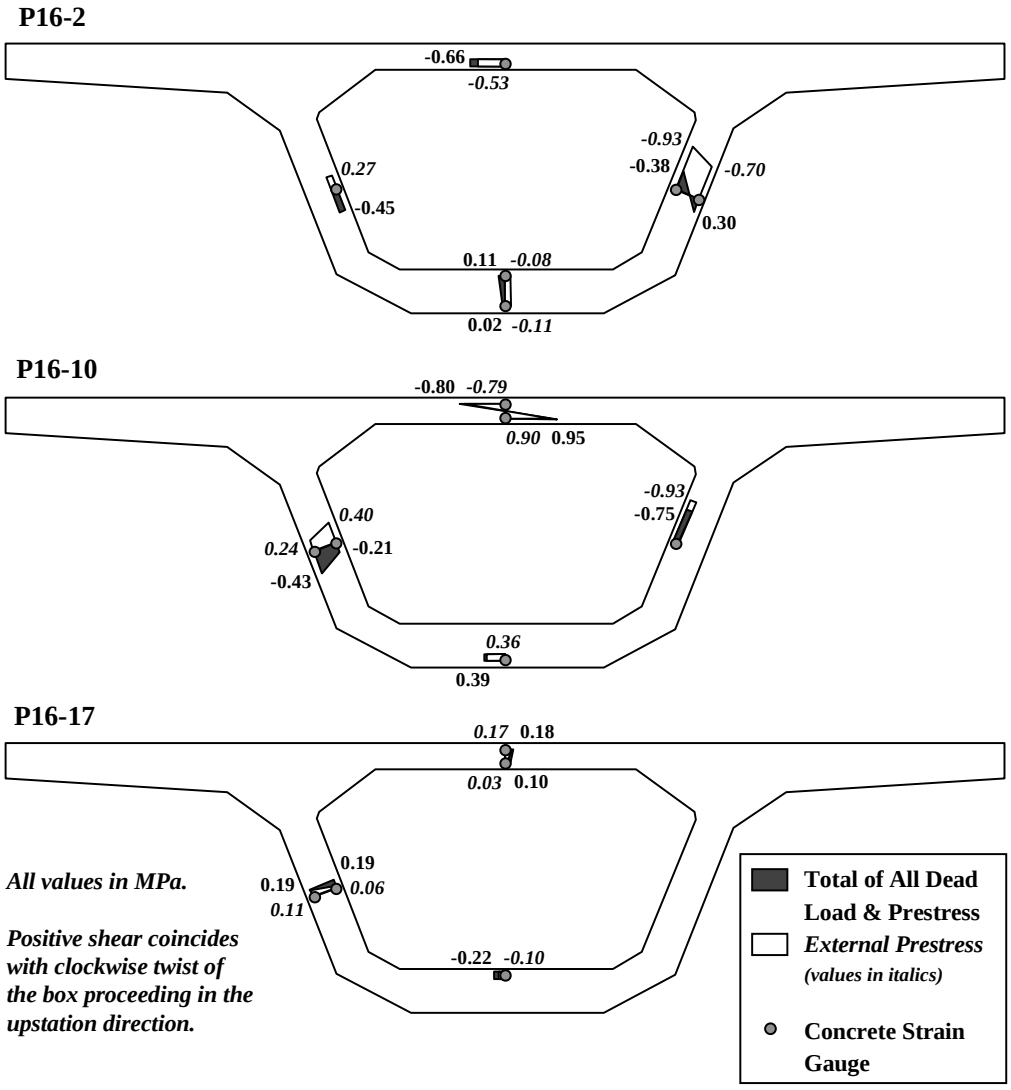

Figure 5.16 - Shear stresses after completion of the continuity operations in Ramp P

5.4 CONCLUSIONS AND RECOMMENDATIONS

5.4.1 Diffusion of Post-Tensioning

5.4.1.1 Conclusions

The AASHTO effective flange width method for normal forces over-estimated the maximum compression from the diffusion of post-tensioning, but only by 10% of the measured value. This error may be due to some uncertainty in the true value of the modulus of elasticity of the concrete. While the beam theory calculation gave a peak stress much closer to the measured, the AASHTO method was much better at predicting the distribution of the stress. Measurements of diffusion of post-tensioning from Roberts' study of the San Antonio Y indicated that the peak stresses were generally underestimated by the AASHTO method by as much as 30 % [19]. Roberts' measured stress data came from Demec point readings which may be less accurate than the concrete strain gauges used to measure the data presented in this chapter. Roberts concluded that the AASHTO method was acceptable within the tolerances given by allowable stresses because the peak stresses occurred over only a small portion of the cross-section, and the $0.4f'_c$ compression limit under service loads is fairly conservative. Based on the results of the San Antonio Y and U.S. 183 studies, no changes need to be made to the recommended AASHTO effective flange method for the actions of normal forces on cross-sections except that directions for the application of the method should be clarified.

Measurements of transverse stresses during post-tensioning indicated that warping of the girder cross-section occurs during the stressing process for pairs of tendons symmetrically placed on both sides of the cross-section. Unless two rams are used simultaneously during the stressing process, one side must be stressed before the other. During the interval in which the ram is moved to the other tendon, the unsymmetrical loading from the first tendon causes transverse bending stresses in the section. However, the transverse stresses measured in Ramp P under these conditions were so small that they were negligible. After both sides were stressed, the transverse stresses were reduced to nearly zero. This behavior is interesting to note, but poses no need for concern.

5.4.1.2 Recommendations

The current AASHTO methods for analysis of the diffusion of post-tensioning were found to be satisfactory for design purposes. The Figure 2.6.2.6.2-4 and the commentary for this section of the code should be changed to indicate that compatibility induced stresses and edge tensile stresses must still be considered near the end of the member just as in post-tensioned anchorage zones. The compressive force should be shown to spread out in a 30^{o} cone into the bottom flange as shown in Figure 5.2. However, the end of the flange cannot be neglected where possible tensile effects occur. Further research to clarify this application is recommended.

5.4.2 Construction Analysis

5.4.2.1 Conclusions

The calculated and measured longitudinal stresses compared well for the free cantilever. However, the free cantilever is a completely determinate case making the structure easy to model. The analysis performed for the fully continuous structure failed to predict the measured longitudinal stresses within reasonable limits. Predicted stresses were off by as much as 50% from the measured stresses. Under the fully continuous case, many of the finer details of the structure become important for predicting the structural behavior. For example, the bearing conditions of the actual bridge can be very important to the distribution of the internal forces within the structure. Idealization of such details in the calculation model could account for some of the differences. In general, accurate modeling of the bridge structure during the design process is very difficult because of the uncertainties of variables which depend entirely upon what happens during the construction process. Though the calculations which were performed were rudimentary, they might be representative of preliminary calculations which would be performed at the early stages of a design process.

There were some indications of shear lag in P16-2 under the fully continuous structural configuration. A slight reduction of the flange width at P16-2 was required for shear lag under the provisions of Section 4.6.2.6.2 of the *AASHTO LRFD Bridge Design Specifications* [2]. The data does not suggest that changes in this section of the code need to be recommended.

Longitudinal stresses in P16-10 after the continuity stressing indicate a sharp peak in stress over the right web. This peak probably originates from the vertical deviator. High stresses were expected near the deviator due to the transfer of forces from the deviation of the external tendons into the rest of the structure. The plane of gauges in P16-10 is probably within the discontinuity zone of the vertical deviator where Bernoulli beam theory does not apply. None of the standard analysis programs that are used for bridge design and generally based on beam theory assumptions would predict such a peak. However, finite element or strut-and-tie modeling would predict compression struts projecting from the corners of the deviator towards the top flange. High stresses in top and bottom extreme fibers caused by local zones are typically not included in service state analysis of a bridge structure, nor are they checked against service load stress criteria from the AASHTO bridge design codes. This accepted omission indicates the serious logical flaw of basing design primarily on allowable stresses but ignoring local stress regions in calculations.

Torsional calculations for the free cantilever indicated very low stresses would occur. Measurements of shear stresses in P16-2 during construction indicated no excessive torsional stresses. Vertical shear stresses were not correctly predicted at P16-2 by beam theory calculations. The differences between the measured and calculated vertical shear stresses at this cross-section may have been due to the proximity of the gauges to the support region and the heavy anchorage diaphragm. However, shear strains were not expected to be large in the webs of the box girder, and the concrete gauges may not be able to accurately measure the small changes in strain that are occurring.

5.4.2.2 Recommendations

No problems were indicated from the construction stresses. At this time, no recommendations based solely on the stress data from the construction process are being made.

CHAPTER 6

LIVE LOAD TEST

6.1 TEST DESCRIPTION

On February 13, 1997, after completion of the structure, but before asphalt had been applied to the deck surface, a live load test was performed on Ramp P. Loading from two lanes of standard HS20 AASHTO live load vehicles were simulated with two pairs of back to back dump trucks. The exact axle loads of the HS20 vehicle could not be reproduced. Therefore, the dump trucks were placed back to back at a spacing that would closely simulate the moment produced by an HS20 truck. Data was recorded for five load cases. Load case 1 was performed to produce a maximum positive moment at midspan in span P16. Load case 2 was performed to produce a maximum negative moment at the pier in span P16. Load case 3 was performed to test the carry-over moment to span P16 from load placed one span away. Load case 4 was performed to produce a maximum torque in the ramp. Load case 5 was performed to test the carry-over moment to span P16 from load placed two spans away. The locations of the dump trucks in these load cases are shown in Figure 6.1. The measured axle loads from the dump trucks used in the live load test are shown in Figure 6.2. Figure 6.3 shows some typical test procedures. The test took place from 8:30 am until 1:30 pm. Zero readings were taken before and after the test to remove thermal effects from the live load stresses.

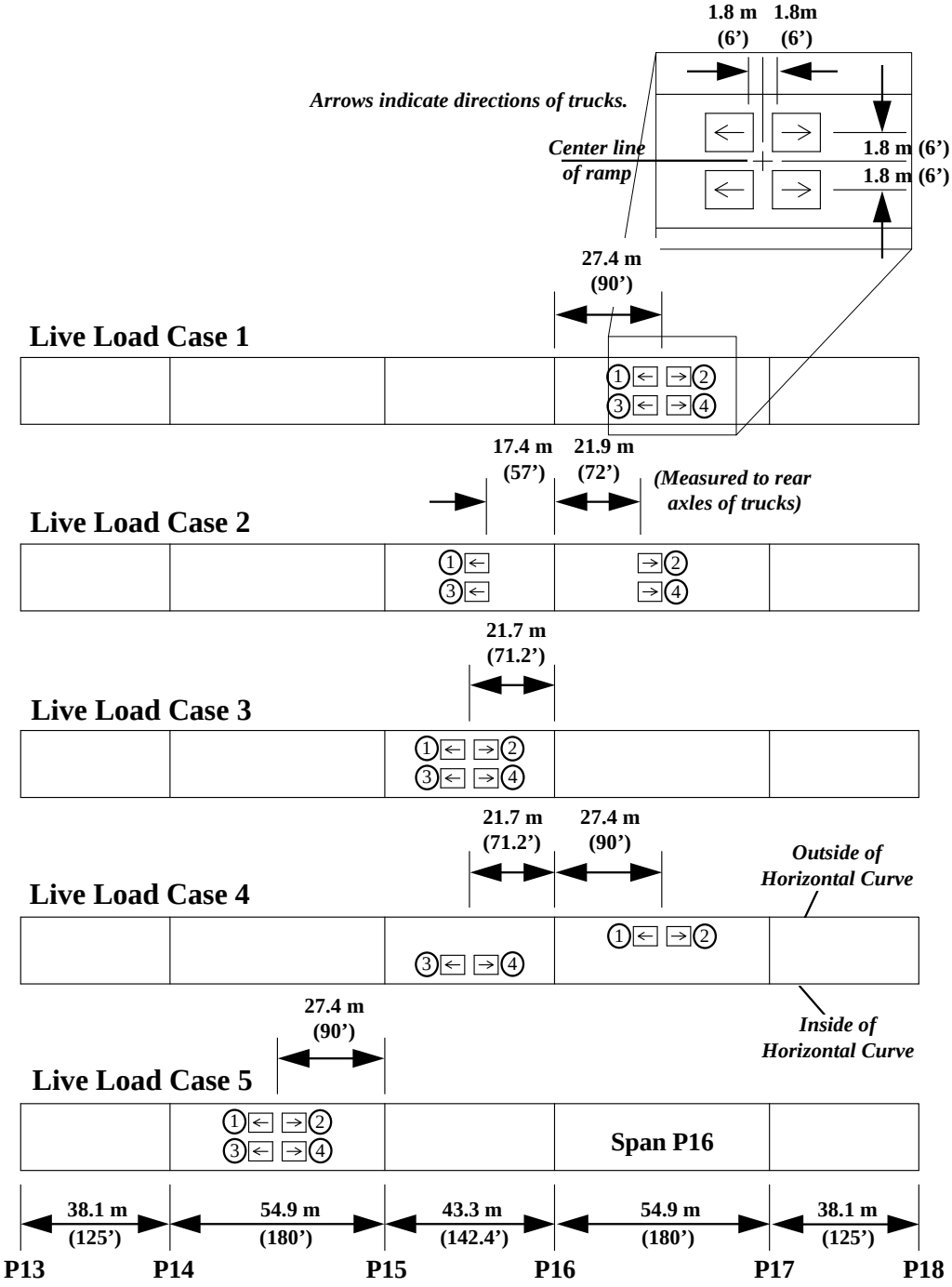

Figure 6.1 - Live load test cases

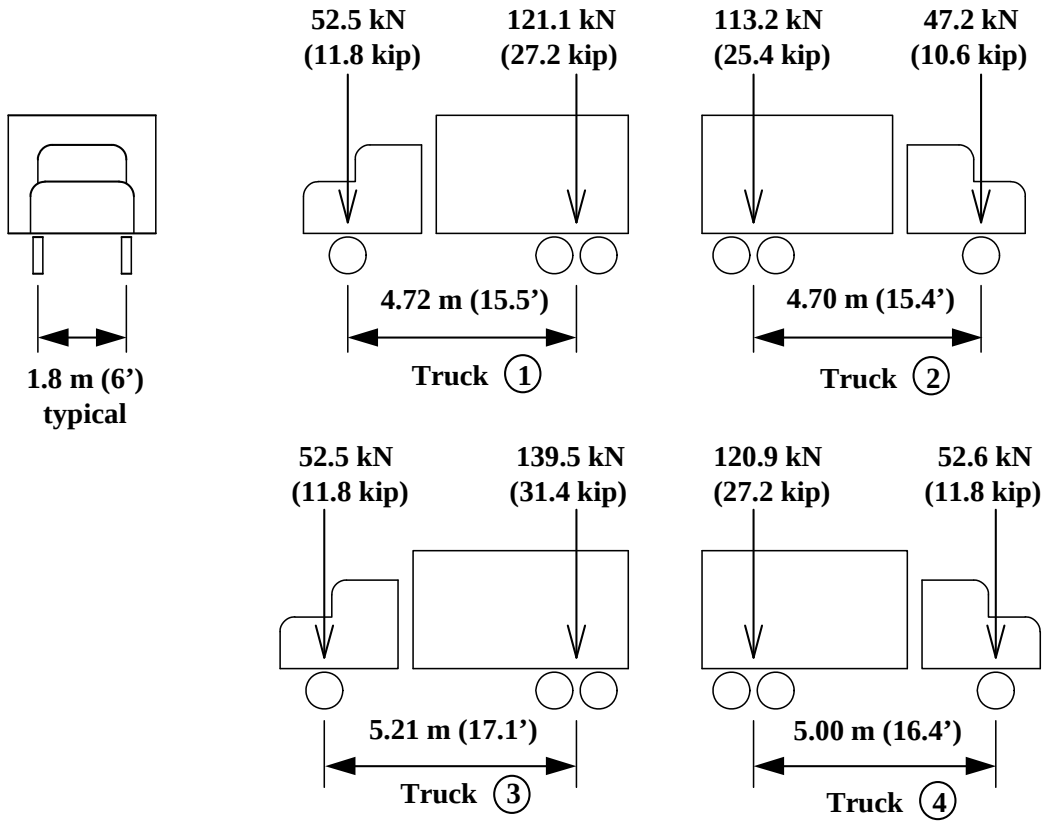

Figure 6.2 - Live load truck axle weights

Figure 6.3 - Pictures of the live load test (load case 4)

6.2 PRESENTATION OF RESULTS

6.2.1 Longitudinal Stresses

Measured longitudinal concrete gauge stresses at P16-2 from each of the live load cases are plotted in Figure 6.4. The plots indicate that the worst negative moment stresses were produced by load case 1. Calculated stresses indicated the same result though the configuration of the live load in load case 2 is more consistent with expectations for a maximum negative live load moment. Load cases 2 and 4 produced similar moments at the pier. The carry over moment from a load two spans over was negligible. All of the live load stresses at P16-2 were significantly smaller than the stresses measured during construction.

Figures 6.5, 6.6, and 6.7 show the measured longitudinal concrete gauge stresses from load cases 1 and 2 for segments P16-2, P16-10, and P16-17 respectively. Calculated stresses at the levels of the strain gauges are also plotted in these figures. A slight reduction of the effective top flange width of P16-2 was required by Section 4.6.4.6.2 of the *AASHTO LRFD Bridge Design Specifications* [2]. The internal forces at each section were calculated using a simple two dimensional frame solver (RISA2D [18]). A description of the input file model is given in Appendix A. The model used for the calculated stresses employs several simplifications. The cross-sections were modeled with their gross properties; no transformations of the prestressing steel were applied. The external tendons were not modeled, and the bearing pads were idealized as either fixed or free connections to the piers. A uniform modulus of elasticity was applied to the entire structure. Stress calculations for each section can be found in Appendix C. The plots of the longitudinal stresses indicate that the calculated results tended to over-estimate the magnitudes of the stresses, particularly in the bottom flange. This may be due to errors in the presumed modulus of elasticity for the concrete in Ramp P. Results from the specimen tests most likely under-estimated the modulus due to differences in the curing conditions between the concrete in the specimens and the concrete in the actual segments (as discussed in Section 3.7.1 in Chapter 3). Thus, when the measured data was converted from strains to stresses using the modulus measured from the specimens, the measured stresses would come out lower than the actual ones. Plots of the stresses for P16-10 in Figure 6.6 indicate that the calculated point of inflection for load case 1 was close to the actual point of inflection. All of the plots indicate that the neutral axis of the sections was close to that calculated from the un-transformed section. Drops in the top flange stress near

the wingtips for segment P16-2 indicate that some shear lag may be occurring. This would be consistent with the location of P16-2 near the support where shear forces are greatest. Some shear lag effect was predicted for the P16-2 cross-section. The average measured stresses for the top and bottom flanges of P16-2 and P16-17 were calculated and compared to the frame solver results. The percent errors of the calculated stresses are presented in Table 6.1.

	Load Case 1			**Load Case 2**		
	Average of Measured (MPa)	**Calculated (MPa)**	**Measured / Calculated**	**Average of Measured (MPa)**	**Calculated (MPa)**	**Measured / Calculated**
P16-2						
Top	-0.794	-1.153	0.689	-0.596	-0.751	0.794
Bottom	1.802	2.319	0.777	1.259	1.510	0.834
P16-17						
Top	1.054	1.349	0.781	0.475	0.605	0.785
Bottom	-2.264	-3.102	0.730	-1.012	-1.391	0.728

Table 6.1 - Comparisons of calculated and measured longitudinal stresses

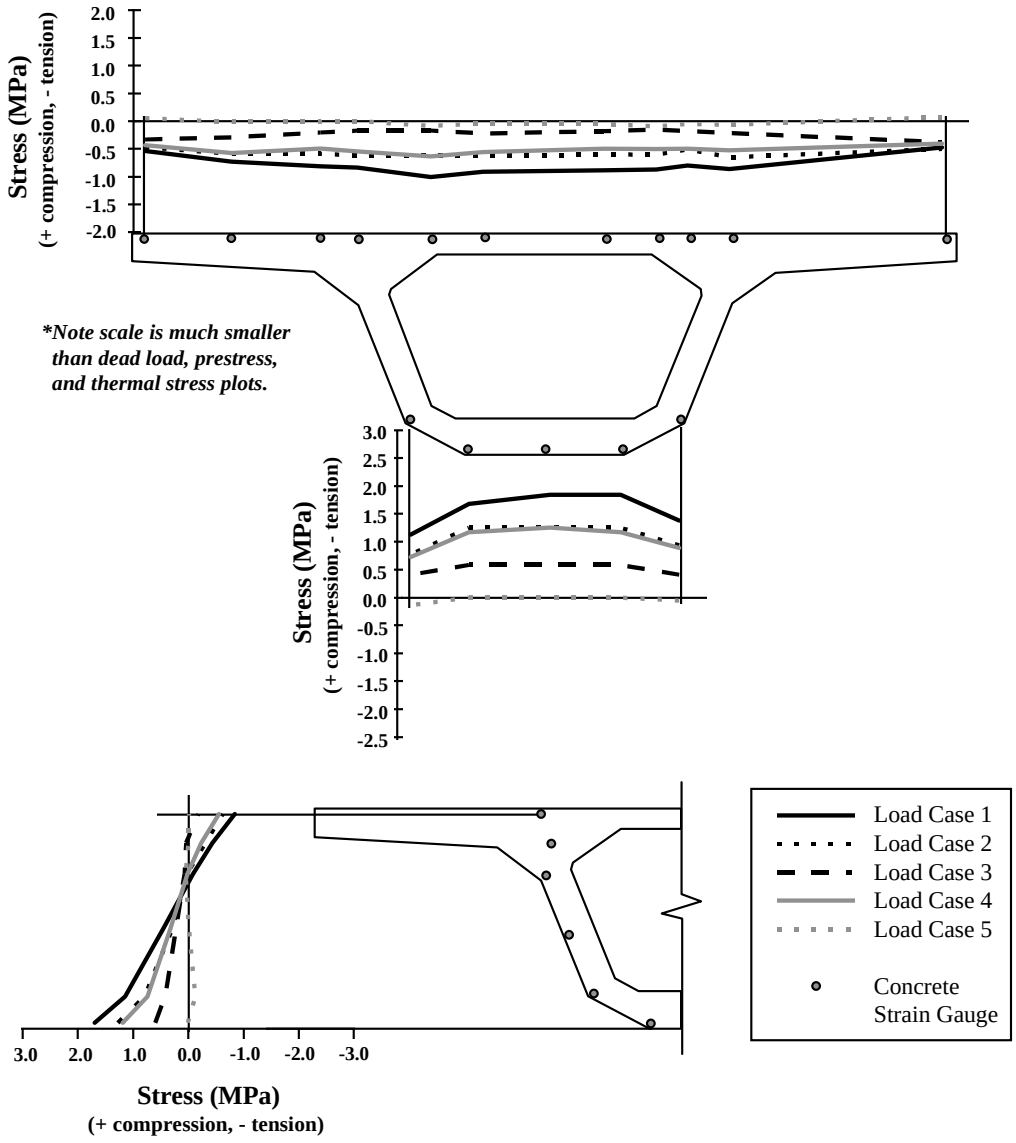

Figure 6.4 - Measured live load longitudinal stresses in P16-2

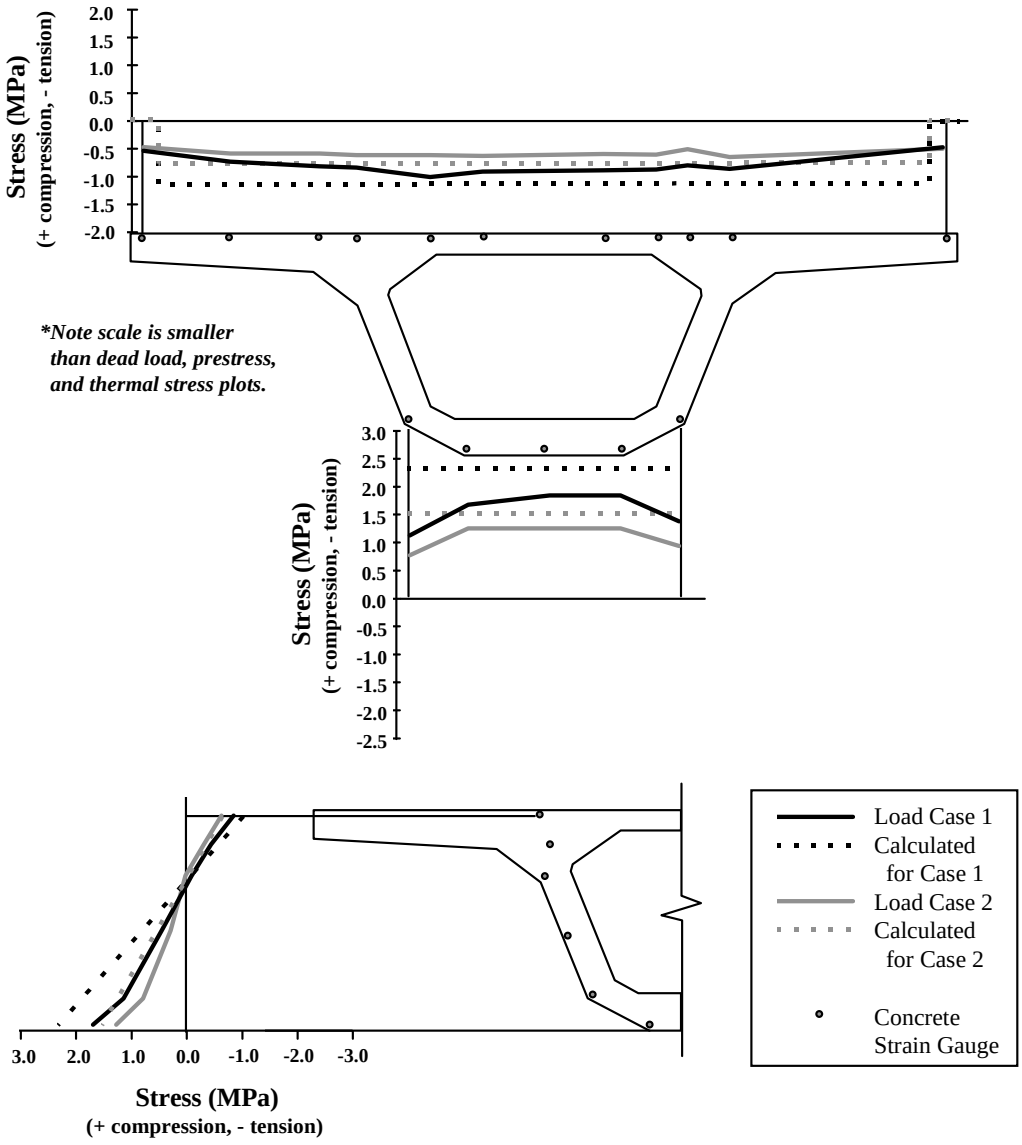

Figure 6.5 - Measured and calculated live load longitudinal stresses in P16-2

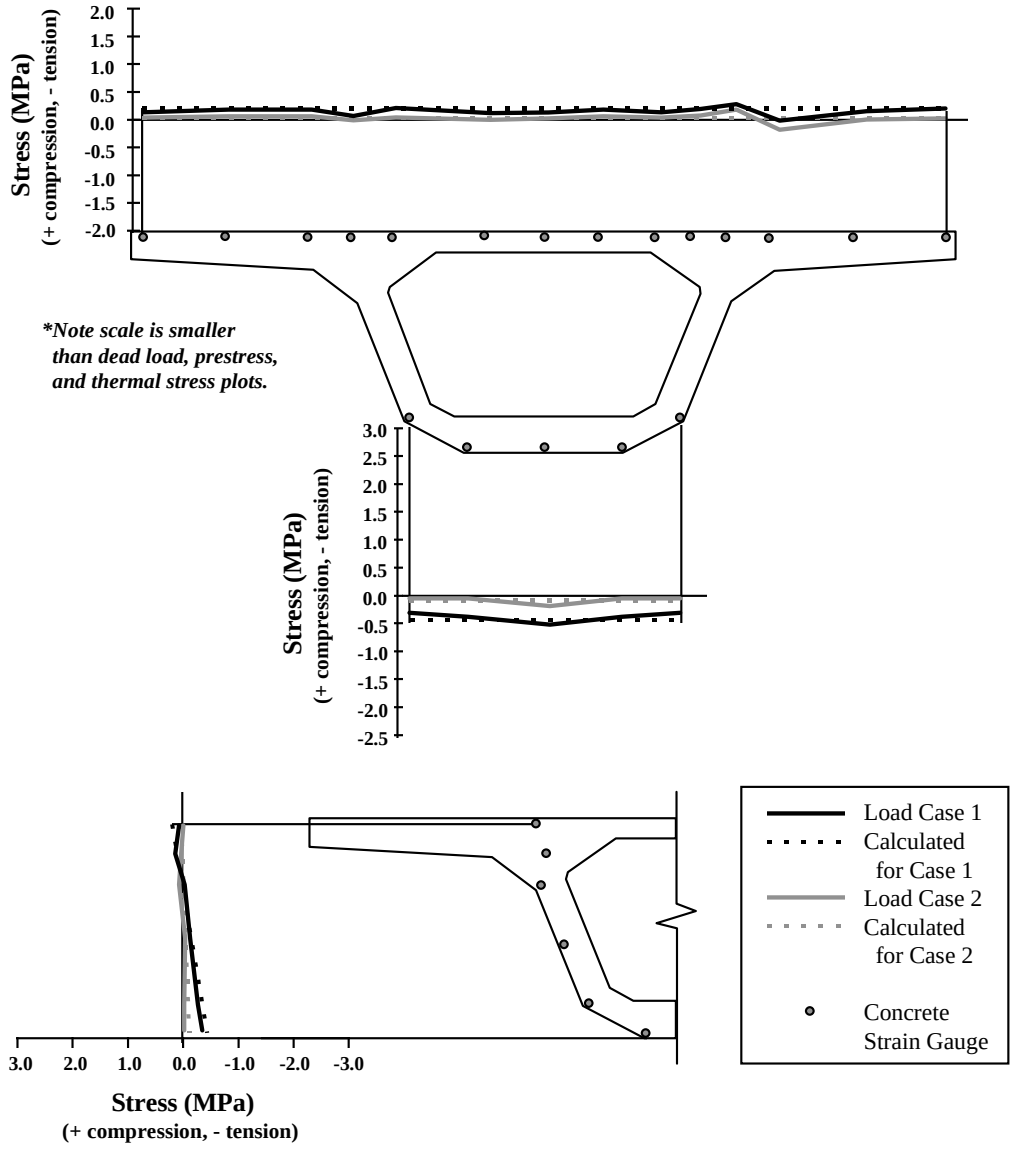

Figure 6.6 - Measured and calculated live load longitudinal stresses in P16-10

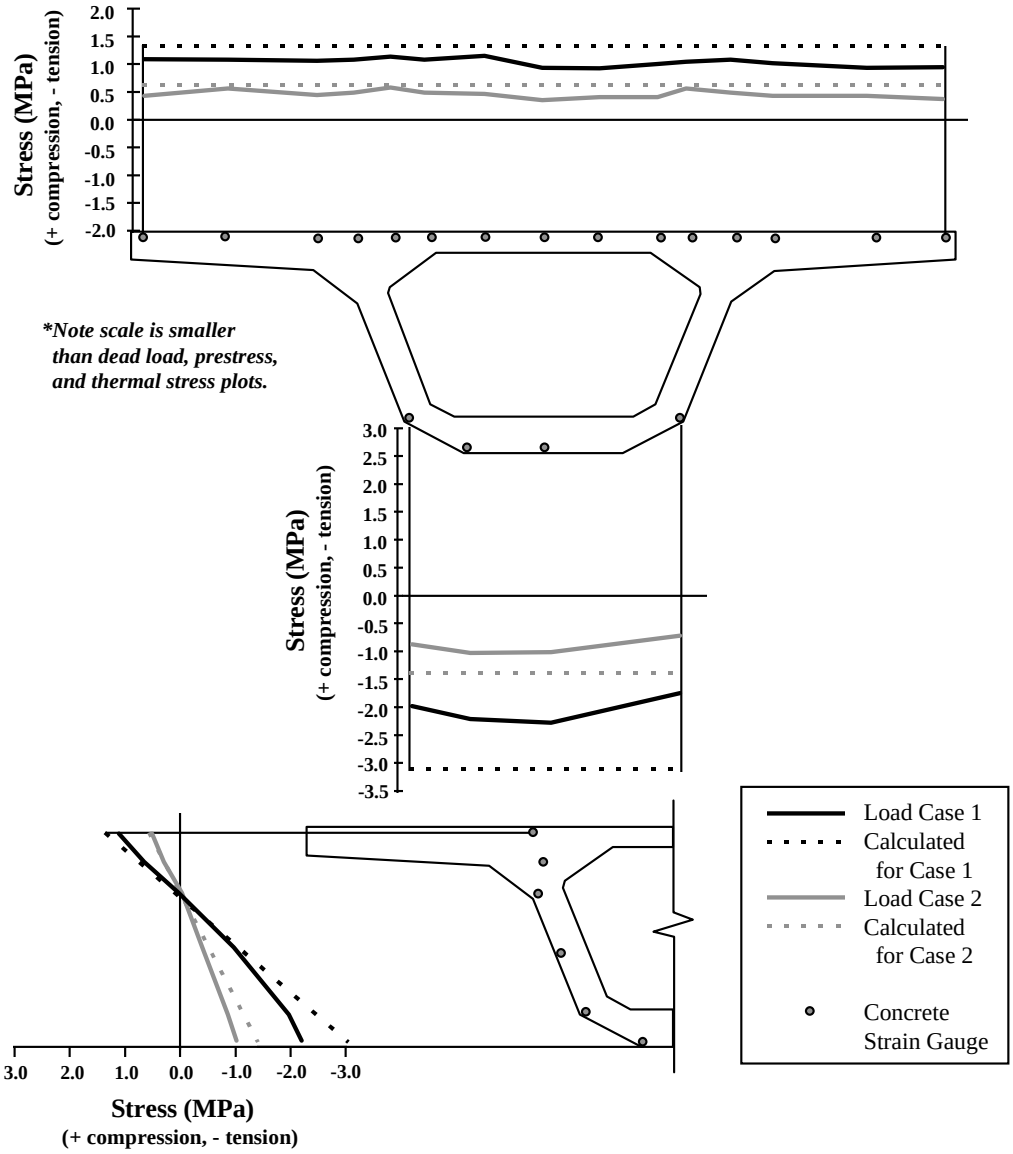

Figure 6.7 - Measured and calculated live load longitudinal stresses in P16-17

6.2.2 Shear Stresses

Shear stresses measured with the concrete gauge rosettes from live load cases 1 and 4 are plotted in Figures 6.8 through 6.9. Positive shear corresponds to clockwise twist of the girder progressing in the upstation direction of the ramp (into the page for all section figures). The measured shear stresses are plotted against calculated shear stresses. These calculations are given in Appendix B. The plots show that the approximate method over-estimated the shear stresses in the girder. The maximum shear stress of 0.16 MPa was measured in P16-17. This value was 29 % of $\sqrt{f'_c}$. The low values of strain associated with these stresses may not have been high enough for the concrete strain gauges to measure properly. Thus the reason for the large disparity between the measured and calculated data.

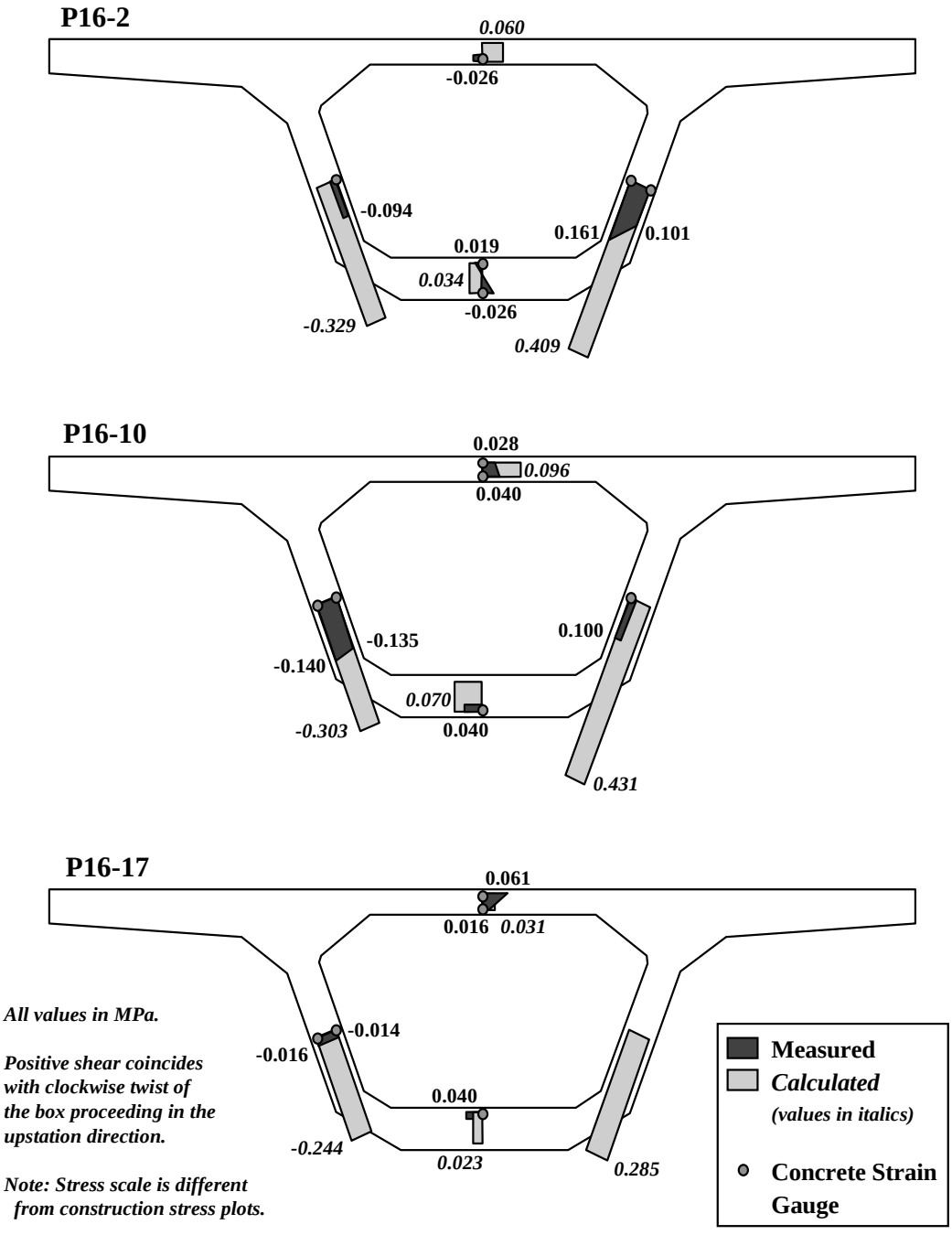

Figure 6.8 - Measured and calculated shear stresses from live load case 1

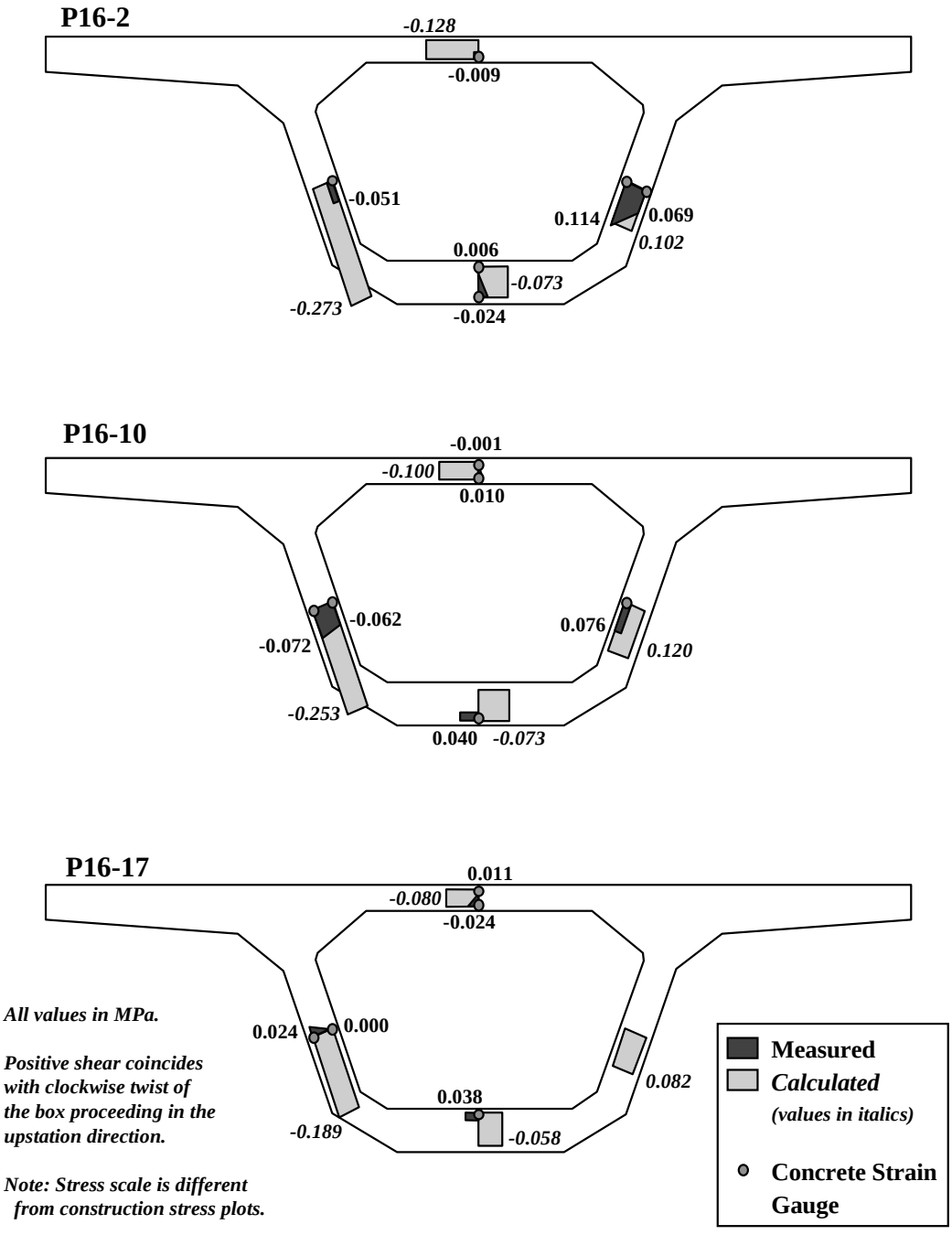

Figure 6.9 - Measured and calculated shear stresses from live load case 4

6.2.3 External Tendon Stresses

Stresses measured in the external tendons from load cases 1, 2, and 3 are plotted in Figures 6.10 through 6.12 respectively. All of the load cases produced negligible stresses in the draped portions of the external tendons. The worst stress increase was 8.4 MPa in the right T3 tendon which was produced by load case 1 with the trucks at the midspan of P16. The left tendon underwent a similar stress increase of 8.0 MPa tension. There seems to be no difference in the behavior between the right side tendons and the left side tendons. No data was available for the left side T1 and T2 tendons on the upstation side of the vertical deviator because of bad gauges. All of the external tendons in Ramp P were composed of nineteen 1.52 cm (0.6") diameter low relaxation strand. The area of each strand was 1.4 cm^2 (0.217 in^2) and the yield stress was 1860 MPa (270 ksi). Live load fatigue should not be a concern for the tendons. Ryals [20] recommends a fatigue limit of 69 MPa (10ksi) for external tendons.

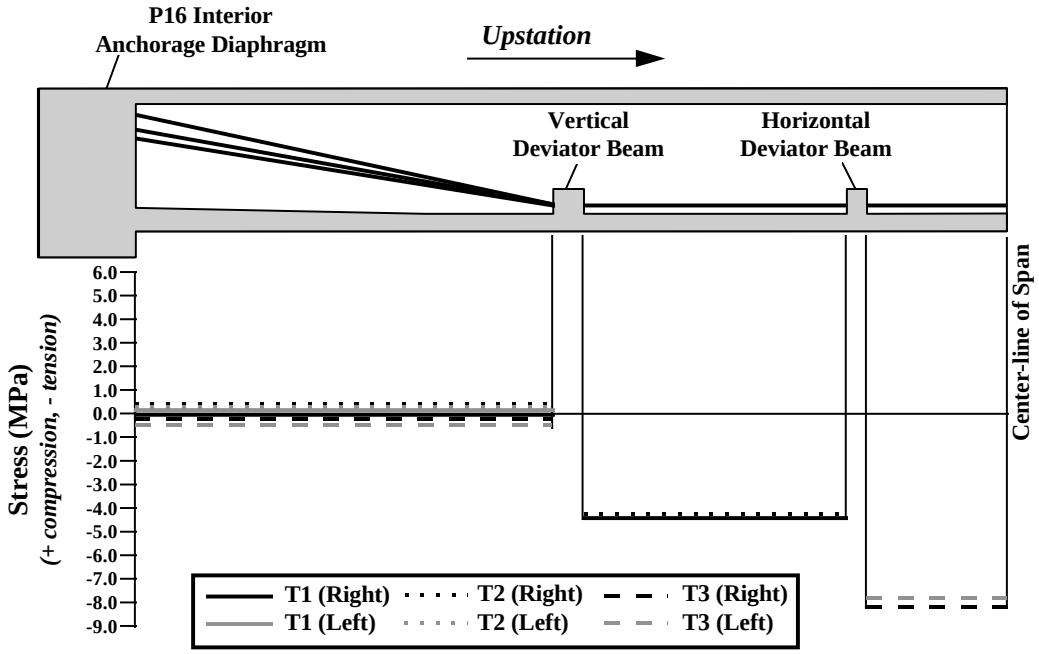

Figure 6.10 - Stresses in the external tendons from live load case 1

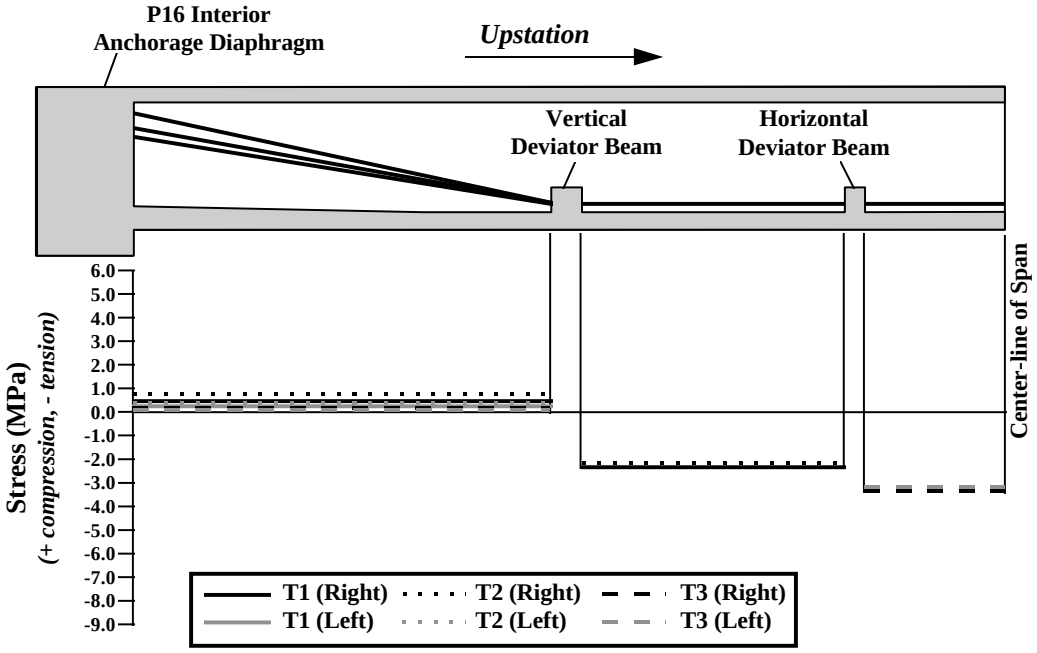

Figure 6.11 - Stresses in the external tendons from live load case 2

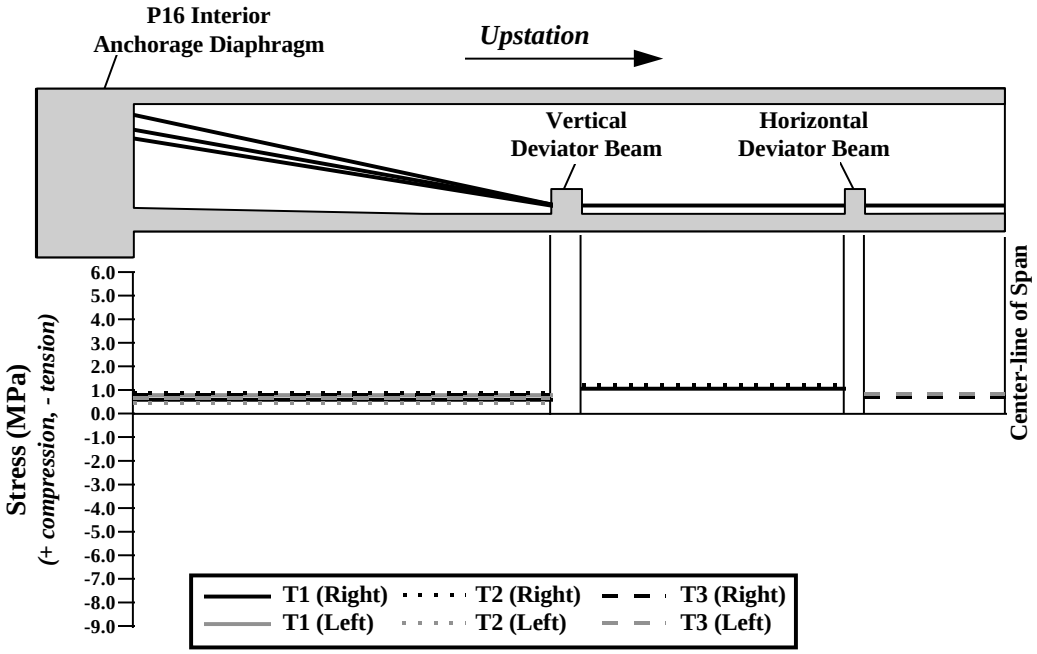

Figure 6.12 - Stresses in the external tendons from live load case 3

6.2.4 Tilt Meter Data

The measured tilts and slopes of the ramp from load cases 1, 2, and 4 are plotted in Figures 6.13 through 6.15 respectively. Positive twist is clockwise as one proceeds in the upstation direction of the bridge. Deflections were calculated by integrating the tilt and slope values. The trapezoidal method was used for the integration. The integrated deflections were shifted so that boundary conditions of zero vertical deflections at piers P16 and P17 were met. Calculated slopes and deflections from a two dimensional (2-D) frame solver (RISA2D [18]) are also plotted. The model used for the calculated values was the same as that used to compare results in Section 6.2.1 for the longitudinal stresses. The same limiting assumptions discussed previously apply to these results. Table 6.2 lists the maximum slopes at the quarter points of span P16 from the measured and calculated results. Table 6.3 lists the maximum deflections at the P16 midspan from the measured and calculated results. The deflections are reported in absolute units as fractions of the span length (59.4 m (180')). The slopes compared favorably despite ignoring the effects of the horizontal curve in the 2-D frame model. Some of the error may be attributable to the modulus of elasticity that was used to model the concrete in the 2-D frame model. As discussed in Section 6.2.1, the values for the modulus of elasticity used in the 2-D frame model may be lower than the actual modulus of elasticity in the concrete of Ramp P. The deflections compared less favorably. Ignoring the transformed tendon areas made the calculation model more flexible than the actual ramp. The modulus used in the calculation model was, again, probably a little low. On the other hand, the integrated values of deflection will be too small because area has been lost off of the measured slope curve where straight line segments have been drawn between data points. The actual slope curve would be more rounded and enclose more area. The maximum calculated deflection was ℓ/5330 and the maximum integrated deflection was ℓ/7410. The true value is probably in between those two.

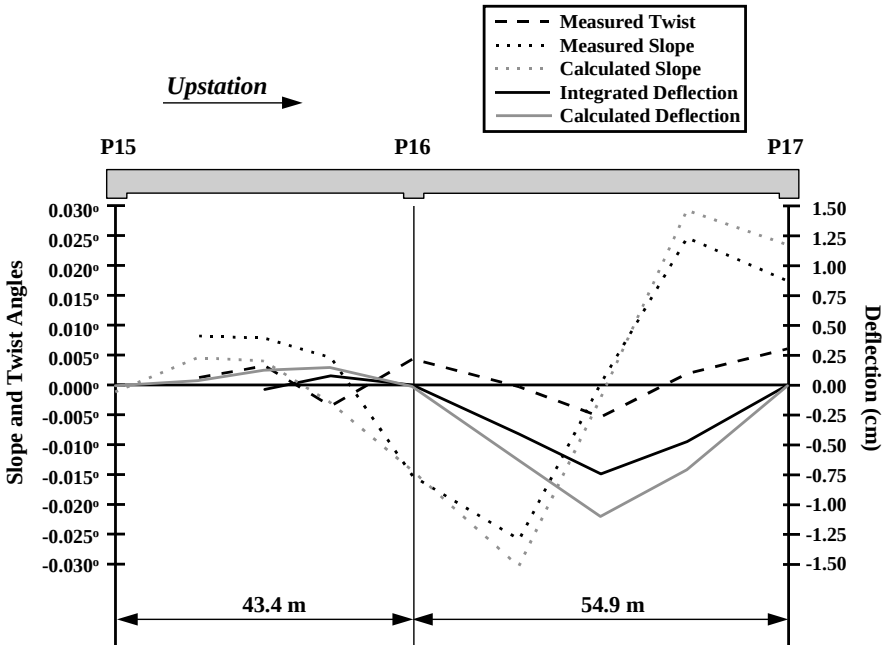

Figure 6.13 - Tilts, slopes, and deflections from live load case 1

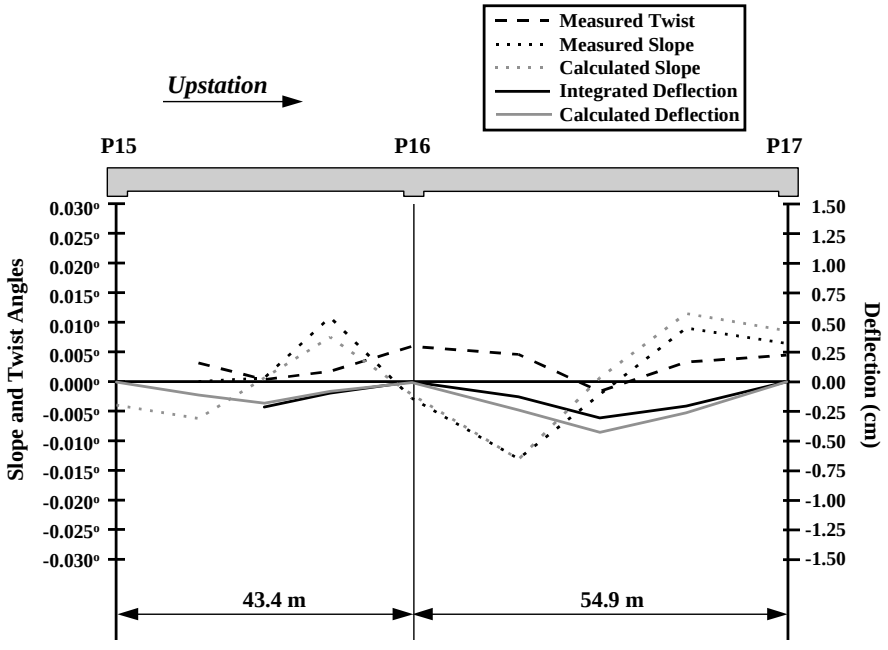

Figure 6.14 - Tilts, slopes, and deflections from live load case 2

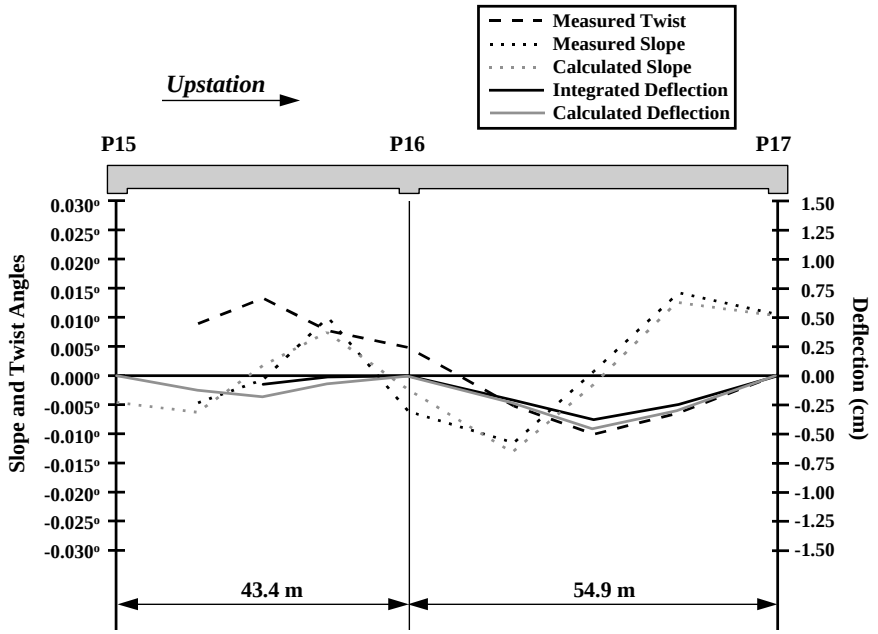

Figure 6.15 - Tilts, slopes, and deflections from live load case 4

	Load Case 1	**Load Case 2**	**Load Case 4**
Downstation Quarter Point			
Measured	$-25.7(10^{-3})$ °	$-13.0(10^{-3})$ °	$-11.4(10^{-3})$ °
Calculated	$-30.9(10^{-3})$ °	$-13.2(10^{-3})$ °	$-13.2(10^{-3})$ °
Measured/Calculated	**0.832**	**0.985**	**0.864**
Upstation Quarter Point			
Measured	$24.6(10^{-3})$ °	$9.1(10^{-3})$ °	$14.2(10^{-3})$ °
Calculated	$29.8(10^{-3})$ °	$11.5(10^{-3})$ °	$12.6(10^{-3})$ °
Measured/Calculated	**0.826**	**0.791**	**1.127**

Table 6.2 - Comparison of measured and calculated slopes

	Load Case 1	**Load Case 2**	**Load Case 4**
Integrated	0.74 cm	0.30 cm	0.38 cm
Calculated	1.11 cm	0.43 cm	0.46 cm
Measured/Calculated	**0.667**	**0.698**	**0.826**
	As Fractions of the Span Length (59.4 m):		
Integrated	ℓ/7410	ℓ/18290	ℓ/14440
Calculated	ℓ/5330	ℓ/13720	ℓ/12910

Table 6.3 - Comparisons of integrated and calculated deflections

6.3 CONCLUSIONS AND RECOMMENDATIONS

6.3.1 Conclusions

Results from the live load test verify reliable service load behavior from the ramp. All of the measured stresses are probably slightly smaller than the true values because the modulus of elasticity used to convert the measured strains into measured stresses was most likely too small. Some shear lag is occurring in P16-2. Section 4.6.2.6.2 of the *AASHTO LRFD Bridge Design Specifications* [2] indicates that shear lag is most likely to occur near support regions and a slight reduction of the effective top flange width was required at P16-2. The small drops in stress at the top flange wingtips in P16-2 are consistent with the AASHTO provisions.

Section 4.6.1.2 of the *AASHTO LRFD Bridge Design Specifications* refers to the analysis of structures curved in plan. Spans on bridges which subtend a central angle less than 12^o may be analyzed as if straight. The angle subtended by span P16 of the U.S. 183 Ramp P is 15.4^o, thus consideration of the ramp's horizontal curve is necessary for its design. The standard practice of most engineers is to analyze the moments, axial forces, and vertical shears using a two-dimensional (2-D) beam program which accounts for prestressing and time effects, and to analyze the torsional shears and transverse moments on the substructure using a three-dimensional (3-D) frame solver which does not model the prestressing or time effects. The calculated results from the 2-D frame solver gave similar shapes for slopes and deflections as well as the longitudinal stress when compared to the measured results. Furthermore, there is little evidence that the horizontal curve of the bridge effected the distribution of live load to the external tendons from the inside of the horizontal curve to the outside. This indicates that the horizontal curve of the ramp had little effect on the distributions of the moment, axial forces, and vertical shears from the live load, and exclusion of consideration of the horizontal curve from calculations of these actions is acceptable for spans with central angles of up to 15.4^o and probably higher.

All of the live load cases produced stresses which were much smaller than the dead load and prestress stresses. Furthermore, the live load deflections were minimal. This would indicate that the bridge probably has a large reserve for additional live load capacity under service conditions.

6.3.2 Recommendations

The effects of torsion on flexural behavior for horizontally curved bridges can be ignored for bridges with individual spans that subtend central arcs of up to 15^{o}. No other recommendations are being made at this time.

CHAPTER 7

THERMAL BEHAVIOR

7.1 TEMPERATURE TRENDS

Daily temperature trends for the Ramp P structure are discussed in this section. Magnitudes for the maximum positive and negative temperature gradients measured through the cross-section are presented. Statistical distributions of the occurrence of positive and negative gradients are tabulated and presented as well.

7.1.1 Daily Temperature Cycles

Measurements in other temperature studies have indicated that the thermal gradient shape shown in Figure 7.1 is generally applicable for concrete box girders [6, 16, 19, 21, 22]. Studies of the thermal gradient shapes from the Ramp P data also indicated that the shape shown in Figure 7.1 was fairly typical for the Ramp P cross-section. Figures 7.3 and 7.4 which show the maximum measured positive and negative thermal gradients confirm this. Based on the characteristics of this typical shape, the daily thermal gradients were evaluated based on adjusted top and bottom temperature magnitudes. To account for variations in ambient temperatures at different times, average thermocouple temperatures at any instant were calculated at three locations: the top of the box, the junction between the webs and the top flange, and the bottom of the box. The average temperature at the junction between the webs and the top flange was then used as a baseline reference temperature and deducted from the measured average top and bottom temperatures. The resulting corrected temperatures were taken as the basis for the determination of the thermal gradients. Figure 7.1 shows the locations of the thermocouples and the critical values of the thermal gradient that were calculated. The terms “top gradient” and “bottom gradient” are used throughout this report to refer to the magnitudes of the thermal gradient at the top and bottom fibers of the section.

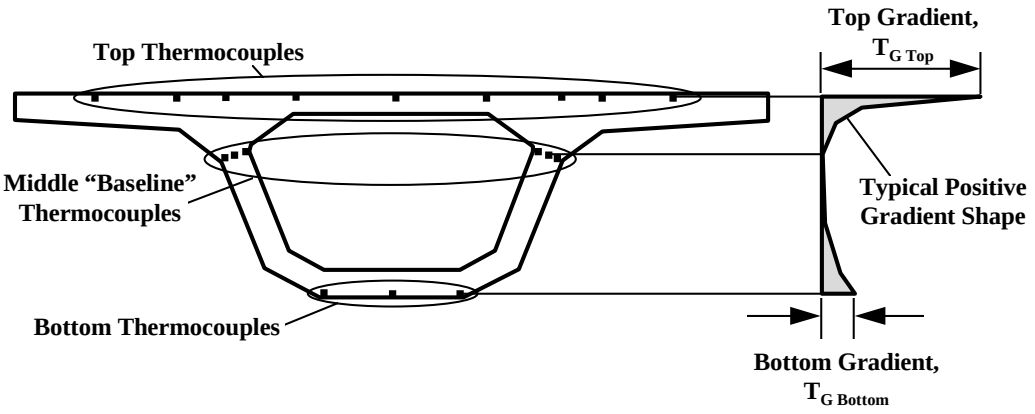

Figure 7.1 - Thermocouples used to calculate thermal gradient magnitudes

A positive gradient is defined as the case where the top flange temperatures exceed the webs and bottom flange temperatures. A negative gradient is defined as the case where the top flange temperatures are lower than the webs and usually the bottom flange temperatures. The maximum positive and negative gradients that were measured in the ramp occurred in March of 1997. Figure 7.2 shows the top and bottom gradient temperatures recorded in Ramp P as well as the ambient air temperature from the month of March 1997. During this month, a large, aberrant positive gradient occurred from the application of the asphalt wearing surface to the top deck of the bridge. This large gradient occurred when the 176 ^{o}C (350 ^{o}F) liquid asphalt was sprayed onto the surface of the deck temporarily heating the concrete. This event was excluded from the statistical counts of the data. Maximum positive gradients generally occurred in the afternoon around 3:00 pm. Maximum negative gradients generally occurred in the early morning at about 7:00 am. Temperature trends for the ramp from the complete set of recorded data up to the time of this writing are presented in Appendix D.

The maximum positive and negative thermal gradients that were measured in Ramp P are shown in Figures 7.3 and 7.4. Temperature values for the all of the thermocouple gauges are presented in a tabular form. Selected thermocouples have been plotted to show the shape of the temperature distribution. It is apparent from the data presented in these figures that the actual gradients which occurred have complex three dimensional distributions that are influenced by the shape of the box cross-section.

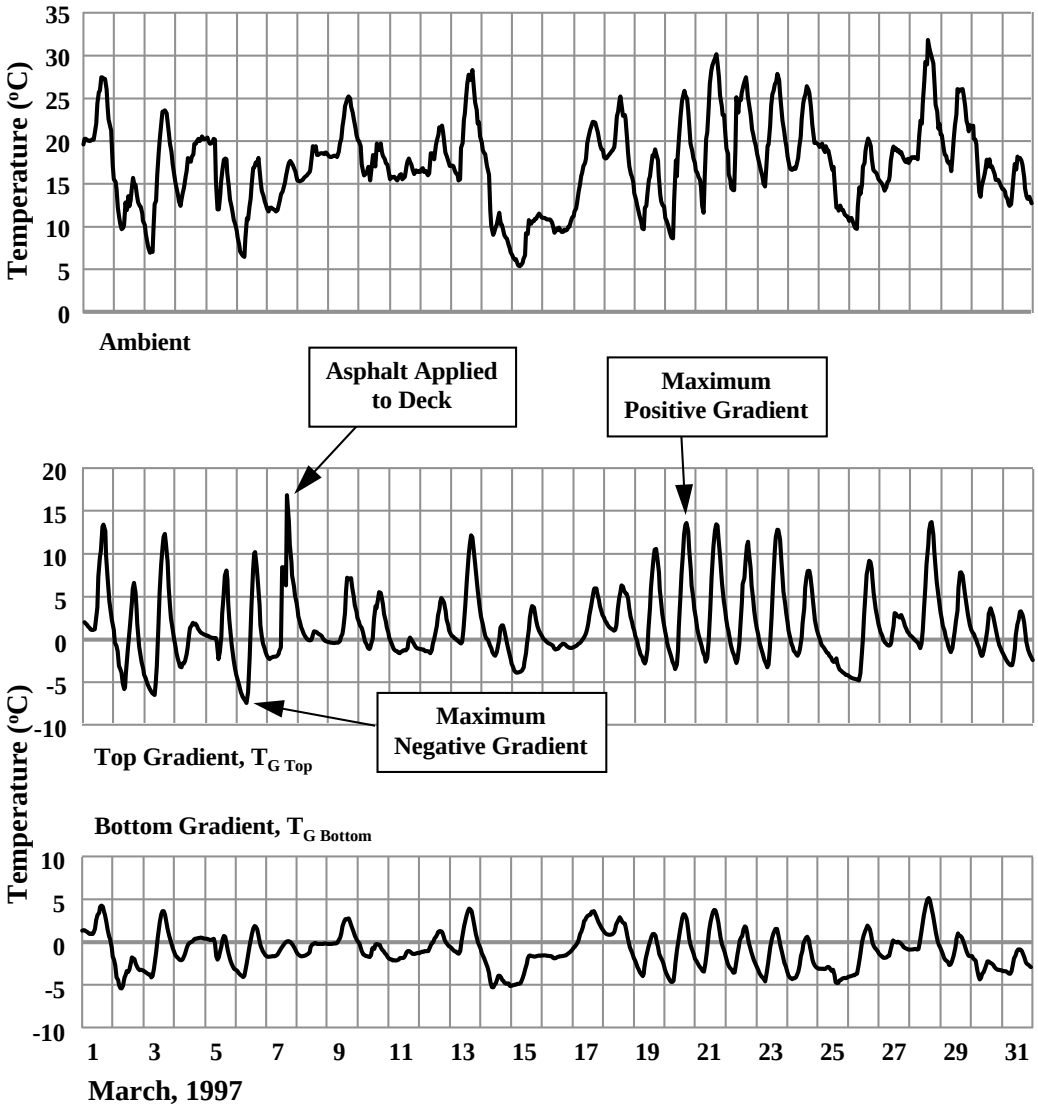

Figure 7.2 - Measured thermal gradients for the month of March 1997

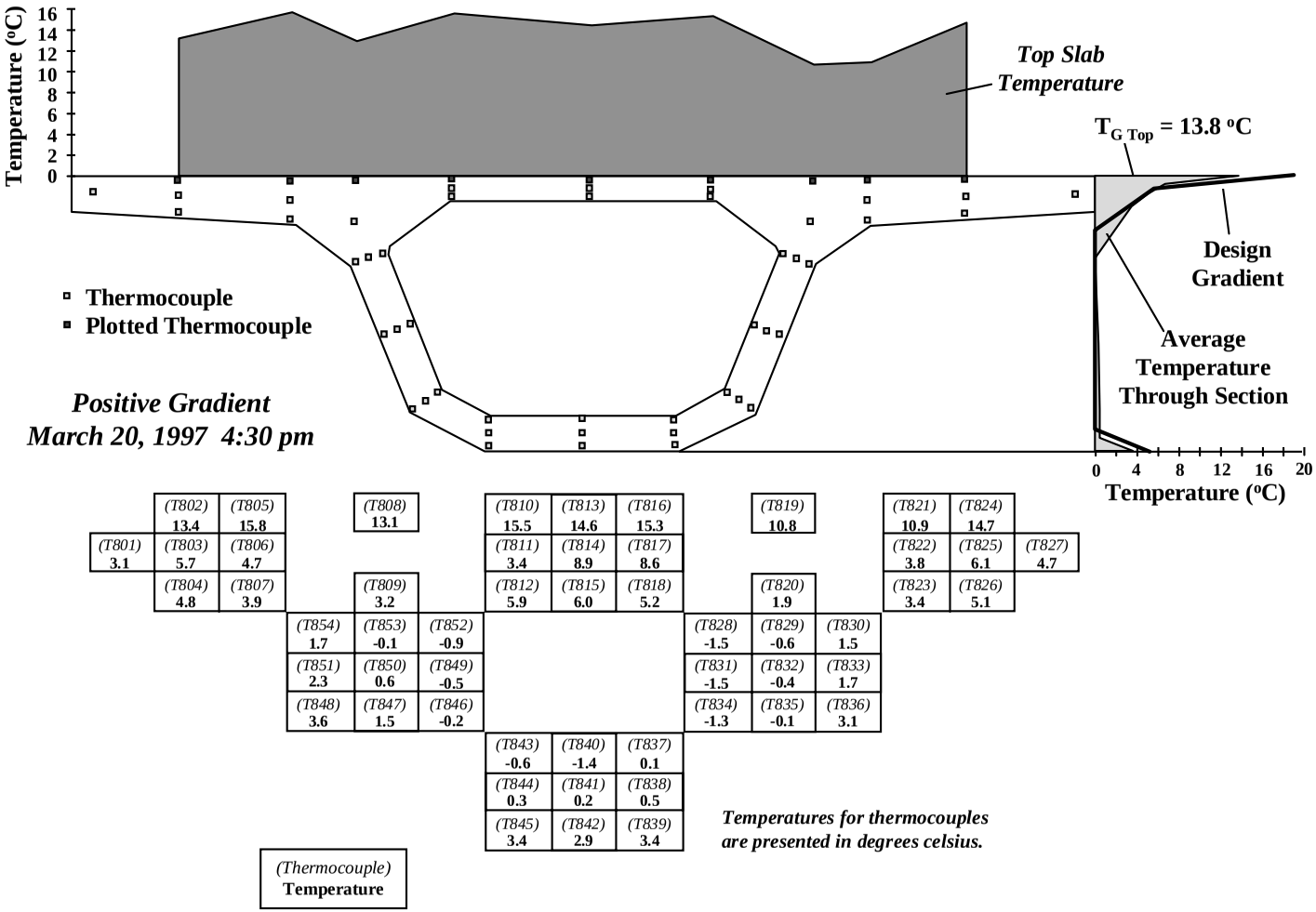

Figure 7.3 - The maximum measured positive gradient (from March 20, 1997)

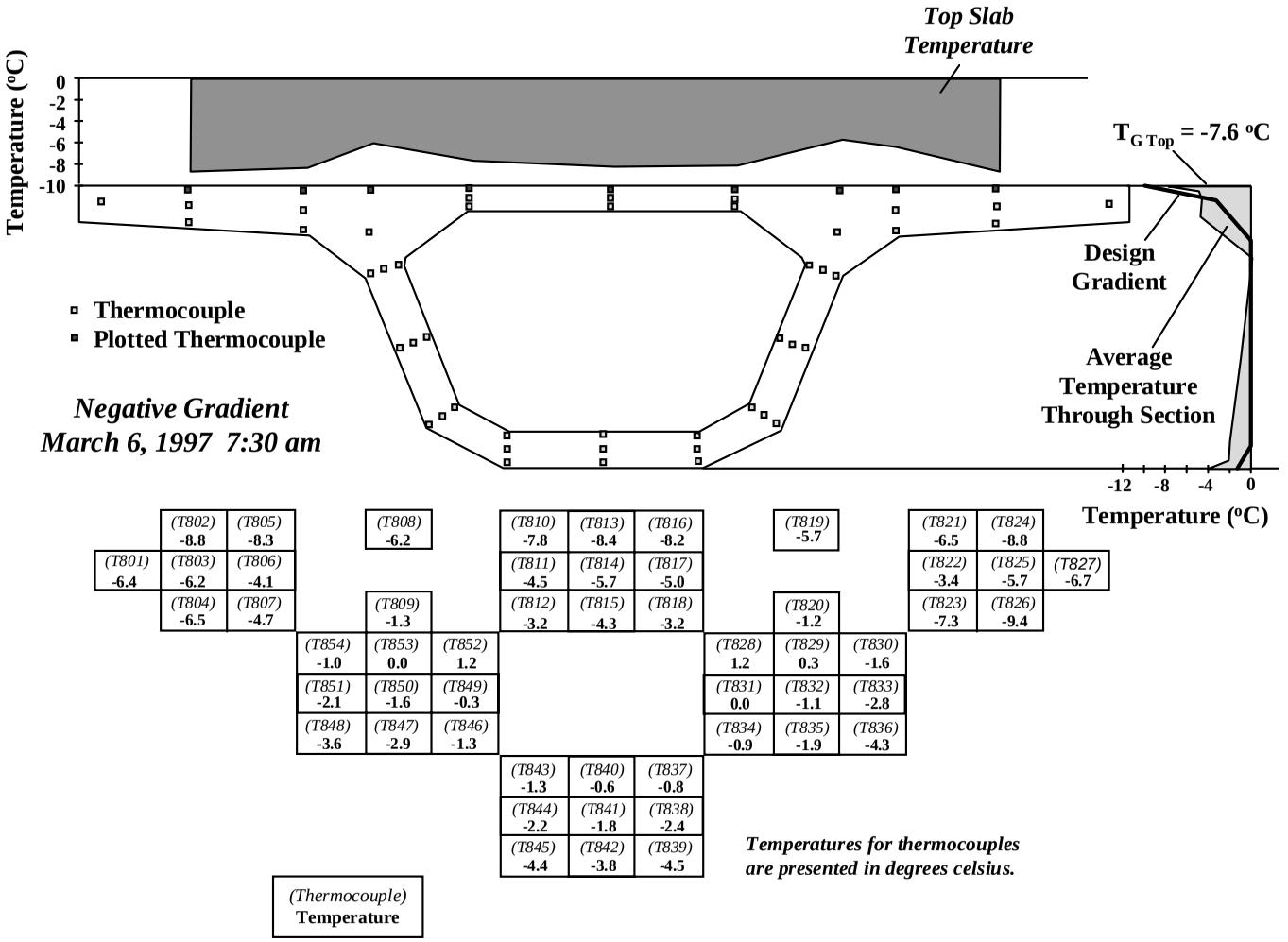

Figure 7.4 - The maximum measured negative gradient (from March 6, 1997)

Figure 7. 1Figure 7. 2Figure 7. 3Figure 7. 4

7.1.2 Statistical Occurrence of Gradients

Positive and negative gradient peaks were tabulated for the periods before and after application of the 5 cm (2") thick asphalt blacktop. The peaks were taken from 24 hour daily time intervals. Occurrence ratios for different magnitudes of the gradients were calculated for the periods before and after the application of the asphalt blacktop. The range of data available before the application of the blacktop included only 98 days of full data. The range of data after the application of the blacktop included 270 days (from the date the asphalt was applied until the time of this writing). Neither of these ranges includes enough data to choose a definite design gradient. The ranges should include at least one year of complete data so that all of the seasonal effects can be included. Continued monitoring of the thermocouples is recommended for a number of years because the statistical distribution can be unfairly weighted by the seasonal effects during a portion of an incomplete year. Each part of the year should be accounted for an equal number of times within the data range. Seasonal effects may vary from year to year as well.

The statistical distributions for the positive and negative gradient daily peaks are plotted in Figures 7.5 through 7.8. The differences between the distributions before and after the asphalt was applied to the deck are due to seasonal weather changes between the times of the year when the sets of data were collected. If the data sets were more complete, design gradient magnitudes would be chosen based on the 95 % fractile of the distributions. For example, values of -7 ^{o}C and 8 ^{o}C would be chosen for the top temperatures respectively of the negative and positive design gradients before the application of an asphalt overlay.

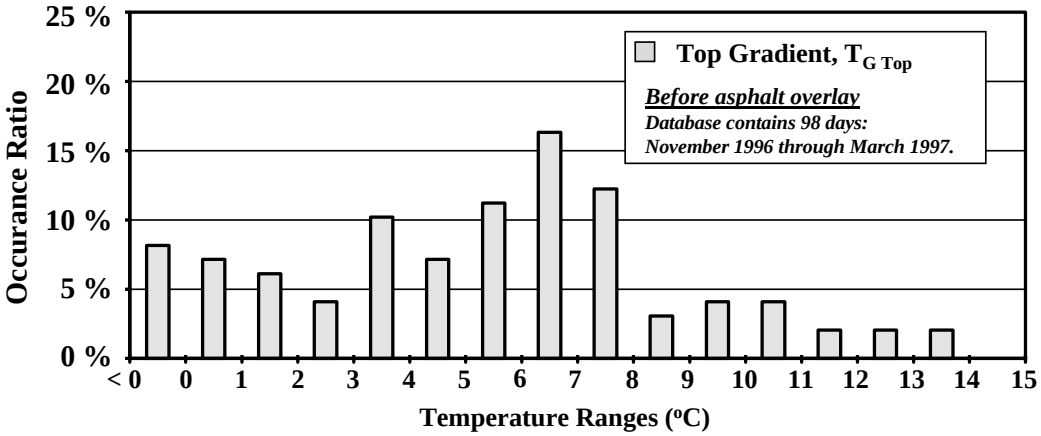

Figure 7.5 - Statistical occurrence of daily peak positive gradients before application of the asphalt blacktop

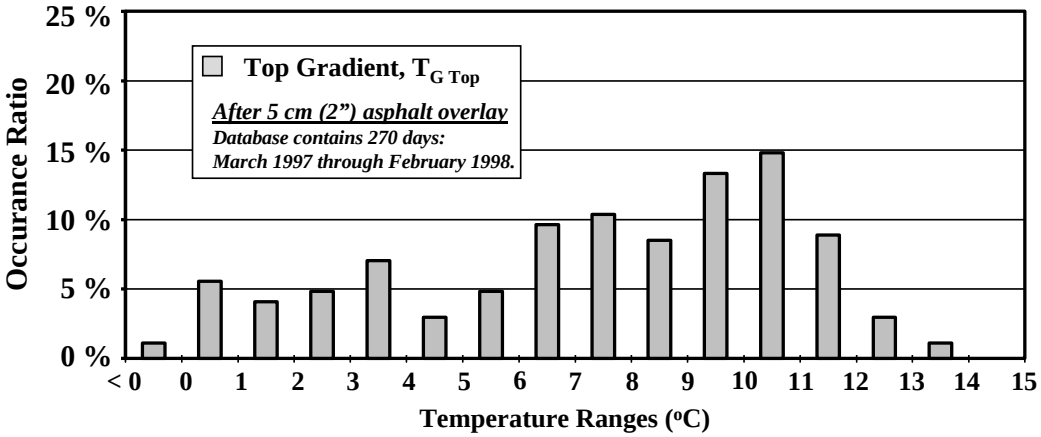

Figure 7.6 - Statistical occurrence of daily peak positive gradients after application of the asphalt blacktop

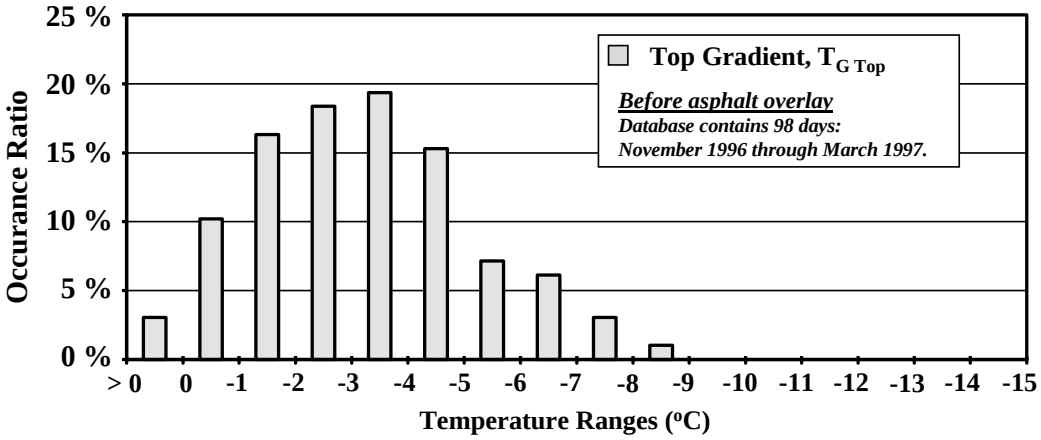

Figure 7.7 - Statistical occurrence of daily peak negative gradients before application of the asphalt blacktop

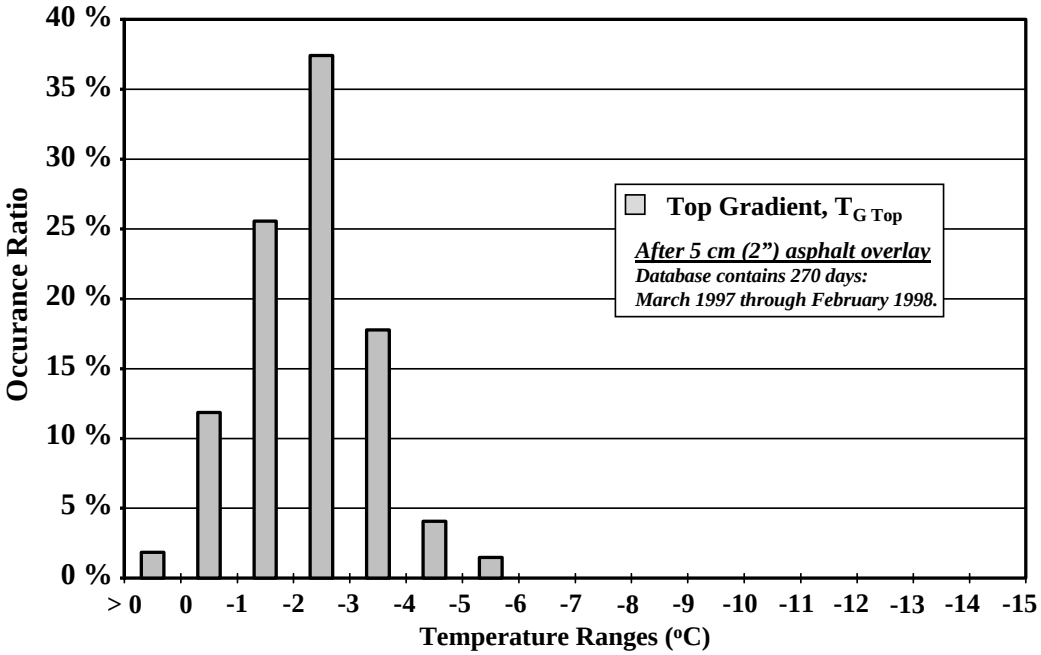

Figure 7.8 - Statistical occurrence of daily peak negative gradients after application of the asphalt blacktop

7.2.1 Longitudinal Stresses

Two calculations of thermal gradient stresses were performed to compare with measured stress values: the stresses caused by the application of the AASHTO LRFD design gradients and the stresses caused by the application of the maximum measured gradients. Both of these sets of stresses were calculated using the recommended design technique in Section 4.6.6 of the *AASHTO LRFD Bridge Design Specifications* [2]. This method relies on the assumptions that the box girder is prismatic and that the cross-section does not warp (i.e. plane sections remain plane). To apply the AASHTO method to the measured temperature distribution, the cross-section was divided into tributary areas for each of the thermocouples. The temperature measured by the thermocouple in a given area was assumed to be constant through that area. The stresses at the centroids of each of these areas were then calculated using the standard method. Figure 7.9 shows how the cross-section was divided up.

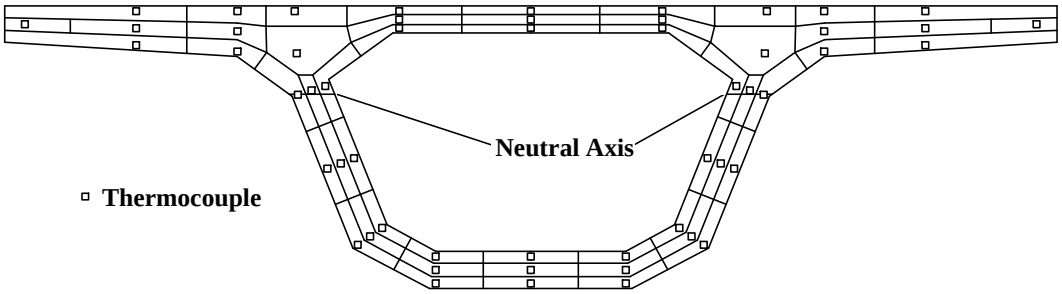

Figure 7.9 - Division of the Ramp P cross-section into tributary areas for each thermocouple gauge

To make the calculated results comparable to the measured data, a uniform temperature had to be added to the non-linear gradients. The measured results come from the change in stress in the gauges between the time of the peak gradient occurrence and some baseline time where the temperature distribution through the cross-section was fairly uniform. Between the time of the baseline and the time of the peak gradient occurrence there is also some uniform change in temperature in the ramp which contributes to the measured stresses. Thus, it is necessary to add some uniform temperature into the calculations to make the comparison between calculated and measured stresses reasonable. Utilizing the difference in measurements between the dates of the

peak gradients and the dates on which the temperature was uniform throughout the section, uniform temperatures of 3.3 ^{o}C and -6.4 ^{o}C were added to the maximum positive and negative gradients (presented in Figures 7.3 and 7.4) respectively. The thermal gradient calculations are given in Appendix E. The measured and calculated longitudinal stresses in P16-2, P16-10, and P16-17 from the design positive gradient and the measured positive gradient are presented in Figures 7.10 through 7.12. The analogous plots for the negative gradient are presented in Figures 7.13 through 7.15.

The plots of the measured stress distributions indicate peaks over the webs of P16-10 and P16-17, but not P16-2. This response indicates that the box girder is warping. P16-2 is restrained by the anchorage diaphragm from distortion of its section, so the absence of peaks over the webs at that section is consistent. The recommended method from the *AASHTO LRFD Bridge Design Specifications* [2] assumes the section will not warp. Thus, the stresses calculated from that method would be expected to match measured results better at P16-2 than at P16-10 and P16-17.

Table 7.1 compares measured stresses with stresses that were calculated using the recommended AASHTO method with the measured applied gradients. Table 7.2 compares measured stresses with the stresses calculated from the application of the design gradients.

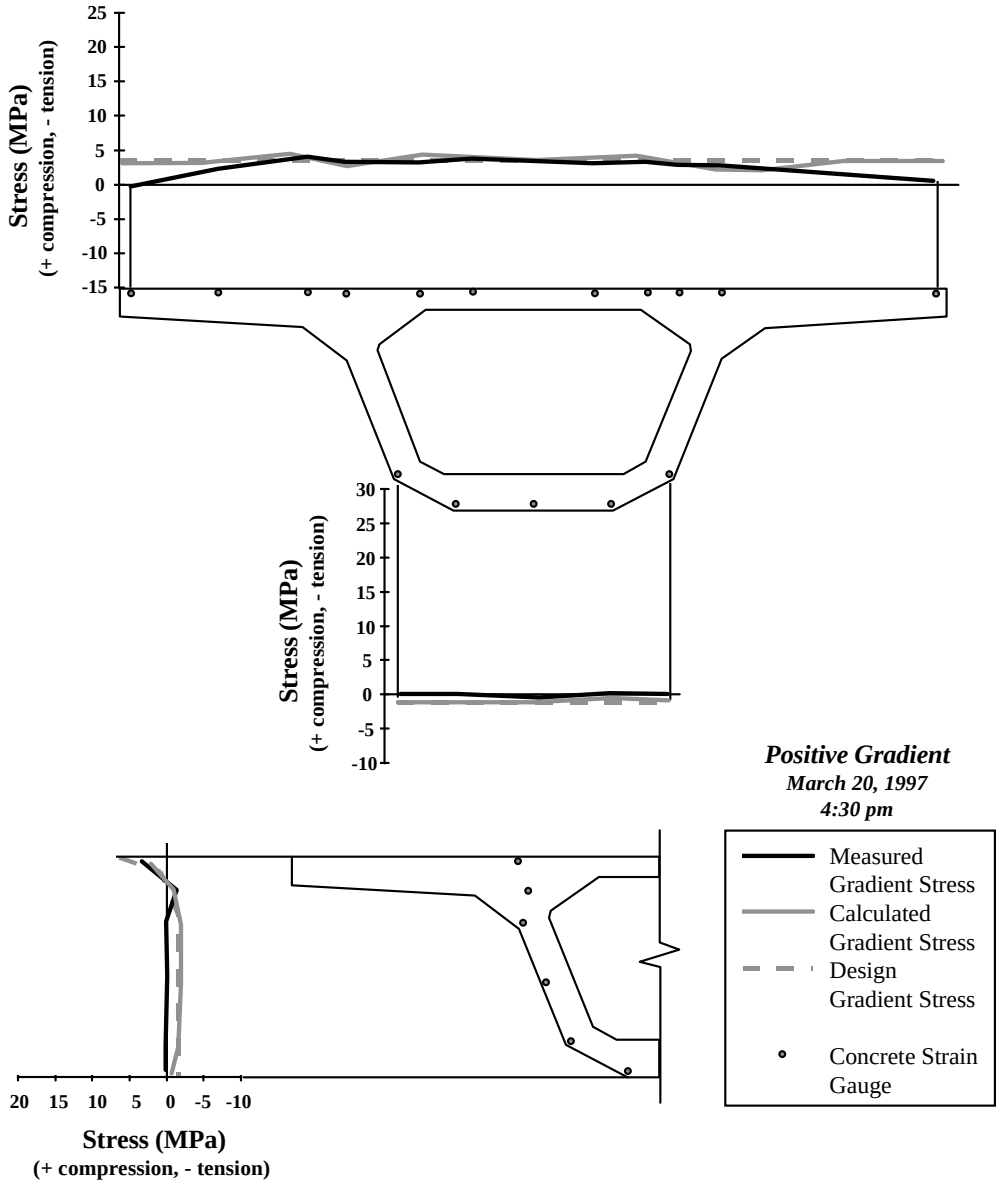

Figure 7.10 - Comparison of measured and calculated positive thermal gradient stresses for P16-2

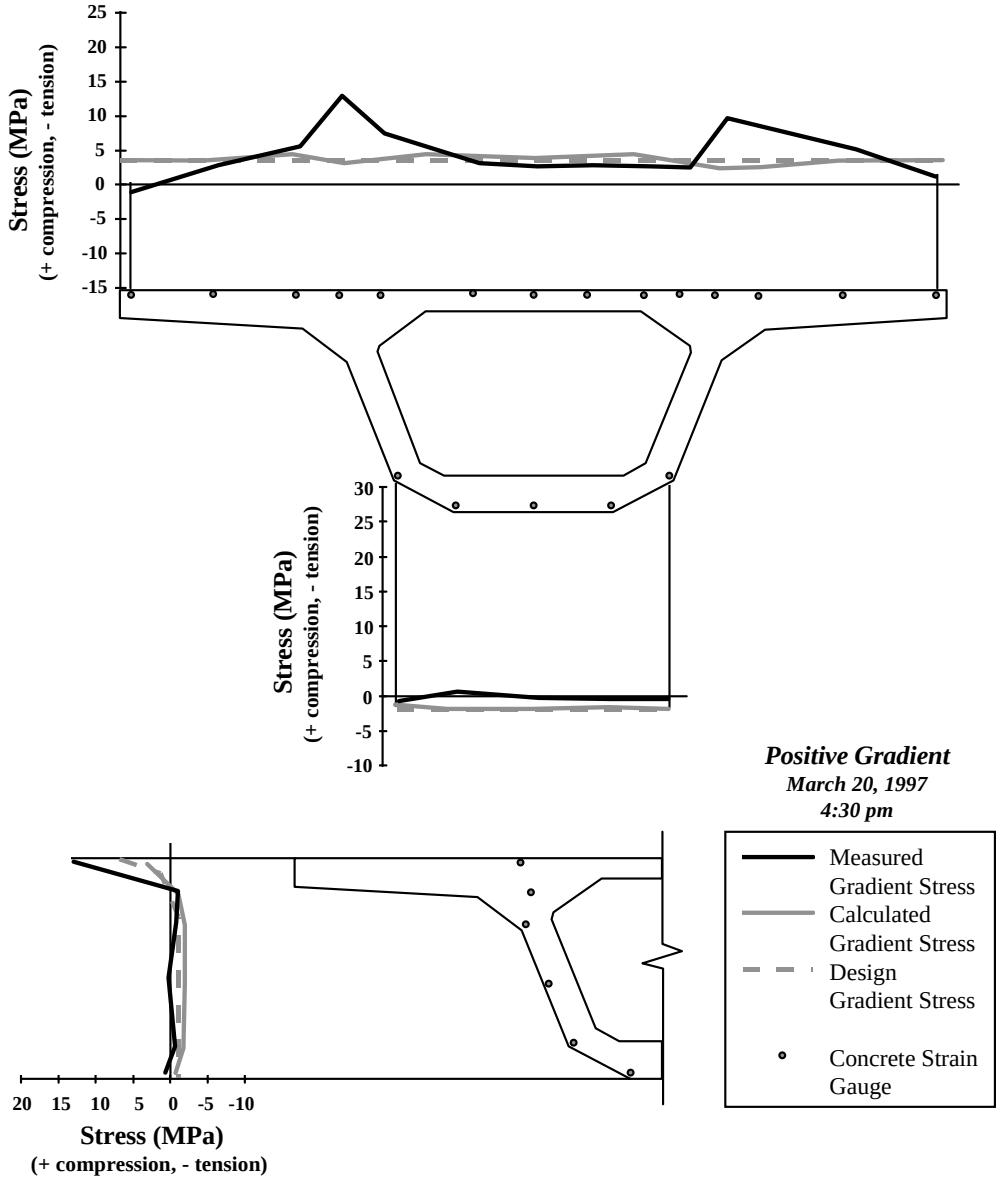

Figure 7.11 - Comparison of measured and calculated positive thermal gradient stresses for P16-10

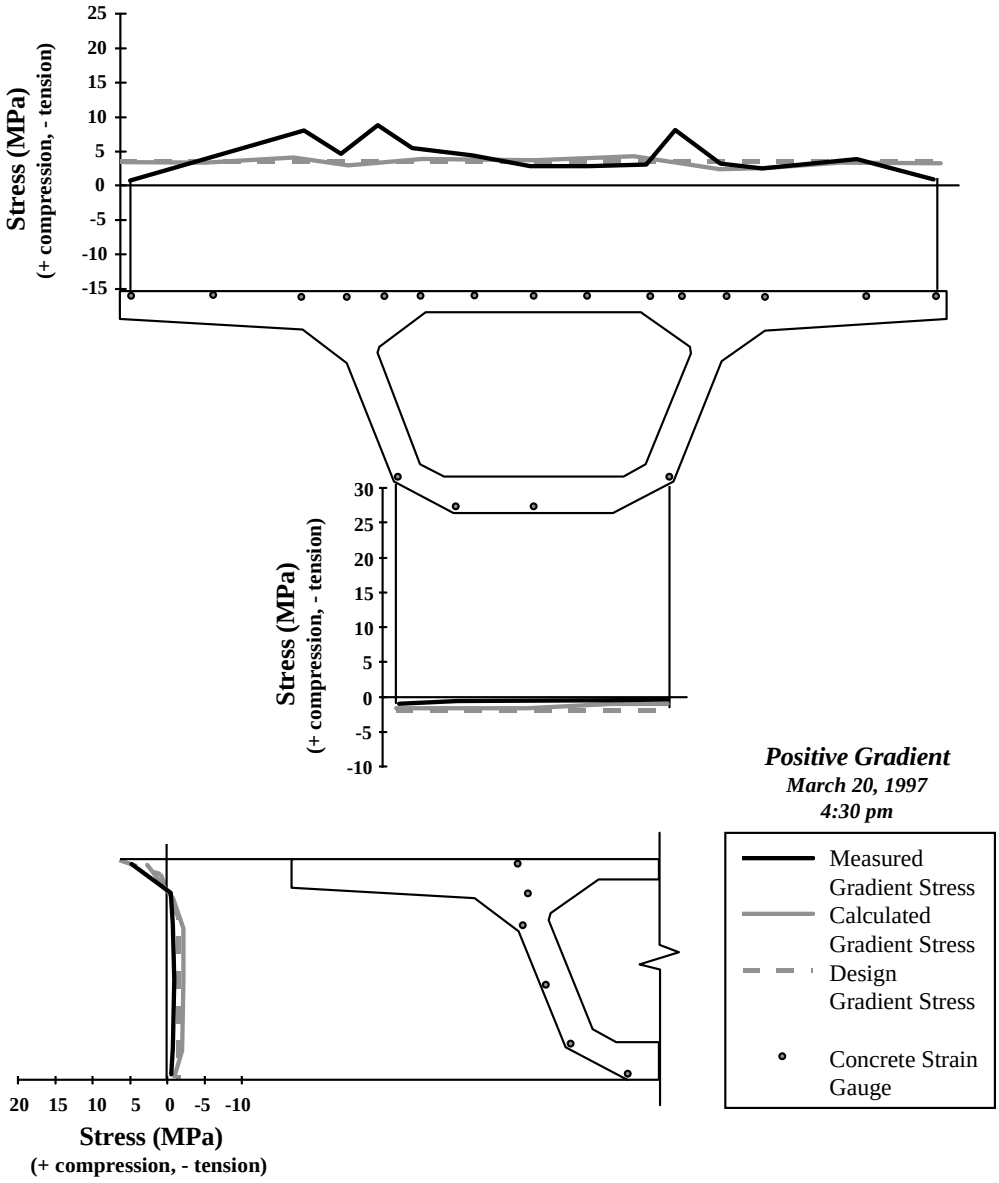

Figure 7.12 - Comparison of measured and calculated positive thermal gradient stresses for P16-17

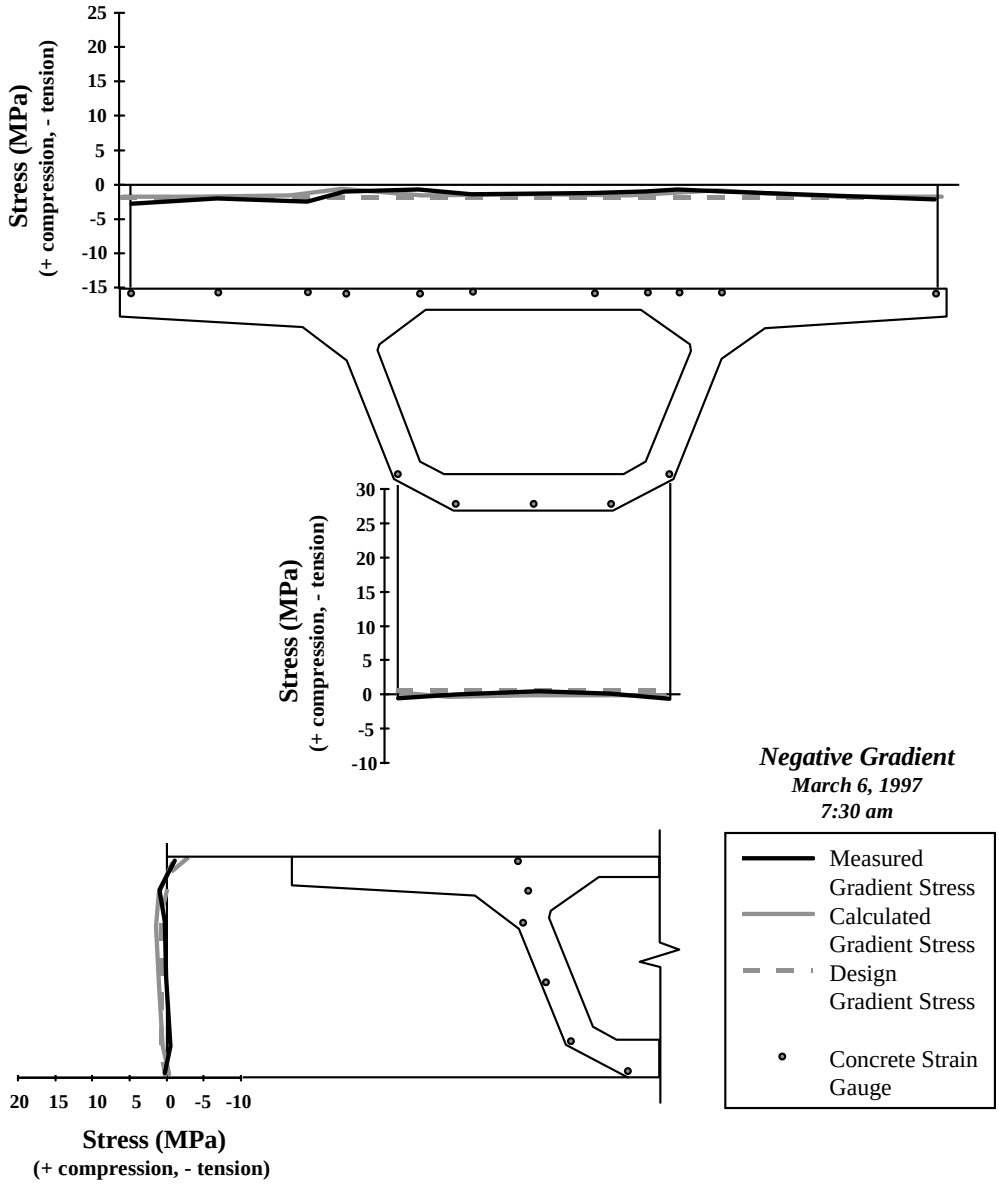

Figure 7.13 - Comparison of measured and calculated negative thermal gradient stresses for P16-2

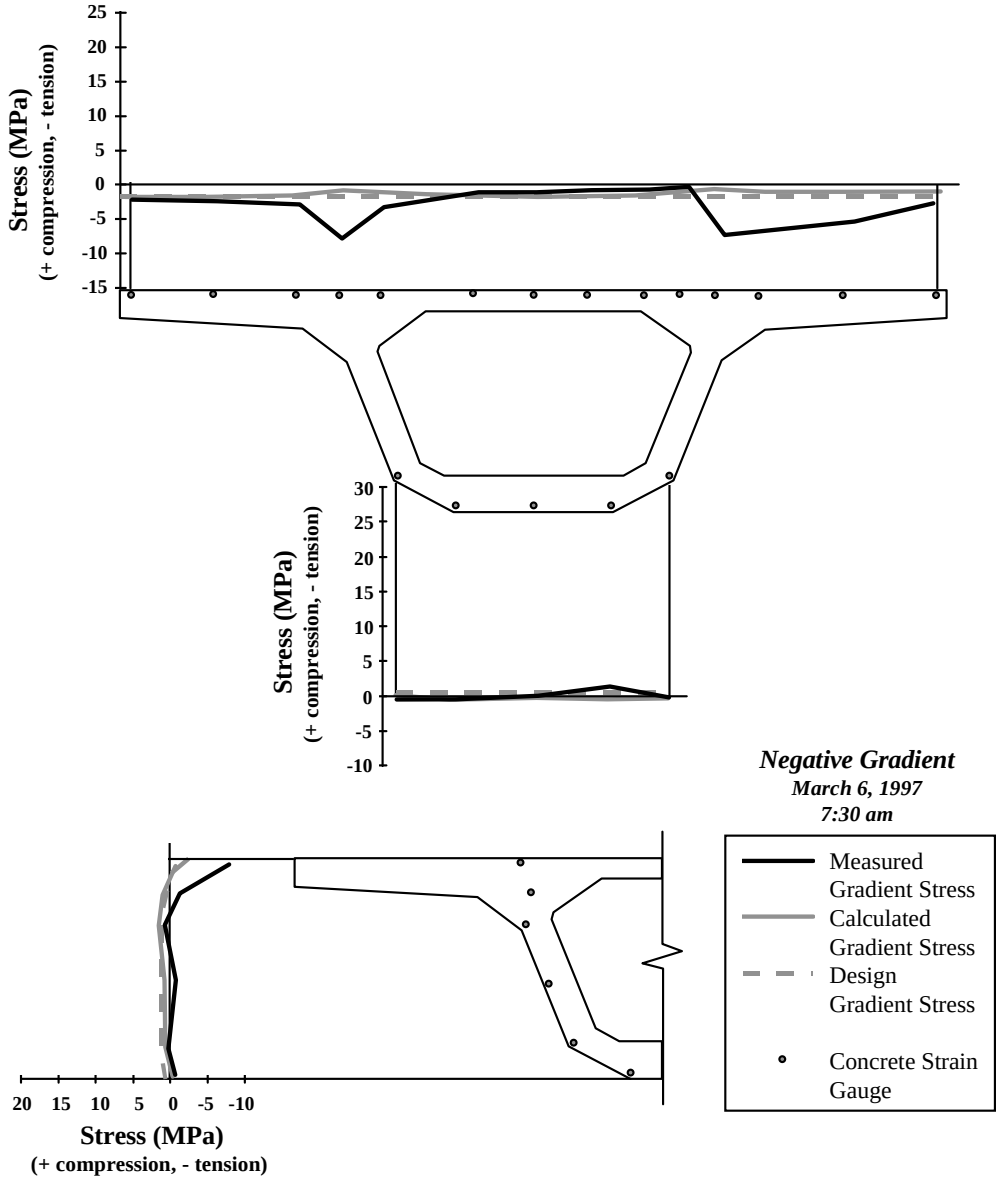

Figure 7.14 - Comparison of measured and calculated negative thermal gradient stresses for P16-10

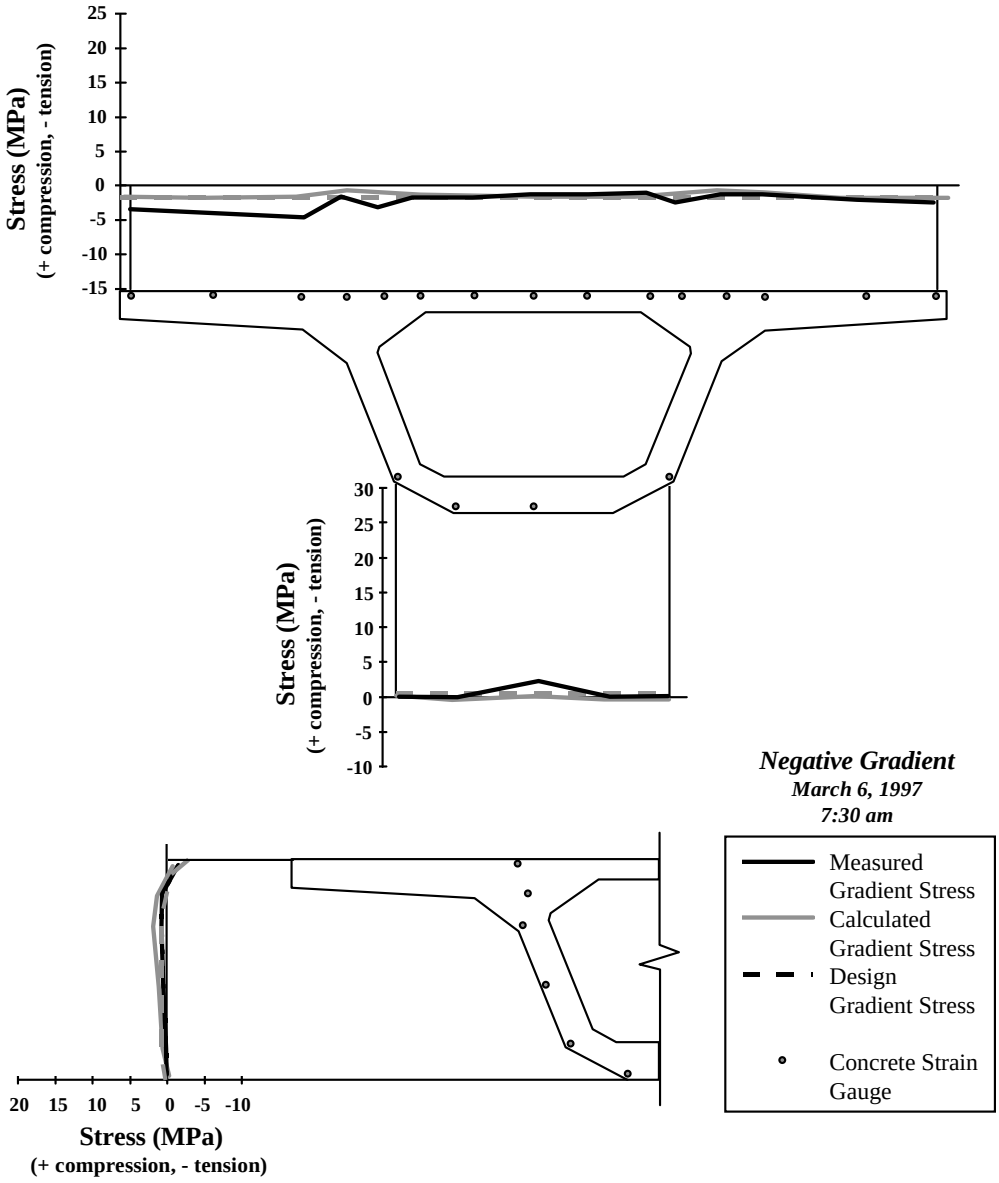

Figure 7.15 - Comparison of measured and calculated negative thermal gradient stresses for P16-17

	Positive Thermal Gradient	Negative Thermal Gradient

Segment	Average Measured	Average Calculated	Measured / Calculated	Average Measured	Average Calculated	Measured / Calculated
P16-2	2.54 MPa	3.04 MPa	0.836	-1.73 MPa	-1.52 MPa	1.138
P16-10	4.61 MPa	3.16 MPa	1.459	-3.21 MPa	-1.55 MPa	2.071
P16-17	4.20 MPa	3.11 MPa	1.350	-2.18 MPa	-1.51 MPa	1.444
	Peak Measured	Peak Calculated	Measured / Calculated	Peak Measured	Peak Calculated	Measured / Calculated
P16-2	4.03 MPa	4.30 MPa	0.937	-2.94 MPa	-2.01 MPa	1.463
P16-10	12.92 MPa	4.41 MPa	2.930	-7.89 MPa	-2.05 MPa	3.849
P16-17	8.90 MPa	4.32 MPa	2.060	-3.33 MPa	-1.98 MPa	1.682

Table 7.1 - Comparison of measured and calculated stresses from measured thermal gradients

	Positive Thermal Gradient			**Negative Thermal Gradient**		
Segment	Peak Measured	Peak Design	Measured / Design	Peak Measured	Peak Design	Measured / Design
P16-2	4.03 MPa	3.57 MPa	1.129	-2.94 MPa	-1.82 MPa	1.615
P16-10	12.92 MPa	3.57 MPa	3.619	-7.89 MPa	-1.81 MPa	4.359
P16-17	8.90 MPa	3.55 MPa	2.507	-3.33 MPa	-1.79 MPa	1.860

Table 7.2 - Comparison of measured and design stresses

No distress has been observed in the Ramp P structure which can be attributed to thermal effects. In order to understand why no such distress has been observed despite the high stresses indicated in Figures 7.10 through 7.15, the total stress state of each segment was examined. Load combinations of dead load, prestress, live load and thermal gradient were combined to produce minimum and maximum stresses for each instrumented segment. These stress distribution are plotted in Figures 7.16 and 7.17. Figure 7.16 shows the measured and calculated load combinations which produced the minimum stresses in each of the cross-sections. These load combinations were not necessarily the same for each cross-section. As can be seen in Figure 7.16, no tension occurs in any of the cross-sections. Figure 7.17 shows the measured and calculated load combinations which produced the maximum stresses in each of the cross-sections. Again, these load combinations were not necessarily the same for each location.

The design 28 day compressive strength of the concrete, f'_c, was 44.8 MPa (6.5 ksi). The actual 28 day compressive strengths of the concrete in the segments are unknown but are sure to be greater than the design strength. The precaster found that he was easily reaching his design

strengths within the first week of curing. Cylinder tests of the concrete in the segments were generally abandoned once the tests indicated that the design strength was achieved. However, 28 day compression tests that were performed on some mainlane concrete cylinders indicated that concrete strengths around 69 MPa (10 ksi) were quite common.

Values of the f'_c, $0.7f'_c$ (the approximate limit of linear elastic behavior in concrete), and $0.45f'_c$ (the maximum allowable compressive stress for segmental bridges from Section 5.9.4.2.1 of the *AASHTO LRFD Bridge Design Specifications* [2]) are also plotted in Figures 7.16 and 7.17. In these plots, f'_c refers to the design strength of the concrete, 44.8 Mpa (6.5 ksi). As can be seen in Figure 7.17, the maximum allowable compressive strength, $0.45f'_c$, was exceeded in P16-10 and P16-17 under combinations of dead load, prestress, live load, and positive thermal gradient. The elastic limit of the concrete was even exceeded in P16-10 near the top of the right web. Under such conditions, the stress data that is presented would no longer be valid because the modulus of elasticity that was used to transform the strain gauge data into stress values could no longer be used. However, because the true compressive strengths of the concrete in the segments were probably much greater than the design strength indicated in the figures, the plotted stress distribution should need no adjustment.

The load combination plots indicate very fine performance from the bridge. No tension is indicated and only a small amount of over-compression can be seen. The over-compression should not pose any concern because the AASHTO allowable compression limit is actually somewhat conservative. Only where the linear elastic range of the concrete is exceeded is there a need for concern, but this only occurs over a small width of the top flange (approximately 30cm (1')) at one cross-section. Much of the rest of the top flange has stresses well below the AASHTO allowable limit.

P16-2: Dead Load + Prestressing + Live Load Case 1 + Negative Gradient

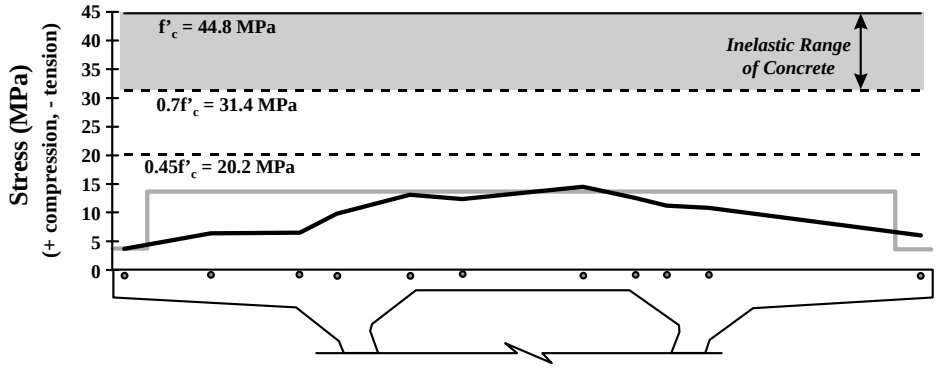

P16-10: Dead Load + Prestressing + Negative Gradient

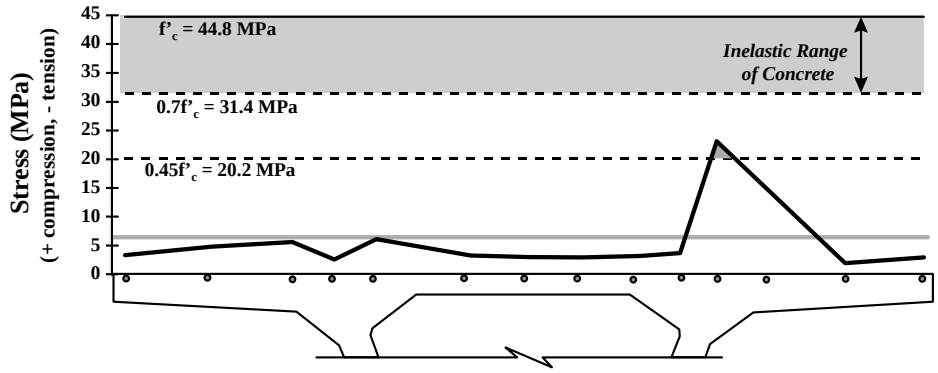

P16-17: Dead Load + Prestressing + Negative Gradient

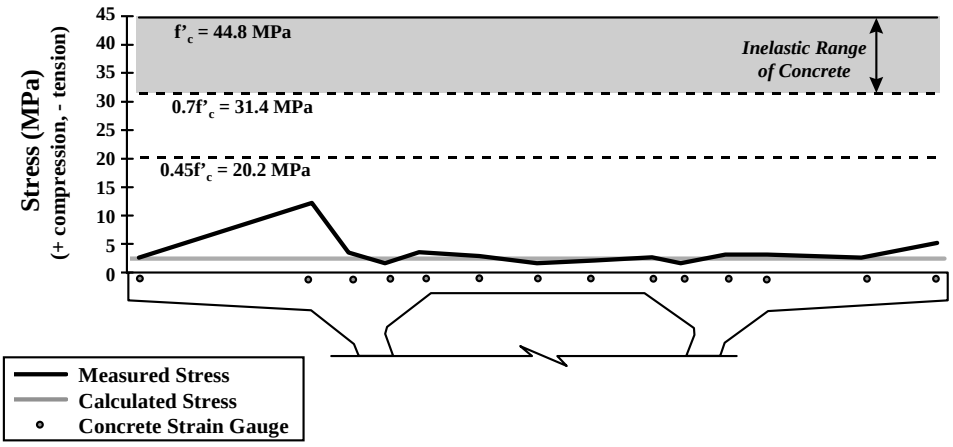

Figure 7.16 - Minimum top flange stress load combinations for P16-2, P16-10, and P16-17

P16-2: Dead Load + Prestressing + Positive Gradient

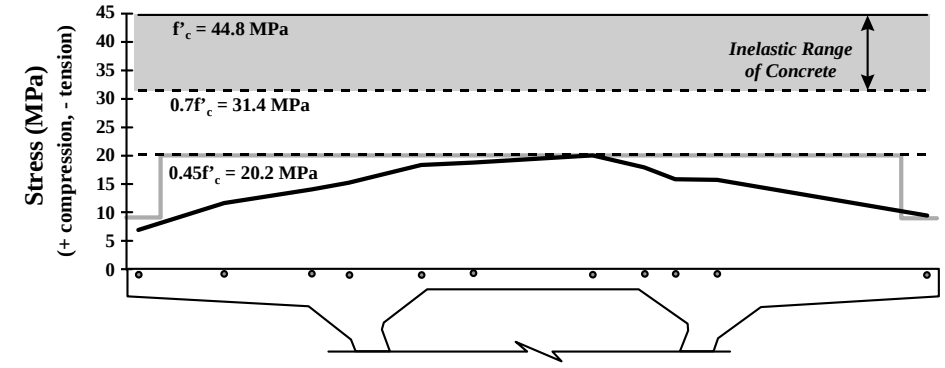

P16-10: Dead Load + Prestressing + Live Load Case 1 + Positive Gradient

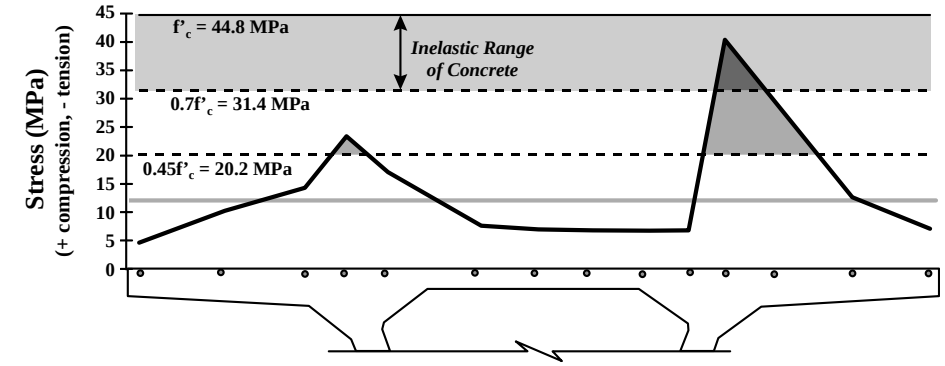

P16-17: Dead Load + Prestressing + Live Load Case 1 + Positive Gradient

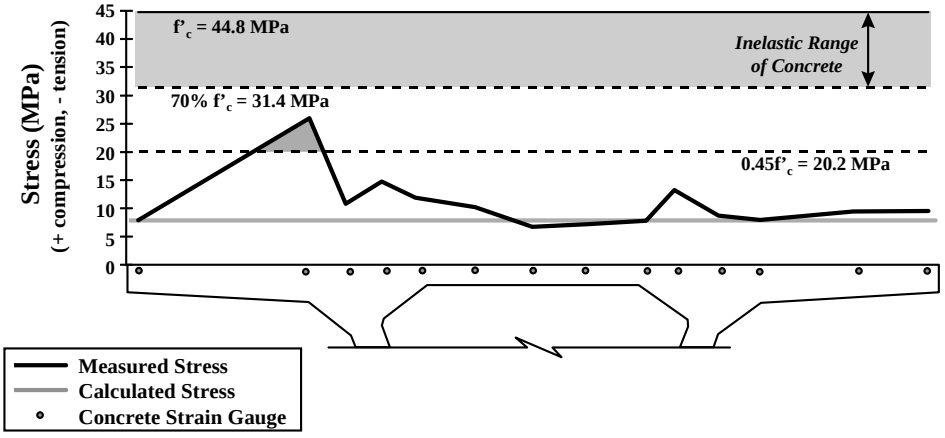

Figure 7.17 - Maximum top flange stress load combinations for P16-2, P16-10, and P16-17

7.2.2 Transverse Stresses

A simple transverse calculation model for the Ramp P cross-section was created and the measured temperatures for the positive and negative thermal gradients were applied to it. The model consisted of a symmetric two-dimensional frame made up of standard beam elements. The gradients measured through the thickness of the flanges and the webs of the ramp were applied to the beam members of the model using the AASHTO recommended method for each member of the model (as described by Figure 2.18 in Chapter 2). A description of the model and calculations for this transverse analysis are given in Appendix E. The results from the model are plotted next to measured transverse stresses from P16-17 in Figure 7.16. Though transverse stresses were measured in P16-2, P16-10, and P16-17, only the stresses from P16-17 were compared with the frame analysis because the P16-2 gauges were too close to the anchorage diaphragm and the P16-10 gauges were too close to the heavy vertical deviator beam, both of which would effect those sections by providing restraint against transverse deformations. The stress plots in Figure 7.18 show that the model did a poor job of predicting the actual transverse stresses caused by the thermal gradients. The percent error for the top flange, top fiber stress was as high as 65% for the negative gradient. If warping of the box girder is occurring as was suggested by the longitudinal stresses, the transverse response of the cross-section to applied thermal gradients would be effected as well. This may account for much of the difference.

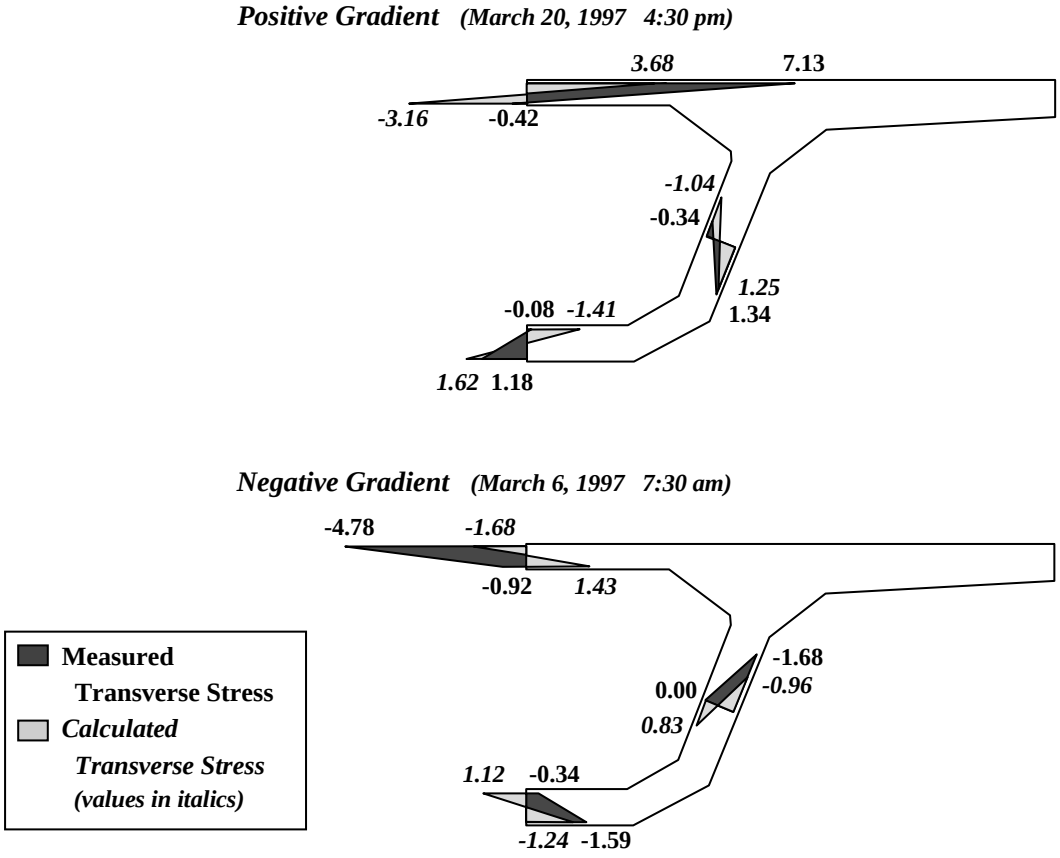

Figure 7.18 - Comparison of measured and calculated transverse flexural stresses from positive and negative thermal gradients for P16-17

7.2.3 External Tendon Stresses

Figures 7.19 and 7.20 show the external tendon stresses caused by the maximum measured positive and negative thermal gradients. As in the longitudinal and transverse stress sections, a small amount of linear temperature change is reflected in the measured stresses (3.3 ^{o}C and -6.4^{o}C for the positive and negative gradient cases respectively). The highest tensile stress change was produced by the positive gradient. The peak stress change was 10.5 MPa tension in tendon T1 on the right side of the girder. The T2 tendon on the same side underwent almost the exact same stress change. A change of 10.5 MPa (1.5 ksi) is about 0.6% of the guaranteed

ultimate tensile strength (GUTS) of 1860 MPa (270 ksi). Fatigue of the tendons due to daily thermal trends should not be a problem. Ryals [20] recommends a fatigue limit of 69 MPa (10ksi).

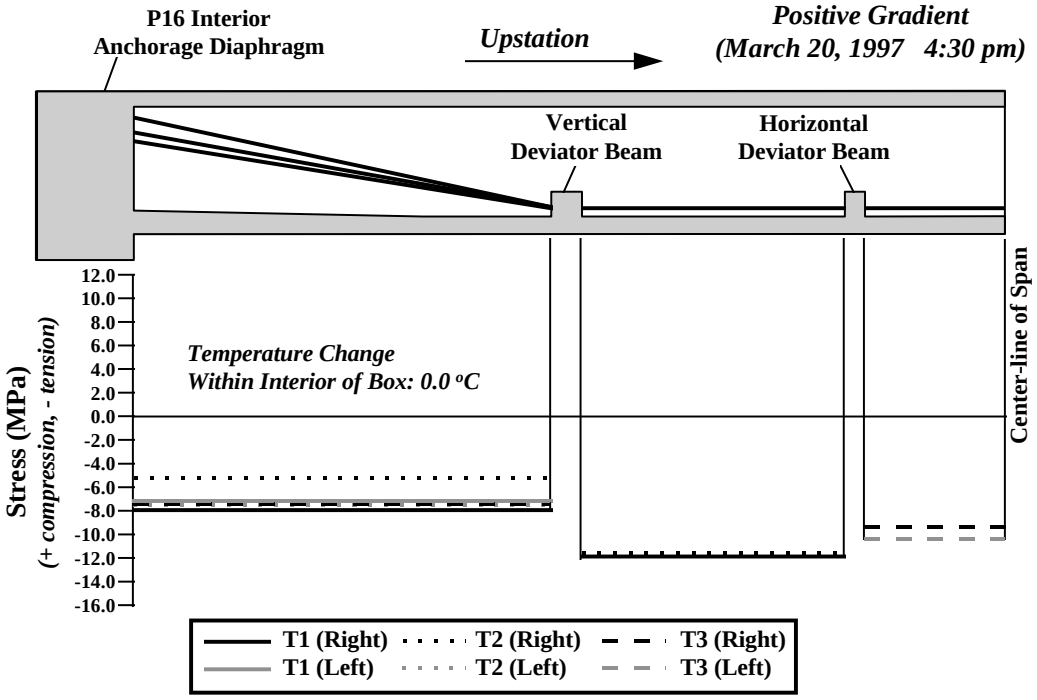

Figure 7.19 - Measured stress changes in the external tendons from the maximum positive gradient

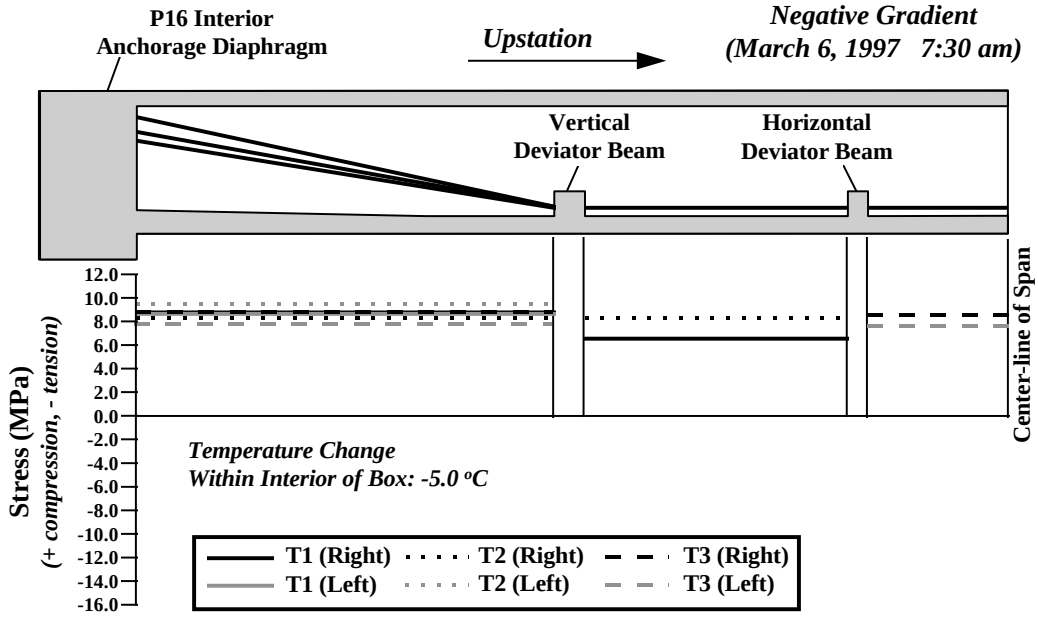

Figure 7.20 - Measured stress changes in the external tendons from the maximum negative gradient

7.3 CONCLUSIONS AND RECOMMENDATIONS

7.3.1 Design Gradients

7.3.1.1 Conclusions

The temperature distributions of the maximum measured positive and negative thermal gradients indicate that the shape of the design gradient from the *AASHTO LRFD Bridge Design Specifications* [2] fits the measured data best when the bottom fiber T_3 temperature is specified at the maximum allowed temperature (2.8 °C for the positive gradient and -1.4 °C for the negative gradient). The code specifies that the "temperature value T_3 shall be taken as 0.0, unless a site-specific study is made to determine an appropriate value, but shall not exceed 5 °F [2.8 °C]." Since it is doubtful that any designer could economically perform an appropriate site-specific study for a full box girder section or would go to the trouble anyway, only one value should be specified for the bottom fiber T_3 temperature. Preferably this value should be greater than 0.0 °C. The

conclusions regarding the shape of the design gradient in this report may not be applicable for types of bridge structures other than concrete box girders. The shape of the cross-section of the bridge undoubtedly effects the distribution of the temperature through the depth of the section.

Temperature gradients not only occurred through the depth of the girder cross section, but through the thickness of the flanges and web walls of the box girder. The *Proposed AASHTO LRFD Guide Specifications for the Design of Segmental Concrete Bridges* [17] currently recommend in Section 6.4.4 of the commentary that transverse analysis for shallow cross-sections may be necessary and that a gradient of plus or minus 5.6 ^{o}C (10 ^{o}F) from the exterior of the box section to the interior may be appropriate. The Ramp P study measured gradients has high as 8.6 ^{o}C (15.5 ^{o}F) through the top flange during the maximum positive gradient and -4.1 ^{o}C (7.4 ^{o}F) during the maximum negative gradient. Stresses of 7.1 MPa (1.0 ksi) compression and 4.8 MPa (0.7 ksi) tension (respectively) were recorded in the top flange with these gradients.

The peak top fiber thermal gradient magnitudes measured in Ramp P were less than the specified design gradient top fiber temperatures for the positive and negative gradients. Furthermore, statistical distributions of the measured gradients show that the peak measured gradient occurs less than 5% out of the range of measured gradients. Ideally, the magnitudes of the design gradient temperatures should be based from measured gradient temperatures that reflect the 95th percentile to match other margins of safety. This would allow for a substantial reduction in the magnitude of the design gradient. At the time of this writing, the ranges of the measured thermal gradients from Ramp P are too incomplete to allow a conclusive recommendation of design gradients for temperature zone 4. Data collection within the next year should allow for a preliminary recommendation of design gradients for box girder sections in temperature zone 4.

7.3.1.2 Recommendations

The AASHTO recommended design gradients should be based on instrumentation studies of actual bridge structures. Such studies should produce at least one year of measured data including all seasonal effects. The design gradient should be statistically determined from the gradient that provides the 95th percentile fractile. The shape of the gradient is likely to vary based on the shape and size of the bridge cross-section. Instrumentation studies of temperature trends in bridge structures should examine thermal distributions across the full cross-section.

The *AASHTO LRFD Bridge Design Specifications* [2] should recommend a transverse gradient for all box girder sections. Recommendations for the shapes and magnitudes of such gradients based on the Ramp P study cannot be made at this time. As stated for the longitudinal design gradients, the recommended gradients should be chosen based on instrumentation studies of actual bridge structures. The transverse gradients that are suggested in Section 6.4.4 of the commentary from the *Proposed AASHTO LRFD Guide Specifications for Design of Segmental Concrete Bridges* [17] should be used for design until definitive transverse gradients are determined.

The maximum values that are allowed for T_3, the bottom fiber temperature from the design gradients in the *AASHTO LRFD Bridge Design Specifications* [2] should be applied to make the design gradients best match the shapes of the thermal gradients measured in Ramp P.

7.3.2 Analysis Methods

7.3.2.1 Conclusions

Measured longitudinal stresses from the Ramp P superstructure indicate that the cross-section of the box may be warping under thermally induced strains. Such warping makes the recommended analysis method from Section 4.6.6 of the *AASHTO LRFD Bridge Design Specifications* [2] unsuitable for determination of the stresses caused by thermal gradients in box girder sections. The peak measured stresses were much greater than the peak stresses predicted by the recommended method. The peak measured compressive stress from the positive gradient was 2.9 times the peak calculated value at the same cross-section. The peak measured tensile stress from the negative gradient was 3.8 times the calculated value at the same cross-section.

Examination of the structure under load combinations including dead load, prestress, live load, and thermal gradient indicated that no tension is occurring in the structure. However, the maximum allowable compression stress from Section 5.9.4.2.1 of the *AASHTO LRFD Bridge Design Specifications* [2] was exceeded for some portions of the top flange in segments P16-10 and P16-17. The portion of the top flange over the right web in segment P16-10 showed stresses exceeding 70% of the specified concrete design strength, f'_c. $0.7f'_c$ is the approximate limit for

linear elastic behavior of the concrete. The peak stress only occurs across a small width of the top flange in P16-10 (about 30cm (1')). Additionally, cylinder tests of the concrete used to precast the segments in Ramp P generally indicated higher concrete strengths than the required design strength (44.8 MPa (6.5 ksi)). Much of the concrete used in the U.S. 183 project achieved 28 day strengths of up to 69 MPa (10ksi). Thus, the true elastic range of the concrete would extend to a much higher stress than is plotted in Figures 7.16 and 7.17. No distress has been observed in Ramp P which can be attributed to thermal gradients or to any other load. This indicates that the maximum allowable compression limit from Section 5.9.4.2.1 of the *AASHTO LRFD Bridge Design Specifications* could be over-conservative.

7.3.2.2 Recommendations

Use of the recommended thermal analysis technique from Section 4.6.6 of the *AASHTO LRFD Bridge Design Specifications* [2] should be re-evaluated. This method is entirely based on the assumption that plane sections remain plane within the loaded cross-section which will not be true if warping occurs. Further study of the problem may yield an effective flange width solution similar to the method commonly used to deal with shear lag. Appropriate methods for the solution of transverse stresses should also be examined. Instrumentation studies which examine stress behavior as well as temperatures through box girder cross-sections are necessary. Until such time, however, advanced methods such as finite element or folded plate analysis techniques could be used to examine thermal behavior in box girders.

The maximum stress limits in Section 5.9.4.2.1 should allow less restrictive stress limitations for maximum stresses that occur across only a small portion of the width of a girder cross-section. Data from Ramp P would tend to suggest that no serious detriment will occur to a bridge if over-compression of concrete only occurs in a small portion of the area of a cross-section.

CHAPTER 8

CONCLUSIONS AND RECOMMENDATIONS

8.1 OVERVIEW

This study represents one phase of field instrumentation and monitoring of the new U.S. 183 elevated highway in Austin, Texas. This phase includes the instrumentation of a five span continuous, precast, segmental, horizontally curved, concrete box girder ramp bridge erected in balanced cantilever. The behavior of this bridge was monitored during construction, under a service level live load test, and under daily applied thermal gradients. Other phases of the field study of the U.S. 183 elevated highway (not included in this report) are the instrumentation and monitoring of an innovative Y-shaped cast-in-place concrete pier, a three span semi-continuous precast segmental concrete box girder mainline superstructure unit constructed span-by-span, and a tall precast segmental hollow box ramp pier.

The program of this study included installation of concrete strain gauge devices in three full cross-sections of one of the spans of the bridge. In each instrumented cross-section, 32 concrete strain gauges were placed longitudinally about the cross-section to monitor the flexural and axial behavior at that section, 24 concrete gauges were grouped by threes into rosette patterns to monitor shear and transverse tensile stresses. The concrete strain gauges provided reliable information on the moments, shears, torsions, and axial loads occurring at the three instrumented cross-sections. An additional 36 strain gauges were placed on external post-tensioning tendons inside the box girder to monitor their structural contribution to the service level performance of the bridge. Finally, 54 thermocouple gauges were placed across one full cross-section to determine the daily thermal gradients occurring in the bridge. A detailed description of the instrumentation placed in the bridge is given in Chapter 3 of this report.

Data presentation as well as observations from the author of the construction process are given in Chapters 4 through 7 of this report. Conclusions and recommendations from each of those chapters are summarized in this chapter.

8.2 LESSONS FROM THE CONSTRUCTION PROCESS

Conclusions and recommendations concerning design and construction practices were drawn from the observations of the construction process made by researchers at the site. The conclusions were divided into three categories: design related, construction related, and inspection related.

8.2.1 Design Related Issues

8.2.1.1 Conclusions

1. A lack of sensitivity to the construction process was demonstrated by the positioning of the access holes at the midspan of the girder, inadequate space allocated for stressing rams, and the overall working conditions inside the box girder which include such details as the placement of the drainage pipes along the midline of the girder cross-section. Neglect in the planning of these details can result in work delays and a decline in the quality of the construction because the skills of the workers are impaired by the difficulties of their work environment.

2. Substantial difficulty in stressing of the external tendons occurred because of their long length (between 90m (300') and 160m (525') stretched over multiple spans). A combination of factors related to the length of these tendons probably resulted in the failure of three external tendons during stressing. The long length of the tendons required a large amount of slack and elongation (about 1.2m (4')) to be pulled through the ram before the final tendon force was reached. The large number of strokes required from the stressing ram made power seating after each stroke necessary to avoid large non uniform seating losses among the strands. The large length of tendon pulled through the ram may have caused formation of a knot in the area of the saddle next to the live end of the tendon. The tendons may have been rubbing against deviation and saddle pipes thus resulting in high friction losses which would be critical over long tendon lengths. Trumpets on the ends of these pipes could have prevented such rubbing. Lastly, the external tendons were very difficult to grout because of their long length. The tendons should have been limited to single span lengths (between 38m (125') and 55m (180')).

3. Uplift of the superstructure from the bearing pads was recorded. The uplift may have been due to torsional effects caused by the external tendons.

4. The ability of the contractor to adjust vertical or horizontal alignment problems of the spans by adjusting the bearings at the piers was seen as a great advantage of the system of construction. This facet of the system, which allows corrections during the construction stages, unbinds designers and contractors from uncertain variables during the planning stages of the bridge.

8.2.1.2 Recommendations

1. Structural designers should consider all facets of the construction of a bridge with keen consideration for the tasks that workers need to perform, where they need to perform the task, what tools and materials they will need to manipulate to perform the task, and under what environmental pressures. This consideration should extend not just to the construction process, but to foreseeable long term inspection and maintenance tasks as well. For segmental projects, particular emphasis should be placed on stressing operations and the space allowed for rams. Detailed records of construction methods used by contractors and the advantages and disadvantages of particular methods should be kept by on-site inspectors and passed on through structural design departments to benefit the knowledge and experience of the designers in regard to construction issues.

2. The length of tendon next to the live end anchorage of long post-tensioning tendons should be left straight and free of deviation saddles to help prevent potential knotting problems in the strands of the tendon. Deviation pipes for external tendons should have trumpeted ends (diabolos ends) to prevent rubbing of the strands against the edges of the pipe. On site inspectors should measure tendon elongations across several strands to verify that all strands elongate the same amount. Inspectors should also require power seating of the wedges every time the ram is stroked especially for long tendons which require many strokes of the ram to reach the design force.

Finally, the lengths of tendons should be limited to stretch across no more than two spans or a maximum length of about 75m (250').

3. Designers should consider the uncertainties of the design process and evaluate design concepts based on the adaptability of details to possible change.

Currently nothing can be recommended concerning the uplift of the superstructure off of the bearing pad until the problem is further observed and analyzed. Most likely, the solution lies in a better understanding of the effects of external tendons on horizontally curved bridges.

8.2.2 Construction Related Issues

8.2.2.1 Conclusions

1. Many of the erection schemes utilized for the construction of Ramp P demonstrated lax construction planning. These schemes included the erection of the interior anchorage segment in two halves and the erection of the first two cantilever segments off of the interior anchorage segment.

2. Poor visualization of the three-dimensional geometry of the bridge was demonstrated in the design of the bottom flange temporary post-tensioning blisters. The location and size of these blisters consistently conflicted with the alignment of the external tendons

8.2.2.2 Recommendations

1. Contractors should consider performing test runs of construction schemes at the precasting yard if time and space permit. Such tests would immediately demonstrate flaws in a proposed scheme and would test the workability of any special construction equipment necessary for a certain task.

2. Erection schemes for precast segments must include measures to correct alignment problems in a quick and easy manner at the time of erection. As already stated, these measures should be pre- tested in such a manner that their viability is guaranteed.

3. Temporary post-tensioning details should allow free access to the components of the stressing system. External systems are best for this. Systems which require internal ducts may not allow such access, and removal of the temporary prestress after its use is no longer required may be difficult. Thus, the contractor should either plan on sacrificing the temporary prestress steel or provide blockouts at coupler points to allow access to the couplers and size the ducts so that plenty of space is available for bars and couplers to easily be pulled through them.

4. Contractors should provide explicit drawings of structural details which demonstrate that no conflicts exist with other components of the bridge structure. Drawings which demonstrate the details of a proposed erection scheme would also help to indicate any flaws in the idealization of untested procedures.

8.2.3 Inspection Related Issues

8.2.3.1 Conclusions

1. A construction delay of one night occurred because two segments of a Ramp P cantilever had their labels switched. The incident could have been avoided had either the contractor's or state's quality assurance personnel verified the labeling of the segments prior to their being trucked to the erection site. It is unknown if such checks were routinely performed at the precasting yard by either team of inspectors.

2. A problem occurred when grout from a transverse post-tensioning duct flowed into a longitudinal post-tensioning duct and obstructed the empty duct. Breaches must have been present in each of the ducts at the time of casting. The inspector present at the time of the casting could have closely inspected all of the ducts, noticed the problem and directed it to be fixed. The incident which occurred and the damage which had to be done to the concrete deck of the box girder to free the duct of grout demonstrate the importance that post-tensioning ducts be kept free of obstructions and thoroughly inspected for breaches before concrete is placed.

3. One of the segmental joints in the ramp demonstrated poor squeeze out of joint epoxy. The gap was noticed by an on-site inspector who directed it to be fixed by injection of epoxy. A similar problem in a mainline joint was not noticed nor fixed, and some spalling in the bottom slab of the girder has been attributed to the voids that were present in the epoxy.

8.2.3.2 Recommendations

1. Quality assurance personnel can easily verify segment labels prior to transport to the site by checking the details of post-tensioning duct locations or special features such as anchorage blisters or deviator beams. Construction and inspection records should be logged verifying the quality and identity of the segment prior to transport to the construction site.

2. Verification of the integrity of post-tensioning ducts should be a priority task before casting of the segment because correction of flaws after placement of the concrete can be difficult. The presence of stiffening pipes in the ducts should be confirmed.

3. Full attention should be given to epoxy squeeze out between joints during erection. The cross-section of the box girder should be as homogeneous as possible for complete and uniform transfer of stress as well as integrity against environmental forces.

8.3 BEHAVIOR UNDER CONSTRUCTION AND LIVE LOADS

The conclusions and recommendations presented in Chapters 5 and 6 are summarized here under two topic headings: stress distributions in box girders and structural behavior. The conclusions and recommendations grouped under the topic of stress distributions are all pertinent to the provisions of Section 4.6.2.6.2 of the *AASHTO LRFD Bridge Design Specifications* [2] concerning effective flange widths for box beam bridges. The conclusions and recommendations grouped under the topic of structural behavior concern other aspects of the bridge's behavior under dead and live loads.

8.3.1 Stress Distributions in Box Girders

8.3.1.1 Conclusions

1. The AASHTO effective flange method for normal forces was used to calculate peak stresses from the diffusion of cantilever post-tensioning that were close to measured values. In order to predict the tension which was measured at the bottom of the cross-section, the compatibility induced tensile zone bounded by the line of inclination of the compressive force distribution had to be included in the effective cross-section.

2. Shear lag under prestressing and live loads was noticed next to the support at pier P16 in both the free cantilever and fully continuous configurations of the structure. Reduction of the top flange width at P16-2 for analysis of stresses had been required under Section 4.6.2.6.2 of the *AASHTO LRFD Bridge Design Specifications* [2]. The data did not suggest that any changes needed to be made to the code provisions.

3. Measured slopes from the live load test of Ramp P compared quite favorably with calculated values. These slopes were quite small. The calculated values were based on full section properties of the bridge. The presence of significant shear lag would have caused a reduction in the effective area of the cross-section in many parts of the bridge. Thus, greater than anticipated deformations of the bridge would have occurred under applied live load.

8.3.1.2 Recommendations

Based on the data gathered from the Ramp P study which includes information on stresses and bridge deformations under applied loading, no changes need to be made to the provisions of Section 4.6.2.6.2 of the *AASHTO LRFD Bridge Design Specifications* [2] for handling shear lag. However, the specifications pertaining to the analysis of normal force effects should be changed to indicate that compatibility induced stresses and edge tensile stresses must still be considered near the end of the member just as in post-tensioned anchorage zones. Figure 4.6.2.6.2-4 should be redrawn to clarify that the compressive force spreads out in a 30^{o} cone which acts across the width and depth of the girder. However, the end of the flange cannot be

neglected where possible tensile effects occur. Further research to clarify this application is recommended.

8.3.2 Structural Response

8.3.2.1 Conclusions

1. Insignificant transverse splitting stresses were measured during the stressing process of the cantilever tendons. This includes symmetrical and unsymmetrical loading from the tendons.

2. A sharp peak in stress from the stressing of external post-tensioning tendons was measured in P16-10. Segment P16-10 contained the deviation block for the external post-tensioning tendons and the peak in stress was probably due to local zone effects.

3. Longitudinal stresses measured for the determinate cantilever were much closer to calculated values than the stresses measured in the fully continuous structure. The difference was probably due to over-idealization of the bearing pads and the omission of the stiffness contribution from the external tendons in the calculation model used for the continuous structure.

4. Measured live load stresses were much less than the measured dead load stresses indicating that the bridge structure has a high reserve for additional live load.

5. Shear stresses measured in the bridge structure under dead, live and prestressing loads were small. The torsional components of these shear stresses were insignificant.

6. No effect from the horizontal curvature was measured in the longitudinal stresses or the stresses in the external tendons. This indicates that the torsional effect on the moment can be safely ignored for bridges which subtend central angles of up to 15^{o}.

7. The stress changes in the external tendons under live load were very small. Fatigue of these tendons from applied live loads should not be a problem.

8.3.2.2 Recommendations

1. Section 4.6.1.2.1 of the *AASHTO LRFD Bridge Design Specifications* [2] allows structures with torsionally stiff closed cross-sections whose central angle subtended by a span is 12^o or less to be analyzed as straight. This provision of the code may be overly conservative. Data from Ramp P suggests that the angle limit may be increased to 15^o or maybe even more. For a bridge such as Ramp P with a horizontal radius of curvature of 221m (726') the current span length limit for straight bridge analysis would be 46.3m (152'). The instrumented span of Ramp P which demonstrated insignificant torsional effects was 54.9m (180'). This recommendation cannot be assigned to the analysis of substructure forces. It is unknown from the current data what transverse moments and shears may have been transmitted into the Ramp P substructure from the horizontal curvature of the bridge.

2. A poor comparison between calculated and measured stresses from the continuity stressing indicates that a more advanced calculation model should have been used for the analysis. Some factors which were not accounted for in the calculations were modeling of the actual bearing pad conditions, modeling of the true age and stiffness of the concrete at the closure pores, and modeling of the external tendons as they were placed in the structure. Structural designers should remember that these details may be too important to neglect for an accurate analysis of a continuous box girder structure.

8.4 THERMAL BEHAVIOR

8.4.1 Shape and Magnitude of Design Gradients

8.4.1.1 Conclusions

1. The shape of the specified positive and negative design gradients from Section 3.12.3 of the *AASHTO LRFD Bridge Design Specifications* [2] matched the shape of

the measured gradients in the Ramp P superstructure best when the maximum allowable magnitude was used for T_3 (the temperature at the bottom of the gradient).

2. The maximum measured gradients in the Ramp P superstructure were significantly less in magnitude than the AASHTO design gradients. Furthermore, the actual maximum gradient has occurred less than 5% out of the total period of measurement. This data would indicate that the design gradients from the AASHTO code are over-severe.

3. Transverse thermal gradients were measured through the thickness of the flanges and webs of the box girder cross-section. The magnitudes of these gradients were higher than the magnitudes suggested for segmental box girder bridges (but not required) by Section 6.4.4 of the commentary of the *Proposed AASHTO LRFD Guide Specifications for Design of Segmental Concrete Bridges* [17]. The *Guide Specifications* suggest a linear temperature difference of ±5.6 ^{o}C (10 ^{o}F) from the exterior to the interior of the box. Measurements from Ramp P showed transverse gradients as high as +8.6 ^{o}C (15.5 ^{o}F) and as low as -4.1 ^{o}C (-7.4 ^{o}F). Corresponding peak transverse stresses of 7.1 MPa (1.0 ksi) compression and 4.8 MPa (0.7 ksi) tension caused by the transverse temperature gradients were measured in the top flange.

8.4.1.2 Recommendations

1. The bottom temperature of the required design gradients, T_3, should be set at the maximum allowed temperature (2.8 ^{o}C (5 ^{o}F) for the positive gradient and -1.4 ^{o}C (-2.5 ^{o}F) for the negative gradient) to best match the shapes for positive and negative thermal gradients that were measured in Ramp P.

2. The design thermal gradients should be based on statistical data from a variety of actual bridge structures under a variety of climatic conditions. In order to accomplish this, instrumentation of bridge superstructure cross-sections using thermister or thermocouple gauges will have to become a standard practice for new bridges.

3. Transverse design of box girder cross-sections should include analysis of a thermal gradient from the interior to the exterior of the box cross-section. Until such time that a thorough statistical database of bridge temperature studies permits the definition of realistic design gradients, the suggested gradients from Section 6.4.4 of the commentary from the *Proposed AASHTO LRFD Guide Specifications for Design of Segmental Concrete Bridges* [17] should be used.

8.4.2 Analysis Methods

8.4.2.1 Conclusions

1. The recommended method for the analysis of non-linear thermal gradients from Section 4.6.6 of the *AASHTO LRFD Bridge Design Specifications* [2] did a poor job of predicting the thermally induced stresses in Ramp P. The flaw in the AASHTO recommended method is the assumption that plane sections remain plane. Peak stresses measured in Ramp P were as much as 2.9 times the calculated peak compression from the maximum positive gradient and as much as 3.8 times the calculated peak tension from the maximum negative gradient.
2. Warping of the box cross-section affects not only the longitudinal stresses but the transverse stresses from applied thermal gradients as well.

3. Service load combinations of dead load, prestress, live load, and thermal gradients indicated that no tension was occurring in the bridge. The prestress was adequate for applied negative gradients. However, some over-compression was indicated under applied positive gradients. No distress has been observed in the bridge which can be attributed to thermal gradients.

8.4.2.2 Recommendations

The method which is recommended in Section 4.6.6 of the *AASHTO LRFD Bridge Design Specifications* [2] needs to be re-evaluated. The effects of applied non-linear thermal gradients on box girder bridges are not as well understood as are other aspects of box girder behavior. Research studies should be implemented to investigate the problem both analytically and experimentally. Analytical studies should use advanced finite element studies to probe the

response of a variety of box girder bridges to applied climatic conditions. Such an approach would allow an understanding of what shapes and magnitudes of thermal gradients occur in different bridge structures under the same climatic stimuli and what structural response occurs in the different bridge structures. Experimental studies should use instrumentation methods to measure both temperatures and stresses occurring in actual bridge structures. This data could be used to verify that a true analytical understanding of the problem is being developed. Additionally, the data would supply statistical information for the selection of realistic design criteria including not only the shapes and magnitudes for design gradients, but reasonable stress limits for thermal gradient loading conditions.

APPENDIX A - RAMP P ANALYSIS MODEL

Node Layout

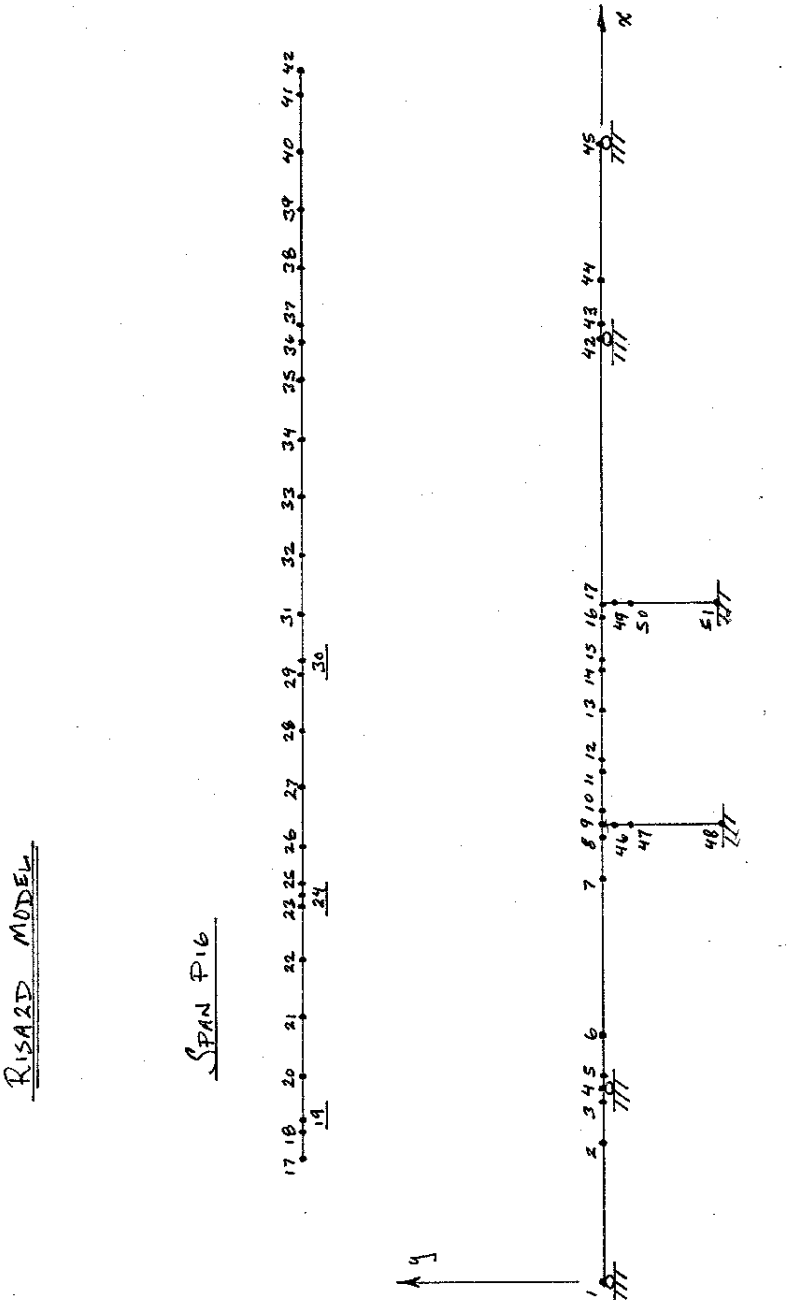

RISA2D Model Coordinates

	Node	x (ft)	y (ft)	notes
Superstructure				
P13	1	0.00	4.813	
	2	92.00	4.813	
	3	120.25	4.701	
P14	4	125.00	4.701	
	5	129.75	4.701	
	6	158.00	4.813	
	7	272.00	4.813	
	8	300.25	4.701	
P15	9	305.00	4.701	
	10	309.75	4.701	
	11	338.00	4.813	
	12	340.59	4.813	Tiltmeter Plate
	13	376.18	4.813	Tiltmeter Plate
	14	411.77	4.813	Tiltmeter Plate
	15	414.36	4.813	
	16	442.61	4.701	
P16	17	447.36	4.701	Tiltmeter Plate
	18	452.11	4.701	P16-2 Instrumentation
	19	453.61	4.707	
	20	461.53	4.739	
	21	470.94	4.776	
	22	480.36	4.813	
	23	489.78	4.813	
	24	491.28	4.813	P16-10 Instrumentation
	25	492.36	4.813	Tiltmeter Plate
	26	499.20	4.813	
	27	508.61	4.813	
	28	518.03	4.813	
	29	527.45	4.813	
	30	528.95	4.813	P16-17 Instrumentation
	31	537.36	4.813	Tiltmeter Plate
	32	547.27	4.813	
	33	556.69	4.813	
	34	566.11	4.813	
	35	575.53	4.813	
	36	582.36	4.813	Tiltmeter Plate
	37	584.94	4.813	
	38	594.36	4.813	
	39	603.78	4.776	
	40	613.19	4.739	
	41	622.61	4.701	
P17	42	627.36	4.701	Tiltmeter Plate
	43	632.11	4.701	
	44	660.36	4.813	
P18	45	752.36	4.813	
Substructure				
	46	305.00	0	
	47	305.00	-9	
	48	305.00	-72	
	50	447.36	0	
	51	447.36	-9	
		447.36	-70	

Effective Flange Width Check

RAMP P EFFECTIVE FLANGE WIDTH CALCULATIONS
(SECTION 4.6.2.6.2 - AASHTO LRFD BRIDGE DESIGN SPECIFICATIONS)

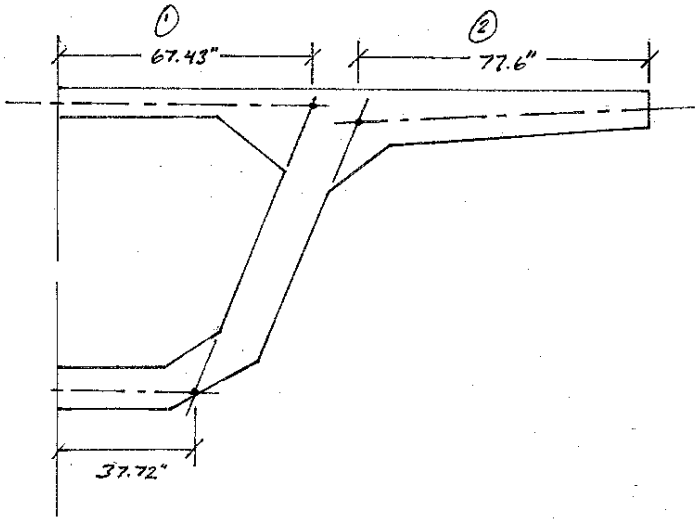

CANTILEVER CONDITION:

$l = 90'$, $l_i = 1.5l = 1.5(90') = 135'$

① $67.43" / (135')(12"/ft) = 0.04 < 0.5$ → no reduction

② $77.6" / (135')(12"/ft) = 0.048 < 0.5$ → no reduction

CONTINUOUS CONDITION:

$l = 180'$, $l_i = 0.6l = 0.6(180') = 108'$

① $67.43" / (108')(12"/ft) = 0.052 \simeq 0.05$ → no significant reduction

② $77.6" / (108')(12"/ft) = 0.06$ $b_s \simeq 0.85$
$b_m \simeq 0.98$ → ignore reduction, not significant

Some slight reduction for P16-2 under continuous span load conditions: $b_s = 0.85$ on outer wings

Effective Flange Width Check

Middle Span

$\ell = 142.36'$, $\ell_i = 0.6\,\ell = 85.4'$

① $67.43" / (85.4')(12"/ft) = 0.066$ $\quad b_s \approx 0.85$, $b_m \approx$ ~~0.98~~ → 1

② $77.6" / (85.4')(12"/ft) = 0.076$ $\quad b_s \approx 0.8$, $b_m \approx$ ~~0.97~~ → 1

End Spans

$\ell = 125'$, $\ell_i = 0.8\ell = 100'$

① $67.43" / (100')(12"/ft) = 0.056$ $\quad b_s \approx 0.90$, $b_m \approx 1.0$

② $77.6" / (100')(12"/ft) = 0.065$ $\quad b_s \approx 0.85$, $b_m \approx$ ~~0.98~~ → 1

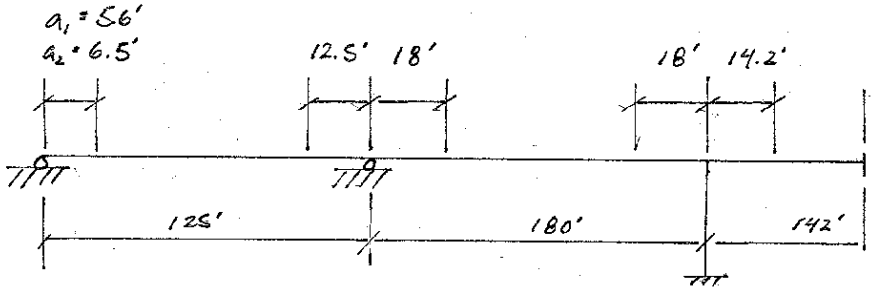

Cross-Section Properties

Section: **Effective Section at P16-2**
Date: **May-97**

Calculation of Flexural Properties

node	x (in)	y (in)	Ai	ybi	xbi	Ix-xi	Iy-yi
1	0.0000	0.0000					
2	0.0000	14.0000	0.00	0.00	0.00	0.00	0.00
3	34.5000	14.0000	241.50	0.72	0.89	23667.00	47907.56
4	43.5000	20.0000	-40.50	-0.15	-0.34	-5913.00	-30936.94
5	60.2500	62.0000	-746.00	-6.54	-8.27	-681844.00	-1012469.65
6	41.2500	76.0000	-1010.75	-14.91	-10.97	-2414344.83	-1316828.26
7	0.0000	76.0000	-1567.50	-25.47	-6.91	-4526940.00	-444533.20
8	0.0000	84.0000	0.00	0.00	0.00	0.00	0.00
9	144.3600	84.0000	6063.12	108.90	93.57	21390687.36	21059044.40
10	144.3600	74.0000	721.80	12.19	22.28	2255384.40	7521087.28
11	87.2197	69.1023	-1760.68	-26.94	-43.59	-4508706.92	-12042466.56
12	70.7933	57.1083	-44.49	-0.60	-0.75	-88861.39	-139368.08
13	52.7500	12.0000	1081.47	7.99	14.28	737321.67	2077975.68
14	30.0000	0.0000	180.00	0.23	1.59	4320.00	157951.88
15	0.0000	0.0000	0.00	0.00	0.00	0.00	0.00
16	0.0000	0.0000	0.00	0.00	0.00	0.00	0.00
17	0.0000	0.0000	0.00	0.00	0.00	0.00	0.00
18	0.0000	0.0000	0.00	0.00	0.00	0.00	0.00
1	0.0000	0.0000	0.00	0.00	0.00	0.00	0.00

Totals:						
	Units in inches	3117.97	55.43	61.78	12184770.28	15877364.11
	Units in feet	21.653	4.619	5.149	587.614	765.691

Properties of Full Section:			
	Area	**43.31 ft^2**	**6236 in^2**
	Ybottom	**4.619 ft**	**55.43 in**
	Ytop	**2.381 ft**	**28.57 in**
	Ix-x	**251.4 ft^4**	**5212887 in^4**
	Iy-y	**1531.4 ft^4**	**31754728 in^4**

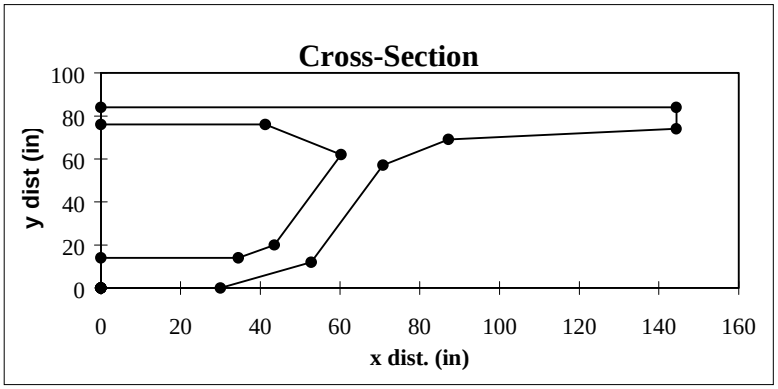

Cross-Section Properties

Section: **Effective Section at P16-2**
Date: **May-97**

Calculation of Torsional Constant

Torsional Constant = 4*(Avg. Thickness)*(Area)^2/(Perimeter) = 8623565 in^4
= **4990.5 ft^4**

node	x (in)	y (in)	Ai	Li	ti (in)	Li*ti
a	0.0000	7.0000				
b	32.2500	7.0000	112.88	32.25	11.00	354.75
c	48.1250	16.0000	-89.56	18.248716	10.50	191.61
d	65.5217	59.5542	-908.85	46.899972	12.00	562.80
e	65.5217	73.0000	-440.50	13.44585	14.50	194.96
f	41.2500	80.0000	-1115.24	25.260899	15.50	391.54
g	0.0000	80.0000	-1650.00	41.25	8.00	330.00

Totals:	Units in inches	-4091.27	177.36
	Units in feet	-28.412	14.780

Properties of Full Section:	Area	56.823	ft^2
		8182.5	in^2
	Perimeter	29.559	ft

Average Thickness:
11.42 in

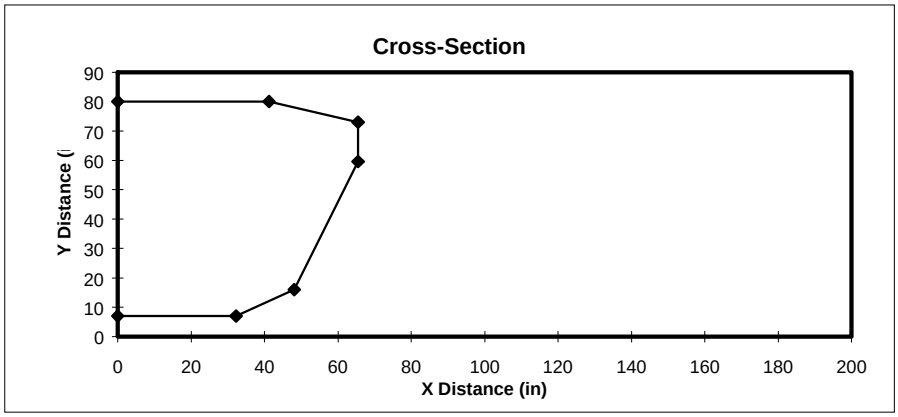

Cross-Section Properties

Section: **Effective Section at P16-2**
Date: **May-97**

Calculation of Shear Properties

Neutral Axis Located at y = 55.4254 in
Calculate Q at y = 41.0000 in

node	x (in)	y (in)	Ai	ybi
4	43.5000	20.0000		
4a	51.8750	41.0000		
5	60.2500	62.0000	-373.00	-5.80
6	41.2500	76.0000	-1010.75	-21.06
7	0.0000	76.0000	-1567.50	-35.97
8	0.0000	84.0000	0.00	0.00
9	144.3600	84.0000	6063.12	153.77
10	144.3600	74.0000	721.80	17.22
11	87.2197	69.1023	-1760.68	-38.03
12	70.7933	57.1083	-44.49	-0.85
11a	64.3500	41.0000	435.36	7.24
4a	51.8750	41.0000	-255.74	-3.17
13	52.7500	12.0000		

Totals:	Units in inches	2208.13	73.35
	Units in feet	15.334	6.112

Calculation of 1st Moment of Inertia, Q:

1) About the x-axis:

Q = (Area above N.A.)*(Distance from N.A. to the C.G. of that Area)
Q = 79146.041 in^3
45.802 ft^3

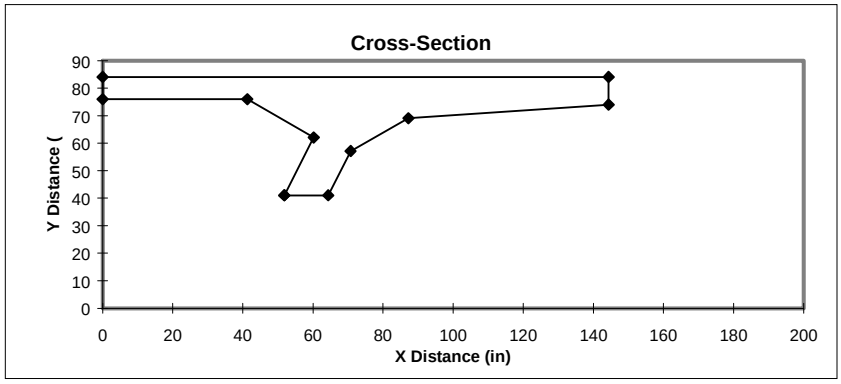

Cross-Section Properties

Section: **Full Section Properties for P16-2 (14" bottom slab thickness)**
Date: **May-97**

Calculation of Flexural Properties

node	x (in)	y (in)	Ai	ybi	xbi	Ix-xi	Iy-yi
1	0.0000	0.0000					
2	0.0000	14.0000	0.00	0.00	0.00	0.00	0.00
3	34.5000	14.0000	241.50	0.69	0.85	23667.00	47907.56
4	43.5000	20.0000	-40.50	-0.14	-0.32	-5913.00	-30936.94
5	60.2500	62.0000	-746.00	-6.25	-7.91	-681844.00	-1012469.65
6	41.2500	76.0000	-1010.75	-14.25	-10.48	-2414344.83	-1316828.26
7	0.0000	76.0000	-1567.50	-24.34	-6.61	-4526940.00	-444533.20
8	0.0000	84.0000	0.00	0.00	0.00	0.00	0.00
9	156.0000	84.0000	6552.00	112.45	104.42	23115456.00	26574912.00
10	156.0000	74.0000	780.00	12.59	24.86	2437240.00	9491040.00
11	87.2197	69.1023	-2162.85	-31.62	-53.74	-5538590.82	-16419477.57
12	70.7933	57.1083	-44.49	-0.57	-0.72	-88861.39	-139368.08
13	52.7500	12.0000	1081.47	7.64	13.65	737321.67	2077975.68
14	30.0000	0.0000	180.00	0.22	1.52	4320.00	157951.88
15	0.0000	0.0000	0.00	0.00	0.00	0.00	0.00
16	0.0000	0.0000	0.00	0.00	0.00	0.00	0.00
17	0.0000	0.0000	0.00	0.00	0.00	0.00	0.00
18	0.0000	0.0000	0.00	0.00	0.00	0.00	0.00
1	0.0000	0.0000	0.00	0.00	0.00	0.00	0.00

Totals:						
	Units in inches	3262.88	56.41	65.53	13061510.62	18986173.42
	Units in feet	22.659	4.701	5.461	629.895	915.614

Properties of Full Section:			
	Area	**45.32 ft^2**	**6526 in^2**
	Ybottom	**4.701 ft**	**56.41 in**
	Ytop	**2.299 ft**	**27.59 in**
	Ix-x	**258.2 ft^4**	**5354265 in^4**
	Iy-y	**1831.2 ft^4**	**37972347 in^4**

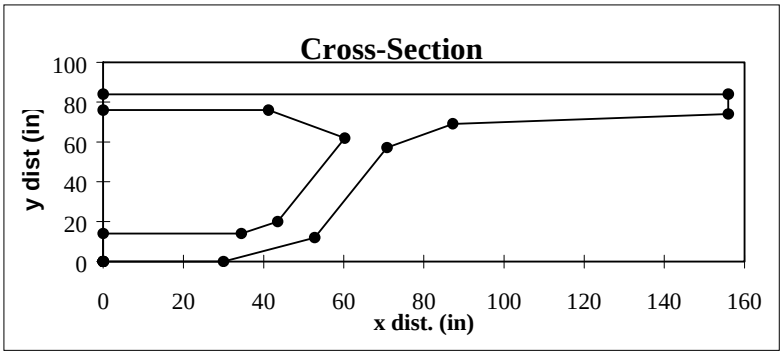

Cross-Section Properties

Section: **Full Section Properties for P16-2 (14" bottom slab thickness)**
Date: **May-97**

Calculation of Torsional Constant

Torsional Constant = 4*(Avg. Thickness)*(Area)^2/(Perimeter) = 8623565 in^4
= **4990.5 ft^4**

node	x (in)	y (in)	Ai	Li	ti (in)	Li*ti
a	0.0000	7.0000				
b	32.2500	7.0000	112.88	32.25	11.00	354.75
c	48.1250	16.0000	-89.56	18.248716	10.50	191.61
d	65.5217	59.5542	-908.85	46.899972	12.00	562.80
e	65.5217	73.0000	-440.50	13.44585	14.50	194.96
f	41.2500	80.0000	-1115.24	25.260899	15.50	391.54
g	0.0000	80.0000	-1650.00	41.25	8.00	330.00

Totals:			
	Units in inches	-4091.27	177.36
	Units in feet	-28.412	14.780

Properties of Full Section:			
	Area	56.823	ft^2
		8182.5	in^2
	Perimeter	29.559	ft

Average Thickness:
11.42 in

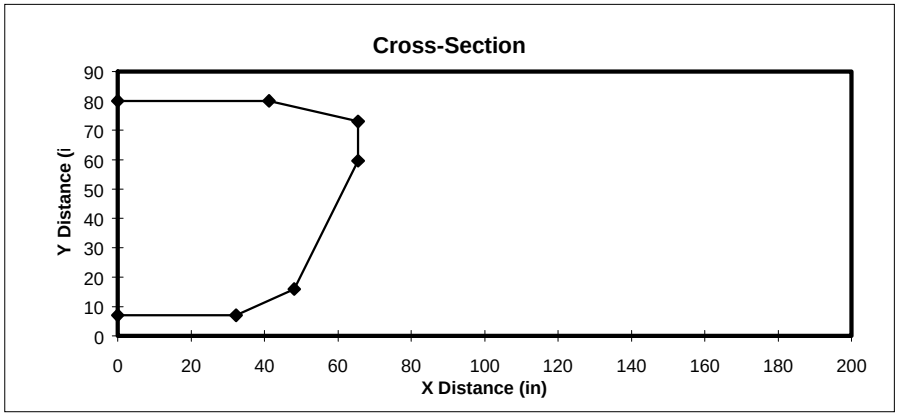

Cross-Section Properties

Section: Full Section Properties for P16-2 (14" bottom slab thickness)
Date: May-97

Calculation of Shear Properties

Neutral Axis Located at y = 56.4144 in
Calculate Q at y = 41.0000 in

node	x (in)	y (in)	Ai	ybi
4	43.5000	20.0000		
4a	51.8750	41.0000		
5	60.2500	62.0000	-373.00	-5.44
6	41.2500	76.0000	-1010.75	-19.76
7	0.0000	76.0000	-1567.50	-33.75
8	0.0000	84.0000	0.00	0.00
9	156.0000	84.0000	6552.00	155.93
10	156.0000	74.0000	780.00	17.46
11	87.2197	69.1023	-2162.85	-43.85
12	70.7933	57.1083	-44.49	-0.80
11a	64.3500	41.0000	435.36	6.79
4a	51.8750	41.0000	-255.74	-2.97
13	52.7500	12.0000		

Totals:	Units in inches	2353.03	73.61
	Units in feet	16.340	6.135

Calculation of 1st Moment of Inertia, Q:

1) About the x-axis:

Q = (Area above N.A.)*(Distance from N.A. to the C.G. of that Area)
Q = 80945.732 in^3
46.844 ft^3

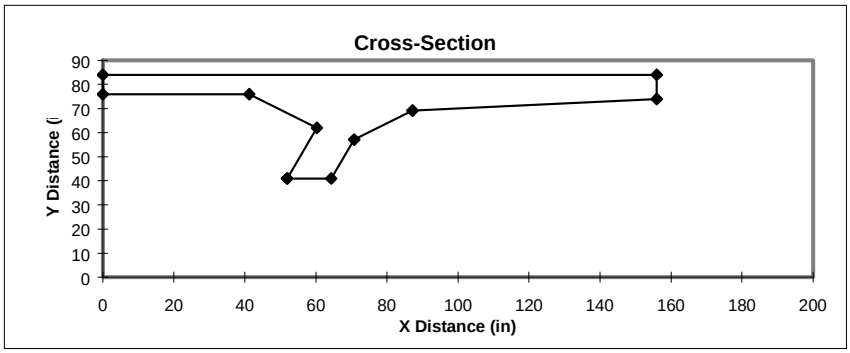

Cross-Section Properties

Section: **Full Section Propoerties for P16-10 and P16-17 (11" Bottom Slab)**
Date: **May-97**

Calculation of Flexural Properties

node	x (in)	y (in)	Ai	ybi	xbi	Ix-xi	Iy-yi
1	0.0000	0.0000					
2	0.0000	11.0000	0.00	0.00	0.00	0.00	0.00
3	30.0000	11.0000	165.00	0.38	0.52	9982.50	24750.00
4	43.5000	20.0000	-60.75	-0.20	-0.47	-7502.63	-41484.66
5	60.2500	62.0000	-746.00	-6.44	-8.15	-681844.00	-1012469.65
6	41.2500	76.0000	-1010.75	-14.68	-10.80	-2414344.83	-1316828.26
7	0.0000	76.0000	-1567.50	-25.08	-6.81	-4526940.00	-444533.20
8	0.0000	84.0000	0.00	0.00	0.00	0.00	0.00
9	156.0000	84.0000	6552.00	115.89	107.61	23115456.00	26574912.00
10	156.0000	74.0000	780.00	12.97	25.62	2437240.00	9491040.00
11	87.2197	69.1023	-2162.85	-32.59	-55.38	-5538590.82	-16419477.57
12	70.7933	57.1083	-44.49	-0.59	-0.74	-88861.39	-139368.08
13	52.7500	12.0000	1081.47	7.87	14.07	737321.67	2077975.68
14	30.0000	0.0000	180.00	0.23	1.57	4320.00	157951.88
15	0.0000	0.0000	0.00	0.00	0.00	0.00	0.00
16	0.0000	0.0000	0.00	0.00	0.00	0.00	0.00
17	0.0000	0.0000	0.00	0.00	0.00	0.00	0.00
18	0.0000	0.0000	0.00	0.00	0.00	0.00	0.00
1	0.0000	0.0000	0.00	0.00	0.00	0.00	0.00

Totals:	Units in inches	3166.13	57.76	67.04	13046236.50	18952468.13
	Units in feet	21.987	4.813	5.586	629.159	913.989

Properties of Full Section:	**Area**	**43.97 ft^2**	**6332 in^2**
	Ybottom	**4.813 ft**	**57.76 in**
	Ytop	**2.187 ft**	**26.24 in**
	Ix-x	**239.7 ft^4**	**4970169 in^4**
	Iy-y	**1828.0 ft^4**	**37904936 in^4**

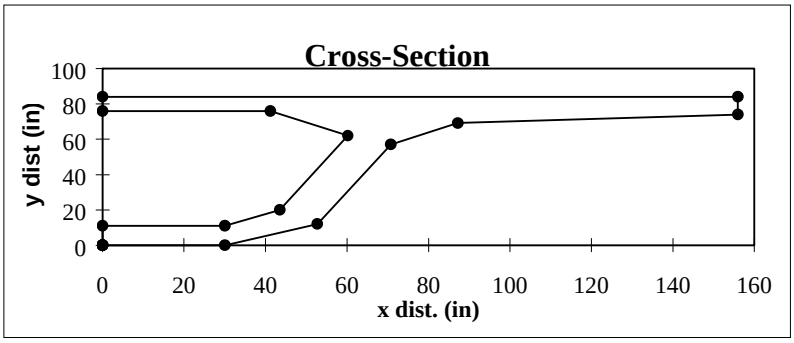

Cross-Section Properties

Section: **Full Section Propoerties for P16-10 and P16-17 (11" Bottom Slab)**
Date: **May-97**

Calculation of Torsional Constant

Torsional Constant = 4*(Avg. Thickness)*(Area)^2/(Perimeter) = 8800183 in^4
= **5092.7 ft^4**

node	x (in)	y (in)	Ai	Li	ti (in)	Li*ti
a	0.0000	5.5000				
b	30.0000	5.5000	82.50	30	11.00	330.00
c	48.1250	16.0000	-107.66	20.946733	10.50	219.94
d	65.5217	59.5542	-908.85	46.899972	12.00	562.80
e	65.5217	73.0000	-440.50	13.44585	14.50	194.96
f	41.2500	80.0000	-1115.24	25.260899	15.50	391.54
g	0.0000	80.0000	-1650.00	41.25	8.00	330.00

Totals:	Units in inches	-4139.74	177.80
	Units in feet	-28.748	14.817

Properties of Full Section:	Area	57.496	ft^2
		8279.5	in^2
	Perimeter	29.634	ft

Average Thickness:
11.41 in

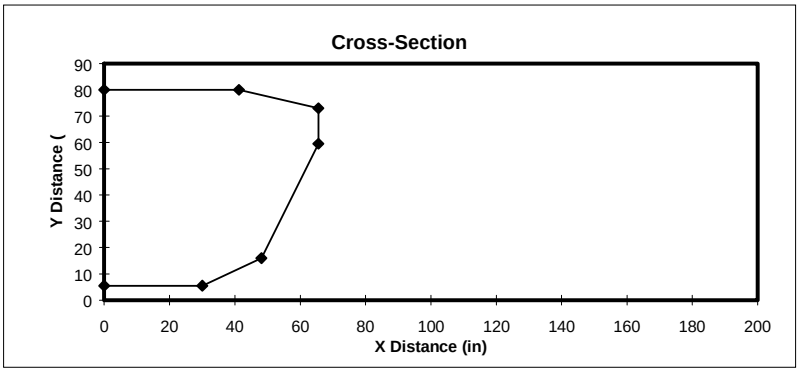

Cross-Section Properties

Section: Full Section Propoerties for P16-10 and P16-17 (11" Bottom Slab)
Date: May-97

Calculation of Shear Properties

Neutral Axis Located at y = 57.7553 in
Calculate Q at y = 41.0000 in

node	x (in)	y (in)	Ai	ybi
4	43.5000	20.0000		
4a	51.8750	41.0000		
5	60.2500	62.0000	-373.00	-5.44
6	41.2500	76.0000	-1010.75	-19.76
7	0.0000	76.0000	-1567.50	-33.75
8	0.0000	84.0000	0.00	0.00
9	156.0000	84.0000	6552.00	155.93
10	156.0000	74.0000	780.00	17.46
11	87.2197	69.1023	-2162.85	-43.85
12	70.7933	57.1083	-44.49	-0.80
11a	64.3500	41.0000	435.36	6.79
4a	51.8750	41.0000	-255.74	-2.97
13	52.7500	12.0000		

Totals:	Units in inches	2353.03	73.61
	Units in feet	16.340	6.135

Calculation of 1st Moment of Inertia, Q:

1) About the x-axis:

Q = (Area above N.A.)*(Distance from N.A. to the C.G. of that Area)

Q = 74635.55 in^3

43.192 ft^3

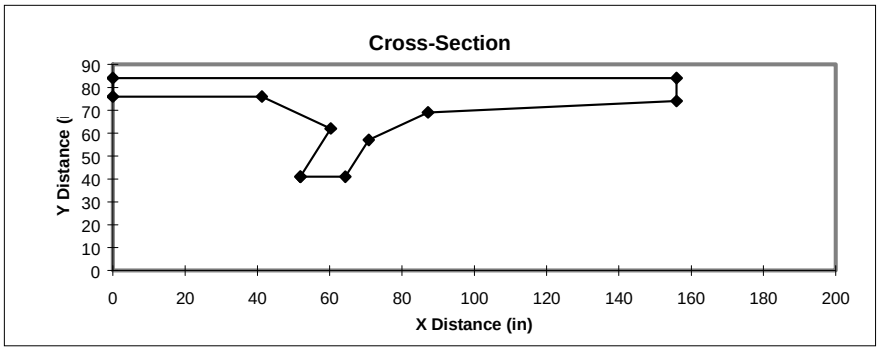

APPENDIX B - CONSTRUCTION CALCULATIONS

Diffusion of Post-Tensioning

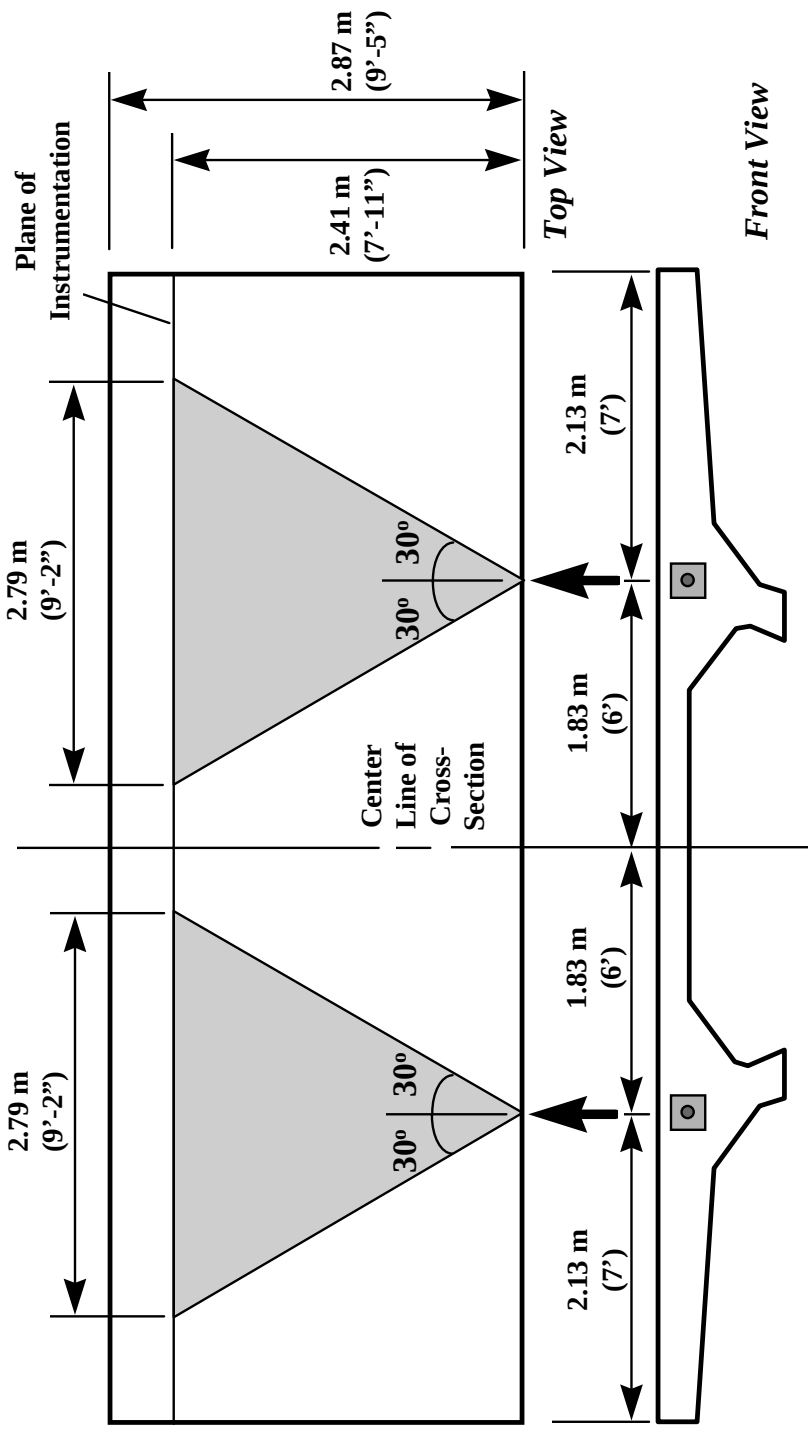

Diffusion of Post-Tensioning

Section: Balanced Cantilever Ramp P Segment P16-10 (Effective width for PT)
Date: May-97

Calculation of Flexural Properties

node	x (in)	y (in)	Ai	ybi	xbi	Ix-xi	Iy-yi
1	0.0000	0.0000					
2	0.0000	11.0000	0.00	0.00	0.00	0.00	0.00
3	30.0000	11.0000	165.00	0.43	0.58	9982.50	24750.00
4	43.5000	20.0000	-60.75	-0.22	-0.53	-7502.63	-41484.66
5	60.2500	62.0000	-746.00	-7.23	-9.15	-681844.00	-1012469.65
6	41.2500	76.0000	-1010.75	-16.48	-12.12	-2414344.83	-1316828.26
7	0.0000	76.0000	-1567.50	-28.16	-7.64	-4526940.00	-444533.20
8	0.0000	84.0000	0.00	0.00	0.00	0.00	0.00
9	127.0000	84.0000	5334.00	105.90	80.06	18818352.00	14338681.00
10	127.0000	73.2251	684.21	12.71	20.54	2117483.89	5517780.50
11	87.2197	69.1023	-1194.66	-20.09	-30.24	-3025888.87	-6931654.32
12	70.7933	57.1083	-44.49	-0.66	-0.83	-88861.39	-139368.08
13	52.7500	12.0000	1081.47	8.83	15.79	737321.67	2077975.68
14	30.0000	0.0000	180.00	0.26	1.76	4320.00	157951.88
15	0.0000	0.0000	0.00	0.00	0.00	0.00	0.00
16	0.0000	0.0000	0.00	0.00	0.00	0.00	0.00
17	0.0000	0.0000	0.00	0.00	0.00	0.00	0.00
18	0.0000	0.0000	0.00	0.00	0.00	0.00	0.00
1	0.0000	0.0000	0.00	0.00	0.00	0.00	0.00

Totals:	Units in inches	2820.52	55.28	58.22	10942078.33	12230800.88
	Units in feet	19.587	4.607	4.851	527.685	589.834

Properties of Full Section:	**Area**	**39.17 ft^2**	**5641 in^2**
	Ybottom	**4.607 ft**	**55.28 in**
	Ytop	**2.393 ft**	**28.72 in**
	Ix-x	**224.0 ft^4**	**4644908 in^4**
	Iy-y	**1179.7 ft^4**	**24461602 in^4**

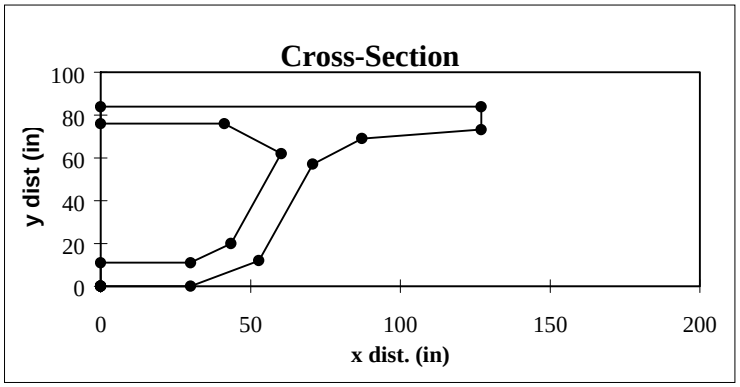

Diffusion of Post-Tensioning

EFFECTIVE FLANGE WIDTH CALCULATION
(FOR DIFFUSION OF CANTILEVER PT)

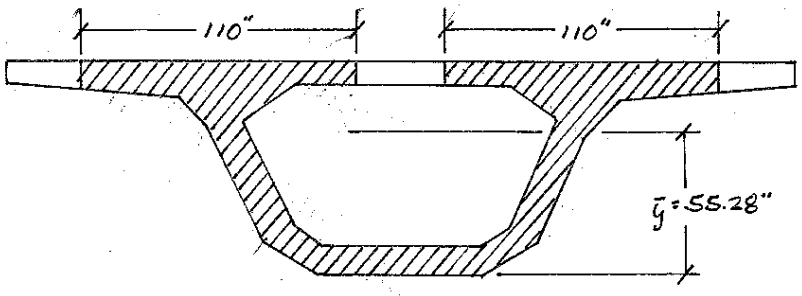

AREA = 5641 in^2
INERTIA = 4644908 in^4

$$\sigma_{Top} = \frac{(1083^k)}{(5641\ in^2)} + \frac{(1083^k)(28.72" - 8")(26.72")}{(4644908\ in^4)} = 0.321\ ksi$$

2.21 MPa

$$\sigma_{Bot} = \frac{(1083^k)}{(5641\ in^2)} + \frac{(1083^k)(28.72" - 8")(-53.28")}{(4644908\ in^4)} = -0.065\ ksi$$

-0.45 MPa

FULL SECTION CALCULATION

AREA = 6332 in^2 $\bar{y}$ = 57.76"
INERTIA = 4970169 in^4

$$\sigma_{Top} = \frac{(1083^k)}{(6332\ in^2)} + \frac{(1083^k)(26.24" - 8")(24.24")}{(4970169\ in^4)} = 0.267\ ksi$$

1.84 MPa

$$\sigma_{Bot} = \frac{(1083^k)}{(6332\ in^2)} + \frac{(1083^k)(26.24" - 8")(-55.76")}{(4970169\ in^4)} = -0.051\ ksi$$

-0.35 MPa

Cantilever Construction

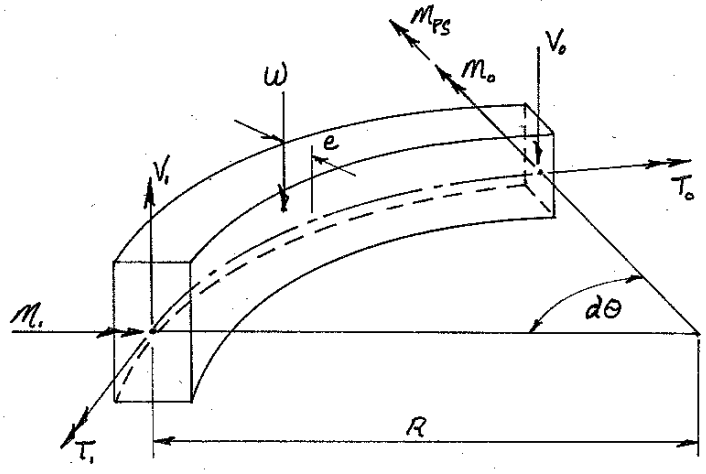

M_{PS} = PRESTRESS MOMENT
W = WEIGHT OF SEGMENT
e = ECCENTRICITY OF WEIGHT
R = RADIUS
$d\theta$ = CENTRAL ANGLE SUB-TENDED BY SEGMENT ARC

$$V_1 = V_o + W \longrightarrow dV = W$$

$$M_1 = V_o \times \left[R \sin(2\theta)\right] + M_o \times \left[\cos(2\theta)\right] + T_o \times \left[-\sin(d\theta)\right] + W \times (R+e) \times \sin(2\theta/2) + M_{PS} \times \cos(2\theta)$$

$$T_1 = V_o \times \left[R - R\cos(2\theta)\right] + M_o \times \left[\sin(2\theta)\right] + T_o \times \left[\cos(2\theta)\right] + W \times \left[R - (R+e)\cos(2\theta/2)\right] + M_{PS} \times \sin(2\theta)$$

Cantilever Construction

Segment Weights

Weight of Vertical Deviator

Cross-Sectional Area: 51.658 sf - 43.974 sf = 7.684 sf
Length: 3.0 ft

Weight = (7.684 sf)(3.0')(0.155 kcf) = 3.57 kips

Weight of Horizontal Deviator

Area: 7.684 sf
Length: 2.0 ft

Weight = (7.684 sf)(2.0')(0.155 kcf) = 2.38 kips

Weight of Anchor Blocks

Area: 49.181 sf - 44.401 sf = 4.780 sf (both blocks)
Length: 5.0 ft

Weight = (4.78 sf)(5.0')(0.155 kcf) = 3.70 kips

Segment	Weight
P16-2	$\frac{1}{2}(45.318\ sf + 44.849\ sf)(9.417')(0.155\ kcf)$ = 65.81 kips
P16-4	$\frac{1}{2}(44.849\ sf + 44.401\ sf)(9.417')(0.155\ kcf) + 3.70^k$ = 68.84 kips
P16-6	$\frac{1}{2}(44.401\ sf + 43.970\ sf)(9.417')(0.155\ kcf) + 3.70^k$ = 68.19 kips
P16-8	$(43.970\ sf)(9.417')(0.155\ kcf)$ = 64.18 kips
P16-10	$64.18^k + 3.57^k$ = 67.75 kips
P16-12	64.18 kips
P16-15	64.18 kips
P16-16	$64.18^k + 2.38^k$ = 66.56 kips
P16-17	64.18 kips

Cantilever Construction

ECCENTRICITY OF BOX DEAD LOAD

$e = \rho_y^2 / R$

ρ_y = RADIUS OF GYRATION ABOUT VERTICAL AXIS
R = RADIUS OF HORIZONTAL CURVE

$$\rho_y = \sqrt{\frac{I_y}{A}}$$

$$= \sqrt{\frac{1828\ ft^4}{43.97\ ft^2}} = 6.45\ ft$$

$$e = \frac{(6.45')^2}{726.2'} = \underline{\underline{0.057\ ft}} = 0.69\ in$$

(+ on outside of curve)

Name: Calculation of Moments and Torques After Completion of Cantilever
Date:

Radius = 726.2 feet

	Forces on Cantilever								
	Segment Properties			Dead Load Forces				Post-Tensioning Forces*	
Segment	Midline Length (ft)	Center of Gravity* (ft)	Shear Center* (ft)	Segment Weight (1) (kips)	Eccentricity* of (1) (ft)	Distributed Loads (2) (k/ft)	Eccentricity* of (2) (ft)	Internal P.T. (3) (kips)	Eccentricity of (3) (ft)
P16-2	9.417	4.70	4.70	65.8	0.00	0.00	0.00	1083	6.58
P16-4	9.417	4.74	4.74	68.8	0.00	0.00	0.00	1083	6.58
P16-6	9.417	4.78	4.78	68.2	0.00	0.00	0.00	1083	6.58
P16-8	9.417	4.81	4.81	64.2	0.00	0.00	0.00	1083	6.58
P16-10	9.417	4.81	4.81	67.8	0.00	0.00	0.00	1083	6.58
P16-12	9.417	4.81	4.81	64.2	0.00	0.00	0.00	1083	6.58
P16-14	9.417	4.81	4.81	64.2	0.00	0.00	0.00	1083	6.58
P16-16	9.417	4.81	4.81	66.6	0.00	0.00	0.00	1083	6.58
P16-17	9.417	4.81	4.81	64.2	0.00	0.00	0.00	0	6.58

* Measured from bottom @ i-node

* Positive towards outside of curve

* Internal P.T. load applied at j-node

	Changes in Shear		Changes in Moment			Changes in Torque		
Δθ (radians)	ΔShear from (1)	ΔShear from (2)	ΔMoment from (1)	ΔMoment from (2)	ΔMoment from (3)	ΔTorque from (1)	ΔTorque from (2)	ΔTorque from (3)
0.01297	65.8	0.0	-310	0	2038	-1.0	0.0	0.0
0.01297	68.8	0.0	-324	0	1997	-1.1	0.0	0.0
0.01297	68.2	0.0	-321	0	1957	-1.0	0.0	0.0
0.01297	64.2	0.0	-302	0	1917	-1.0	0.0	0.0
0.01297	67.8	0.0	-319	0	1917	-1.0	0.0	0.0
0.01297	64.2	0.0	-302	0	1917	-1.0	0.0	0.0
0.01297	64.2	0.0	-302	0	1917	-1.0	0.0	0.0
0.01297	66.6	0.0	-314	0	1917	-1.0	0.0	0.0
0.01297	64.2	0.0	-302	0	0	-1.0	0.0	0.0

Length	Cummulative from Post-Tensioning					
to	Shear		Moment		Torque	
@ i node	*@ i node*	*@ j node*	*@ i node*	*@ j node*	*@ i node*	*@ j node*
0.0	0.0	0.0	15571	15572	0.0	0.0
9.4	0.0	0.0	13534	13535	0.0	0.0
18.8	0.0	0.0	11538	11539	0.0	0.0
28.3	0.0	0.0	9582	9583	0.0	0.0
37.7	0.0	0.0	7666	7667	0.0	0.0
47.1	0.0	0.0	5750	5750	0.0	0.0
56.5	0.0	0.0	3833	3834	0.0	0.0
65.9	0.0	0.0	1917	1917	0.0	0.0
75.3	0.0	0.0	0	0	0.0	0.0
84.8	0.0		0		0.0	

Length	Cummulative From Dead Load					
to	Shear		Moment		Torque	
@ i node	*@ i node*	*@ j node*	*@ i node*	*@ j node*	*@ i node*	*@ j node*
0.0	594.0	528.2	-24946	-19673	-963.8	-675.5
9.4	528.2	459.4	-19673	-15030	-675.5	-451.6
18.8	459.4	391.2	-15030	-11029	-451.6	-283.6
28.3	391.2	327.0	-11029	-7651	-283.6	-163.5
37.7	327.0	259.2	-7651	-4892	-163.5	-83.2
47.1	259.2	195.0	-4892	-2754	-83.2	-34.6
56.5	195.0	130.8	-2754	-1220	-34.6	-9.8
65.9	130.8	64.2	-1220	-302	-9.8	-1.0
75.3	64.2	0.0	-302	0	-1.0	0.0
84.8	0.0		0		0.0	

Length	Cummulative Forces						Length	Cummulative Post-Tensioning	
to	Shear		Moment		Torque		to	Axial	
@ i node	*@ i node*	*@ j node*	*@ i node*	*@ j node*	*@ i node*	*@ j node*	*@ i node*	*@ i node*	*@ j node*
0.0	594.0	528.2	-9374.9	-4100.3	-963.8	-675.5	0.0	8664.0	8664.0
9.4	528.2	459.4	-6138.5	-1494.5	-675.5	-451.6	9.4	7581.0	7581.0
18.8	459.4	391.2	-3491.5	509.8	-451.6	-283.6	18.8	6498.0	6498.0
28.3	391.2	327.0	-1447.2	1932.4	-283.6	-163.5	28.3	5415.0	5415.0
37.7	327.0	259.2	15.5	2774.7	-163.5	-83.2	37.7	4332.0	4332.0
47.1	259.2	195.0	857.8	2996.1	-83.2	-34.6	47.1	3249.0	3249.0
56.5	195.0	130.8	1079.2	2613.3	-34.6	-9.8	56.5	2166.0	2166.0
65.9	130.8	64.2	696.4	1614.6	-9.8	-1.0	65.9	1083.0	1083.0
75.3	64.2	0.0	-302.3	0.0	-1.0	0.0	75.3	0.0	0.0
84.8	0.0	0.0	0.0	0.0	0.0	0.0	84.8	0.0	

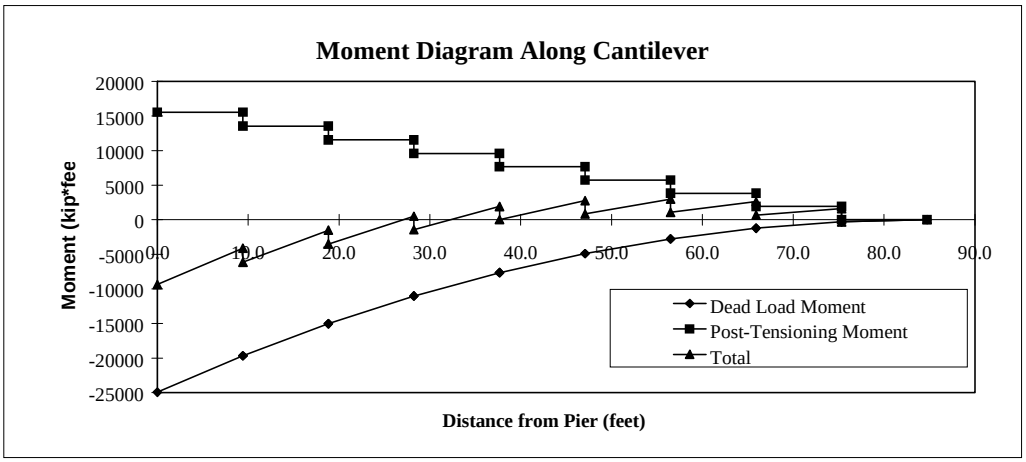
Moment Diagram Along Cantilever
Moment (kip*fee
20000
15000
10000
5000
0
-5000
-10000
-15000
-20000
-25000
0.0
10.0
20.0
30.0
40.0
50.0
60.0
70.0
80.0
90.0
Dead Load Moment
Post-Tensioning Moment
Total
Distance from Pier (feet)

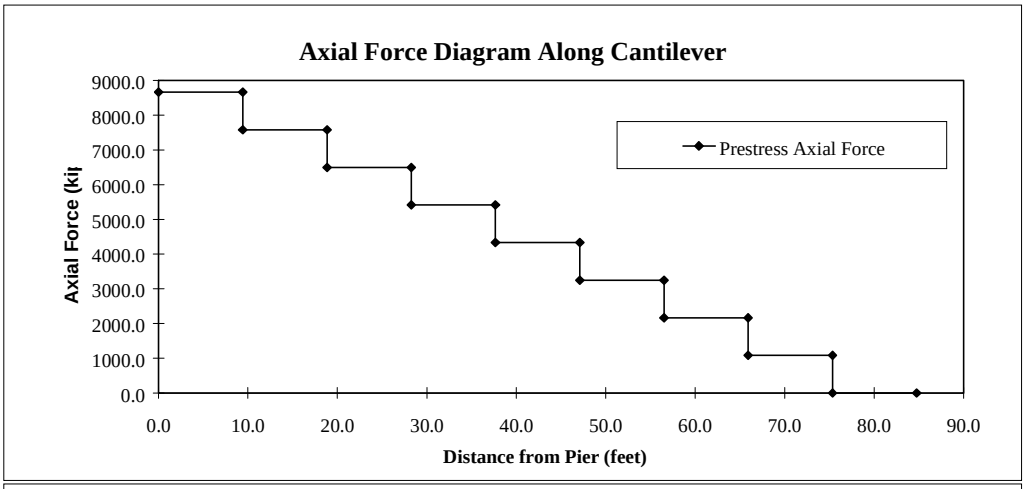
Axial Force Diagram Along Cantilever
Axial Force (kip
9000.0
8000.0
7000.0
6000.0
5000.0
4000.0
3000.0
2000.0
1000.0
0.0
0.0
10.0
20.0
30.0
40.0
50.0
60.0
70.0
80.0
90.0
Prestress Axial Force
Distance from Pier (feet)

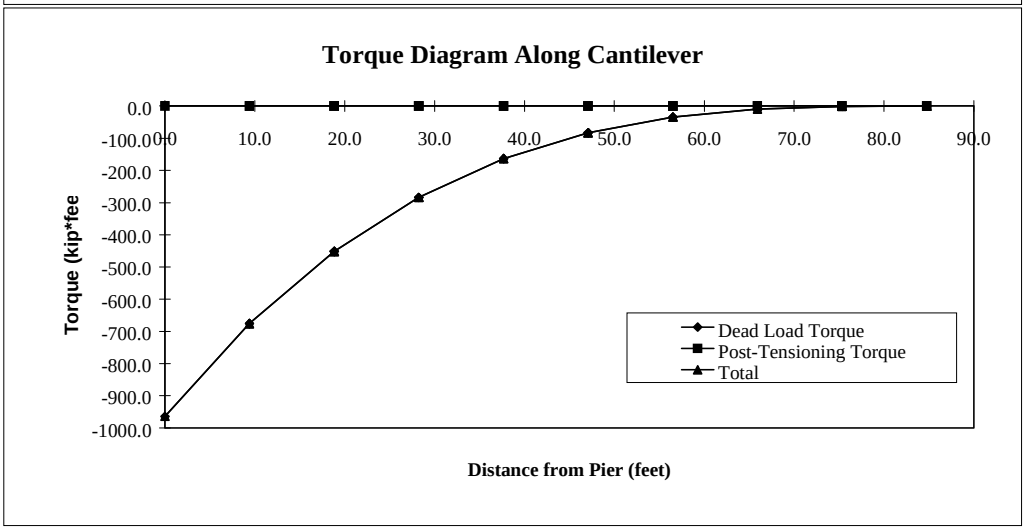
Torque Diagram Along Cantilever
Torque (kip*fee
0.0
-100.0
-200.0
-300.0
-400.0
-500.0
-600.0
-700.0
-800.0
-900.0
-1000.0
0.0
10.0
20.0
30.0
40.0
50.0
60.0
70.0
80.0
90.0
Dead Load Torque
Post-Tensioning Torque
Total
Distance from Pier (feet)

Cantilever Construction

Calculation of Longitudinal Flexural Stresses

P16-2

Dead Load

$$\sigma_{Top} = \frac{(-24939^{k\cdot ft})(12"/ft)(25.59")}{(5354265\ in^4)} = -1.430\ ksi$$

$-9.862\ MPa$

$$\sigma_{Bot} = \frac{(-24939^{k\cdot ft})(12"/ft)(-54.41")}{(5354265\ in^4)} = 3.041\ ksi$$

$20.969\ MPa$

Post-Tensioning

$$\sigma_{Top} = \frac{(8664^k)}{(6526\ in^2)} + \frac{(15544^{k\cdot ft})(12"/ft)(25.59")}{(5354265\ in^4)} = 2.219\ ksi$$

$15.301\ MPa$

$$\sigma_{Bot} = \frac{(8664^k)}{(6526\ in^2)} + \frac{(15544^{k\cdot ft})(12"/ft)(-54.41")}{(5354265\ in^4)} = -0.569\ ksi$$

$-3.916\ MPa$

Total

$\sigma_{Top} = -1.430\ ksi + 2.219\ ksi = 0.789\ ksi$ $\quad 5.440\ MPa$

$\sigma_{Bot} = 3.041\ ksi - 0.569\ ksi = 2.472\ ksi$ $\quad 17.044\ MPa$

Cantilever Construction

CALCULATION OF LONGITUDINAL FLEXURAL STRESSES

P16-10

DEAD LOAD

$$\sigma_{Top} = \frac{(-7648\ k\cdot ft)(12"/ft)(24.24")}{(4970169\ in^4)} = -0.448\ ksi$$

$$-3.086\ MPa$$

$$\sigma_{Bot} = \frac{(-7648\ k\cdot ft)(12"/ft)(-55.76")}{(4970169\ in^4)} = 1.030\ ksi$$

$$7.100\ MPa$$

POST-TENSIONING

$$\sigma_{Top} = \frac{(4332^k)}{(6332\ in^2)} + \frac{(7663\ k\cdot ft)(12"/ft)(24.24")}{(4970169\ in^4)} = 1.133\ ksi$$

$$7.809\ MPa$$

$$\sigma_{Bot} = \frac{(4332^k)}{(6332\ in^2)} + \frac{(7663\ k\cdot ft)(12"/ft)(-55.76")}{(4970169\ in^4)} = -0.348\ ksi$$

$$-2.396\ MPa$$

TOTAL

$$\sigma_{Top} = -3.086\ MPa + 7.809\ MPa = 4.723\ MPa$$

$$\sigma_{Bot} = 7.100\ MPa - 2.396\ MPa = 4.704\ MPa$$

Calculation of Shear Stresses

P16-2 Dead Load

Right Web

$$\frac{(593.9^{k})(80946\ in^3)}{(5354265\ in^4)(2)(12")} + \frac{(929.6^{k\cdot ft})(12"/ft)}{2(8183\ in^2)(12")}$$

$= 0.374\ ksi + 0.0568\ ksi = 0.431\ ksi$

$2.971\ MPa$

Left Web

$= -0.374\ ksi + 0.0568\ ksi = -0.317\ ksi$

$-2.188\ MPa$

Top T-Flange

$$\frac{(929.6^{k\cdot ft})(12"/ft)}{2(8183\ in^2)(8")} = 0.0852\ ksi$$

$0.587\ MPa$

Bottom Flange

$$\frac{(929.6^{k\cdot ft})(12"/ft)}{2(8183\ in^2)(14")} = 0.0487\ ksi$$

$0.336\ MPa$

Continuity Post-Tensioning

EQUIVALENT POST-TENSIONING LOADS

TENDON T21 $9 \times 0.6"\phi$

$P_{T21} = 2(9)(0.217\ in^2)(0.77)(270^{ksi}) = \underline{812\ kips}$

eccentricity = "57.76" + 6.5" = -51.26 inches

$M_{T21} = (-51.26")(812^k) = -41600\ k\text{-}in = \underline{-3470\ k\text{-}ft}$

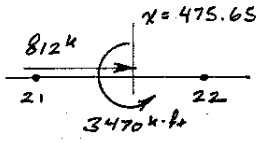

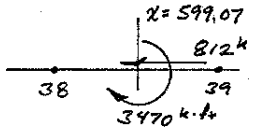

TENDON T22 (same as T21)

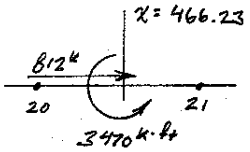

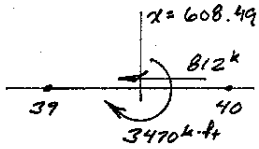

EQUIVALENT TENDON LOADS

TENDON T1 (19 x 0.6")

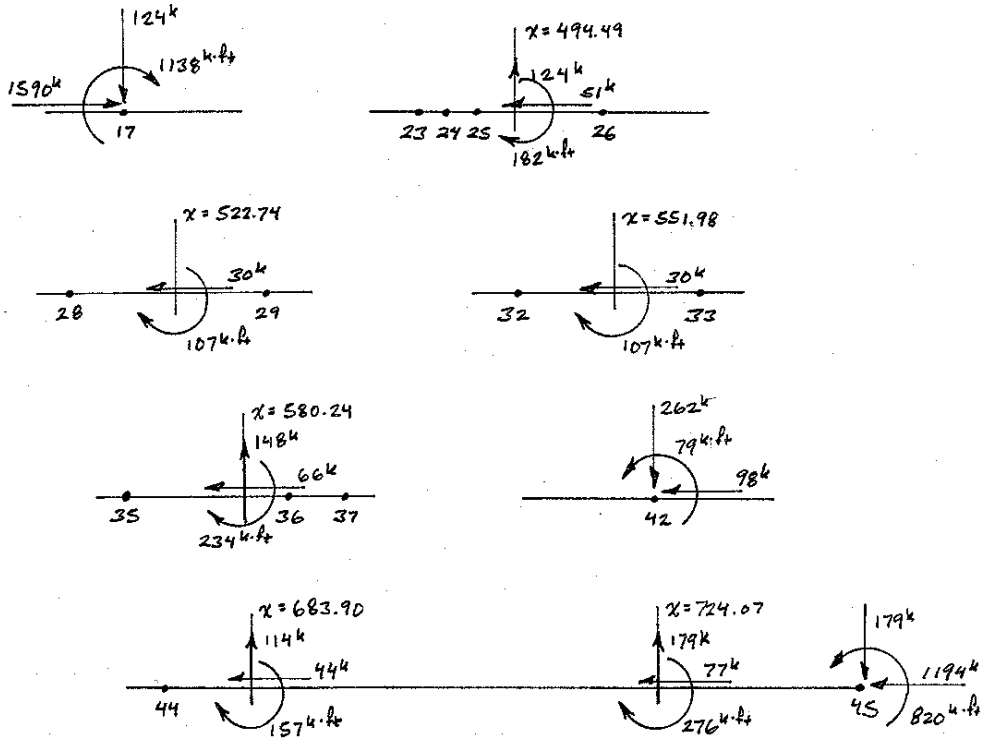

Continuity Post-Tensioning

EQUIVALENT TENDON LOADS

TENDON T2

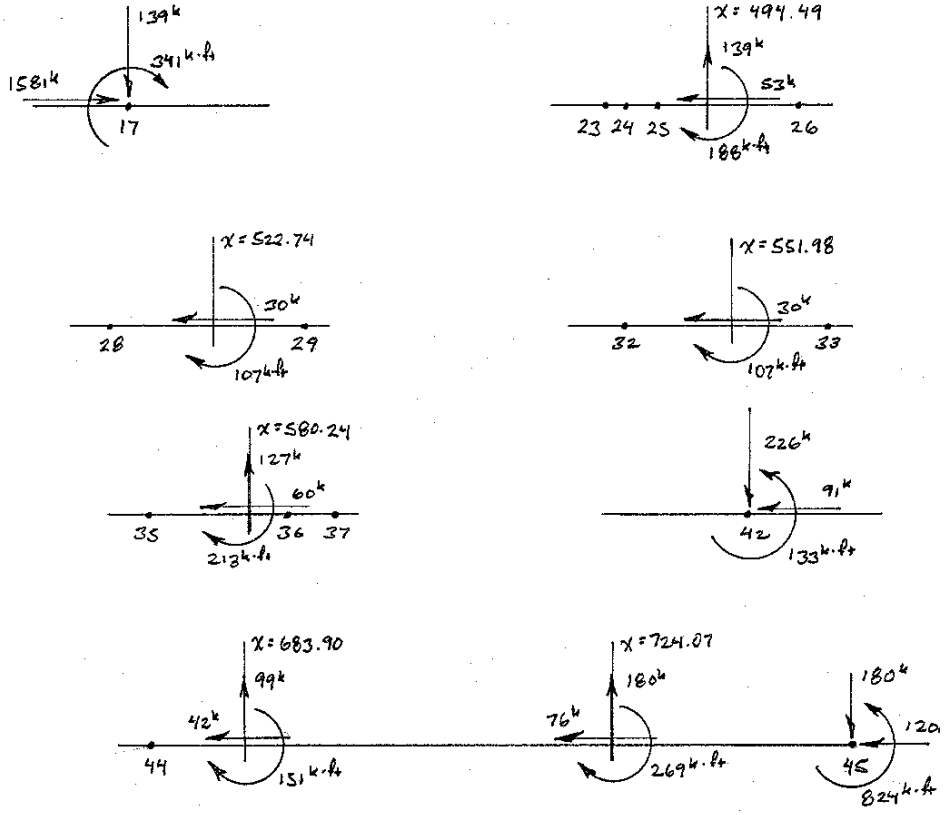

Continuity Post-Tensioning

EQUIVALENT TENDON LOADS

TENDON T3 (Upstation Stressing)
(19 × 0.6")

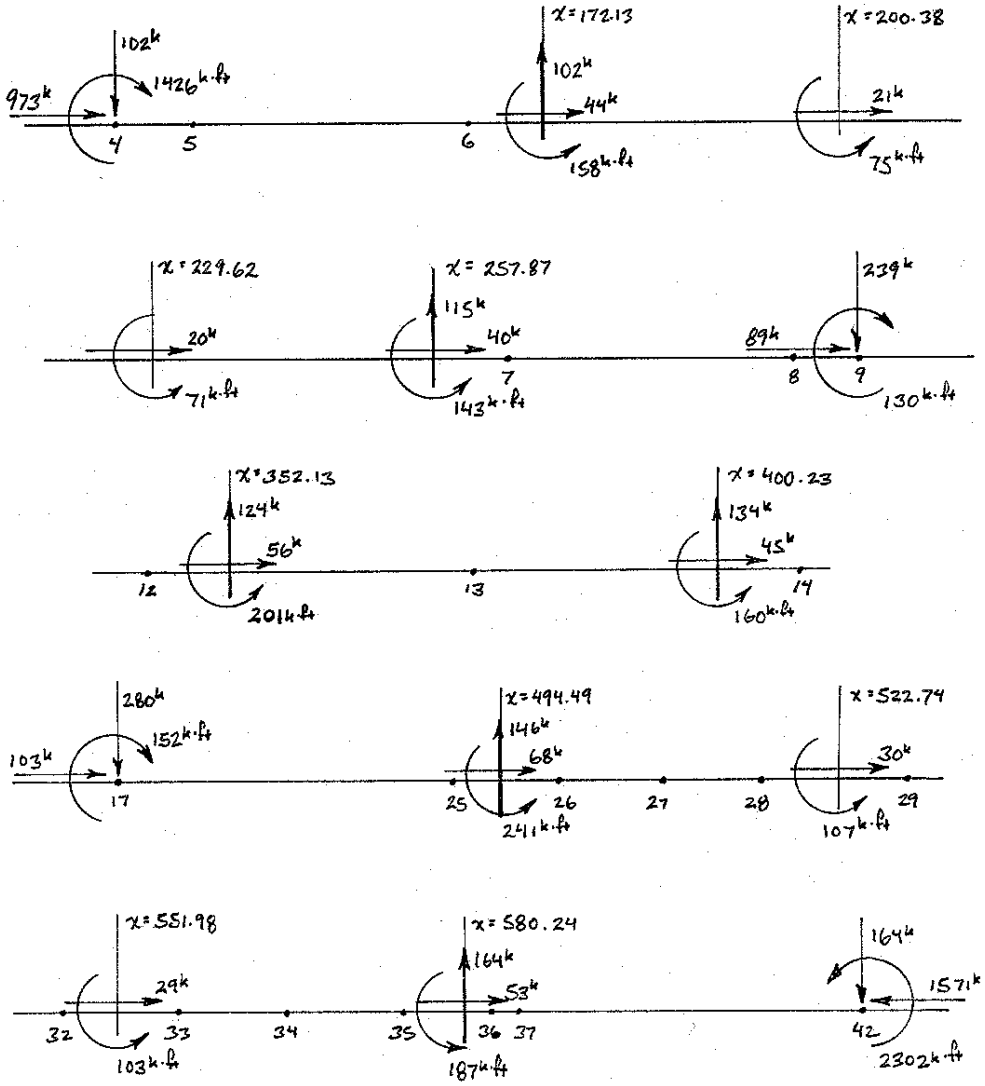

Continuity Post-Tensioning

CALCULATION OF STRESSES FROM STRESSING OF CONTINUITY TENDONS

SUMMARY OF RISA2D RESULTS

	P16-2		P16-10		P16-17	
TENDON STRESSED	AXIAL (kip)	MOMENT (kip·ft)	AXIAL (kip)	MOMENT (kip·ft)	AXIAL (kip)	MOMENT (kip·ft)
T21	0	2282	812	-1431	812	-1590
T22	0	2615	812	-1122	812	-1306
T1	1589	3071	1590	-1794	1509	-1934
T2	1581	2942	1582	-2172	1499	-2039
T3	1390	4765	1391	-1220	1489	-2380
TOTALS	4560	15675	6187	-7739	6121	-9249

Continuity Post-Tensioning

STRESSES FROM CONTINUITY TENDONS

P16-2

$$\sigma_{Top} = \frac{(4560^{k})}{(6236\ in^{2})} + \frac{(15675^{k\cdot ft})(12)(26.57")}{(5212887\ in^{4})} = 1.690\ ksi$$

11.65 MPa

$$\sigma_{Bot} = \frac{(4560^{k})}{(6236\ in^{2})} + \frac{(15675^{k\cdot ft})(12)(-53.43")}{(5212887\ in^{4})} = -1.197\ ksi$$

-8.25 MPa

P16-10

$$\sigma_{Top} = \frac{(6187^{k})}{(6332\ in^{2})} + \frac{(-7739^{k\cdot ft})(12)(24.24")}{(4970169\ in^{4})} = 0.524\ ksi$$

3.61 MPa

$$\sigma_{Bot} = \frac{(6187^{k})}{(6332\ in^{2})} + \frac{(-7739^{k\cdot ft})(12)(-55.76")}{(4970169\ in^{4})} = 2.019\ ksi$$

13.92 MPa

P16-17

$$\sigma_{Top} = \frac{(6121^{k})}{(6332\ in^{2})} + \frac{(-9249^{k\cdot ft})(12)(24.24")}{(4970169\ in^{4})} = 0.425\ ksi$$

2.93 MPa

$$\sigma_{Bot} = \frac{(6121^{k})}{(6332\ in^{2})} + \frac{(-9249^{k\cdot ft})(12)(-55.76")}{(4970169\ in^{4})} = 2.212\ ksi$$

15.25 MPa

APPENDIX C - LIVE LOAD CALCULATIONS

Live Load Calculations

AXLE LOADS AND LOCATIONS

LOAD CASE 1

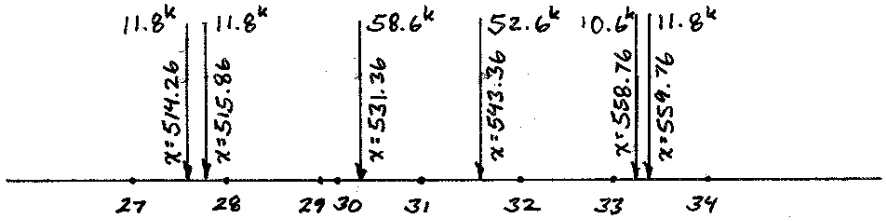

LOAD CASE 2

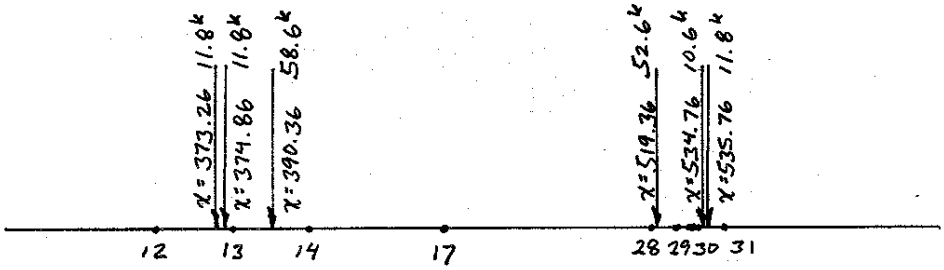

LOAD CASE 4

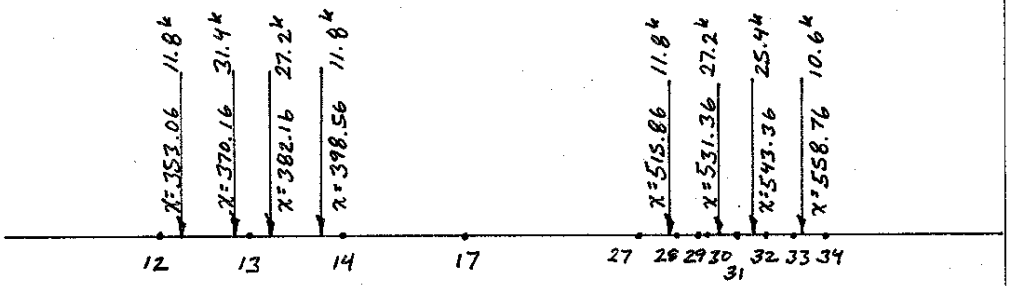

Live Load Calculations

RISA2D RESULTS

NODE	LOAD CASE 1		LOAD CASE 2		LOAD CASE 4	
	AXIAL (kip)	MOMENT (kip·ft)	AXIAL (kip)	MOMENT (kip·ft)	AXIAL (kip)	MOMENT (kip·ft)
19 (P16-2)	0.34	-2733.59	0.20	-1779.61		
24 (P16-10)	-0.17	468.08	-0.10	111.87		
30 (P16-17)	0.00	3341.96	0.00	1498.91		
	DISP. (in)	ROT. (radians)	DISP. (in)	ROT. (radians)	DISP. (in)	ROT. (radians)
9 (P15)	0.00062	-0.00001	-0.00091	-0.00008	-0.00118	-0.00009
12	0.01799	0.00008	-0.04563	-0.00011	-0.05147	-0.00012
13	0.05527	0.00007	-0.07199	0.00001	-0.07312	0.00004
14	0.06398	-0.00005	-0.03299	0.00014	-0.02914	0.00013
17 (P16)	-0.00337	-0.00027	-0.00349	-0.00004	-0.00302	-0.00005
25	-0.25351	-0.00054	-0.09597	-0.00023	-0.09382	-0.00023
31	-0.43851	-0.00003	-0.17050	0.00001	-0.18126	-0.00003
36	-0.28106	0.00052	-0.10407	0.00020	-0.11954	0.00022
42 (P17)	-0.00000	0.00042	-0.00000	0.00015	-0.00000	0.00018

Live Load Calculations

Calculation of Flexural Stresses

P16-2 Load Case 1

$$\sigma_{Top} = \frac{(-2234\ k\cdot ft)(12)(26.57")}{(5212887\ in^4)} = -0.167\ ksi = -1.153\ MPa$$

$$\sigma_{Bot} = \frac{(-2734\ k\cdot ft)(12)(-53.43")}{(5212887\ in^4)} = 0.336\ ksi = 2.319\ MPa$$

Load Case 2

$$\sigma_{Top} = \frac{(-1780\ k\cdot ft)(12)(26.57)}{(5212887\ in^4)} = -0.109\ ksi = -0.751\ MPa$$

$$\sigma_{Bot} = \frac{(-1780\ k\cdot ft)(12)(-53.43")}{(5212887\ in^4)} = 0.219\ ksi = 1.510\ MPa$$

P16-10 Load Case 1

$$\sigma_{Top} = \frac{(468\ k\cdot ft)(12)(24.24")}{(4970169\ in^4)} = 0.027\ ksi = 0.189\ MPa$$

$$\sigma_{Bot} = \frac{(468\ k\cdot ft)(12)(-55.76")}{(4970169\ in^4)} = -0.063\ ksi = -0.434\ MPa$$

Load Case 2

$$\sigma_{Top} = \frac{(112\ k\cdot ft)(12)(24.24")}{(4970169\ in^4)} = 0.0066\ ksi = 0.045\ MPa$$

$$\sigma_{Bot} = \frac{(112\ k\cdot ft)(12)(-55.76")}{(4970169\ in^4)} = -0.0151\ ksi = -0.104\ MPa$$

P16-17 Load Case 1

$$\sigma_{Top} = \frac{(3342\ k\cdot ft)(12)(24.24")}{(4970169\ in^4)} = 0.196\ ksi = 1.35\ MPa$$

$$\sigma_{Bot} = \frac{(3342\ k\cdot ft)(12)(-55.76")}{(4970169\ in^4)} = -0.450\ ksi = -3.10\ MPa$$

Load Case 2

$$\sigma_{Top} = \frac{(1499\ k\cdot ft)(12)(24.24")}{(4970169\ in^4)} = 0.088\ ksi = 0.605\ MPa$$

$$\sigma_{Bot} = \frac{(1499\ k\cdot ft)(12)(-55.76")}{(4970169\ in^4)} = -0.202\ ksi = -1.39\ MPa$$

Live Load Calculations

Moment/Radius Distributed Torque Load

Radius of Bridge: 726.2 ft

	Load Case 1		Load Case 4	
Node	Moment (k*ft)	M/R (k*ft/ft)	Moment (k*ft)	M/R (k*ft/ft)
17	-3265	-4.50	-1914	-2.64
18	-2861	-3.94	-1709	-2.35
19	-2734	-3.76	-1645	-2.27
20	-2060	-2.84	-1303	-1.79
21	-1261	-1.74	-897	-1.24
22	-460	-0.63	-490	-0.67
23	341	0.47	-84	-0.12
24	468	0.64	-19	-0.03
25	560	0.77	27	0.04
26	1141	1.57	322	0.44
27	1941	2.67	728	1.00
28	2672	3.68	1109	1.53
29	3250	4.48	1405	1.93
30	3342	4.60	1452	2.00
31	3507	4.83	1552	2.14
32	3329	4.58	1494	2.06
33	2860	3.94	1294	1.78
34	2237	3.08	1015	1.40
35	1557	2.14	715	0.98
36	1064	1.47	498	0.69
37	878	1.21	416	0.57
38	198	0.27	116	0.16
39	-483	-0.67	-185	-0.25
40	-1162	-1.60	-484	-0.67
41	-1842	-2.54	-784	-1.08
42	-2185	-3.01	-936	-1.29

Live Load Calculations

SIGN CONVENTIONS

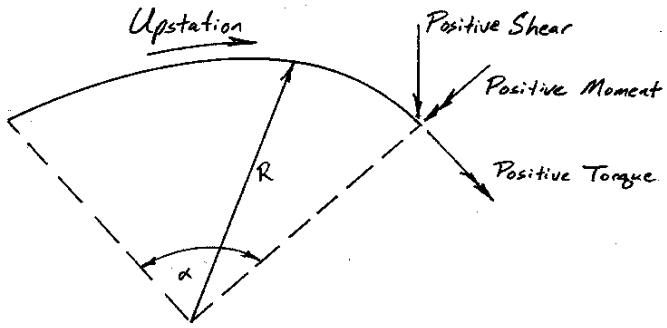

RISA2D RESULTS

NODE	LOAD CASE 1		LOAD CASE 4	
	Shear (kip)	Torsion (kip·ft)	Shear (kip)	Torsion (kip·ft)
19 (P16-2)	84.99	94.68	43.15	-202.92
24 (P16-10)	84.99	153.45	43.15	-159.71
30 (P16-17)	61.39	49.59	31.35	-128.49

Live Load Calculations

CALCULATION OF SHEAR STRESSES

P16-2 LOAD CASE 1

R. WEB

$$\frac{(84.99^{k})(80946\ in^3)}{(5354265\ in^4)(2)(12\ in)} + \frac{(94.68^{k\cdot ft})(12^{in/ft})}{2(8183\ in^2)(12\ in)}$$

0.05354 ksi + 0.00579 ksi = 0.05933 ksi

0.409 MPa

L. WEB

-0.05354 ksi + 0.00579 ksi = -0.04775 ksi

-0.329 MPa

TOP FLANGE

$$\frac{(94.68^{k\cdot ft})(12^{in/ft})}{2(8183\ in^2)(8\ in)} = 0.00868\ ksi$$

0.060 MPa

BOTTOM FLANGE

$$\frac{(94.68^{k\cdot ft})(12^{in/ft})}{2(8183\ in^2)(14\ in)} = 0.00496\ ksi$$

0.034 MPa

LOAD CASE 4

R. WEB

$$\frac{(43.15^{k})(80946\ in^3)}{(5354265\ in^4)(2)(12\ in)} + \frac{(-202.92^{k\cdot ft})(12^{in/ft})}{2(8183\ in^2)(12\ in)}$$

0.02718 ksi - 0.01240 ksi = 0.01478 ksi

0.102 MPa

L. WEB

-0.02718 ksi - 0.01240 ksi = -0.03958 ksi

-0.273 MPa

TOP FLANGE

$$\frac{(-202.92^{k\cdot ft})(12^{in/ft})}{2(8183\ in^2)(8\ in)} = -0.01860\ ksi$$

-0.128 MPa

BOTTOM FLANGE

$$\frac{(-202.92^{k\cdot ft})(12^{in/ft})}{2(8183\ in^2)(14\ in)} = -0.01063\ ksi$$

-0.073 MPa

Live Load Calculations

Calculation of Shear Stresses

P16-10 Load Case 1

R. WEB

$$\frac{(84.99^{k})(74636\ in^3)}{(4970169\ in^4)(2)(12\ in)} + \frac{(153.45\ k\cdot ft)(12\ in/ft)}{2(8279\ in^2)(12\ in)}$$

$0.05318\ ksi + 0.00927\ ksi = 0.06245\ ksi$

$0.431\ MPa$

L. WEB

$-0.05318\ ksi + 0.00927\ ksi = -0.04391\ ksi$

$-0.303\ MPa$

TOP FLANGE

$$\frac{(153.45\ k\cdot ft)(12\ in/ft)}{2(8279\ in^2)(8\ in)} = 0.01390\ ksi$$

$0.096\ MPa$

BOTTOM FLANGE

$$\frac{(153.45\ k\cdot ft)(12\ in/ft)}{2(8279\ in^2)(11\ in)} = 0.01011\ ksi$$

$0.070\ MPa$

Load Case 4

R. WEB

$$\frac{(43.15^{k})(74636\ in^3)}{(4970169\ in^4)(2)(12\ in)} + \frac{(-159.71\ k\cdot ft)(12\ in/ft)}{2(8279\ in^2)(12\ in)}$$

$0.02700\ ksi + (-0.00965\ ksi) = 0.01735\ ksi$

$0.120\ MPa$

L. WEB

$-0.02700\ ksi - 0.00965\ ksi = -0.03665\ ksi$

$-0.253\ MPa$

TOP FLANGE

$$\frac{(-159.71\ k\cdot ft)(12\ in/ft)}{2(8279\ in^2)(8\ in)} = -0.01447\ ksi$$

$-0.100\ MPa$

BOTTOM FLANGE

$$\frac{(-159.71\ k\cdot ft)(12\ in/ft)}{2(8279\ in^2)(11\ in)} = -0.01052\ ksi$$

$-0.073\ MPa$

Live Load Calculations

Calculation of Shear Stresses

P16-17 Load Case 1

R. WEB

$$\frac{(61.39^{k})(74636\ in^3)}{(4970169\ in^4)(2)(12\ in)} + \frac{(49.59\ k\cdot ft)(12\ in/ft)}{2(8279\ in^2)(12\ in)}$$

$$0.03841\ ksi + 0.00299\ ksi = 0.04140\ ksi$$

0.285 MPa

L. WEB

$$-0.03841\ ksi + 0.00299\ ksi = -0.03542\ ksi$$

-0.244 MPa

TOP FLANGE

$$\frac{(49.59\ k\cdot ft)(12\ in/ft)}{2(8279\ in^2)(8\ in)} = 0.00449\ ksi$$

0.031 MPa

BOTTOM FLANGE

$$\frac{(49.59\ k\cdot ft)(12\ in/ft)}{2(8279\ in^2)(11\ in)} = 0.00327\ ksi$$

0.023 MPa

Load Case 4

R. WEB

$$\frac{(31.35^{k})(74636\ in^3)}{(4970169\ in^4)(2)(12\ in)} + \frac{(-128.49\ k\cdot ft)(12\ in/ft)}{2(8279\ in^2)(12\ in)}$$

$$0.01962\ ksi - 0.00776\ ksi = 0.01186\ ksi$$

0.082 MPa

L. WEB

$$-0.01962\ ksi - 0.00776\ ksi = -0.02738\ ksi$$

-0.189 MPa

TOP FLANGE

$$\frac{(-128.49\ k\cdot ft)(12\ in/ft)}{2(8279\ in^2)(8\ in)} = -0.01164\ ksi$$

-0.080 MPa

BOTTOM FLANGE

$$\frac{(-128.49\ k\cdot ft)(12\ in/ft)}{2(8279\ in^2)(11\ in)} = -0.00847\ ksi$$

-0.058 MPa

APPENDIX D - THERMAL GRADIENT DATA

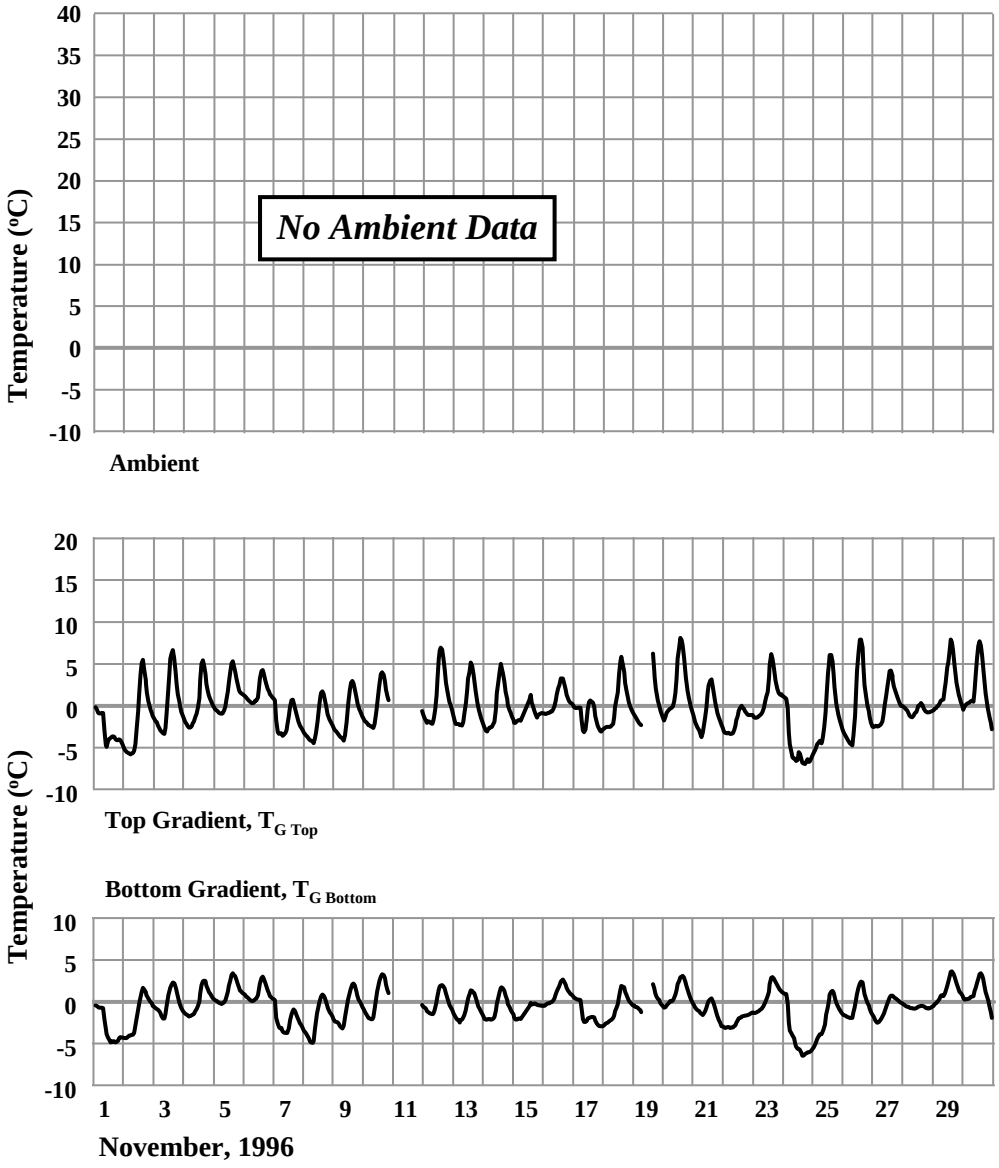
Temperature (ºC)
40
35
30
25
20
15
10
5
0
-5
-10
No Ambient Data
Ambient
20
15
10
5
0
-5
-10
Top Gradient, T G Top
Bottom Gradient, T G Bottom
10
5
0
-5
-10
1
3
5
7
9
11
13
15
17
19
21
23
25
27
29
November, 1996

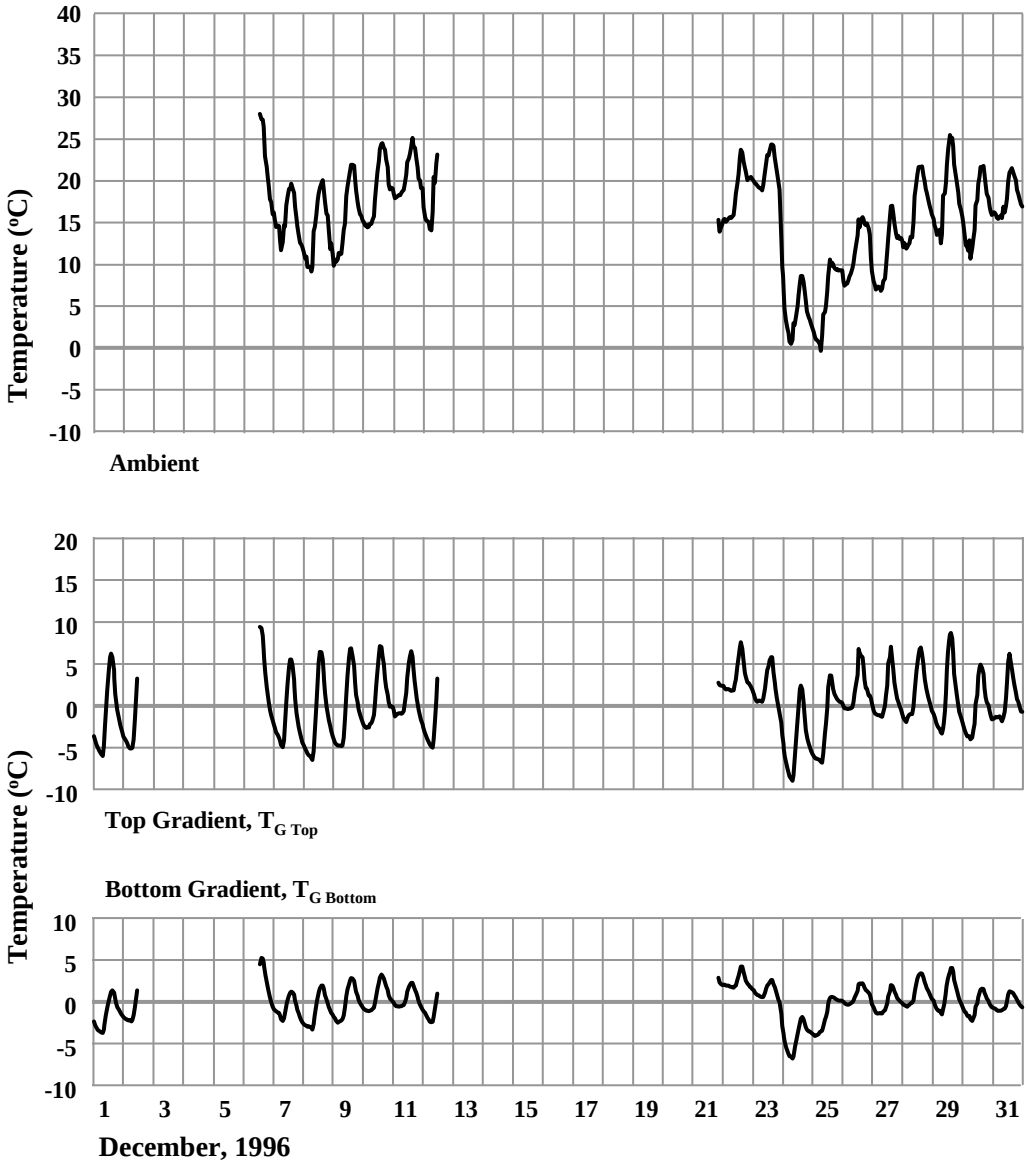
Temperature (ºC)
40
35
30
25
20
15
10
5
0
-5
-10
Ambient
Temperature (ºC)
20
15
10
5
0
-5
-10
Top Gradient, $T_{G\ Top}$
Bottom Gradient, $T_{G\ Bottom}$
10
5
0
-5
-10
1
3
5
7
9
11
13
15
17
19
21
23
25
27
29
31
December, 1996

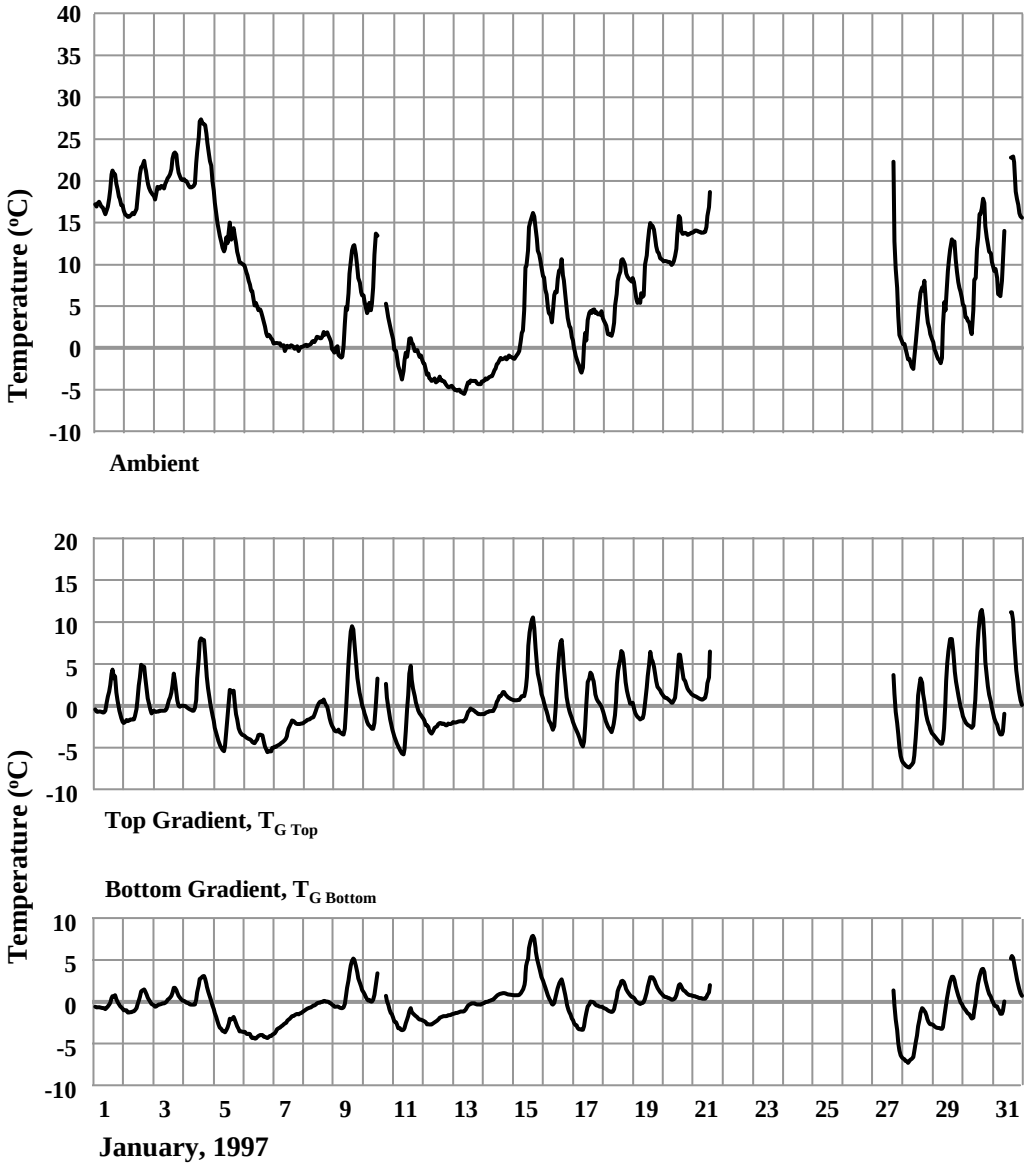
Temperature (ºC)
40
35
30
25
20
15
10
5
0
-5
-10
Ambient
Temperature (ºC)
20
15
10
5
0
-5
-10
Top Gradient, $T_{G\ Top}$
Bottom Gradient, $T_{G\ Bottom}$
Temperature (ºC)
10
5
0
-5
-10
1
3
5
7
9
11
13
15
17
19
21
23
25
27
29
31
January, 1997

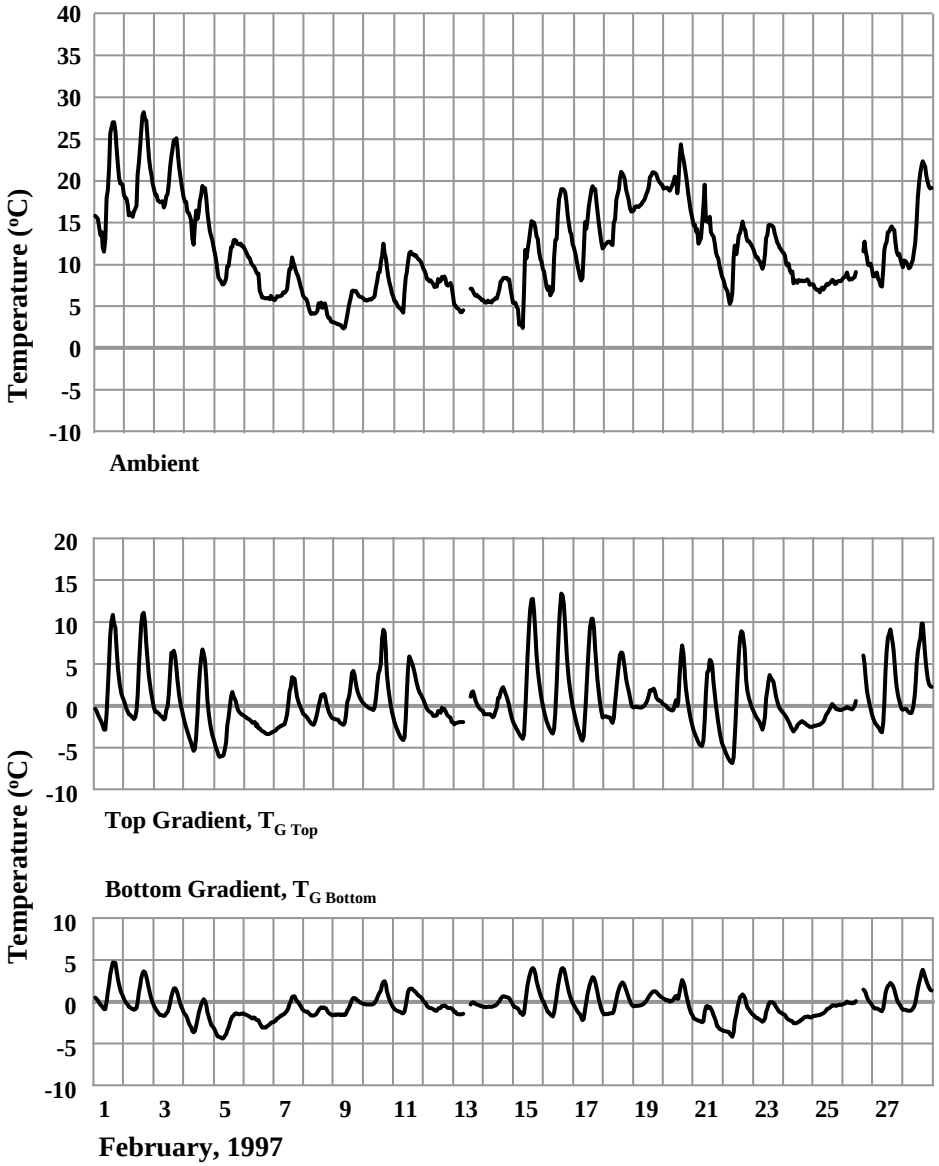
Temperature (ºC)
40
35
30
25
20
15
10
5
0
-5
-10
Ambient
20
15
10
5
0
-5
-10
Top Gradient, T G Top
Bottom Gradient, T G Bottom
10
5
0
-5
-10
1
3
5
7
9
11
13
15
17
19
21
23
25
27
February, 1997

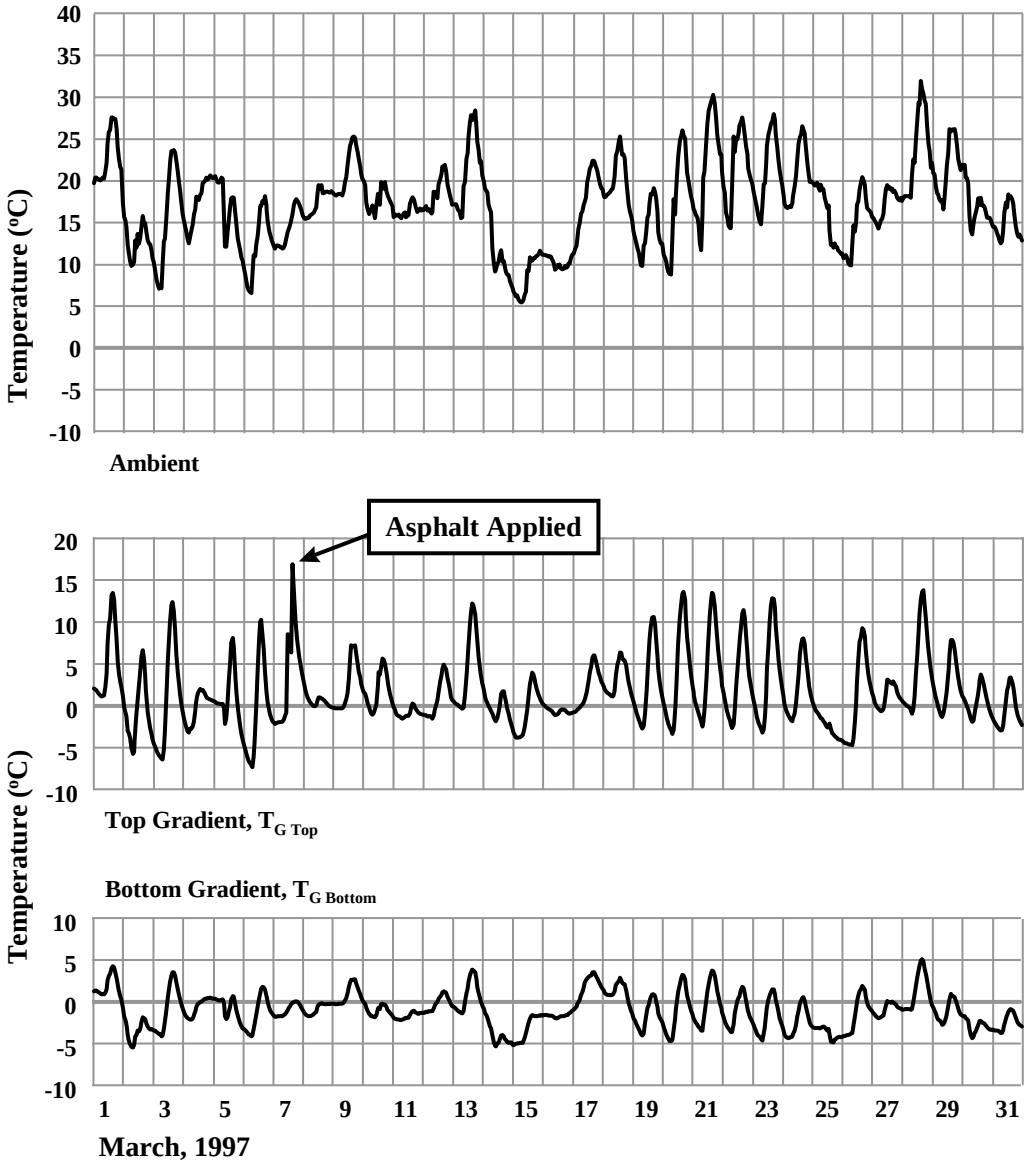
Temperature (ºC)
40
35
30
25
20
15
10
5
0
-5
-10
Ambient
Asphalt Applied
20
15
10
5
0
-5
-10
Top Gradient, $T_{G\ Top}$
Bottom Gradient, $T_{G\ Bottom}$
10
5
0
-5
-10
1 3 5 7 9 11 13 15 17 19 21 23 25 27 29 31
March, 1997

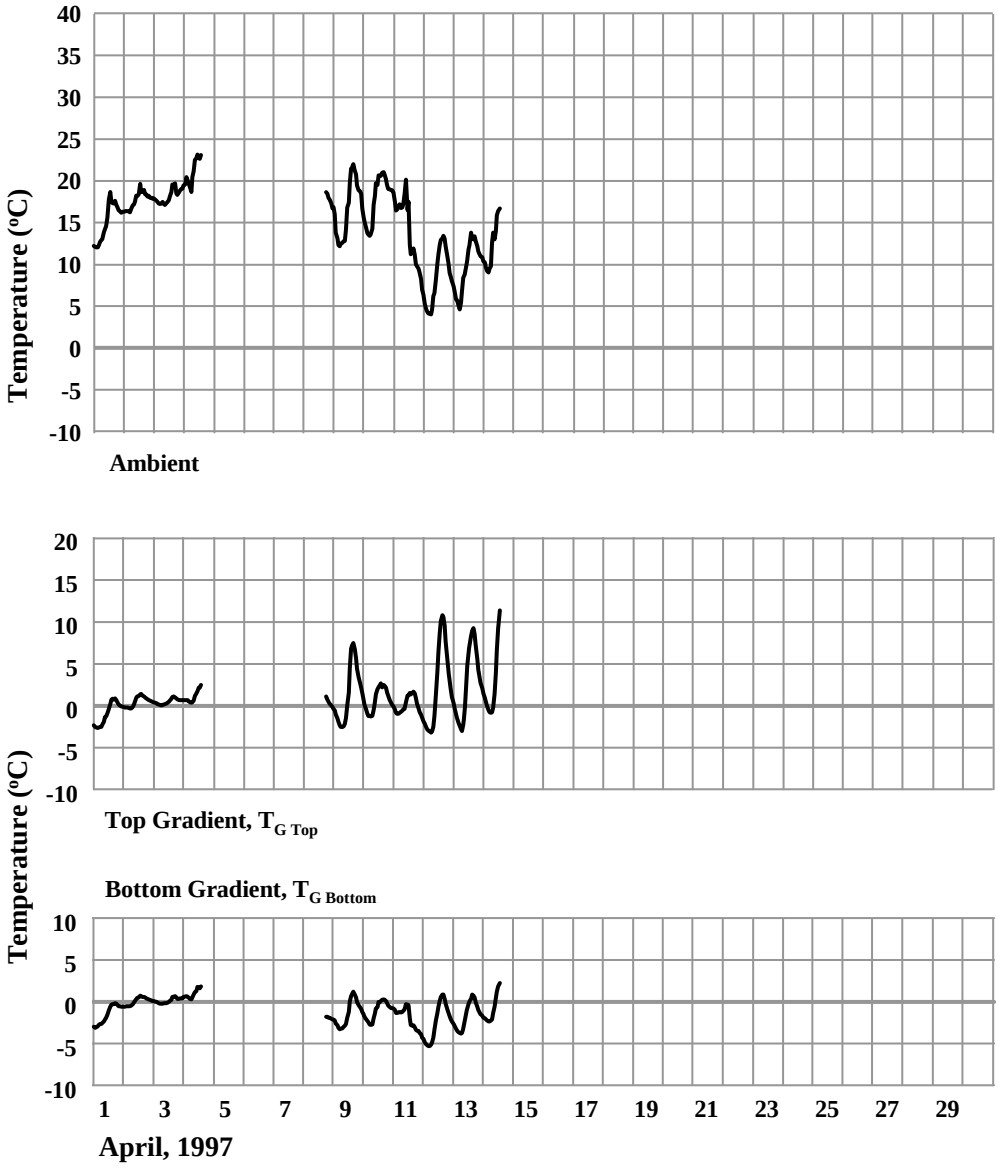
Temperature (ºC)
40
35
30
25
20
15
10
5
0
-5
-10
Ambient
20
15
10
5
0
-5
-10
Top Gradient, T G Top
Bottom Gradient, T G Bottom
10
5
0
-5
-10
1
3
5
7
9
11
13
15
17
19
21
23
25
27
29
April, 1997

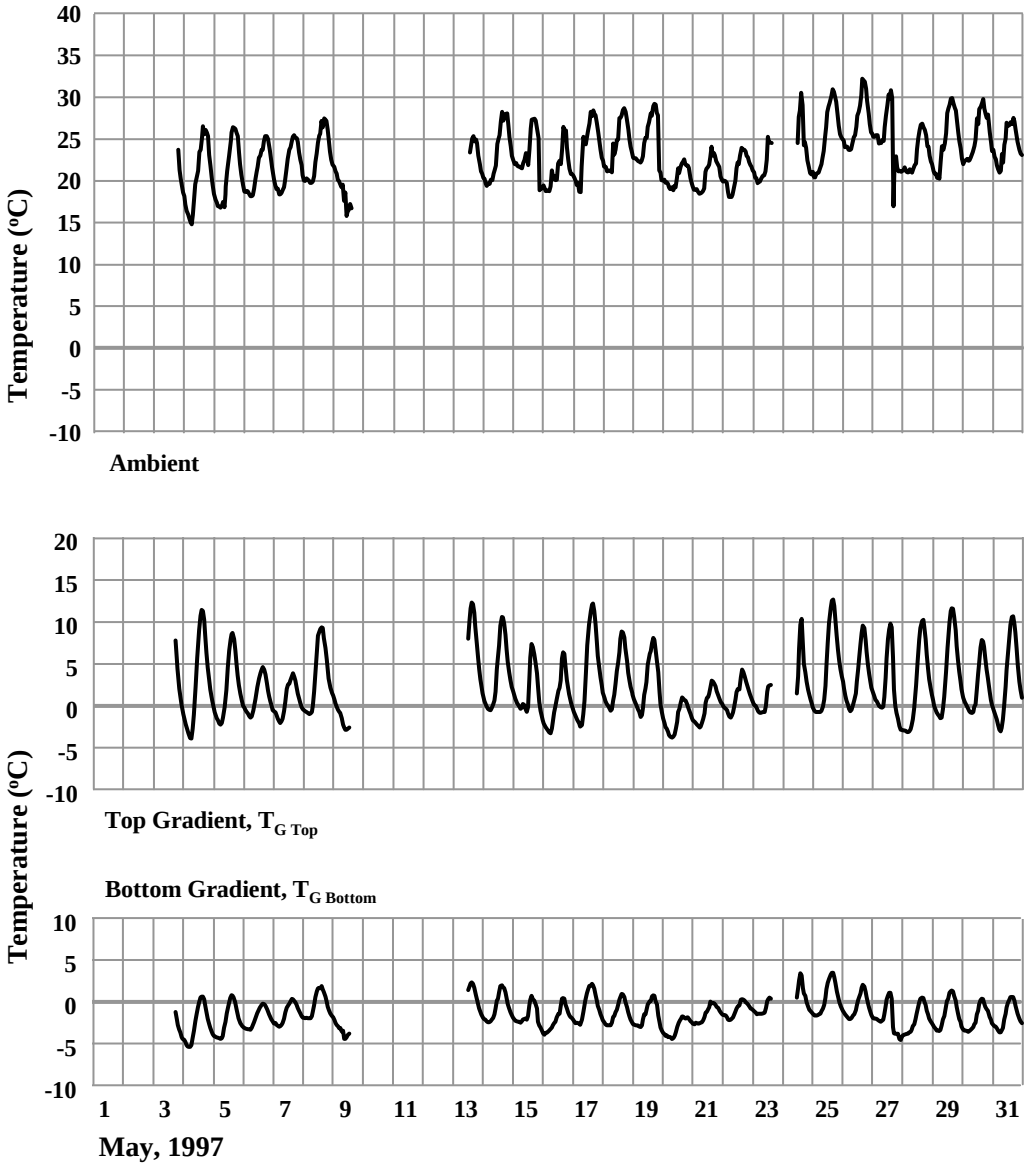
Temperature (ºC)
40
35
30
25
20
15
10
5
0
-5
-10
Ambient
Temperature (ºC)
20
15
10
5
0
-5
-10
Top Gradient, $T_{G\ Top}$
Bottom Gradient, $T_{G\ Bottom}$
10
5
0
-5
-10
1
3
5
7
9
11
13
15
17
19
21
23
25
27
29
31
May, 1997

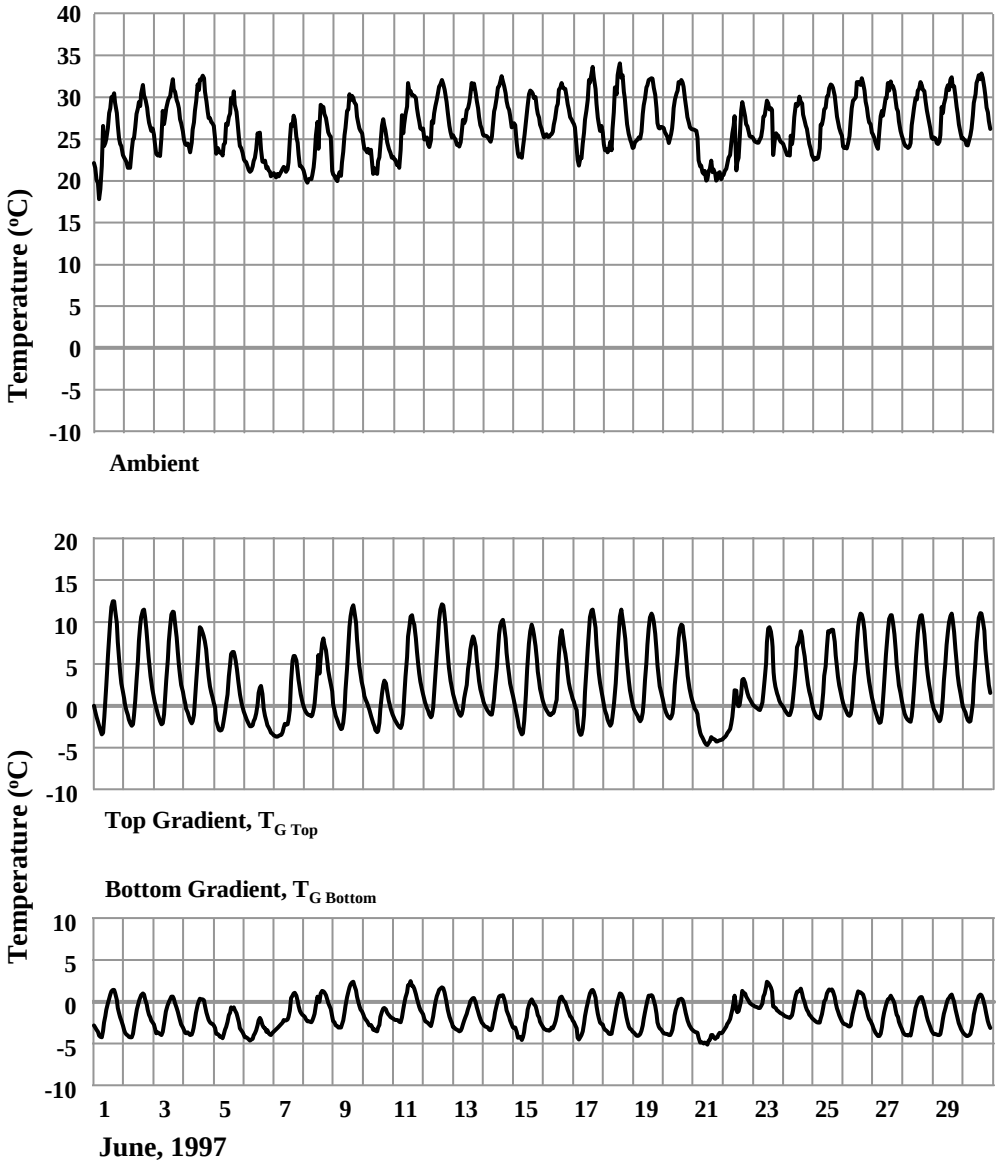
Temperature (ºC)
40
35
30
25
20
15
10
5
0
-5
-10
Ambient
Temperature (ºC)
20
15
10
5
0
-5
-10
Top Gradient, $T_{G\ Top}$
Bottom Gradient, $T_{G\ Bottom}$
10
5
0
-5
-10
1
3
5
7
9
11
13
15
17
19
21
23
25
27
29
June, 1997

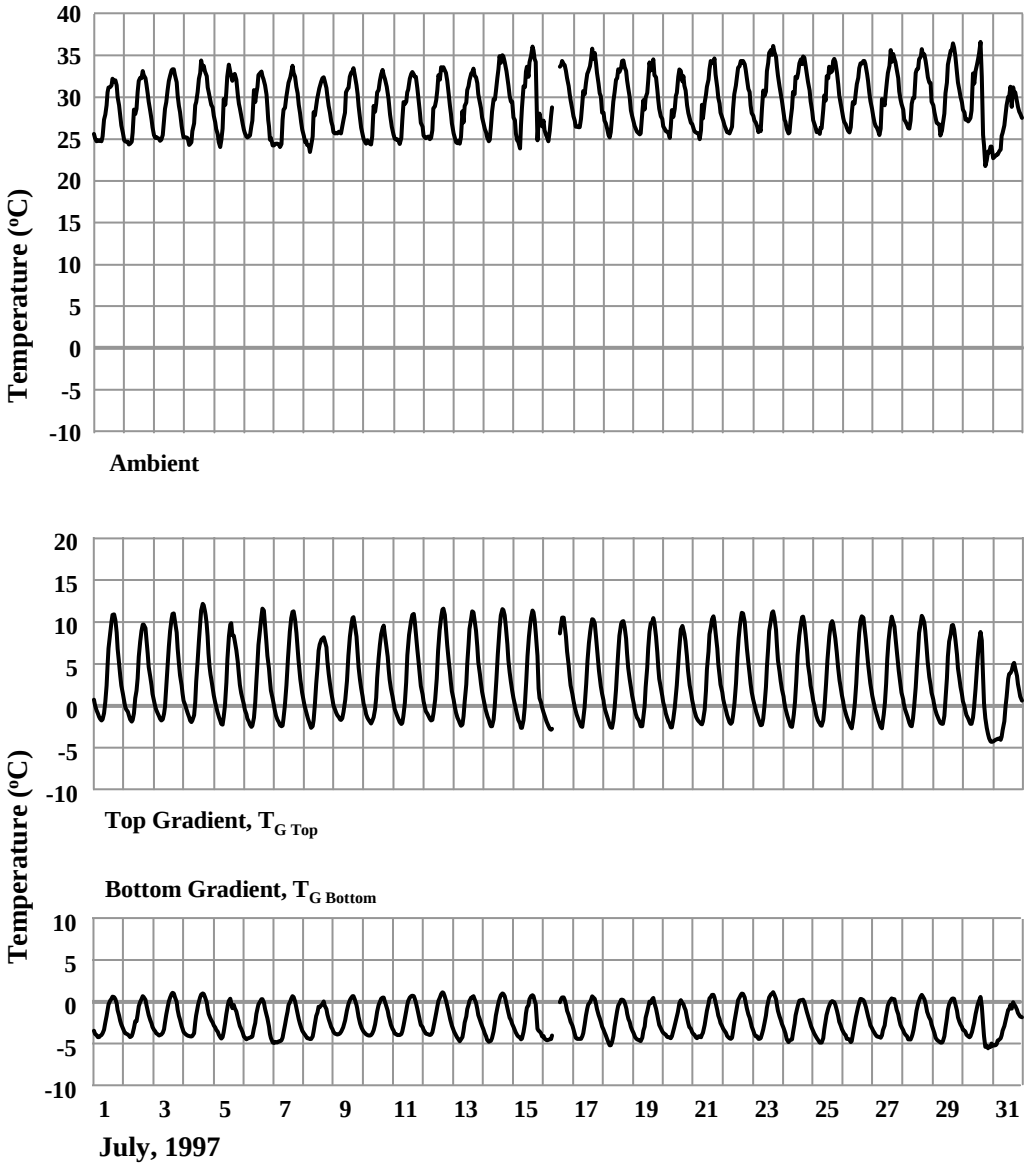
Temperature (ºC)
40
35
30
25
20
15
10
5
0
-5
-10
Ambient
Temperature (ºC)
20
15
10
5
0
-5
-10
Top Gradient, T G Top
Bottom Gradient, T G Bottom
Temperature (ºC)
10
5
0
-5
-10
1 3 5 7 9 11 13 15 17 19 21 23 25 27 29 31
July, 1997

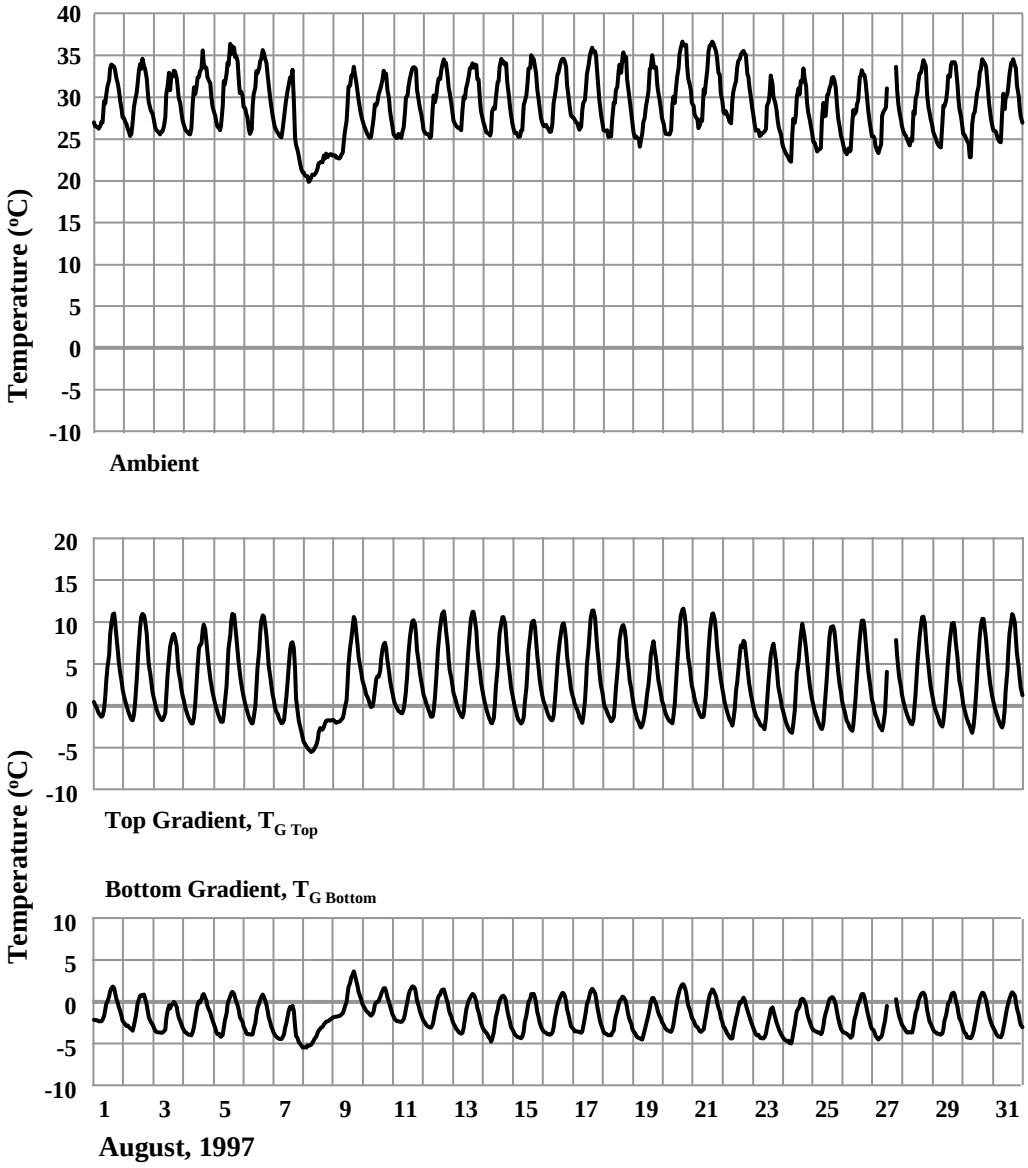
Temperature (ºC)
40
35
30
25
20
15
10
5
0
-5
-10
Ambient
Temperature (ºC)
20
15
10
5
0
-5
-10
Top Gradient, $T_{G\ Top}$
Bottom Gradient, $T_{G\ Bottom}$
10
5
0
-5
-10
1 3 5 7 9 11 13 15 17 19 21 23 25 27 29 31
August, 1997

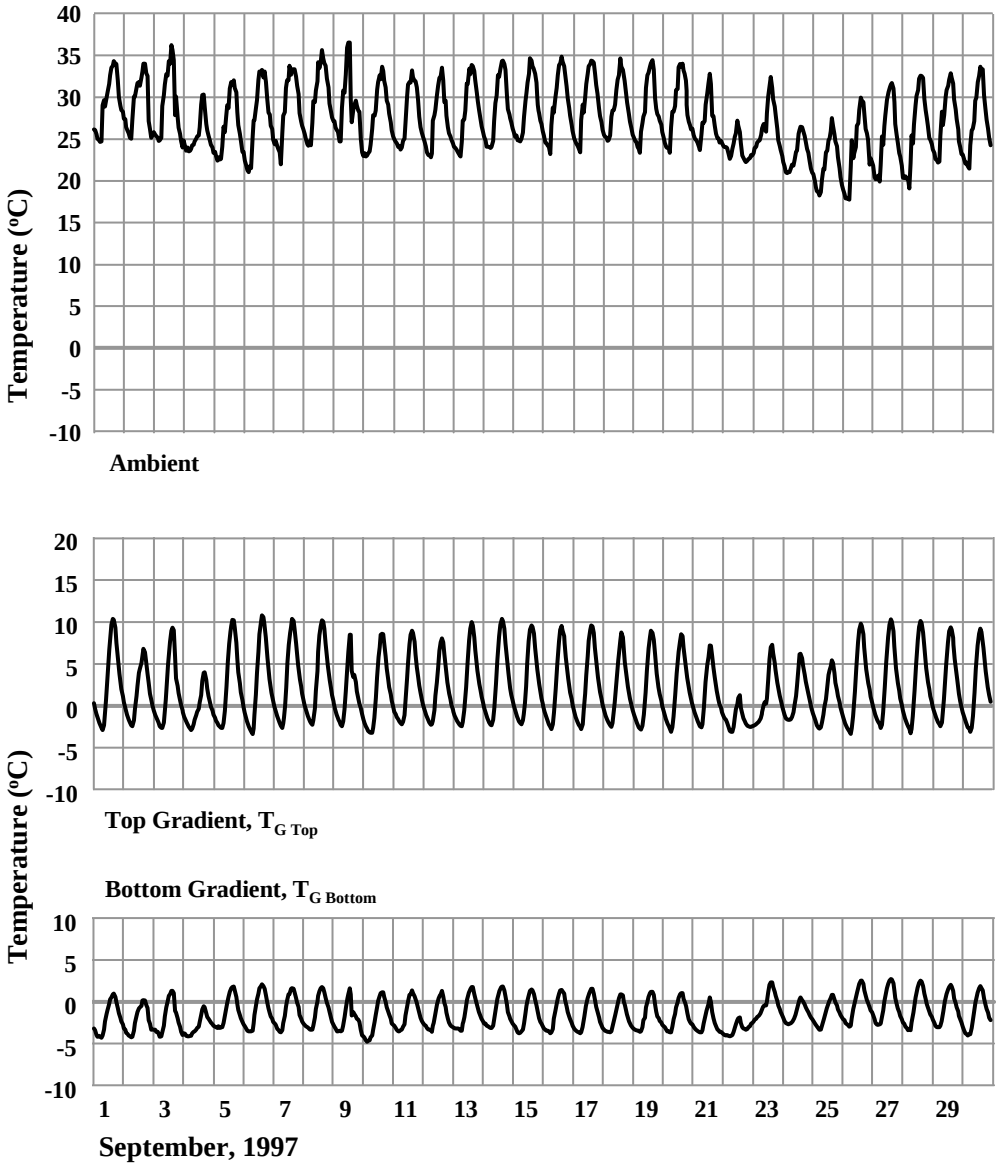
Temperature (ºC)
40
35
30
25
20
15
10
5
0
-5
-10
Ambient
20
15
10
5
0
-5
-10
Top Gradient, T G Top
Bottom Gradient, T G Bottom
10
5
0
-5
-10
1
3
5
7
9
11
13
15
17
19
21
23
25
27
29
September, 1997

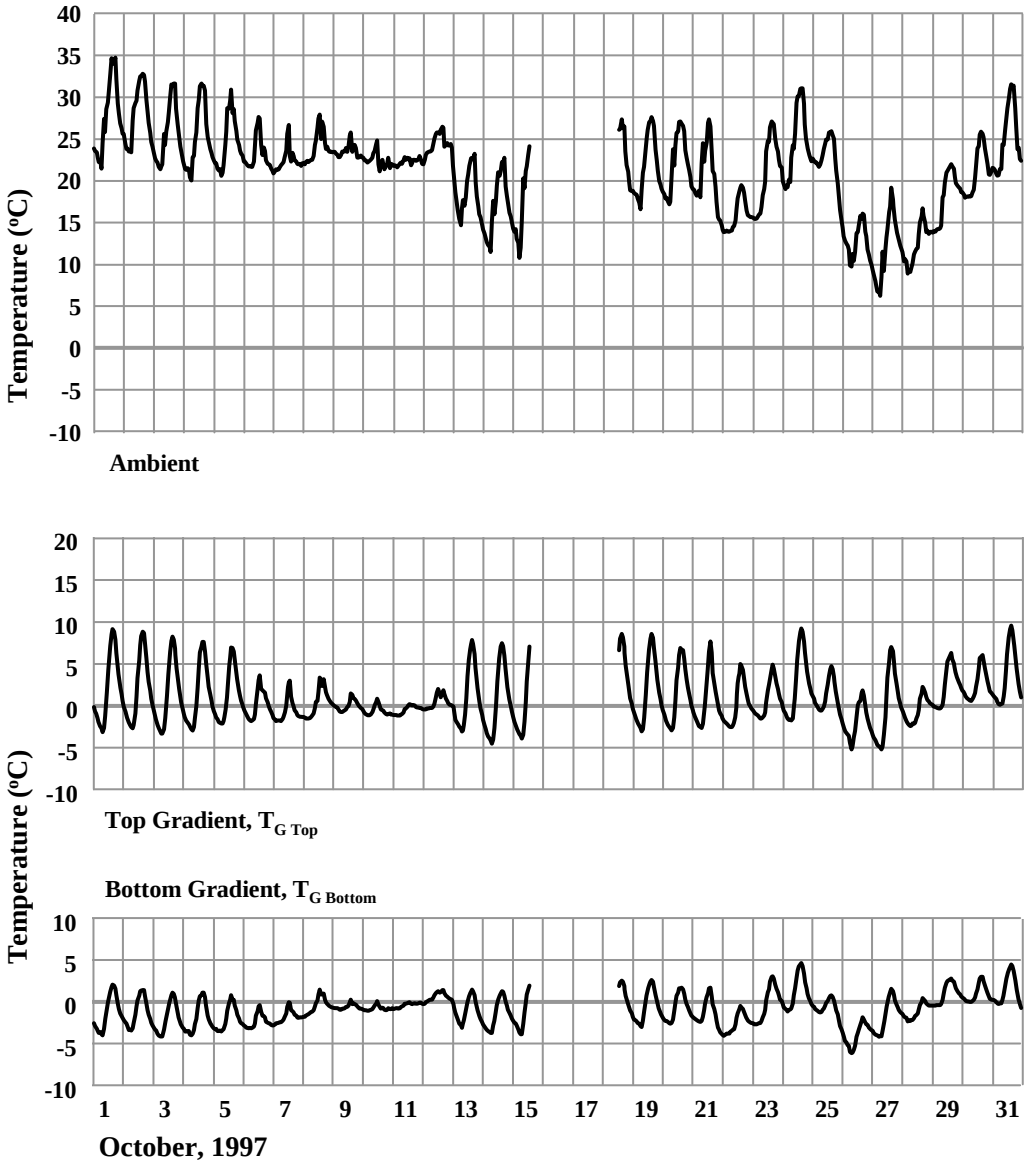
Temperature (ºC)
40
35
30
25
20
15
10
5
0
-5
-10
Ambient
Temperature (ºC)
20
15
10
5
0
-5
-10
Top Gradient, $T_{G\ Top}$
Bottom Gradient, $T_{G\ Bottom}$
10
5
0
-5
-10
1
3
5
7
9
11
13
15
17
19
21
23
25
27
29
31
October, 1997

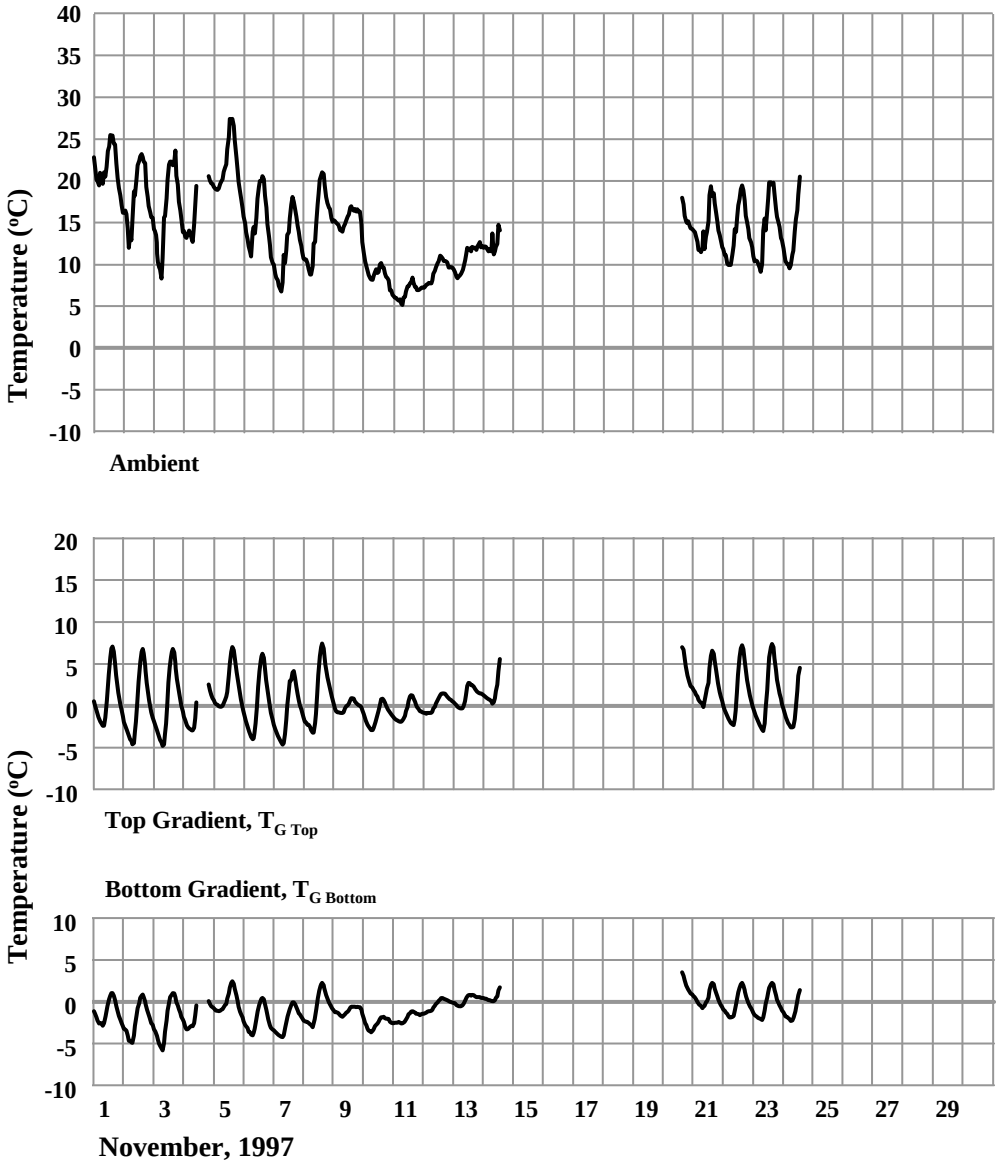
Temperature (ºC)
40
35
30
25
20
15
10
5
0
-5
-10
Ambient
20
15
10
5
0
-5
-10
Top Gradient, T G Top
Bottom Gradient, T G Bottom
10
5
0
-5
-10
1
3
5
7
9
11
13
15
17
19
21
23
25
27
29
November, 1997

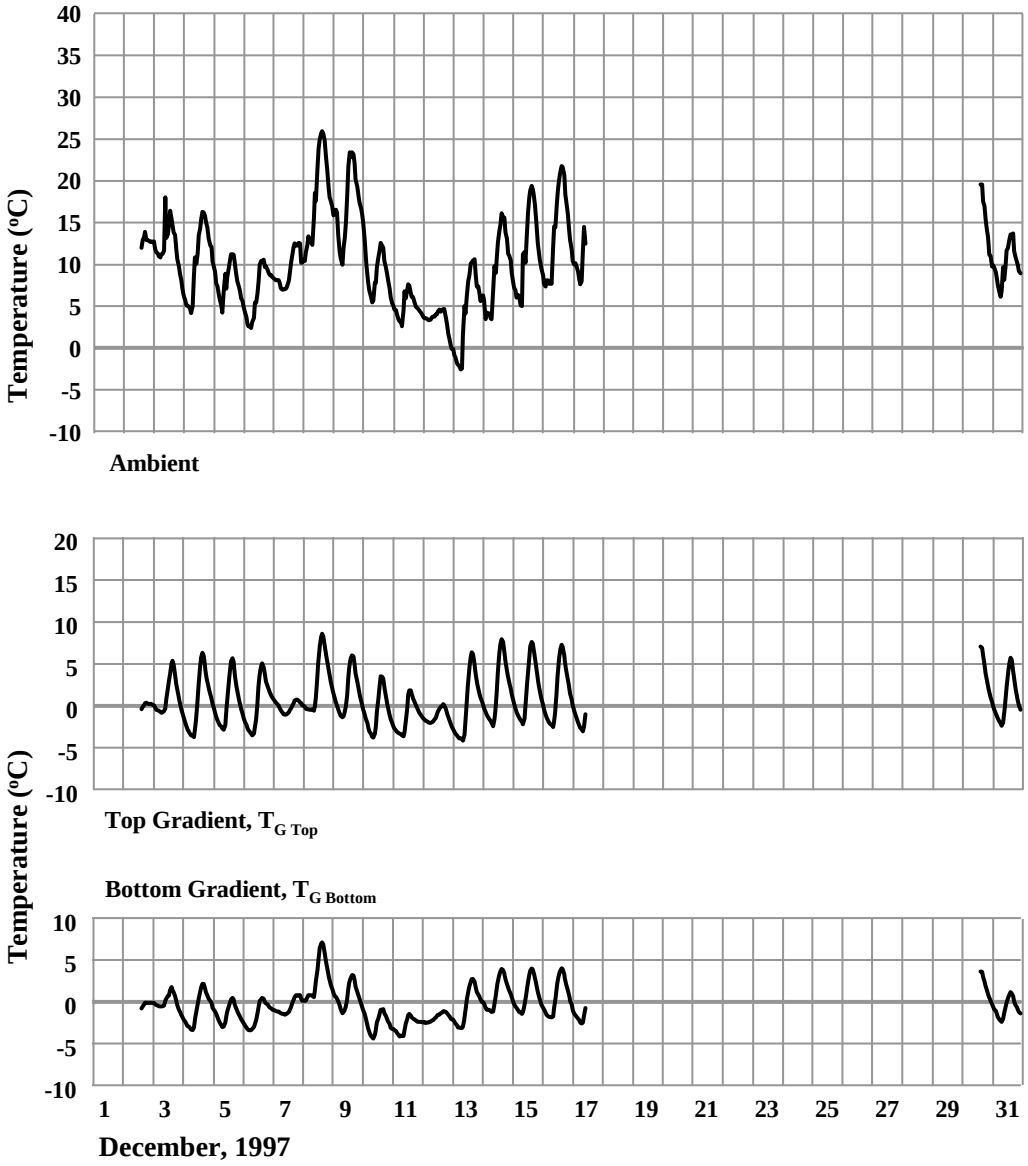
Temperature (ºC)
40
35
30
25
20
15
10
5
0
-5
-10
Ambient
20
15
10
5
0
-5
-10
Top Gradient, $T_{G\ Top}$
Bottom Gradient, $T_{G\ Bottom}$
10
5
0
-5
-10
1
3
5
7
9
11
13
15
17
19
21
23
25
27
29
31
December, 1997

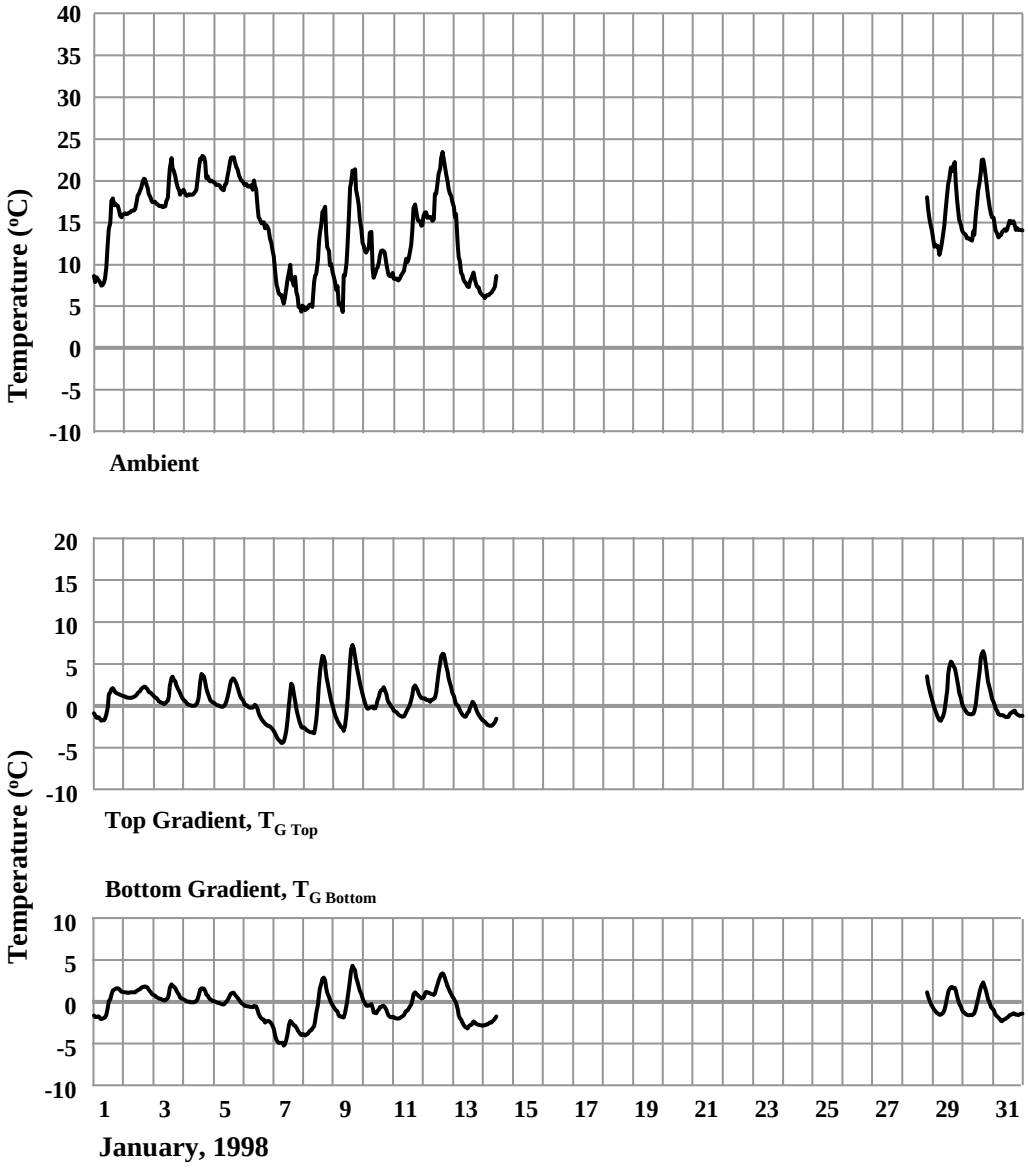
Temperature (ºC)
40
35
30
25
20
15
10
5
0
-5
-10
Ambient
20
15
10
5
0
-5
-10
Top Gradient, $T_{G\ Top}$
Bottom Gradient, $T_{G\ Bottom}$
10
5
0
-5
-10
1
3
5
7
9
11
13
15
17
19
21
23
25
27
29
31
January, 1998

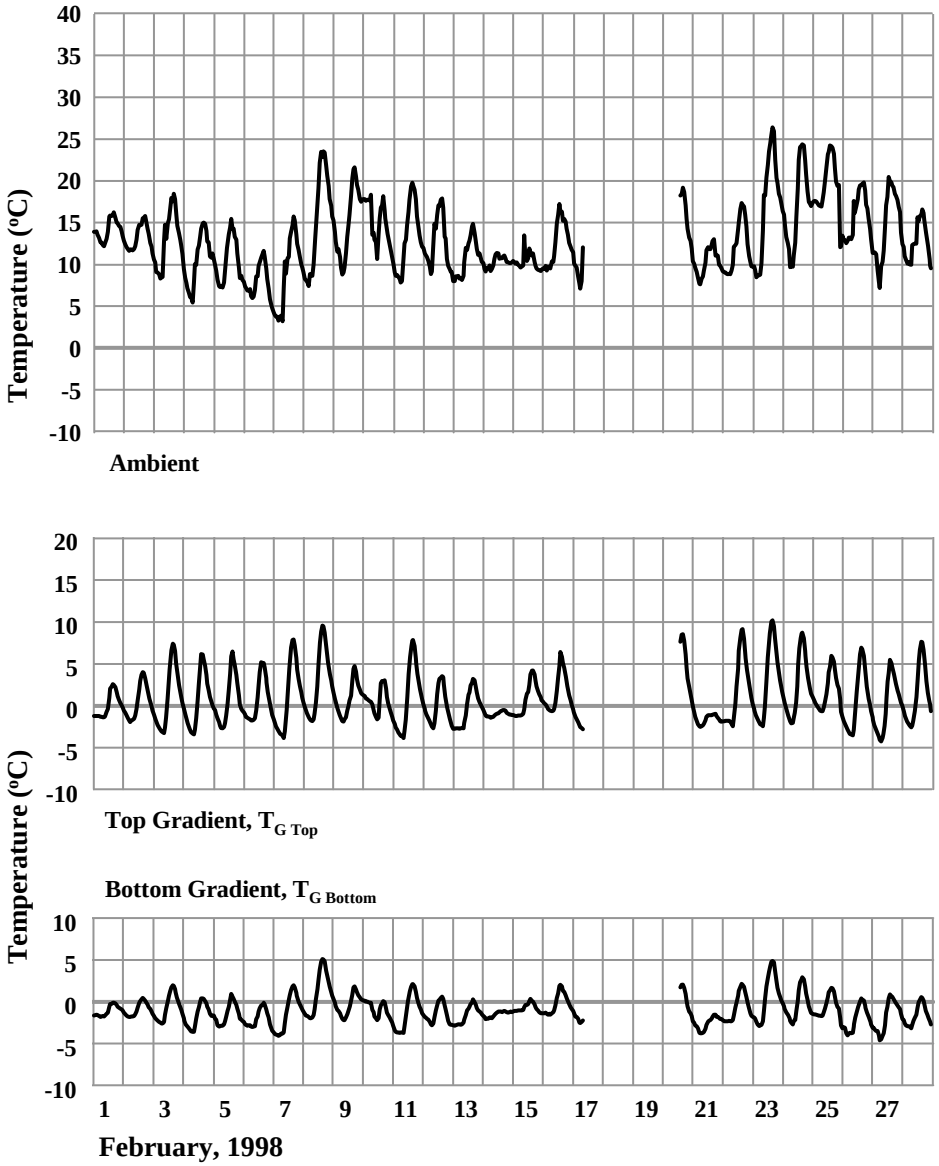
Temperature (ºC)
40
35
30
25
20
15
10
5
0
-5
-10
Ambient
20
15
10
5
0
-5
-10
Top Gradient, $T_{G\ Top}$
Bottom Gradient, $T_{G\ Bottom}$
10
5
0
-5
-10
1
3
5
7
9
11
13
15
17
19
21
23
25
27
February, 1998

APPENDIX E - THERMAL GRADIENT CALCULATIONS

AASHTO Design Gradient Calculation

AASHTO LRFD Design Thermal Gradients

(1994 Edition, Section 3.12.3)

Austin, TX ⟶ Zone 2

2" of Asphalt

Positive Gradient

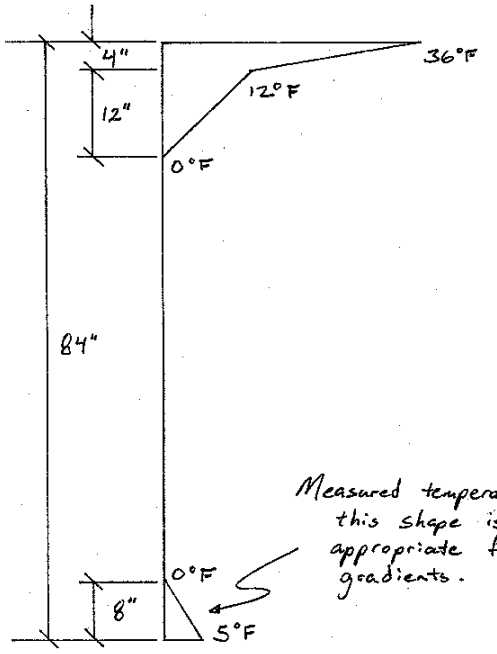

Negative Gradient

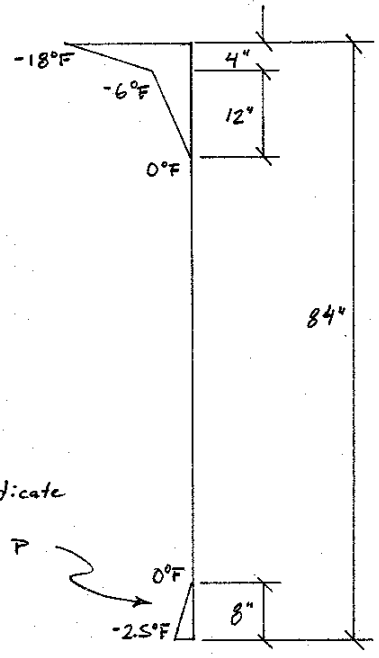

Measured temperatures indicate this shape is more appropriate for Ramp P gradients.

from $y = 0"$ to $8"$

$T_{G+} = -0.625y + 5$ $\quad T_{G-} = 0.3125y - 2.5$

from $y = 68"$ to $80"$

$T_{G+} = y - 68$ $\quad T_{G-} = -0.5y + 34$

from $y = 80"$ to $84"$

$T_{G+} = 6y - 468$ $\quad T_{G-} = -3y + 234$

AASHTO Design Gradient Calculation

DESIGN GRADIENT CALCULATIONS

BOX STRIP AREAS (FOR 11" BOTTOM FLANGE SEGMENT)

from $y = 0$ to 11

$$A(y) = [60 + 3.792y]\,dy$$

from $y = 11$ to 12

$$A(y) = [33 + 0.792y]\,dy$$

from $y = 12$ to 20

$$A(y) = [68.9 - 2.200y]\,dy$$

from $y = 20$ to 57.1083

$$A(y) = 24.852\,dy$$

from $y = 57.1083$ to 62

$$A(y) = [-85.886 + 1.940y]\,dy$$

from $y = 62$ to 69.1023

$$A(y) = [-303.624 + 5.454y]\,dy$$

from $y = 69.1023$ to 74

$$A(y) = [-2055.21 + 30.8y]\,dy$$

from $y = 74$ to 76

$$A(y) = [23.214 + 2.714y]\,dy$$

from $y = 76$ to 84

$$A(y) = 312\,dy$$

AASHTO Design Gradient Calculation

AASHTO LRFD Recommended Analysis Method

(1994 Edition, Section 4.6.6)

Positive Gradient

$$A_c T_{wG} = \iint T_G \, dw \, dz = \int T_G \, dA$$

$$= \int_0^8 (-0.625y + 5)(60 + 3.792y)\, dy + \int_{68}^{69.1023} (y - 68)(-303.624 + 5.454y)\, dy + \int_{69.1023}^{74} (y - 68)(-2055.21 + 30.8y)\, dy + \int_{74}^{76} (y - 68)(23.214 + 2.714y)\, dy + \int_{76}^{80} (y - 68)(312)\, dy + \int_{80}^{84} (6y - 468)(312)\, dy$$

$$= \left[-0.79y^3 - 9.27y^2 + 300y\right]_0^8 + \left[1.818y^3 - 337.248y^2 + 20646.432y\right]_{68}^{69.1023} + \left[10.267y^3 - 2074.805y^2 + 139754.28y\right]_{69.1023}^{74} + \left[0.905y^3 - 80.669y^2 - 1578.552y\right]_{74}^{76} + \left[156y^2 - 21216y\right]_{76}^{80} + \left[936y^2 - 146016y\right]_{80}^{84}$$

POSITIVE GRADIENT (CON'T)

$$= (1402 - 0) + (416203 - 416160) + (3140619 - 3137709) + (-188641 + 191829) + (-698880 + 711360) + (-5660928 + 5690880)$$

$$= \underline{49975 \text{ in}^2 \cdot {}^\circ\text{F}}$$

$$\phi I_c/\alpha = \iint T_G z \, dw \, dz = \int T_G z \, dA$$

$$= \int_0^8 (-0.625y + 5)(y - 57.76)(60 + 3.792)\, dy + \int_{68}^{69.1023} (y - 68)(y - 57.76)(-303.624 + 5.454y)\, dy + \int_{69.1023}^{74} (y - 68)(y - 57.76)(-2055.21 + 30.8y)\, dy + \int_{74}^{76} (y - 68)(y - 57.76)(23.214 + 2.714y)\, dy + \int_{76}^{80} (y - 68)(y - 57.76)(312)\, dy + \int_{80}^{84} (6y - 468)(y - 57.76)(312)\, dy$$

$$= \left[-0.5925y^4 + 39.45y^3 + 685.45y^2 - 17328y\right]_0^8 + \left[1.3635y^4 - 329.84y^3 + 29803y^2 - 1192538y\right]_{68}^{69.1023} + \left[7.7y^4 - 1976.21y^3 + 189718y^2 - 8072207y\right]_{69.1023}^{74} + \left[0.6785y^4 - 106.03y^3 + 3870y^2 + 91177y\right]_{74}^{76}$$

AASHTO Design Gradient Calculation

POSITIVE GRADIENT (CON'T)

$$+ \left[104y^3 - 19618.6y^2 + 1225436y \right]_{76}^{80}$$

$$+ \left[624y^3 - 127071.4y^2 + 8433884y \right]_{80}^{84}$$

$$= (-76984 - 0) + (-17841735 + 17842257)$$
$$+ (-128358636 + 128400741)$$
$$+ (5374183 - 5319209) + (25723840 - 25469606)$$
$$+ (181677754 - 180941760)$$

$$= \underline{1010845 \text{ in}^3 \cdot {}^\circ\text{F}}$$

NEGATIVE GRADIENT

$$A_c T_{uG} = (-0.5)(49975 \text{ in}^2 \cdot {}^\circ\text{F}) = \underline{-24988 \text{ in}^2 \cdot {}^\circ\text{F}}$$

$$\phi I_c / \alpha = (-0.5)(1010845 \text{ in}^3 \cdot {}^\circ\text{F}) = \underline{-505423 \text{ in}^3 \cdot {}^\circ\text{F}}$$

AASHTO Design Gradient Calculation

Calculation of Internal Stresses

$$\sigma_E = E(\alpha T_G - \alpha T_{uG} - \phi z)$$

Positive Gradient

P16-2

$T_{uG} = (49975\ in^2 \cdot °F)/(6526\ in^2) = 7.7\ °F$

$\phi/\alpha = (1010845\ in^3 \cdot °F)/(5354265\ in^4) = 0.1888\ °F/$

$\alpha = 5.0(10^{-6})\ \varepsilon/°F \qquad E = 6400\ ksi$

$y = 84$, $\sigma_E = (6400)(5.0(10^{-6}))(36 - 7.7 - (0.1888)(84 - 56.41))$

$= 0.739\ ksi$

$y = 80$, $\sigma_E = (6400)(5.0(10^{-6}))(12 - 7.7 - (0.1888)(80 - 56.41))$

$= -0.005\ ksi$

$y = 68$, $\sigma_E = (6400)(5.0(10^{-6}))(0 - 7.7 - (0.1888)(68 - 56.41))$

$= -0.316\ ksi$

$y = 8$, $\sigma_E = (6400)(5.0(10^{-6}))(0 - 7.7 - (0.1888)(8 - 56.41))$

$= 0.046\ ksi$

$y = 0$, $\sigma_E = (6400)(5.0(10^{-6}))(5 - 7.7 - (0.1888)(0 - 56.41))$

$= 0.254\ ksi$

P16-10

$T_{uG} = (49975\ in^2 \cdot °F)/(6332\ in^2) = 7.9\ °F$

$\phi/\alpha = (1010845\ in^3 \cdot °F)/(4970169\ in^4) = 0.2034\ °F/in$

$\alpha = 5.4(10^{-6})\ \varepsilon/°F \qquad E = 5900\ ksi$

$y = 84$, $\sigma_E = (5900)(5.4(10^{-6}))(36 - 7.9 - (0.2034)(84 - 57.76))$

$= 0.725\ ksi$

AASHTO Design Gradient Calculation

POSITIVE GRADIENT (CON'T)

$y = 80$, $\sigma_E = (5900)(5.4(10^{-6}))(12 - 7.9 - (0.2034)(80 - 57.76))$

$= -0.013$ ksi

$y = 68$, $\sigma_E = (5900)(5.4(10^{-6}))(0 - 7.9 - (0.2034)(68 - 57.76))$

$= -0.318$ ksi

$y = 8$, $\sigma_E = (5900)(5.4(10^{-6}))(0 - 7.9 - (0.2034)(8 - 57.76))$

$= 0.071$ ksi

$y = 0$, $\sigma_E = (5900)(5.4(10^{-6}))(5 - 7.9 - (0.2034)(0 - 57.76))$

$= 0.282$ ksi

P16-17

Same as P16-10, but multiply by ratio of coefficients of thermal expansion.

$y = 84$, $\sigma_E = (0.728)\left(\frac{5.2}{5.4}\right) = 0.698$ ksi

$y = 80$, $\sigma_E = (-0.013)\left(\frac{5.2}{5.4}\right) = -0.013$ ksi

$y = 68$, $\sigma_E = (-0.318)\left(\frac{5.2}{5.4}\right) = -0.306$ ksi

$y = 8$, $\sigma_E = (0.071)\left(\frac{5.2}{5.4}\right) = 0.068$ ksi

$y = 0$, $\sigma_E = (0.282)\left(\frac{5.2}{5.4}\right) = 0.271$ ksi

AASHTO Design Gradient Calculation

Equivalent Thermal Loads

T_{uG} and ϕ based on 11" bottom flange section.

T_u taken as the average temperature difference at the tops of the webs between the peak day and the baseline day.

Positive Gradient

$N = EA_c \alpha (T_u + T_{uG})$

$= \frac{1}{3}(6400 + 5900 + 5900)(5.2(10^{-6}))(6332)(3.3°F + 7.9°F)$

$= \underline{2237 \text{ kips}}$

$M = EI_c \phi$

$= (6067 \text{ ksi})(5.2(10^{-6}))(101084.5 \text{ in}^3 \cdot °F)$

$= \underline{31891 \text{ kip} \cdot \text{in}}$

Negative Gradient

$N = (6067)(5.2(10^{-6}))(6332)(-6.4°F - 4.0°F)$

$= \underline{-2078 \text{ kips}}$

$M = (6067)(5.2(10^{-6}))(-505423 \text{ in}^2 \cdot °F)$

$= \underline{-15945 \text{ kip} \cdot \text{in}}$

AASHTO Design Gradient Calculation

Calculation of Secondary Moments

Linear Thermal Expansion

N = Equivalent Axial Load for Thermal Expansion

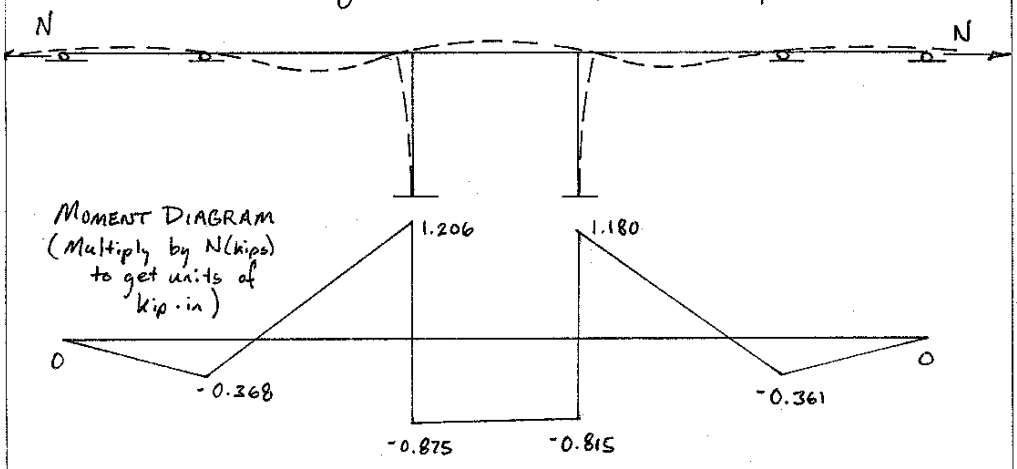

Uniform Gradient Curvature

M = Equivalent Moment for Curvature

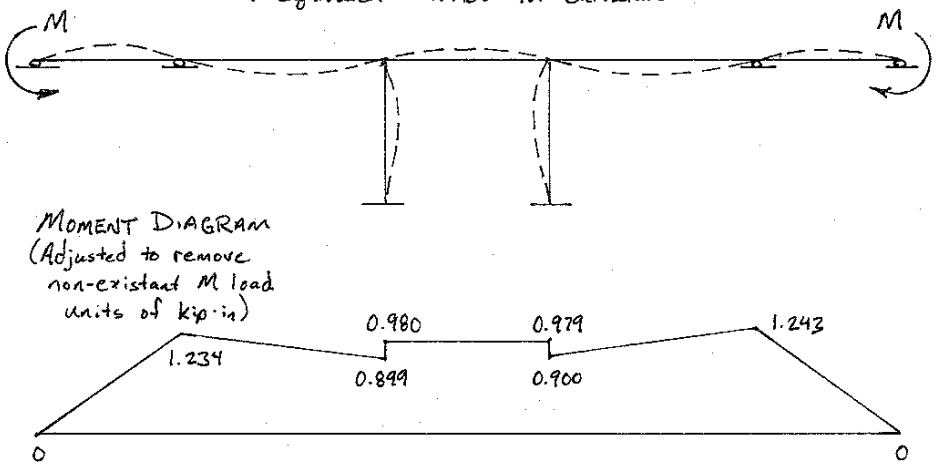

Positive Gradient

N = 2237 kips
M = 31891 kip*in

P16-2 I_{x-x} = 5354265 in^4
y_{bottom} = 56.41 in
N factor = 1.126 in
M factor = 0.911

Y (in)	Internal Stress (ksi)	Secondary Moment Stress (ksi)	Total (ksi)	**Total (MPa)**
84	0.739	0.163	0.902	**6.22**
80	-0.005	0.139	0.134	**0.92**
68	-0.316	0.068	-0.248	**-1.71**
8	0.046	-0.285	-0.239	**-1.65**
0	0.254	-0.333	-0.079	**-0.54**
82	0.367	0.151	0.518	**3.57**
2	0.237	-0.321	-0.084	**-0.58**

P16-10 I_{x-x} = 4970169 in^4
y_{bottom} = 57.76 in
N factor = 0.804 in
M factor = 0.983

Y (in)	Internal Stress (ksi)	Secondary Moment Stress (ksi)	Total (ksi)	**Total (MPa)**
84	0.725	0.175	0.900	**6.21**
80	-0.013	0.148	0.135	**0.93**
68	-0.318	0.068	-0.250	**-1.72**
8	0.071	-0.332	-0.261	**-1.80**
0	0.282	-0.385	-0.103	**-0.71**
82	0.356	0.162	0.518	**3.57**
2	0.264	-0.372	-0.108	**-0.74**

P16-17 I_{x-x} = 4970169 in^4
y_{bottom} = 57.76 in
N factor = 0.481 in
M factor = 1.071

Y (in)	Internal Stress (ksi)	Secondary Moment Stress (ksi)	Total (ksi)	**Total (MPa)**
84	0.698	0.186	0.884	**6.10**
80	-0.013	0.158	0.145	**1.00**
68	-0.306	0.073	-0.233	**-1.61**
8	0.068	-0.353	-0.285	**-1.96**
0	0.271	-0.409	-0.138	**-0.95**
82	0.343	0.172	0.514	**3.55**
2	0.254	-0.395	-0.141	**-0.97**

Negative Gradient

N = -2078 kips
M = -15945 kip*in

P16-2 I_{x-x} = 5354265 in^4
y_{bottom} = 56.41 in
N factor = 1.126 in
M factor = 0.911

Y (in)	Internal Stress (ksi)	Secondary Moment Stress (ksi)	Total (ksi)	Total (MPa)
84	-0.370	-0.087	-0.456	**-3.15**
80	0.003	-0.074	-0.071	**-0.49**
68	0.158	-0.037	0.121	**0.84**
8	-0.023	0.152	0.129	**0.89**
0	-0.127	0.178	0.051	**0.35**
82	-0.183	-0.081	-0.264	**-1.82**
2	-0.101	0.171	0.070	**0.49**

P16-10 I_{x-x} = 4970169 in^4
y_{bottom} = 57.76 in
N factor = 0.804 in
M factor = 0.983

Y (in)	Internal Stress (ksi)	Secondary Moment Stress (ksi)	Total (ksi)	Total (MPa)
84	-0.363	-0.092	-0.455	**-3.13**
80	0.007	-0.078	-0.071	**-0.49**
68	0.159	-0.036	0.123	**0.85**
8	-0.035	0.174	0.139	**0.96**
0	-0.141	0.202	0.061	**0.42**
82	-0.178	-0.085	-0.263	**-1.81**
2	-0.115	0.195	0.080	**0.55**

P16-17 I_{x-x} = 4970169 in^4
y_{bottom} = 57.76 in
N factor = 0.481 in
M factor = 1.071

Y (in)	Internal Stress (ksi)	Secondary Moment Stress (ksi)	Total (ksi)	Total (MPa)
84	-0.349	-0.095	-0.444	**-3.06**
80	0.007	-0.081	-0.074	**-0.51**
68	0.153	-0.037	0.116	**0.80**
8	-0.034	0.181	0.147	**1.01**
0	-0.136	0.210	0.074	**0.51**
82	-0.171	-0.088	-0.259	**-1.79**
2	-0.111	0.203	0.092	**0.64**

Analysis of Measured Gradients Using AASHTO Method

Tributary Regions for Thermocouple Gauges

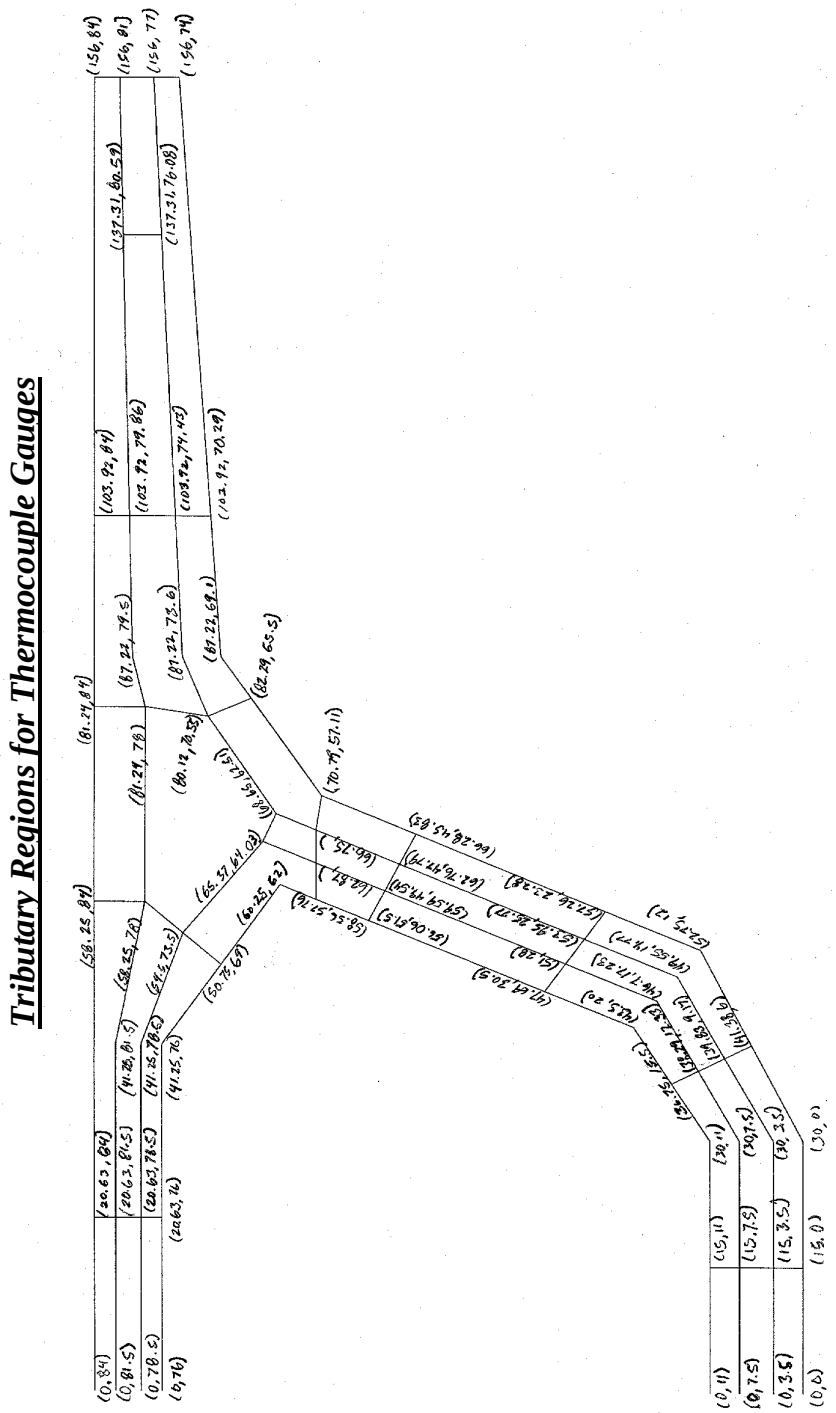

Analysis of Measured Gradients Using AASHTO Method

Positive Gradient Temperatures (°F) - March 20, 1997

	91.8	96.5	91.4	95.9	94.0	95.4	87.4	87.5	94.3	
73.2	78.0	76.3		73.7	83.6	83.2		74.9	78.8	76.2
	76.8	75.2	73.7	78.4	78.5	77.2	71.6	74.5	77.4	
		71.3	67.9	66.5		65.7	67.1	71.0		
		72.4	69.1	67.1		65.3	67.2	71.2		
		74.8	70.7	67.6		65.6	67.8	73.8		
				66.7	65.3	68.1				
				68.5	68.3	68.7				
				74.3	73.4	74.3				

Baseline Temperatures (°F) - March 9, 1997

	64.5	64.8	64.5	64.6	64.5	64.7	64.6	64.5	64.6	
64.3	64.4	64.5		64.4	64.3	64.4		64.7	64.5	64.4
	64.9	64.8	64.6	64.4	64.3	64.5	64.9	65.0	64.9	
		65.0	64.9	64.9		65.0	65.0	65.1		
		64.9	64.7	64.7		64.7	64.7	64.9		
		65.0	64.7	64.6		64.6	64.6	64.9		
				64.6	64.5	64.5				
				64.6	64.6	64.6				
				64.9	64.8	64.9				

Differences (°F)

	27.3	31.7	26.9	31.3	29.5	30.8	22.8	23.0	29.7	
8.9	13.6	11.8		9.3	19.4	18.8		10.2	14.3	11.8
	12.0	10.4	9.1	14.0	14.2	12.7	6.8	9.5	12.5	
		6.3	3.0	1.6		0.7	2.1	5.9		
		7.5	4.4	2.5		0.6	2.5	6.4		
		9.8	6.0	2.9		1.0	3.2	9.0		
				2.1	0.8	3.5				
				3.9	3.7	4.1				
				9.4	8.6	9.5				

Gradient (°F)

	24.0	28.5	23.6	28.0	26.2	27.5	19.5	19.7	26.4	
5.6	10.3	8.5		6.0	16.1	15.5		6.9	11.0	8.5
	8.7	7.1	5.8	10.7	10.9	9.4	3.5	6.2	9.2	
		3.0	-0.3	-1.7		-2.6	-1.1	2.7		
		4.2	1.1	-0.8		-2.7	-0.8	3.1		
		6.6	2.7	-0.4		-2.3	-0.1	5.7		
				-1.2	-2.5	0.3				
				0.6	0.4	0.9				
				6.1	5.3	6.2				

Uniform Temperature (°F): 3.3

Analysis of Measured Gradients Using AASHTO Method

Positive Gradient Plane Section Calculation
From March 20, 1997

Temperatures (^{o}F)

	27.3	31.7	26.9	31.3	29.5	30.8	22.8	23.0	29.7	
8.9	13.6	11.8		9.3	19.4	18.8		10.2	14.3	11.8
	12.0	10.4	9.1	14.0	14.2	12.7	6.8	9.5	12.5	
		6.3	3.0	1.6		0.7	2.1	5.9		
		6.3	3.0	1.6		0.7	2.1	5.9		
		7.5	4.4	2.5		0.6	2.5	6.4		
		9.8	6.0	2.9		1.0	3.2	9.0		
				2.1	0.8	3.5				
				3.9	3.7	4.1				
				9.4	8.6	9.5				

Areas (in^{2})

	185.9	103.5	137.9	123.8	103.2	123.8	137.9	103.5	185.9	
79.5	166.0	137.0		126.6	123.8	126.6		137.0	166.0	79.5
	185.9	104.5	276.0	102.6	103.2	102.6	276.0	104.5	185.9	
		97.3	21.4	92.4		92.4	21.4	97.3		
		45.7	35.2	31.2		31.2	35.2	45.7		
		91.7	84.0	95.9		95.9	84.0	91.7		
		93.1	78.8	79.5		79.5	78.8	93.1		
				81.2	105.0	81.2				
				96.5	120.0	96.5				
				92.4	105.0	92.4				

Centers of Gravity (in)

	24.4	23.9	23.2	24.4	25.0	24.4	23.2	23.9	24.4	
20.9	20.0	18.6		21.1	22.2	21.1		18.6	20.0	20.9
	16.1	13.4	14.3	17.8	19.5	17.8	14.3	13.4	16.1	
		5.3	2.8	7.9		7.9	2.8	5.3		
		-5.7	-4.6	-3.6		-3.6	-4.6	-5.7		
		-22.1	-20.0	-17.9		-17.9	-20.0	-22.1		
		-37.1	-40.1	-42.9		-37.1	-40.1	-42.9		
				-47.7	-48.5	-47.7				
				-51.3	-52.3	-51.3				
				-54.7	-56.0	-54.7				

Analysis of Measured Gradients Using AASHTO Method

Positive Gradient Plane Section Calculation
From March 20, 1997

Full Section Properties	
A_C=	6330 in^2
I_C=	4970200 in^4
y_{CG}=	57.76 in

T_{UG} =	12.00 ^oF
N_{UG} =	2396 kips
Φ =	1.0E-06 rad/in
M_{TG} =	30976 kip*in

P16-2	
E=	6400 ksi
α=	5.00E-06 $\varepsilon/^oF$

P16-10	
E=	5900 ksi
α=	5.40E-06 $\varepsilon/^oF$

P16-17	
E=	5900 ksi
α=	5.20E-06 $\varepsilon/^oF$

T_G*dA

	5079	3285	3712	3871	3046	3807	3144	2376	5521	
709	2254	1611		1181	2396	2381		1393	2377	936.5
	2222	1084	2503	1433	1462	1306	1863	990	2327	
		616	65	150		62	46	578		
		289	107	51		21	75	271		
		689	367	235		58	209	582		
		916	473	233		80	250	833		
				172	85	287				
				375	448	400				
				868	901	873				

T_G*dA*z

	124126	78612	86273	94497	76131	92925	73069	56866	134939	
14821	44995	29967		24887	53277	50175		25915	47447	19573
	35744	14554	35772	25513	28501	23249	26622	13291	37449	
		3289	180	1180		488	127	3086		
		-1634	-486	-182		-75	-343	-1534		
		-15220	-7334	-4201		-1029	-4179	-12869		
		-33960	-18969	-9993		-2947	-10022	-35746		
				-8208	-4126	-13706				
				-19250	-23392	-20487				
				-47494	-50459	-47798				

Analysis of Measured Gradients Using AASHTO Method

Positive Gradient Plane Section Calculation
From March 20, 1997

Internal Stresses (psi) (- tension, + compression)

	330	474	325	456	396	440	193	194	406	
-236	-81	-130		-224	89	80		-181	-57	-144
	-107	-140	-188	-54	-59	-94	-262	-169	-89	
		-216	-305	-384		-414	-334	-229		
		-144	-257	-308		-339	-285	-157		
		2	-113	-188		-247	-173	-35		
		175	72	-8		-108	-19	185		
				-3	-39	43				
				78	79	86				
				277	259	278				

Secondary Moment Stresses (psi) (- tension, + compression)

Axial moment factor 1.126

P16-2 Secondary moment factor 0.911

	152	149	145	152	156	152	145	149	152	
130	124	116		131	138	131		116	124	130
	100	84	89	111	121	111	89	84	100	
		33	17	49		49	17	33		
		-35	-28	-22		-22	-28	-35		
		-138	-124	-111		-111	-124	-138		
		-231	-250	-267		-231	-250	-267		
				-297	-302	-297				
				-319	-325	-319				
				-341	-349	-341				

Total Thermal Gradient Stresses (psi)

P16-2

	482	*623*	*469*	*608*	*552*	*592*	*338*	*342*	*558*	
-106	*44*	*-14*		*-93*	*228*	*211*		*-65*	*67*	*-14*
	-7	*-57*	*-99*	*57*	*63*	*17*	*-173*	*-86*	*11*	
		-183	*-288*	*-335*		*-365*	*-316*	*-196*		
		-179	*-285*	*-331*		*-361*	*-314*	*-192*		
		-136	*-237*	*-299*		*-358*	*-297*	*-173*		
		-56	*-178*	*-275*		*-339*	*-268*	*-82*		
				-299	*-341*	*-254*				
				-241	*-246*	*-233*				
				-64	*-90*	*-62*				

Analysis of Measured Gradients Using AASHTO Method

Positive Gradient Plane Section Calculation
From March 20, 1997

Internal Stresses (psi) (- tension, + compression)

	340	484	335	466	407	450	203	204	416	
-225	-71	-120		-213	99	89		-171	-47	-134
	-99	-133	-180	-45	-49	-85	-254	-162	-81	
		-213	-302	-378		-409	-331	-225		
		-146	-258	-309		-339	-286	-159		
		-9	-122	-196		-255	-182	-46		
		156	52	-29		-126	-38	163		
				-26	-62	20				
				53	53	61				
				249	231	251				

Axial moment factor **0.804**

P16-10 **Secondary moment factor** **0.983**

	159	156	151	159	163	159	151	156	159	
136	130	121		137	145	137		121	130	136
	105	88	93	116	127	116	93	88	105	
		35	18	51		51	18	35		
		-37	-30	-23		-23	-30	-37		
		-144	-130	-117		-117	-130	-144		
		-242	-261	-280		-242	-261	-280		
				-311	-316	-311				
				-334	-341	-334				
				-357	-365	-357				

P16-10

	499	*640*	*486*	*625*	*570*	*609*	*355*	*360*	*575*	
-88	*60*	*1*		*-75*	*244*	*227*		*-50*	*83*	*3*
	6	*-46*	*-87*	*71*	*78*	*31*	*-161*	*-74*	*24*	
		-178	*-284*	*-327*		*-357*	*-313*	*-191*		
		-183	*-288*	*-332*		*-362*	*-316*	*-196*		
		-153	*-252*	*-312*		*-371*	*-312*	*-190*		
		-86	*-209*	*-308*		*-367*	*-299*	*-117*		
				-336	*-378*	*-291*				
				-282	*-287*	*-274*				
				-108	*-134*	*-106*				

Analysis of Measured Gradients Using AASHTO Method

Positive Gradient Plane Section Calculation
From March 20, 1997

Internal Stresses (psi) (- tension, + compression)

	322	461	317	443	386	427	191	191	395	
-221	-72	-120		-210	91	81		-169	-50	-133
	-99	-131	-176	-47	-51	-85	-248	-159	-81	
		-206	-292	-366		-395	-319	-218		
		-140	-247	-297		-326	-275	-152		
		-4	-113	-185		-241	-171	-39		
		159	59	-18		-113	-28	167		
				-14	-49	30				
				62	63	70				
				252	235	254				

Axial moment factor **0.481**

P16-17 **Secondary moment factor** **1.071**

	169	165	161	169	173	169	161	165	169	
144	138	128		146	154	146		128	138	144
	111	93	99	123	135	123	99	93	111	
		37	19	54		54	19	37		
		-39	-32	-25		-25	-32	-39		
		-153	-138	-124		-124	-138	-153		
		-256	-277	-296		-256	-277	-296		
				-329	-335	-329				
				-354	-361	-354				
				-378	-387	-378				

P16-17

	491	*626*	*478*	*612*	*559*	*596*	*351*	*357*	*564*	
-77	*66*	*9*		*-64*	*244*	*227*		*-40*	*88*	*11*
	12	*-39*	*-78*	*76*	*83*	*38*	*-149*	*-66*	*30*	
		-169	*-273*	*-312*		*-341*	*-300*	*-181*		
		-179	*-279*	*-321*		*-351*	*-306*	*-191*		
		-156	*-251*	*-308*		*-365*	*-309*	*-192*		
		-98	*-218*	*-315*		*-369*	*-305*	*-130*		
				-343	*-384*	*-300*				
				-292	*-298*	*-284*				
				-126	*-152*	*-125*				

Analysis of Measured Gradients Using AASHTO Method

Positive Gradient Plane Section Calculation
From March 20, 1997

Total Thermal Gradient Stresses (MPa)

P16-2

	3.32	*4.30*	*3.24*	*4.19*	*3.81*	*4.08*	*2.33*	*2.36*	*3.85*	
-0.73	*0.30*	*-0.10*		*-0.64*	*1.57*	*1.45*		*-0.45*	*0.46*	*-0.10*
	-0.05	*-0.39*	*-0.68*	*0.39*	*0.43*	*0.12*	*-1.19*	*-0.59*	*0.08*	
		-1.26	*-1.99*	*-2.31*		*-2.52*	*-2.18*	*-1.35*		
		-1.24	*-1.97*	*-2.28*		*-2.49*	*-2.16*	*-1.32*		
		-0.94	*-1.63*	*-2.06*		*-2.47*	*-2.05*	*-1.19*		
		-0.39	*-1.23*	*-1.90*		*-2.34*	*-1.85*	*-0.57*		
				-2.06	*-2.35*	*-1.75*				
				-1.66	*-1.70*	*-1.61*				
				-0.44	*-0.62*	*-0.43*				

Total Thermal Gradient Stresses (MPa)

P16-10

	3.44	*4.41*	*3.35*	*4.31*	*3.93*	*4.20*	*2.45*	*2.48*	*3.97*	
-0.61	*0.41*	*0.01*		*-0.52*	*1.69*	*1.56*		*-0.34*	*0.57*	*0.02*
	0.04	*-0.32*	*-0.60*	*0.49*	*0.54*	*0.22*	*-1.11*	*-0.51*	*0.17*	
		-1.23	*-1.96*	*-2.25*		*-2.46*	*-2.16*	*-1.31*		
		-1.26	*-1.98*	*-2.29*		*-2.50*	*-2.18*	*-1.35*		
		-1.05	*-1.74*	*-2.15*		*-2.56*	*-2.15*	*-1.31*		
		-0.59	*-1.44*	*-2.13*		*-2.53*	*-2.06*	*-0.80*		
				-2.32	*-2.61*	*-2.01*				
				-1.94	*-1.98*	*-1.89*				
				-0.74	*-0.93*	*-0.73*				

Total Thermal Gradient Stresses (MPa)

P16-17

	3.38	*4.32*	*3.29*	*4.22*	*3.85*	*4.11*	*2.42*	*2.46*	*3.89*	
-0.53	*0.45*	*0.06*		*-0.44*	*1.69*	*1.56*		*-0.28*	*0.61*	*0.08*
	0.08	*-0.27*	*-0.54*	*0.52*	*0.57*	*0.26*	*-1.03*	*-0.46*	*0.20*	
		-1.17	*-1.88*	*-2.15*		*-2.35*	*-2.07*	*-1.25*		
		-1.23	*-1.92*	*-2.22*		*-2.42*	*-2.11*	*-1.31*		
		-1.08	*-1.73*	*-2.12*		*-2.52*	*-2.13*	*-1.32*		
		-0.67	*-1.50*	*-2.17*		*-2.54*	*-2.10*	*-0.90*		
				-2.37	*-2.65*	*-2.07*				
				-2.01	*-2.05*	*-1.96*				
				-0.87	*-1.05*	*-0.86*				

Analysis of Measured Gradients Using AASHTO Method

Negative Gradient Temperatures (^{o}F) - March 6, 1997

	44.7	45.3	49.0	46.2	45.1	45.4	49.8	48.7	44.6	
49.3	49.6	53.2		52.1	50.0	51.2		54.3	50.4	48.8
	49.3	52.3	57.6	54.5	52.5	54.3	57.9	53.8	50.2	
		58.3	60.0	61.7		61.8	60.3	57.2		
		56.5	57.2	59.2		59.7	58.0	55.1		
		53.9	55.0	57.6		58.2	56.6	52.7		
				57.6	58.7	58.3				
				56.2	56.7	55.8				
				52.5	53.3	52.4				

Baseline Temperatures (^{o}F) - March 5, 1997

	66.9	66.7	66.5	66.6	66.6	66.6	66.5	66.7	66.8	
67.2	67.1	66.9		66.5	66.6	66.6		66.8	67.1	67.2
	67.3	67.1	66.3	66.5	66.6	66.5	66.4	67.0	67.3	
		66.5	66.2	66.1		66.1	66.2	66.5		
		66.6	66.3	66.2		66.1	66.3	66.6		
		66.8	66.6	66.3		66.3	66.4	66.8		
				66.3	66.1	66.2				
				66.5	66.4	66.5				
				66.8	66.6	66.8				

Differences (^{o}F)

	-22.2	-21.4	-17.5	-20.4	-21.5	-21.2	-16.7	-18.0	-22.3	
-17.9	-17.6	-13.7		-14.5	-16.7	-15.4		-12.5	-16.7	-18.4
	-18.0	-14.8	-8.7	-12.1	-14.1	-12.2	-8.5	-13.2	-17.0	
		-8.2	-6.3	-4.3		-4.3	-5.9	-9.3		
		-10.1	-9.2	-7.0		-6.4	-8.3	-11.4		
		-12.9	-11.6	-8.7		-8.0	-9.8	-14.1		
				-8.8	-7.4	-7.9				
				-10.3	-9.7	-10.7				
				-14.3	-13.3	-14.4				

Gradient (^{o}F)

	-15.8	-15.0	-11.1	-14.0	-15.1	-14.8	-10.3	-11.6	-15.9	
-11.5	-11.2	-7.3		-8.1	-10.3	-9.0		-6.1	-10.3	-12.0
	-11.6	-8.4	-2.3	-5.7	-7.7	-5.8	-2.1	-6.8	-10.7	
		-1.8	0.1	2.0		2.1	0.5	-2.9		
		-3.7	-2.8	-0.6		-0.1	-2.0	-5.0		
		-6.5	-5.2	-2.4		-1.7	-3.5	-7.7		
				-2.4	-1.0	-1.6				
				-3.9	-3.3	-4.3				
				-7.9	-6.9	-8.0				

Uniform Temperature (^{o}F): -6.4

Analysis of Measured Gradients Using AASHTO Method

Negative Gradient Plane Section Calculation
From March 6, 1997

Temperatures (^{o}F)

	-22.2	-21.4	-17.5	-20.4	-21.5	-21.2	-16.7	-18.0	-22.3	
-17.9	-17.6	-13.7		-14.5	-16.7	-15.4		-12.5	-16.7	-18.4
	-18.0	-14.8	-8.7	-12.1	-14.1	-12.2	-8.5	-13.2	-17.0	
		-8.2	-6.3	-4.3		-4.3	-5.9	-9.3		
		-8.2	-6.3	-4.3		-4.3	-5.9	-9.3		
		-10.1	-9.2	-7.0		-6.4	-8.3	-11.4		
		-12.9	-11.6	-8.7		-8.0	-9.8	-14.1		
				-8.8	-7.4	-7.9				
				-10.3	-9.7	-10.7				
				-14.3	-13.3	-14.4				

Areas (in^{2})

	185.9	103.5	137.9	123.8	103.2	123.8	137.9	103.5	185.9	
79.5	166.0	137.0		126.6	123.8	126.6		137.0	166.0	79.5
	185.9	104.5	276.0	102.6	103.2	102.6	276.0	104.5	185.9	
		97.3	21.4	92.4		92.4	21.4	97.3		
		45.7	35.2	31.2		31.2	35.2	45.7		
		91.7	84.0	95.9		95.9	84.0	91.7		
		93.1	78.8	79.5		79.5	78.8	93.1		
				81.2	105.0	81.2				
				96.5	120.0	96.5				
				92.4	105.0	92.4				

Centers of Gravity (in)

	24.4	23.9	23.2	24.4	25.0	24.4	23.2	23.9	24.4	
20.9	20.0	18.6		21.1	22.2	21.1		18.6	20.0	20.9
	16.1	13.4	14.3	17.8	19.5	17.8	14.3	13.4	16.1	
		5.3	2.8	7.9		7.9	2.8	5.3		
		-5.7	-4.6	-3.6		-3.6	-4.6	-5.7		
		-22.1	-20.0	-17.9		-17.9	-20.0	-22.1		
		-37.1	-40.1	-42.9		-37.1	-40.1	-42.9		
				-47.7	-48.5	-47.7				
				-51.3	-52.3	-51.3				
				-54.7	-56.0	-54.7				

Analysis of Measured Gradients Using AASHTO Method

Negative Gradient Plane Section Calculation
From March 6, 1997

Full Section Properties	
A_C=	6330 in^2
I_C=	4970200 in^4
y_{CG}=	57.76 in

T_{UG} =	-13.34 ^oF
N_{UG} =	-2665 kips
Φ =	-4.6E-07 rad/in
M_{TG} =	-13945 kip*in

P16-2	
E=	6400 ksi
α=	5.00E-06 $\varepsilon/^oF$

P16-10	
E=	5900 ksi
α=	5.40E-06 $\varepsilon/^oF$

P16-17	
E=	5900 ksi
α=	5.20E-06 $\varepsilon/^oF$

T_G*dA

	-4127	-2215	-2413	-2526	-2219	-2625	-2303	-1863	-4146	
-1423	-2922	-1877		-1836	-2067	-1950		-1713	-2772	-1462.8
	-3346	-1547	-2401	-1241	-1455	-1252	-2346	-1379	-3160	
		-798	-135	-397		-397	-126	-905		
		-375	-222	-134		-134	-208	-425		
		-926	-773	-671		-614	-697	-1045		
		-1201	-914	-692		-636	-772	-1313		
				-715	-777	-641				
				-994	-1164	-1033				
				-1321	-1397	-1331				

T_G*dA*z

	-100863	-53003	-56084	-61648	-55448	-64066	-53520	-44582	-101318	
-29742	-58315	-34910		-38678	-45980	-41079		-31853	-55333	-30573
	-53840	-20771	-34313	-22098	-28360	-22281	-33524	-18525	-50849	
		-4261	-373	-3131		-3131	-350	-4832		
		2117	1011	483		483	947	2401		
		20468	15441	12003		10974	13930	23103		
		44521	36673	29672		23577	30982	56315		
				34070	37692	30586				
				50970	60831	52949				
				72329	78218	72835				

Analysis of Measured Gradients Using AASHTO Method

Negative Gradient Plane Section Calculation
From March 6, 1997

Internal Stresses (psi) (- tension, + compression)

	-211	-187	-64	-154	-187	-179	-39	-78	-214	
-84	-77	44		25	-42	-3		82	-48	-100
	-101	-7	191	92	33	89	197	44	-69	

	180	234	313		313	246	145
	148	212	279		279	225	113
	38	73	150		169	102	-3
	-96	-63	22		61	-5	-151

4	47	33
-54	-38	-67
-193	-164	-196

Secondary Moment Stresses (psi) (- tension, + compression)

Axial moment factor **1.126**

P16-2 **Secondary moment factor** **0.911**

	-77	-76	-73	-77	-79	-77	-73	-76	-77	
-66	-63	-59		-67	-70	-67		-59	-63	-66
	-51	-42	-45	-56	-62	-56	-45	-42	-51	

	-17	-9	-25		-25	-9	-17
	18	14	11		11	14	18
	70	63	57		57	63	70
	117	127	136		117	127	136

151	153	151
162	165	162
173	177	173

Total Thermal Gradient Stresses (psi)

P16-2

	-288	*-263*	*-138*	*-231*	*-266*	*-256*	*-112*	*-154*	*-292*	
-150	*-140*	*-15*		*-41*	*-112*	*-70*		*23*	*-111*	*-166*
	-152	*-49*	*146*	*36*	*-28*	*33*	*152*	*2*	*-120*	

	164	*225*	*288*		*288*	*238*	*128*
	166	*226*	*290*		*290*	*239*	*131*
	108	*137*	*207*		*226*	*165*	*67*
	22	*64*	*157*		*178*	*121*	*-16*

155	*200*	*184*
108	*127*	*95*
-20	*13*	*-23*

Analysis of Measured Gradients Using AASHTO Method

Negative Gradient Plane Section Calculation
From March 6, 1997

Internal Stresses (psi) (- tension, + compression)

	-215	-191	-69	-158	-192	-184	-44	-83	-219	
-88	-81	39		21	-46	-8		78	-52	-104
	-104	-10	187	88	29	85	193	41	-73	
		178	232	310		310	245	143		
		148	212	278		278	225	113		
		43	78	153		172	106	2		
		-87	-54	31		69	3	-141		
				15	57	43				
				-43	-27	-56				
				-180	-151	-183				

Axial moment factor **0.804**

P16-10 **Secondary moment factor** **0.983**

	-78	-76	-74	-78	-80	-78	-74	-76	-78	
-67	-64	-59		-67	-71	-67		-59	-64	-67
	-51	-43	-46	-57	-62	-57	-46	-43	-51	
		-17	-9	-25		-25	-9	-17		
		18	15	11		11	15	18		
		71	64	57		57	64	71		
		118	128	137		118	128	137		
				152	155	152				
				164	167	164				
				175	179	175				

P16-10

	-293	*-268*	*-143*	*-236*	*-271*	*-262*	*-118*	*-159*	*-297*	
-155	*-145*	*-20*		*-47*	*-117*	*-75*		*18*	*-116*	*-171*
	-156	*-53*	*141*	*31*	*-33*	*28*	*148*	*-2*	*-124*	
		161	*223*	*285*		*285*	*236*	*126*		
		166	*227*	*290*		*290*	*239*	*131*		
		114	*141*	*210*		*229*	*170*	*72*		
		31	*74*	*168*		*187*	*131*	*-4*		
				167	*212*	*195*				
				121	*140*	*108*				
				-5	*27*	*-8*				

Analysis of Measured Gradients Using AASHTO Method

Negative Gradient Plane Section Calculation
From March 6, 1997

Internal Stresses (psi) (- tension, + compression)

	-205	-182	-64	-150	-182	-174	-40	-78	-208	
-83	-76	40		22	-42	-6		77	-48	-98
	-99	-8	181	87	30	84	188	41	-68	
		172	224	299		299	236	139		
		142	204	268		268	216	109		
		39	73	146		164	100	-1		
		-88	-56	25		63	-1	-140		
				9	50	37				
				-47	-31	-59				
				-179	-151	-182				

Axial moment factor **0.481**

P16-17 **Secondary moment factor** **1.071**

	-80	-78	-76	-80	-82	-80	-76	-78	-80	
-68	-65	-61		-69	-73	-69		-61	-65	-68
	-53	-44	-47	-58	-64	-58	-47	-44	-53	
		-17	-9	-26		-26	-9	-17		
		18	15	12		12	15	18		
		72	65	58		58	65	72		
		121	131	140		121	131	140		
				156	158	156				
				167	171	167				
				179	183	179				

P16-17

	-285	*-260*	*-140*	*-230*	*-264*	*-254*	*-115*	*-156*	*-288*	
-151	*-141*	*-21*		*-47*	*-115*	*-74*		*16*	*-114*	*-166*
	-151	*-52*	*135*	*29*	*-34*	*26*	*141*	*-3*	*-121*	
		155	*215*	*273*		*273*	*227*	*121*		
		161	*219*	*279*		*279*	*231*	*127*		
		111	*138*	*204*		*223*	*165*	*71*		
		33	*75*	*165*		*184*	*130*	*0*		
				165	*208*	*193*				
				121	*140*	*109*				
				0	*31*	*-3*				

Analysis of Measured Gradients Using AASHTO Method

Negative Gradient Plane Section Calculation
From March 6, 1997

Total Thermal Gradient Stresses (MPa)

P16-2

	-1.99	-1.81	-0.95	-1.59	-1.83	-1.77	-0.77	-1.06	-2.01	
-1.03	-0.97	-0.10		-0.28	-0.77	-0.48		0.16	-0.77	-1.14
	-1.05	-0.34	1.00	0.25	-0.19	0.23	1.05	0.01	-0.83	
		1.13	1.55	1.98		1.98	1.64	0.88		
		1.14	1.56	2.00		2.00	1.65	0.90		
		0.75	0.94	1.42		1.56	1.14	0.46		
		0.15	0.44	1.08		1.23	0.84	-0.11		
				1.07	1.38	1.27				
				0.74	0.88	0.65				
				-0.14	0.09	-0.16				

Total Thermal Gradient Stresses (MPa)

P16-10

	-2.02	-1.85	-0.99	-1.63	-1.87	-1.80	-0.81	-1.10	-2.05	
-1.07	-1.00	-0.14		-0.32	-0.81	-0.52		0.13	-0.80	-1.18
	-1.07	-0.36	0.97	0.22	-0.23	0.19	1.02	-0.01	-0.85	
		1.11	1.54	1.96		1.96	1.63	0.87		
		1.15	1.56	2.00		2.00	1.65	0.91		
		0.78	0.97	1.45		1.58	1.17	0.50		
		0.22	0.51	1.16		1.29	0.91	-0.03		
				1.15	1.46	1.35				
				0.83	0.97	0.74				
				-0.04	0.19	-0.06				

Total Thermal Gradient Stresses (MPa)

P16-17

	-1.96	-1.79	-0.96	-1.58	-1.82	-1.75	-0.80	-1.07	-1.98	
-1.04	-0.97	-0.14		-0.32	-0.79	-0.51		0.11	-0.78	-1.15
	-1.04	-0.36	0.93	0.20	-0.23	0.18	0.97	-0.02	-0.83	
		1.07	1.48	1.88		1.88	1.56	0.84		
		1.11	1.51	1.93		1.93	1.59	0.88		
		0.77	0.95	1.41		1.53	1.14	0.49		
		0.23	0.52	1.14		1.27	0.90	0.00		
				1.14	1.44	1.33				
				0.83	0.96	0.75				
				0.00	0.22	-0.02				

Transverse Gradient Analysis

TRANSVERSE ANALYSIS MODEL

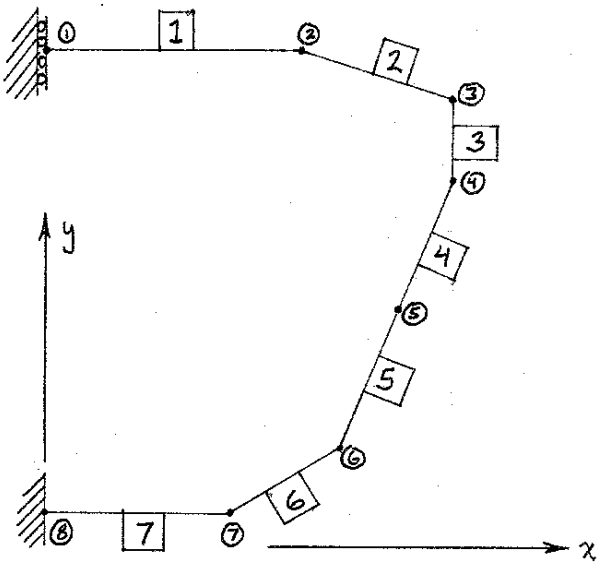

NODE	X (in)	Y (in)
1	0.0000	80.0000
2	41.2500	80.0000
3	65.5217	73.0000
4	65.5217	59.5542
5	56.8234	37.7771
6	48.1250	16.0000
7	30.0000	5.5000
8	0.0000	5.5000

Positive Gradient P16-17

Transverse Gradient Analysis

Material Properties	
Coefficient of Thermal Expansion:	5.20E-06 / °F
Modulus of Elasticity:	5900 ksi

Node	Outside Temp. (°C)	Middle Temp. (°C)	Inside Temp. (°C)
1	29.5	19.4	14.2
2	30.8	18.8	12.7
3	22.8	6.8	0.7
4	5.9	2.1	0.7
5	6.4	2.5	0.6
6	9.0	3.2	1.0
7	9.5	4.1	3.5
8	8.6	3.7	0.8

	Average Temperatures												RISA2D Results		Unrestrained Force Results	
Member	Outside Temp. (°C)	Middle Temp. (°C)	Inside Temp. (°C)	Average Thickness (in)	Area (in^2)	Inertia (in^2)	Temp. Area 1	Temp. Area 2	Temp. C.G. 1	Temp. C.G. 2	N (kip)	M (kip*in)	Axial (kip)	Moment (kip*in)	Axial (kip)	Moment (kip*in)
1	30.15	19.10	13.45	8.0	96	512	99	65	2.15	-1.88	60.23	-32.79	60.23	0.74	0.00	33.53
2	26.80	12.80	6.70	15.5	186	5832	153	76	4.33	-3.47	84.31	-148.15				
3	14.35	4.45	0.70	14.5	174	10000	68	19	4.26	-2.75	31.96	-88.05				
4	6.15	2.30	0.65	12.0	144	1728	25	9	3.46	-2.44	12.59	-24.30	12.59	9.10	0.00	33.40
5	7.70	2.85	0.80	12.0	144	1728	32	11	3.46	-2.44	15.68	-30.48				
6	9.25	3.65	2.25	10.5	126	1158	34	15	3.00	-2.42	18.17	-23.68				
7	9.05	3.90	2.15	11.0	132	1331	36	17	3.11	-2.48	19.24	-25.61	19.24	7.69	0.00	33.30

	Outside Temp.	Middle Temp.	Inside Temp.	Average Thickness	Area	Inertia	Temp.	Temp.	Temp.	Temp.	N	M	Internal Stresses Outside	Internal Stresses Inside	Total Stresses Outside	Total Stresses Inside
Node	(°C)	(°C)	(°C)	(in)	(in^2)	(in^2)	Area 1	Area 2	C.G. 1	C.G. 2	(kip)	(kip*in)	(ksi)	(ksi)	(ksi)	(ksi)
1	29.50	19.40	14.20	8.0	96	512	98	67	2.14	-1.90	60.75	-30.04	0.272	-0.197	0.534	-0.459
5	6.40	2.50	0.60	12.0	144	1728	27	9	3.44	-2.39	13.25	-25.62	0.104	-0.074	0.182	-0.151
8	8.60	3.70	0.80	11.0	132	1331	34	12	3.12	-2.16	17.01	-28.96	0.135	-0.104	0.235	-0.204

Negative Gradient P16-17

Transverse Gradient Analysis

Material Properties	
Coefficient of Thermal Expansion:	5.20E-06 / °F
Modulus of Elasticity:	5900 ksi

Node	Outside Temp. (°C)	Middle Temp. (°C)	Inside Temp. (°C)
1	-21.5	-16.7	-14.1
2	-21.2	-15.4	-12.2
3	-16.7	-8.5	-4.3
4	-9.3	-5.9	-4.3
5	-11.4	-8.3	-6.4
6	-14.1	-9.8	-8.0
7	-14.4	-10.7	-7.9
8	-13.3	-9.7	-7.4

	Average Temperatures												RISA2D Results		Unrestrained Force Results	
Member	Outside Temp. (°C)	Middle Temp. (°C)	Inside Temp. (°C)	Average Thickness (in)	Area (in^2)	Inertia (in^2)	Temp. Area 1	Temp. Area 2	Temp. C.G. 1	Temp. C.G. 2	N (kip)	M (kip*in)	Axial (kip)	Moment (kip*in)	Axial (kip)	Moment (kip*in)
1	-21.35	-16.05	-13.15	8.0	96	512	-75	-58	2.09	-1.93	-49.04	16.10	-48.92	1.88	-0.12	-14.22
2	-18.95	-11.95	-8.25	15.5	186	5832	-120	-78	4.17	-3.64	-72.90	78.87				
3	-13.00	-7.20	-4.30	14.5	174	10000	-73	-42	3.97	-3.32	-42.31	56.12				
4	-10.35	-7.10	-5.35	12.0	144	1728	-52	-37	3.19	-2.86	-33.02	22.09	-33.06	-0.84	0.04	-22.93
5	-12.75	-9.05	-7.20	12.0	144	1728	-65	-49	3.17	-2.89	-42.03	24.52				
6	-14.25	-10.25	-7.95	10.5	126	1158	-64	-48	2.77	-2.51	-41.27	21.31				
7	-13.85	-10.20	-7.65	11.0	132	1331	-66	-49	2.89	-2.62	-42.42	23.02	-42.54	-3.70	0.12	-26.72

													Internal Stresses		Total Stresses	
Node	Outside Temp. (°C)	Middle Temp. (°C)	Inside Temp. (°C)	Average Thickness (in)	Area (in^2)	Inertia (in^2)	Temp. Area 1	Temp. Area 2	Temp. C.G. 1	Temp. C.G. 2	N (kip)	M (kip*in)	Outside (ksi)	Inside (ksi)	Outside (ksi)	Inside (ksi)
1	-21.50	-16.70	-14.10	8.0	96	512	-76	-62	2.08	-1.94	-50.81	14.53	-0.130	0.097	-0.243	0.207
5	-11.40	-8.30	-6.40	12.0	144	1728	-59	-44	3.16	-2.87	-37.99	22.09	-0.086	0.067	-0.139	0.121
8	-13.30	-9.70	-7.40	11.0	132	1331	-63	-47	2.89	-2.63	-40.60	21.90	-0.100	0.081	-0.180	0.162

REFERENCES

1. *AASHTO Guide Specifications for Design and Construction of Segmental Concrete Bridges*. American Association of State Highway and Transportation Officials. 1989.

2. *AASHTO LRFD Bridge Design Specifications*. 1st ed. American Association of State Highway and Transportation Officials. 1994.

3. *AASHTO Standard Specifications for Highway Bridges*. American Association of State Highway and Transportation Officials. 1989.

4. Andres, V. A. "Verification of Force Distribution in an Innovative Bridge Pier." Master's Thesis. The University of Texas at Austin. Austin, TX. December, 1995.

5. Arréllaga, J. A. "Instrumentation Systems for Post-Tensioned Segmental Box Girder Bridges." Master's Thesis. The University of Texas at Austin. Austin, TX. December, 1991.

6. Bonzon, W. S. "Thermal Gradients in Segmentally Constructed Hollow Box Bridge Piers." Master's Thesis. The University of Texas at Austin. Austin, TX. December, 1996.

7. Davis, R. T. "Measurement Based Performance Evaluation of a Segmental Concrete Bridge." Ph.D. Dissertation. The University of Texas at Austin. Austin, TX. May, 1998. *(expected data of completion)*

8. Hyzak, M. D. "Bridge Deformation Monitoring." Master's Thesis. The University of Texas at Austin. Austin, TX. May, 1998. *(expected data of completion)*

9. Kollbrunner, C. F. and K. Basler. *Torsion in Structures*. Springer-Verlag Berlin/Heidelburg. New York. 1969.

10. Kristek, V. *Theory of Box Girders*. John Wiley and Sons. New York. 1979.

11. Menn, C. *Prestressed Concrete Bridges*. Bérkhäuser Verlag. Basel, Germany. 1990.

12. Nakai, H. and C. H. Yoo. *Analysis and Design of Curved Steel Bridges*. McGraw-Hill, Inc. New York. 1988.

13. *1983 Ontario Highway Bridge Design Code*. Highway Engineering Division. Toronto, Ontario. 1983.

14. Petroski, H. *Engineers of Dreams*. Alfred A. Knopf. New York. 1995.

15. Podolny, W., Jr. and J. M. Muller. *Construction and Design of Prestressed Concrete Segmental Bridges*. John Wiley and Sons, Inc. New York. 1982.

16. Potgieter, I. C. and W. L. Gamble. “Response of Highway Bridges to Nonlinear Temperature Distributions.” Report No. FHWA/IL/UI-201. University of Illinois at Urbana-Champaign. Urbana, IL. April, 1983.

17. *Proposed AASHTO Guide Specifications for Design and Construction of Segmental Concrete Bridges*. American Association of State Highway and Transportation Officials. March, 1997.

18. RISA2D. v3.03. Program for DOS. RISA Technologies. Lake Forest, CA. 1993.

19. Roberts, C. L., J. E. Breen, and M. E. Kreger. “Measurement Based Revisions for Segmental Bridge Design and Construction Criteria.” Report No. CTR 0-1234-3F. Center for Transportation Research. The University of Texas at Austin. Austin, TX. August, 1993.

20. Ryals, K. K., J. E. Breen, and M. E. Kreger. “Fretting Fatigue in External Post-Tensioned Tendons.” Report No. CTR 3-5-89/2-1211-1F. Center for Transportation Research. The University of Texas at Austin. Austin, TX. December, 1992.

21. “Steel, Concrete and Composite Bridges, Part I, General Statement.” British Standard BS 5400. British Standards Institution. Crowthorne. Berkshire, England. 1978.

22. Wood, B. A. “Thermal Gradients and Their Effects on Segmental Concrete Box Girder Bridges.” Master’s Thesis. The University of Texas at Austin. Austin, TX. August, 1997.